



OBSERVATOIRE DE LA COTE D'AZUR

OBSERVATOIRE DE PARIS
SYSTÈMES DE RÉFÉRENCE TEMPS-ESPACE
UMR8630 / CNRS, PSL

Time and General Relativity

Temps et relativité générale

JOURNÉES 2023 ☆

SYSTÈMES DE RÉFÉRENCE SPATIO-TEMPORELS

☆ NICE, 11-13 SEPTEMBER

OBSERVATOIRE DE LA COTE D'AZUR

OBSERVATOIRE DE PARIS
SYSTÈMES DE RÉFÉRENCE TEMPS-ESPACE
UMR8630 / CNRS, PSL

Time and General Relativity

Temps et Relativité Générale

Edited by

Actes publiés par

C. BIZOUARD, A. FIENGA & F. PAGANELLI

ISBN 978-2-901057-74-1

JOURNÉES 2023 ☆

SYSTÈMES DE RÉFÉRENCE SPATIO-TEMPORELS

☆ NICE, 11-13 SEPTEMBER



TABLE OF CONTENTS

PREFACE	v
ORGANIZING COMMITTEE	vi
LIST OF PARTICIPANTS	vii
SCIENTIFIC PROGRAM	ix
LIST OF POSTERS	xiii
SESSION I: Reference Systems - Earth Rotation	1
Bizouard C., Becker O., Bourgoïn A.: Evolution of the applications of the Earth rotation time	3
Biskupek L., Müller J.: Determination of earth orientation parameters from Lunar Laser Ranging data	12
Pavlov D.: Prospects and caveats of determining Earth Orientation Parameters from Lunar Laser Ranging data	19
Naghibi E., Delizo-Salabit C., Karabasov S.: Excitations of the Earth's Chandler wobble and length of day by the southern ocean	25
Escapa A., Baenas T., Ferrándiz J. M.: Effect of the tidal mass redistribution on the Earth secular changes in Length of Day	33
Davis M., Byram S., Stamatakos N.: Recent improvements to the IERS Rapid Service / Prediction Center combined EOP solution	39
Escapa A., Baenas T., Ferrándiz J. M.: A revised value of the Earth dynamical ellipticity $H_{IAU2006}$	45
SESSION I: Reference System - Space and time	49
Schlicht A., Marz S., Vollmair P.: How to establish a geodesy and time reference in space?	51
Baguet D., Rambaux N., Fienga A., Briaud A., Hussmann H., Gastineau M.: Introduction of tidal models in lunar ephemerides	58
Osetrova A., Titov O., Melnikov A.: Radio sources with large changes in the apparent coordinates	64
Hilton J.L., Makarov V.V., Kaplan G.H., Hennessey G.S.: A proposal for using Very Long Baseline Interferometer observations to improve lunar ephemerides	73
Defraigne P., Meynadier F., Tavella P.: Looking for a lunar reference timescale	81
Archinal B., Conrad A., Duxbury T., Hestroffer D., Jorda L., Kirk R., Klioner S., Margot J.-L., Oberst J., Paganelli F., Ping J., Seidelmann K., Tholen D., Williams I.: The cartographic lunar reference frame	87
Hu H., Tang K.: Lunar declination angle with global great earthquakes	94
Zhang J., Zhang B.: VLBI astrometry of radio stars to link radio and optical celestial reference frames	99
SESSION II : Time - Measurement, transfer and dissemination	103
Kopf A. J.: Taking the leap: the move to continuous UTC	105
Bourgoïn A., Teysandier P., Tortora P., Zannon M. : Time and frequency transfers in optical spacetime	108
Titov O.: The VLBI correlator ambiguity and the relativistic group delay model	118
SESSION III : General Relativity: recent highlights and tests in solar system	123
Bizouard M. A.: Recent findings in ground-based gravitational-wave detectors	125
Chalumeau A.: Results from the search for the very-low frequency gravitational waves with the EPTA DR2 and the InPTA DR1	135

Métris G., Rodrigues M., Bergé J.: The microscope space mission to test the equivalence principle	143
Fienga A., Minazzoli O., Mariani V., Hees A., Bernus L., Di Ruscio A., Durante D., Gastineau M., Laskar J., Iess L.: Testing General Relativity and alternative theories with Planetary and Lunar Ephemerides	152
Pavlov D., Dolgakov I.: General relativity tests by the dynamics of the solar system . . .	156
Tian W.: Relativistic tests with Lunar Laser Ranging and planetary radio tracking data .	161
Mariani V., Fienga A., Minazzoli O., Laskar J., Gastineau M.: Bayesian approaches for orbitography: application to fundamental physics	168
Minazzoli O.: Solar system phenomenology of entangled relativity	176
Zschocke S.: Total light deflection in the gravitational field of solar system bodies . . .	184

PREVIOUS JOURNEES **193**

PREFACE

Four years after the *Journées Astrometry, Earth Rotation and Reference Systems in the Gaia Era* organized by the Observatoire de Paris at Sorbonne University in October 2019, the twenty-third edition of the Journées colloquium took place from 11 to 13 September 2023 in Nice at Université Côte d'Azur and Observatoire de la Côte d'Azur.

During three decades the Journées "saga", such coined by Yaroslav Yatskiv in Alicante, held in Paris and in other European cities, was lead by Nicole Capitaine. Since 2017 its organisation was entrusted to the second generation of scientists involed in space geodesy and astrometry. This is an unique forum devoted to the topic of space-time reference systems, involving both the techniques that allow to realize them and their fondamental or pratical applications, sweeping astrometry, astro-geodesy, and solar system dynamics. Its organization has been the result of an active and continuing cooperation between the *Systèmes de Référence Temps Espace* Department (SYRTE) of Paris Observatory and other European institutions. Although this is a European conference, experts from every continent are taking part. During the latest meeting there were attendants coming from Europa, Asia, America, and Oceania. The scientific program included 57 oral talks and 12 posters.

The colloquium was split in three sessions. The first covered the topic of space-time reference systems and their realisation, considering also the determination, application, and prediction of Earth rotation changes. With 5 talks and 3 posters a special attention was paid to the development of space-time Lunar reference systems. The second session was more specifically devoted to the time and frequency, considering their measurements, transfer and dissemination. Finally the third session treated General Relativity tests in the solar system.

For the third time, the Journées proceedings are not in paper format but limited to an electronic edition, that can be downloaded from: <https://syрте.obspm.fr/astro/journees2023/LATEX/JOURNEES2023.pdf> along with the slides of the oral presentations and posters. Having estimated that their results are too preliminary or are already published in peer-reviewed journal, some authors did not submit paper.

The proceedings availability will be maintained for years. They will also be put on an electronic archive. Flora Paganelli has extensively contributed to the review of the submitted papers, bringing many editing corrections. Olivier Becker set up the upolad system and the LateX layout.

We want to thank all the participants in these Journées, particularly the invited speakers and the SOC members for their excellent presentations and their invaluable commitment.

We acknowledge the support received from the University Côte d'Azur and the Observatoire de la Côte d'Azur. But, before all, we congratulate the members of the Local Organizing Committee for their work, contributing to open and fruitful scientific exchanges.

Agnès FIENGA, Chair of the LOC, Christian BIZOUARD, Chair of the SOC
15 September 2024

Scientific Organizing Committee

BIZOUARD Christian, *Observatoire de Paris, IERS*, France

DEFRAIGNE Pascale, *Observatoire Royal de Belgique*, Belgium

ESCAPA Alberto, *University of León*, Spain

FIENGA Agnès, *Observatoire de la Côte d'Azur*, France

GROSS Richard, *Jet Propulsion Laboratory*, USA

KLIONER Sergei, *Lohrmann Observatorium, Technische Universität Dresden*, Germany

NASTULA Jolanta, Co-chair, *Centrum Badan Kosmicznych PAN*, Poland

Local Organizing Committee

BARACHE Christophe, *Observatoire de Paris*, France

AUFEUVRE Magali, *GeoAzur*, France

BECKER Olivier, *Observatoire de Paris*, France

BOUGHADEMI Alexandre, *Université Côte d'Azur*, France

FIENGA Agnès, *Observatoire de la Côte d'Azur*, France

MARIANI Vincenzo, *Université Côte d'Azur*, France

MERCIER Valérie, *Université Côte d'Azur*, France

LIST OF PARTICIPANTS

Archinal Brent (planetmeasurer@gmail.com)
Baguet Daniel (daniel.baguet@gmail.com)
Bellerose Julie (julie.bellerose@jpl.nasa.gov)
Bertrand Bruno (bruno.bertrand@oma.be)
Biskupek Liliane (biskupek@ife.uni-hannover.de)
Bizouard Christian (christian.bizouard@obspm.fr)
Bizouard Marie Anne (marianne.bizouard@oca.eu)
Boughanemi Alexandre (alexandre.boughanemi@gmail.com)
Bourgoin Adrien (adrien.bourgoin@obspm.fr)
Briaud Arthur (briaud@geoazur.unice.fr)
Chalumeau Aurélien (aurelien.chalumeau@unimib.it)
CHENG Yuting (yu-ting.cheng@obspm.fr)
Cleva Frederic (cleva@oca.eu)
Colmenares Nicholas (nicholas.r.colmenares@nasa.gov)
Courde Clément (clement.courde@geoazur.unice.fr)
Davis Maria (maria.a.davis33.civ@us.navy.mil)
Defraigne Pascale (p.defraigne@oma.be)
Dell Simone 'Agnello (simone.dellagnello@Inf.infn.it)
Deng Huarong (dhr@shao.ac.cn)
Dill Robert (dill@gfz-potsdam.de)
Eckl Johann (johann.eckl@bkg.bund.de)
Escapa Alberto (alberto.escapa@unileon.es)
Thomas Marshall Eubanks (tme@space-initiatives.com)
Ferguson Michael (fergie@jpl.nasa.gov)
José Manuel Ferrándiz (jm.ferrandiz@ua.es)
fienga agnes (agnes.fienga@oca.eu)
Fu Honglin (fhl@ynao.ac.cn)
gao Jian (gaoj@cho.ac.cn)
Gross Richard (Richard.Gross@jpl.nasa.gov)
Guo Jiang (jiang.guo@oma.be)
Haifeng Zhang (hfzfhz@126.com)
Hanssen James (james.l.hanssen.civ@us.navy.mil)
Hees Aurelien (aurelien.hees@obspm.fr)
Heinkelmann Robert (heinkelmann@gfz-potsdam.de)
Hestroffer Daniel (hestro@imcce.fr)
Hilton James (james.l.hilton12.civ@us.navy.mil)
Huang Yong (yongh@shao.ac.cn)
Jacobs Christopher (Chris.Jacobs@jpl.nasa.gov)
Klioner Sergei (Sergei.Klioner@tu-dresden.de)
Kopf Andy (andrew.j.kopf.civ@us.navy.mil)
Li Zhulian (lzh@ynao.ac.cn)
Li Yuqiang (recobaself@163.com)
Makley Nick (nicholas.r.makley@nga.mil)
Mariani Vincenzo (vmariani@geoazur.unice.fr)
Mariey Hervé (herve.mariety@oca.eu)
Mercier Valerie (valerie.mercier@geoazur.unice.fr)

Metris Gilles (Gilles.Metris@geoazur.unice.fr)
two Meynadier Frédéric (Frederic.Meynadier@bipm.org)
Michalczak Maciej (mmichalc@agh.edu.pl)
Miltiadis Chatzinikos (Miltiadis.Xatzinikos@obspm.fr)
Minazzoli Olivier (ominazzoli@gmail.com)
Moffett Mark (mark.moffett@ukho.gov.uk)
Müller J ürgen (mueller@ife.uni-hannover.de)
Naghibi Elnaz (elnaz.naghibi@gmail.com)
Nastula Jolanta (nastula@cbk.waw.pl)
Paganelli Flora (fpaganel@nrao.edu)
Park Ryan (Ryan.S.Park@jpl.nasa.gov)
Partyka Aleksander (apartyka@cbk.waw.pl)
peil steve (steven.e.peil.civ@us.navy.mil)
Petrov Leonid (Leonid.Petrov@lpetrov.net)
Pinat Elisa (elisa.pinat@oma.be)
Radulesco Nicholas (Nicholas.Radulesco@oca.eu)
Rambaux Nicolas (Nicolas.Rambaux@obspm.fr)
Schlicht Anja (anja.schlicht@tum.de)
Sonia Guessoum (gs74@gcloud.ua.es)
Stamatakos Nicholas (nicholas.g.stamatakos.civ@us.navy.mil)
Stewart Susan (susan.stewart25.civ@us.navy.mil)
Tang Kai (tangkai@shao.ac.cn)
Tanga Paolo (Paolo.Tanga@oca.eu)
Taris Franç ois (francois.taris@obspm.fr)
Tavella Patrizia (patrizia.tavella@bipm.org)
Tian Wei (tianwei@shao.ac.cn)
Titov Oleg (oleg.titov@ga.gov.au)
Vollmair Peter (peter.vollmair@tum.de)
Wilmot Toni (toni.wilmot@ukho.gov.uk)
Winska Malgorzata (malgorzata.winska@pw.edu.pl)
Xu Minghui (minghui.xu@gfz-potsdam.de)
Yang Yongzhang (yang.yongzhang@ynao.ac.cn)
Jingdong Zhang (zhangjingdong@shao.ac.cn)
Zhongping Zhang (zpzpzp7821@163.com)
Sven Zschocke (sven.zschocke@tu-dresden.de)

SCIENTIFIC PROGRAMME

Monday September 11

08:15-09:00 Registration - Registration

09:00-09:15 Welcome (Theatre) - Agnès Fienga - Christian Bizouard

09:15-10:50 Reference System (Theatre) - Earth Rotation Determination / application

09:15-09:50 : Advances in estimation of the Earth orientation parameters from observation - *Leonid Petrov, NASA Goddard Space Flight Center*

09:50-10:05 : Evolution of the applications of the Earth rotation time - *Christian Bizouard, Observatoire de Paris SYRTE UMR8630 - GRGS*

10:05-10:20 : The JTRF2020 EOP Series - *Richard Gross, Jet Propulsion Laboratory, California Institute of Technology*

10:20-10:35 : Determination of Earth orientation parameters from Lunar Laser Ranging data - *Liliane Biskupek, Institute of Geodesy, Leibniz University Hannover*

10:35-10:50 : Prospects and caveats of determining Earth orientation parameters from lunar laser ranging data - *Dmitry Pavlov, St. Petersburg State University*

10:50-11:20 Coffee Break (Salle des actes)

11:20-12:20 Reference System (Theatre) - Earth orientation modeling

11:20-11:35 : Excitations of the Earth's Chandler wobble and length of day by the Southern Ocean - *Elnaz Naghbi, University of East London*

11:35-11:50 : Effect of the tidal mass redistribution on the Earth secular changes in length of day - *Alberto Escapa, Department of Aerospace Engineering, University of León, 24071 León, Spain*

11:50-12:05 : A new Earth's post-Newtonian long-term precession model - *Kai Tang, Shanghai Astronomical Observatory, Chinese Academy of Science*

12:05-12:20 : How to establish a geodesy and time reference in space? - *Anja Schlicht, FESG, Technical University of Munich*

12:20-13:45 Lunch (Salle des actes)

13:45-15:00 Reference System (Theatre) - Earth orientation Prediction

13:45-14:00 : Recent and future improvements to the IERS Rapid Service / Prediction Center combined EOP solution - *Maria Davis, U.S. Naval Observatory*

14:00-14:15 : Do we need model-based EAM forecast longer than 6-days to improve EOP predictions? - *Robert Dill, GFZ Potsdam*

14:15-14:30 : Short-term prediction of UT1-UTC and LOD obtained via Dynamic Mode Decomposition and Vector Autoregressive Model. - *Maciej Michalczak, AGH University of Krakow*

14:30-14:45 : Summary of the Second Earth Orientation Parameters Prediction Comparison Campaign achievements in terms of Earth rotation parameters - *Jolanta Nastula, Centrum Badań Kosmicznych Polskiej Akademii Nauk (CBK PAN)*

14:45-15:00 : The short-term prediction of Polar Motion and LOD using the Multivariate Multistep 1D Convolutional Neural Networks with Multioutput strategy. - *Guessoum Sonia, Sonia Guessoum, Santiago Belda, Jose M. Ferrandiz, Sadegh Modiri, Sujata Dhar, Robert Heinkelmann, Harald Schuh*

15:00-15:30 Coffee break (Salle des actes)

15:30-17:20 Reference System (Theatre) - Space and Time

- 15:30-16:05 : The K-band (24 GHz) Celestial Reference Frame: Current Status and Roadmap - *Christopher Jacobs, Jet Propulsion Laboratory - California Institute of Technology*
- 16:05-16:20 : Case study of position differences between VLBI and Gaia - *Minghui Xu, German Research Centre for Geosciences - Helmholtz-Centre Potsdam*
- 16:20-16:35 : Introduction of tidal models in lunar ephemerides - *Daniel Baguet, Institut de Mécanique Céleste et de Calcul des Ephémérides*
- 16:35-16:50 : Radio Sources with large changes in the apparent coordinates - *Angelina Osetrova, St. Petersburg University*
- 16:50-17:05 : A Proposal for Using Very Long Baseline Interferometer Observations to Improve Lunar Ephemerides - *James Hilton, U.S. Naval Observatory*
- 17:05-17:20 : The lunar solid inner core and the mantle overturn - *Arthur Briaud, Observatoire de la Côte d'Azur*

17:20-17:30 Reference System (Salle des actes) - Poster Session

- 17:20-17:22 : Contributions of GNSS observations to UT1 in the ultra-rapid and subdiurnal bands - *Yuting CHENG, SYRTE*
- 17:22-17:24 : A revised value of the Earth dynamical ellipticity HIAU2006 - *Escapa Alberto, University of León*
- 17:24-17:26 : Analysis of the EOP reference series and their impact on the analysis of the Second Earth Orientation Parameters Prediction Comparison Campaign (2nd EOP PCC) results - *Aleksander Partyka, Centrum Bada? Kosmicznych PAN*
- 17:26-17:28 : Assessment of precession-nutation predictions based on the results of the Second Earth Orientation Parameters Prediction Comparison Campaign (2nd EOP PCC) - *Malgorzata Winska, Warsaw University of Technology [Warsaw]*

Tuesday, September 12, 2023

09:00-10:35 Time (Theatre) - Measurement, transfert and dissimulation

- 09:00-09:35 : Towards a continuous UTC - *Patrizia TAVELLA, Bureau International des Poids et Mesures*
- 09:35-09:50 : Taking the Leap: Moving to Continuous UTC - *Andy Kopf, United States Naval Observatory*
- 09:50-10:05 : Colocation of high-precision geodetic observation methods for time synchronization in context of the ACES-Mission: a simulation study - *Peter Vollmair, FESG*
- 10:05-10:20 : Time and frequency transfers in optical spacetime - *Adrien Bourgoin, Systèmes de Référence Temps Espace*
- 10:20-10:35 : The developments of Laser Timer Transfer with Chinese Space Station - *Zhang Haifeng, Shanghai Astronomical Observatory of Chinese Academy of Sciences*
- 10:35-11:05 Coffee break (Salle des actes)

11:05-12:05 Time (Theatre) - Measurement, transfert and dissimulation

- 11:05-11:20 : The VLBI correlator ambiguity and the relativistic group delay model - *Oleg Titov, Geoscience Australia*
- 11:20-11:35 : GPS/Galileo IPPP time links of ROB based on Atomium software - *Jiang Guo, Royal Observatory of Belgium*

11:35-11:50 : Could optical atomic clocks contribute to the study of the Earth's temporal gravity field variations? - *Chatzinikos Miltiadis, Observatoire de Paris*

11:50-11:55 Time (Salle des actes) - Poster Session

11:50-11:52 : Mission of lunar orbiter of CAS and Laser Time Transfer - *Zhongping Zhang, Shanghai Astronomical Observatory of Chinese Academy of Sciences - Deng Huarong, Shanghai Astronomical Observatory of Chinese Academy of Sciences*

11:52-11:54 : Time synchronization for Bi-static Laser Ranging via Fiber-based Time and Frequency Transfer - *Huarong Deng, Shanghai Astronomical Observatory of Chinese Academy of Sciences*

11:55-13:30 Lunch (Salle des actes)

13:30-14:45 Reference System (Theatre) - Lunar space-time reference system

13:30-13:45 : Relativistic reference systems and time scales for all solar system bodies using the IAU 2000 framework - *Sergei Klioner, Lohrmann-Observatorium, Technische Universität Dresden*

13:45-14:00 : Looking for a Lunar Reference Timescale - *Pascale Defraigne, Royal Observatory of Belgium [Brussels]*

14:00-14:15 : Relativistic Lunar Time, Lunar Dynamics and A Proposal for an Adjusted Lunar Time - *Thomas Marshall Eubanks, Space Initiatives Inc*

14:15-14:30 : The Cartographic Lunar Reference Frame - *Brent Archinal, U. S. Geological Survey, Astrogeology Science Center, 2255 N. Gemini Drive, Flagstaff, AZ 86004; barchinal@usgs.gov*

14:30-14:45 : Emerging Lunar Standards - *Susan Stewart, U.S. Naval Observatory*

14:45-15:15 Coffee break (Salle des actes)

15:15-16:35 General Relativity (Theatre) - Recent Highlights

15:15-15:50 : Recent findings of the LIGO-Virgo-KAGRA collaboration - *Marie Anne Bizouard, Astrophysique Relativiste Théories Expériences Métrologie Instrumentation Signaux*

15:50-16:05 : Results from the search for very-low frequency gravitational waves with the EPTA DR2 and InPTA DR1 - *Aurélien Chalumeau, Dipartimento di Fisica "Giuseppe Occhialini" = Department of Physics "Giuseppe Occhialini" [Milano-Bicocca]*

16:05-16:20 : The MICROSCOPE experiment to test the Equivalence Principle in space - *Gilles METRIS, Observatoire de la Côte d'Azur*

16:20-16:35 Reference System (Salle des actes) - Poster session II

16:20-16:22 : Lunar declination angle with global great earthquakes - *Kai Tang, Shanghai Astronomical Observatory, Chinese Academy of Science*

16:22-16:24 : VLBI Astrometry of Radio Stars to Link Radio and Optical Celestial Reference Frames - *Jingdong Zhang, Shanghai Astronomical Observatory, University of Chinese Academy of Sciences [Beijing]*

16:24-16:26 : The X/Ka 2023b Celestial Frame - *Christopher Jacobs, Jet Propulsion Laboratory - California Institute of Technology*

16:26-16:28 : The XS Celestial (8 GHz) Reference Frame: current status and plans - *Christopher S. Jacobs, Jet Propulsion Laboratory, California Institute of Technology*

16:28-16:30 : Imaging, modelfitting and source structure corrections for the K-band (24 GHz) Celestial Reference Frame - *Christopher Jacobs, Jet Propulsion Laboratory, California Institute of Technology*

16:30-16:32 : K-band (24 GHz) Celestial Reference Frame - *Christopher S. Jacobs, et Propulsion Laboratory - California Institute of Technology*

16:32-16:34 : Lunar reference systems framework - *Nicolas Rambaux, Sorbonne Université, Institut de Mécanique Céleste et Calcul des Ephémérides*

19:00-22:30 Visit and Dinner at the Mont-Gros

Visit of the Grande Coupole designed by G. Eiffel and the Universarium museum and Dinner

Wednesday, September 13, 2023

09:05-10:35 General Relativity (Theatre) - Tests in the solar system

09:05-09:20 : Testing General relativity with planetary ephemerides - *Agnes Fienga, Geoazur*

09:20-09:35 : General relativity tests by the dynamics of the Solar system - *Dmitry Pavlov, St. Petersburg State University*

09:35-09:50 : Relativistic tests with lunar laser ranging and planetary radio tracking data - *Wei Tian, Shanghai Astronomical Observatory, Chinese Academy of Science*

09:50-10:05 : Using LLR Data for Testing Various Versions of the Equivalence Principle - *Jürgen Müller, Leibniz University Hannover, Institute of Geodesy*

10:05-10:35 Coffee break (Salle des actes)

10:35-12:20 General Relativity (Theatre) - Tests in the solar system II

10:35-10:50 : Bayesian test of the mass of the graviton with planetary ephemerides - *Vincenzo Mariani, Geoazur, Observatoire de la Côte d'Azur*

10:50-11:05 : Searching for large dark matter clumps using the Galileo Satnav clock variations - *Bruno Bertrand, Royal Observatory of Belgium*

11:05-11:20 : Questioning the Planck Time: Is It Truly an Elementary Unit of Time? - *Olivier Minazzoli, ARTEMIS UMR 7250*

11:20-11:35 : Total light deflection in the gravitational field of solar system bodies - *Zschocke Sven, Technical University Dresden*

12:20-14:00 Lunch (Salle des actes)

LIST OF POSTERS

Reference System - Poster Session I

- Contributions of GNSS observations to UT1 in the ultra-rapid and subdiurnal bands - Yuting CHENG, SYRTE
- A revised value of the Earth dynamical ellipticity HIAU2006 - Escapa Alberto, University of León
- Analysis of the EOP reference series and their impact on the analysis of the Second Earth Orientation Parameters Prediction Comparison Campaign (2nd EOP PCC) results - Aleksander Partyka, Centrum Bada? Kosmicznych PAN
- Assessment of precession-nutation predictions based on the results of the Second Earth Orientation Parameters Prediction Comparison Campaign (2nd EOP PCC) - Malgorzata Winska, Warsaw University of Technology [Warsaw]

Time

- Mission of lunar orbiter of CAS and Laser Time Transfer - Zhongping Zhang, Shanghai Astronomical Observatory of Chinese Academy of Sciences - Deng Huarong, Shanghai Astronomical Observatory of Chinese Academy of Sciences
- Time synchronization for Bi-static Laser Ranging via Fiber-based Time and Frequency Transfer - Huarong Deng, Shanghai Astronomical Observatory of Chinese Academy of Sciences

Reference System - Poster session II

- Lunar declination angle with global great earthquakes - Kai Tang, Shanghai Astronomical Observatory, Chinese Academy of Science
- VLBI Astrometry of Radio Stars to Link Radio and Optical Celestial Reference Frames - Jingdong Zhang, Shanghai Astronomical Observatory, University of Chinese Academy of Sciences [Beijing]
- The X/Ka 2023b Celestial Frame - Christopher Jacobs, Jet Propulsion Laboratory - California Institute of Technology
- The XS Celestial (8 GHz) Reference Frame: current status and plans - Christopher S. Jacobs, Jet Propulsion Laboratory, California Institute of Technology
- Imaging, modelfitting and source structure corrections for the K-band (24 GHz) Celestial Reference Frame - Christopher Jacobs, Jet Propulsion Laboratory, California Institute of Technology
- K-band (24 GHz) Celestial Reference Frame - Christopher S. Jacobs, et Propulsion Laboratory - California Institute of Technology
- Lunar reference systems framework - Nicolas Rambaux, Sorbonne Université, Institut de Mécanique Céleste et Calcul des Ephémérides

Session Ia

REFERENCE SYSTEMS : EARTH ROTATION

EVOLUTION OF THE APPLICATIONS OF THE EARTH ROTATION TIME

Christian Bizouard, Olivier Becker, Adrien Bourgoïn

Observatoire de Paris - France - christian.bizouard@obspm.fr

ABSTRACT. In the 1930's the discovery of the instability of the Earth's rotation time shacked its status as Universal Time (UT), i.e. the world's standard clock. Until the 1970's, the instabilities of the Earth rotation time were more perceived as time defects to be eliminated in the realization of the UT, basis of any civil time, than an Earth Rotation Parameter to monitor for geophysical studies and achieving geolocalization. From 1955, it was renamed UT1 and UT2 for its deseasonalized version. Finally it was substituted in 1972 with the more stable Coordinated Universal Time (UTC), an atomic time, nevertheless kept synchronized with UT1 to within 0.9 s through the insertion of leap second since 1972, announced in IERS Bulletin C six months in advance. The radio-dissemination of UTC enabled the practice of star navigation at long distance to within 450 m, an error consistent with the optical observations. In 1988 with the demise of the Bureau International de l'Heure, the official determination of UT1 was entrusted to the International Earth Rotation Service created in 1987, and UT1 was incorporated into the Earth Orientation Parameters, that made possible to determine the rotation transformation between celestial and Earth-fixed space coordinate systems with an accuracy of 0.5 mas. Requesting today an error of 10 μ s on UT1 the Global Navigation Space Systems (GNSS), appeared in the 1990's, make the UTC approximation of UT1 to within 0.9 s - or even to within 0.1 s when incorporating IERS Bulletin D correction - obsolete. In this respect, UT1 is monitored daily by VLBI. Since the 1970's, UT1 irregularity has thwarted all prognoses, and its variations became an invaluable source of information on the Earth properties and the global processes that affect it, namely tides and geophysical fluid transports.

1. EARTH'S ROTATION TIME AS MEAN SOLAR TIME TILL THE 17TH CENTURY AND ITS OTHER AVATARS

Since the ancient times to nowadays, time computation has been linked to the counting of the Sun's diurnal cycles and of their parts. In civilian life, people used the duration from the Sunrise to the Sunset divided in twelve hours varying with the season, while, for astronomical dating, the astronomers considered the solar day between two successive noon, or apparent Solar Time (AST), measured by sundials.

However, due to the non-uniform Sun's motion, AST presents an inequality. Therefore it is replaced by the time of an imaginary uniformly moving Sun on the Equator — the Mean Solar Time, MST – by removing a correction called the equation of time (EOT):

$$\text{MST} = \text{AST} - \text{EOT} .$$

The EOT was first mentioned in Ptolemy's Almagest (2nd century), and its first correct expression was published by Huygens (1665).

Prior to the invention of accurate mechanical clocks in the mid-17th century, sundials were the only reliable timepieces, and AST was the generally accepted standard. Mean Solar Time began to supplant AST in national almanacs and ephemerides in the early 19th century.

The mean solar time of a given meridian represents the first realization of the Earth's rotation time (ERT) with the convention that $\text{ERT} = 12$ hours when the mean Sun crosses the meridian. As a time scale, ERT is composed of an integer number of mean solar day from an origin of date,

and a fraction of day. The ERT can be defined more generally from the rotation angle θ of a “zero” terrestrial meridian (Paris, Greenwich, etc..) with respect to a celestial origin located in the mean equatorial plane, given the analytic expression $\theta = f(ERT)$. With the mean Sun as celestial origin, a full period of rotation contain conventionally 24 hours or 86400 s, that will be considered as invariable until the beginning 20th century.

If we take for celestial origin the mean vernal point (free from nutation), the rotation period, namely the sidereal day, becomes $D_{sid} \approx 86164.0905$ s, and we obtain the so-called mean sidereal time, of which the most famous version, the Greenwich Mean Sidereal time (GMST), refers to the meridian of the Greenwich Observatory. Actually a part of the GMST variation is caused by the precession of the equinox, and a correction has to be applied to recover the pure Earth Rotation Angle (ERA) with respect to stars. Therefore, as favoured by the IAU since 2000, the mean vernal point was replaced by a non rotating origin on the true equator to obtain directly ERA, and in turn ERT or Universal Time 1 (UT1) through the linear law

$$ERA = ERA_0 + \Omega_{stel}(UT1 - UT1_0) \quad (1)$$

where $ERA_0 = 2\pi 0.779057273264 \approx -79.53^\circ$, the angular frequency Ω_{stel} corresponds to the rotation period $D_{stel} = 86164.0989$ s with respect to stars or 86400 s TAI with respect to the mean Sun – see Petit and Luzum (2014), Eq. 5.14. Notice that D_{stel} is about 1.3 ms larger than D_{sid} .

Until the 1980s, ERT was measured by observing the passage of the stars (GMST) or the passage of the sun (AST) in the meridian plane, using meridian circles (telescope mounted on a fixed, horizontal, east–west axis) or transit instruments (axis not necessarily fixed in the east-west direction).

2. ACCURACY OF MAN MADE CLOCKS UNTIL THE 1930

The Figure 1 illustrates the evolution of the precision of the man-made clocks since the apparition of weight-driven crown well in the 14 century. We notice that ERT was more stable than man-made clocks until the 1930s. As its access requires precise astronomical observations, it was “maintained” over periods of time shorter than a few days by mechanical clocks, of which the first generation, invented in the 14th c, was the weight-driven crown wheel.

3. FROM ZERO-MERIDIAN TIME KEEPING FOR NAVIGATION AND MAPPING TO UNIVERSAL TIME

While latitude determination was done to 1° since the antiquity by observing stars of know declination, obtaining the longitude with respect to a reference meridian was an hard task until the modern era.

The longitude λ of the local meridian with respect to a zero meridian can be determined from the hour angle H of a celestial body with known right ascension α if the Zero Mean Sidereal Time $ZMST(t)$ at the instant t of the observation, is known. Indeed, from Figure 2, we can see that $\lambda = \alpha + H - ZMST(t)$ (H is positive in the clockwise direction). So, the determination of longitude is linked with the knowledge of $ZMST(t)$ and finally to the Mean Solar Time $t = ERT$ of the zero meridian.

Until the 17th century, it was difficult and even impossible to transport the ERT of a reference meridian over long distance, mapping and navigation relied on a time deduced from lunar observations, with errors in longitude ranged from 2° to 25° . From the 18th century, mechanical clocks – notably thanks to the English inventor Harrison – started to insure a mobile time keeping of ERT over seas and long journey. It resulted considerable progress in navigation and mapping.

In the middle of the 19th century, the ERT, as the MST of some “zero” national meridian (Paris, Greenwich, Pulkovo, Washington, ...) began to be disseminated by telegraphs. Also essential

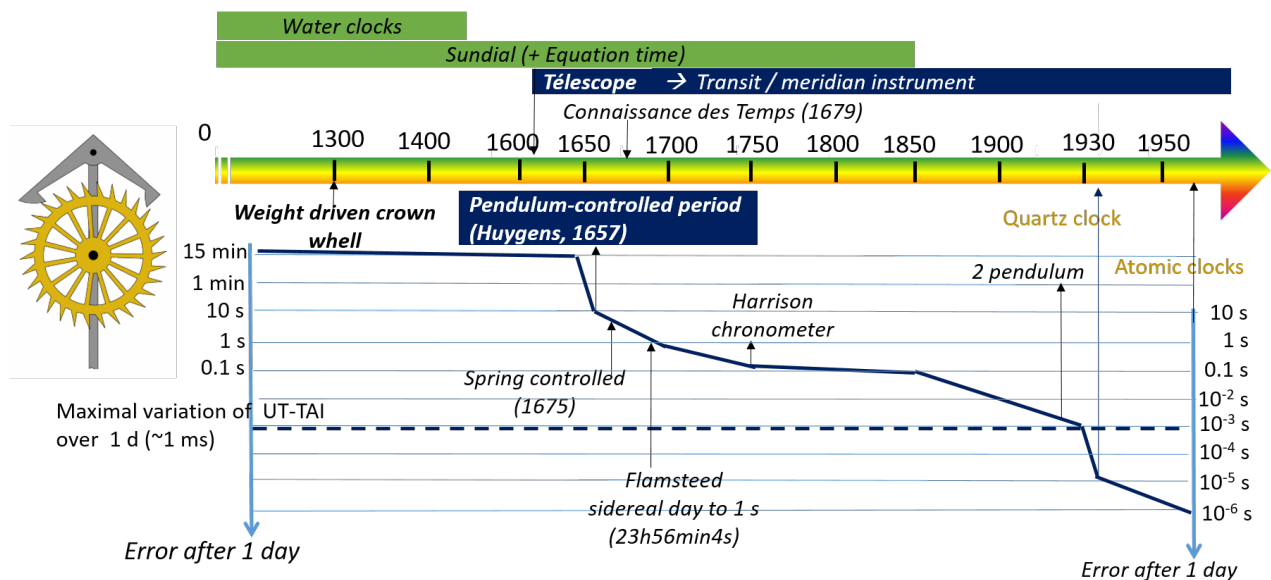


Figure 1: Evolution of the precision of the man-made clocks since the apparition of weight-driven crown wheel

for establishing coherent railway timetables, it became little by little the national time standard, replacing the local AST. In France, the MST of Paris Observatory that from 1826 began to define the legal time in Paris was gradually adopted by large French cities until it became the legal hour throughout France in 1891.

Growing international commerce and communications led a group of 26 nations to adopt in 1884 a single prime meridian, defining the international origin of longitude and the MST, known as Greenwich Mean Time (GMT), renamed Universal Time (UT) by the IAU in 1928.

Still, man-made clocks were not sufficiently synchronized with the Earth's rotation time, and GMT had to be adjusted through astronomical observations every few days. In the early the 20th Century, different radio services around the world began broadcasting in local time zones in relation to GMT (to within 1 s). In 1912, the BIH (Bureau international de l'heure) at the Paris Observatory began collecting those broadcasts: after elimination of their possible systematic errors and including Paris Observatory observations, the BIH could maintain and disseminate an universal version of GMT.

4. UT FLUCTUATIONS WITH RESPECT TO EPHEMERIS TIME

As early as 1686 Newton stated in his *Principia*:

It may be, that there is no such thing as an uniform motion, whereby time may be accurately measured.

In 1715 Flamsteed tried to measure variations in diurnal rotation speed with huge pendulums, in vain. Kant (1754) proposed the hypothesis of tidal braking:

Accordingly, there can be no further doubt that the perpetual motion of the world ocean from east to west, as it is a real and considerable force, always contributes somewhat to the diminution of the axial rotation of the Earth, the results of which must become infallibly perceptible over long periods.

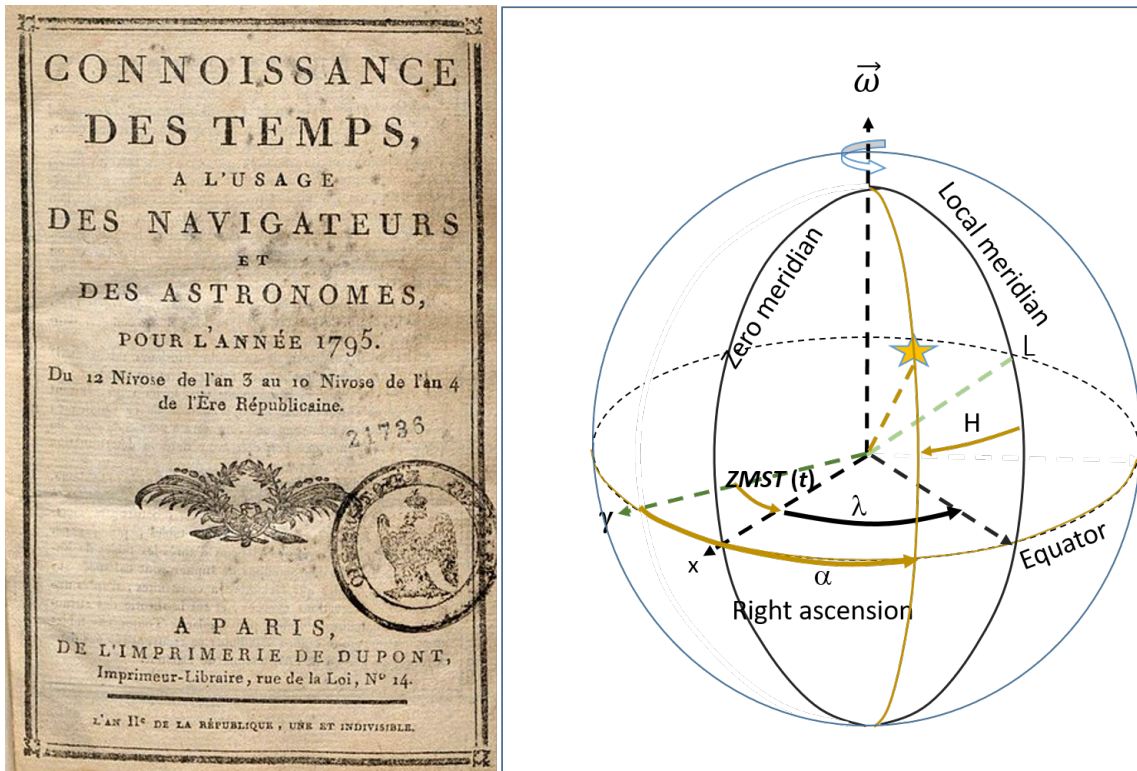


Figure 2: Principle of the longitude determination from stars

Laplace (1827) concluded that the influence of the global geophysical mass redistribution was out of reach of the observations of its epoch. The English geophysicist Darwin (1809-1882) proved that the mechanism of tidal braking involves a Moon's increasing distance.

If GMT (equivalently UT) is not uniform, it will fluctuate with respect to the Newtonian time t deduced from planet longitude L through its theoretical expression $L(t)$. There t is the Ephemeris Time (ET) formally defined in 1952 and continued by Terrestrial Time TT from the 1970's. As noticed by the American astronomer Newcomb (1835-1909), the Moon's and Mercure ephemeris calculated in UT did not agree with more recent observations. This questioned the uniformity of the Earth's rotation. Finally, de Sitter (1926) and Spencer Jones (1939) detected UT instability of up to 10 s over multi-decade periods, as shown in the left hand side of Figure 3. The corresponding length of day offset with respect to $D_0 = 86400$ s TAI, given by

$$\Delta D = D - D_0 = -D_0 \frac{d(UT - TT)}{dt}, \quad (2)$$

presents decennial variations of a few ms, as shown on the right hand side of Figure 3. Based on ancient solar eclipse records, the length of day increases over the long term at the rate of about 1.6 ms/cy, causing a parabolic variation in TT-UT as recorded over significant periods (Stephenson and Morrison, 1984).

5. UT VARIATIONS FROM MAN-MADE CLOCKS SINCE THE 1930's

From the 1930's the astronomical realisation of time through UT or ET began to face the competition of the artificial time realized by the quartz clocks based upon the piezoelectric phenomenon discovered in the 1880's. During the period 1935-1937, Scheibe and Adelsberger (1936) at the Physikalisch-Technischen Reichsanstalt (PTR, the today's PTB) found a seasonal variation

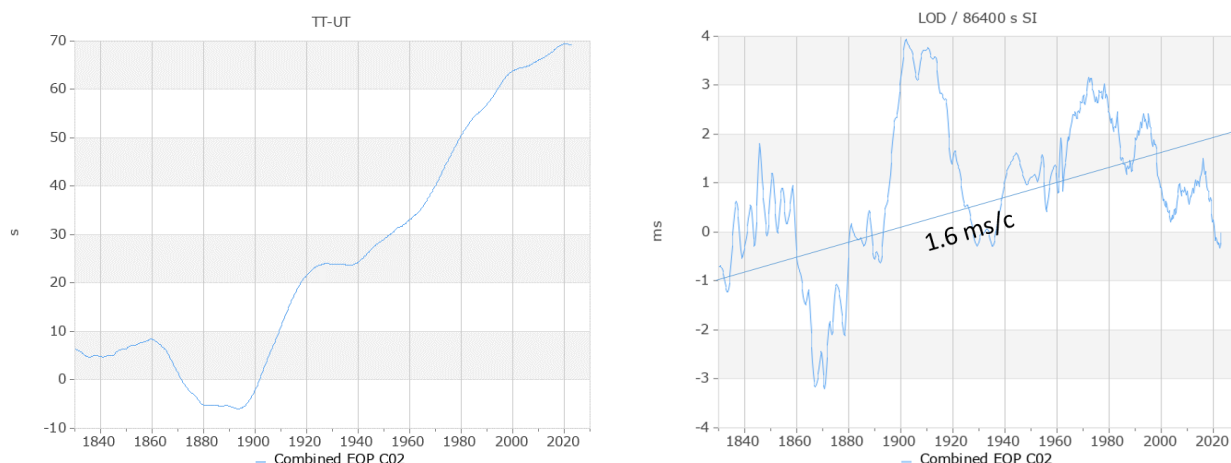


Figure 3: Decadal fluctuation of TT–UT (left) and Length of day offset with respect to 86400 s TAI (right)

in UT with respect to the quartz clocks they had realized. In the same time Nicolas Stoyko (1937) at Paris Observatory found a variation of about 0.02 s in the differences between the UT-aligned mechanical clocks of Paris Observatory/USNO and the time of the PTR quartz clocks obtained by radio receiver.

By the 1950s, the quartz oscillator could be coupled to an atomic resonator for enhanced timekeeping stability. That led to the adoption in 1958 of the International Atomic Time (TAI) for scientific purposes.

As the axis of rotation moves relative to the Earth’s crust with a quasi-seasonal oscillation of a few tenths of a second, the Greenwich meridian, which runs from the geographic pole, is not the astronomical meridian from which the Earth’s angle of rotation must be determined. A correction depending on polar motion has to be applied to the rough astrometric UT, or UT0 measured from Greenwich meridian, giving the Earth rotation time UT1, formally distinguished from UT0 in 1955. From 1955, an empirical seasonal variation was eliminated in UT1 to restore a more uniform UT called UT2. When International Atomic Time began on January 1, 1958, its initial value was taken to be UT2.

Until the 1980’s UT1 was monitored with respect to TAI by astrometric observations dated in TAI. The advent of Very Long Base line interferometry (VLBI) in the 1970 changes all that, enabling very accurate determination of UT1 with a today precision of 8 μ s.

6. INVENTION OF UTC “SYNCHRONIZED” WITH UT1 TO WITHIN 0.9 s

As the UT had been declined in the Earth’s rotation time UT1 from 1955, from 1961 it was also declined in an atomic time version synchronized with UT1 with a certain tolerance and called *Universal Time Coordinated* (UTC). Until 1972, it has been synchronized with UT2 to within 0.05 s by applying episodically frequency correction. In 1972 UTC became the accepted basis for international timekeeping and replaced UT2. Since then, UTC has been stable like TAI, except it is sometimes shifted on December 31 or June 30 by one second to match UT1 within 0.9 s, producing the time step function UTC–TAI shown in Figure 5. Unadjusted TAI, by contrast, has advanced on UT1 by some 27 seconds since 1972.

As proved by (2) and visible in Figure 4, UT1–TAI decreases when LOD is positive, and increases when LOD is negative. In the 1970s, the seasonal average length of day was not expected to fall below 86400 s, as it will from 2020. Therefore UT1 catches up with UTC since 2020.

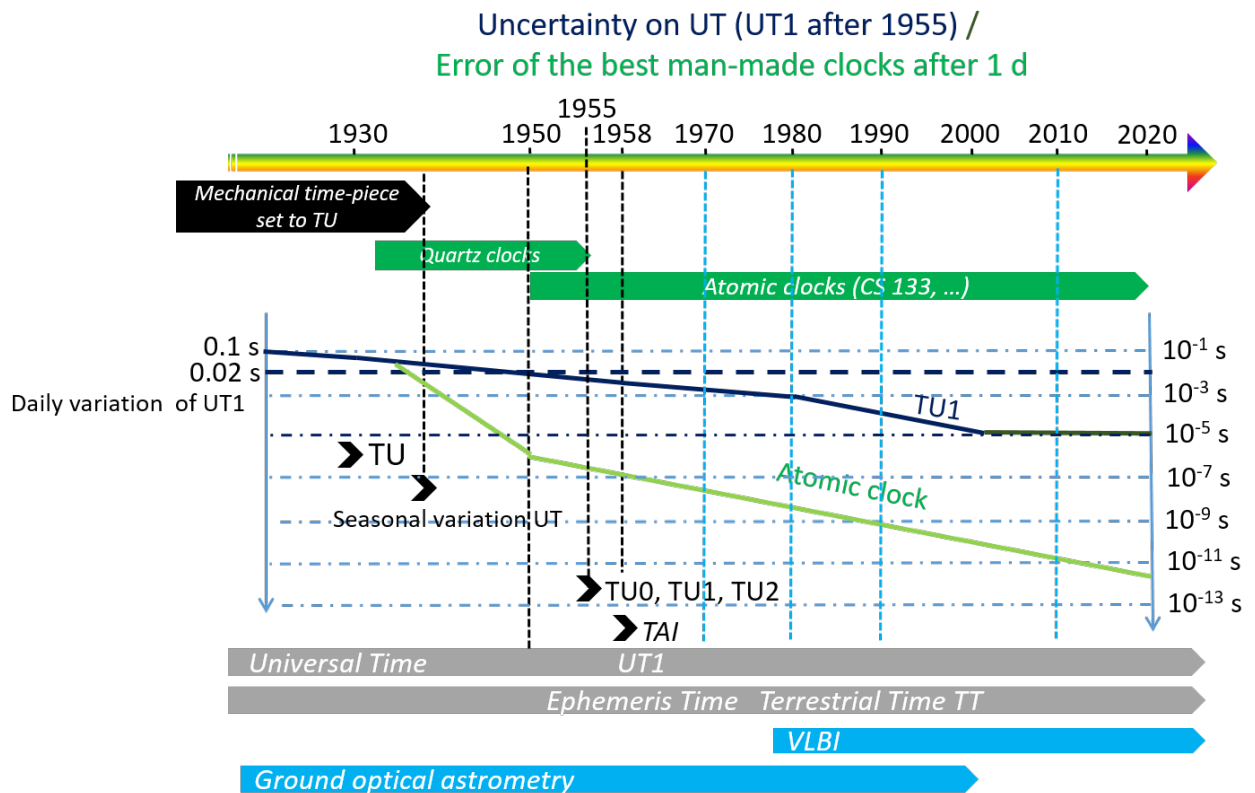


Figure 4: Evolution of UT/ UT1 uncertainty and error in best clocks since 1930.

7. UT1–TAI IN THE REALM OF GEOPHYSICS

An invaluable source of fundamental informations for geophysicists and astronomers is accessible through the LOD or UT1 time derivative to within a factor, for it is directly related to Earth angular momentum changes caused by a great variety of astronomical and geophysical processes:

- the LOD secular trend is related to the Earth-Moon system dynamics (≈ 2.5 ms/cy), slightly compensated by the Earth's flattening decrease due to post-glacial rebound (≈ -1 ms/cy) ;
- the decadal or multi-decadal trend reflect the core mantle-interaction and generation of the geomagnetic field, and in a less extend water redistribution between ice continental sheets and oceans;
- zonal tides with periods ranging from 7 days to 18.6 years cause a solid Earth deformation, in turn regular variations in the Earth's inertia moment and in LOD depending on the Earth's rheology (Bizouard et al, 2022);
- except at tidal periods, the spectrum between 2 days and a few years mostly results from atmospheric transports – see Figure 6
- the periodic effects at the zonal tidal periods bring information the mantle theology ;
- the diurnal and semi-diurnal oscillations mostly stem from ocean dynamic tides ; a smaller part stems from non-tidal ocean circulation, atmospheric mass transports, and tidal torque on the non-axisymmetric Earth's mass distribution.

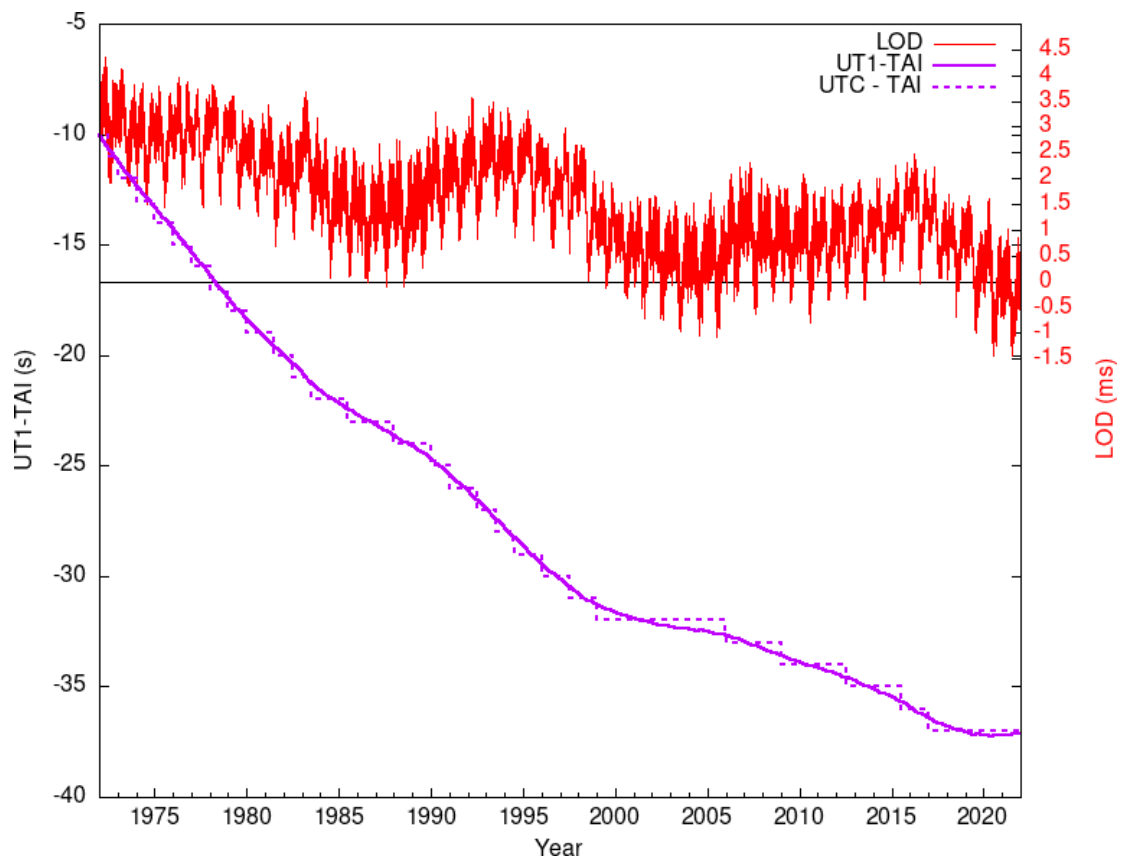


Figure 5: LOD with respect to 86400 s TAI, differences UT1–TAI, and step function since 1972.

8. UT1 AS AN EARTH ROTATION PARAMETER MONITORED BY IERS

In 1987, BIH's disappeared. Its astronomical activities devoted to UT1 determination became part of the International Earth Rotation Service (IERS), now the International Earth Rotation and Reference Systems Service. Decision to introduce a one second shift in UTC depends on astronomical monitoring of UT1–UTC and was entrusted to IERS. Whereas today UT2 is irrelevant, UT0 is still used for LLR processing.

Since 1997, the IERS Earth Orientation Center located at Paris Observatory publishes Bulletin C every six months (on 1 January and 1 July), announcing whether a leap second will be added to UTC on either 30 June or 31 December. Leap second occurrences are as unpredictable as the long term multi-decadal length of day variations.

9. HOW THE ADVENT OF SATELLITE NAVIGATION IN 1990's HAS CHANGED THE GAME

Until the 1990s, the astronomical pointing needs of navigation were satisfied by the radio broadcasting of UTC, occasionally completed with a UT1–UTC correction to within 0.1s, published in IERS Bulletin D (45 m equatorial arc precision). But, the advent of global navigation satellite systems (GNSS), first with the American Global Positioning system (GPS) in the 1990s, made previous time precision obsolete. Indeed, for a common real-time positioning to 1 m, UT1 must be known within at least 2 ms; an ultra-precise geodetic positioning to 4 mm at the Earth surface requires UT1 at 10 μ s level.

GNSS and other astro-geodetic techniques are based on UT1–UTC values determined by the Very Long Baseline Interferometry (VLBI). Their daily operational values reach a precision of about

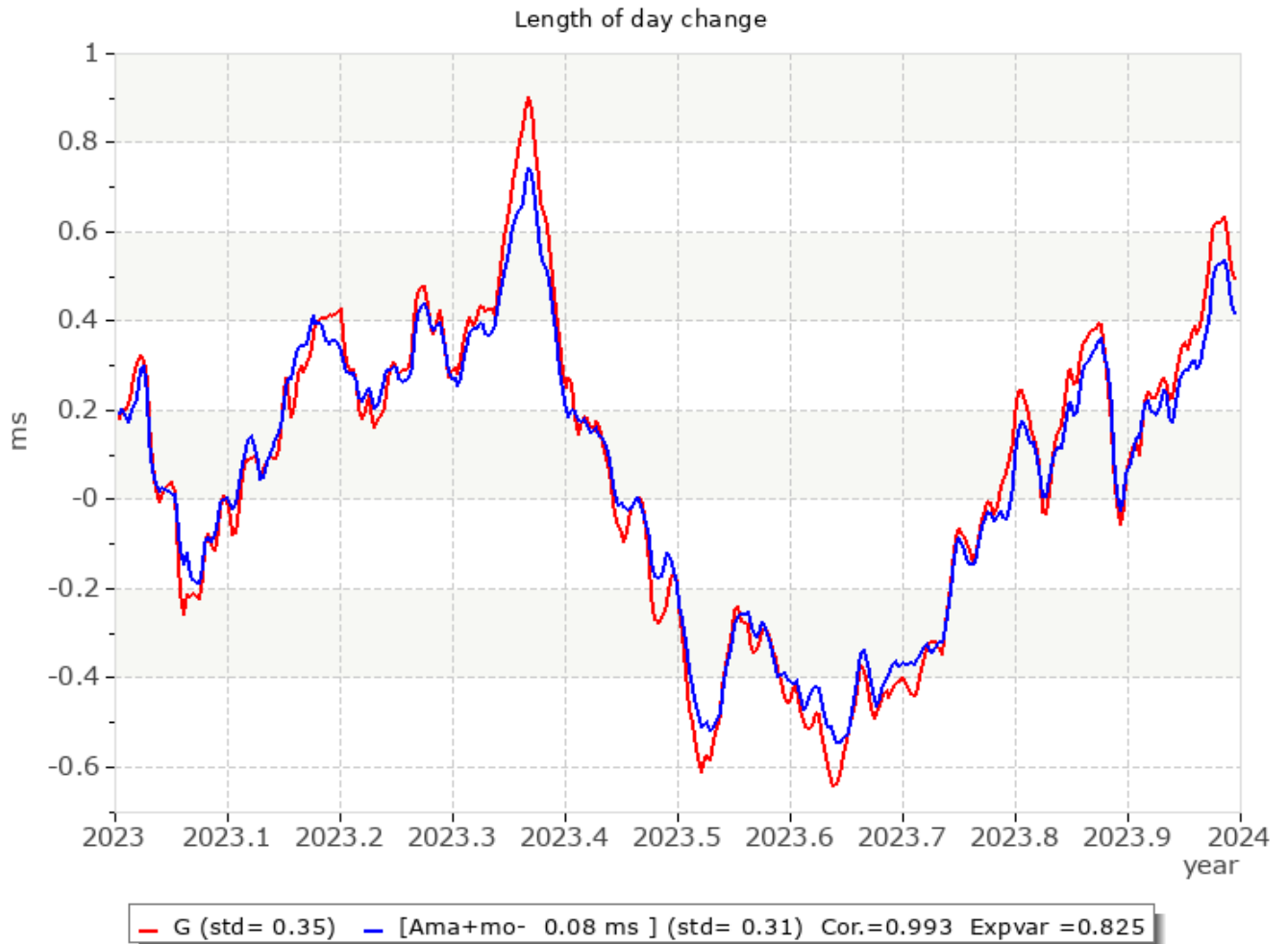


Figure 6: Effect of atmospheric transports on LOD (blue curve) superimposed to observed LOD change (red curve) according to <https://hpiers.obspm.fr/eop-pc/index.php?index=excitactive&lang=en>.

30 μ s, as recorded in IERS Bulletin A, with final values with a 6 μ s precision published 20–30 days later in the IERS C04 series, Bulletin B.

10. CONCLUSION

Earth rotation time has a long history dating back to ancient times. Fundamentally it results from the counting of the Earth's rotation cycles with respect to a celestial direction, than can be the apparent Sun "regularised" by the mean Sun, the mean vernal equinox, and the non-rotating origin. Since 1972 it has been supplanted by atomic clocks as a time-keeper (UTC), but the monitoring of its irregularities to 10 μ s and less remains essential for space navigation from the Earth more than ever since the advent of GNSS, and is a valuable source of information on the Earth and global processes affecting it. Whereas UTC as a proxy of UT1, and the corresponding leap second system are now obsolete for the mentioned application, the role of UTC as the basis of all accurate dating and worldwide synchronization will be strengthened over the coming year.

11. REFERENCES

- Bizouard, C., Fernández, L. and Zotov, L., 2022, Admittance of the Earth Rotational Response to Zonal Tide Potential, *Journal of Geophysical Research: Solid Earth* 127, doi: 10.1029/2021JB022962
- Kant, I., 1754, Untersuchung der Frage, ob die Erde in ihrer Umdrehung um die Achse, wodurch sie die Abwechslung des Tages und der Nacht hervorbringt, einige Veränderung seit den ersten zeiten ihres Ursprungs erlitten habe und woraus man sich ihrer versichern könne, welche von der königl. Akademie der Wissenschaften zu Berlin zum Preise für das jetztlaufende Jahr aufgegeben worden. In *Kant's gesammelte Schriften* (Vol. 1), pp. 183–191.
- Laplace, P. S., 1827, *Exposition du système du monde*, Sixth ed., p. 344.
- Petit, Gérard and Luzum, Brian (eds.), 2010, *IERS Conventions 2010*, Frankfurt am Main: Verlag des Bundesamts für Kartographie und Geodäsie, 179 p., available on <http://tai.bipm.org/iers/conv2010/conv2010.html>
- Scheibe, A. and Adelsberger, U., 1936, Schwankungen der astronomischen Tageslänge und der astronomischen Zeitbestimmung nach der Quartzuhren der Physikalischen-Technischen Reichsanstalt (Deviations of the astronomical length of the day and the astronomical time measurements using the quartz clocks of the PTR), *Phys. Z.* 37, p. 185–203
- de Sitter, W., 1927, "Further note on the discontinuous changes of the Earth's rotation and their possible effect on the intensity of gravity", *Bulletin of the Astronomical Institutes of the Netherlands*, 130(4), pp. 69–70.
- Spencer Jones, H., 1926, "The rotation of the Earth", *M. N. Roy. As. Soc.*, 87:4–31.
- Stephenson, F. R. and Morrison, L. V., 1984, *Phil. Trans. R. Soc. Lond. A*, 313, p. 47.
- Stoyko, N., 1937, "Sur la périodicité dans l'irrégularité de la rotation de la Terre", *C. R., Paris*, 205, pp. 79–81.

DETERMINATION OF EARTH ORIENTATION PARAMETERS FROM LUNAR LASER RANGING DATA

L. BISKUPEK, J. MÜLLER

Institute of Geodesy (IfE), Leibniz University Hannover, Germany
- biskupek@ife.uni-hannover.de

ABSTRACT. The Earth-Moon distance has been measured with Lunar Laser Ranging (LLR) since 1969. In recent years, there have been improvements in both, observations and analysis. The normal points (NPs) now are better distributed over the lunar orbit and retro-reflectors, the measurements have achieved a higher accuracy, and the number of NPs per night is larger compared to the years before 2015. By analysing LLR data, Earth Orientation Parameters (EOPs) such as the Earth rotation phase $\Delta UT1$, terrestrial pole coordinates, and nutation coefficients, as corrections to the MHB2000 model, can be determined along with other parameters of the Earth-Moon system in a least-squares adjustment. The accuracies of the estimated values have improved significantly, reaching values of about $14 \mu\text{s}$ for $\Delta UT1$, 0.5 mas for x_p and 0.7 mas for y_p . Focusing on the determination of corrections of the nutation coefficients to the MHB2000 model, significantly smaller correction values and accuracies better than 0.01 mas are achieved now.

1. INTRODUCTION

Lunar Laser Ranging (LLR) measures the distance between observatories on the Earth and retro-reflectors on the Moon. The first observation was made at the end of 1969, and up to six observatories have been in operation since then. Currently four observatories perform regular measurements: the Observatoire de la Côte d'Azur (OCA), France; the Apache Point Observatory Lunar Laser ranging Operation (APOLLO), USA; the Matera Laser Ranging Observatory (MLRO), Italy; and the Geodetic Observatory Wettzell (WLRS), Germany. In the past also the McDonald Laser Ranging Station (MLRS), USA, and the Lure Observatory on Maui/Hawaii (LURE), USA, contributed to the measurements. On the Moon there are five retro-reflectors where laser pulses from the observatories are reflected back to Earth.

With the analysis of the LLR data, contributions to terrestrial, lunar and celestial reference frames [Müller et.al. (2009), Hofmann et.al. (2018), Pavlov (2019)] as well as to the orientation of the Earth [Zerhouni & Capitaine (2009), Biskupek et.al. (2012), Hofmann et.al. (2018), Cheng et.al. (2019), Singh et.al. (2022), Biskupek et.al. (2024)] and the Moon [Pavlov et.al. (2016)] are possible. Furthermore the understanding of the lunar interior [Williams et.al. (2013)] can be investigated. One major task of LLR is to test the validity of General Relativity in the solar system, e.g., the equivalence principle, temporal variation of the gravitational constant G , Yukawa term, metric parameters, and geodetic precession [Williams et.al. (2012), Viswanathan et.al. (2018), Hofmann et.al. (2018), Zhang et.al. (2020), Biskupek et.al. (2021)].

The LLR data set used in the current analysis consists of 31620 normal points (NPs) over the time span April 1970–July 2023, see Figure 1. Since 2015, laser pulses with infra-red wavelength have been used at OCA and WLRS to measure the Earth-Moon distance, which makes it possible to track the Moon near new and full Moon [Chabé et.al. (2020); Eckl et.al. (2019)]. This development allows for a better coverage of the lunar orbit throughout the synodic month. By having a better coverage of the lunar orbit, it becomes possible to estimate various parameters of the Earth-Moon system with reduced internal correlation and higher accuracy. This improvement,

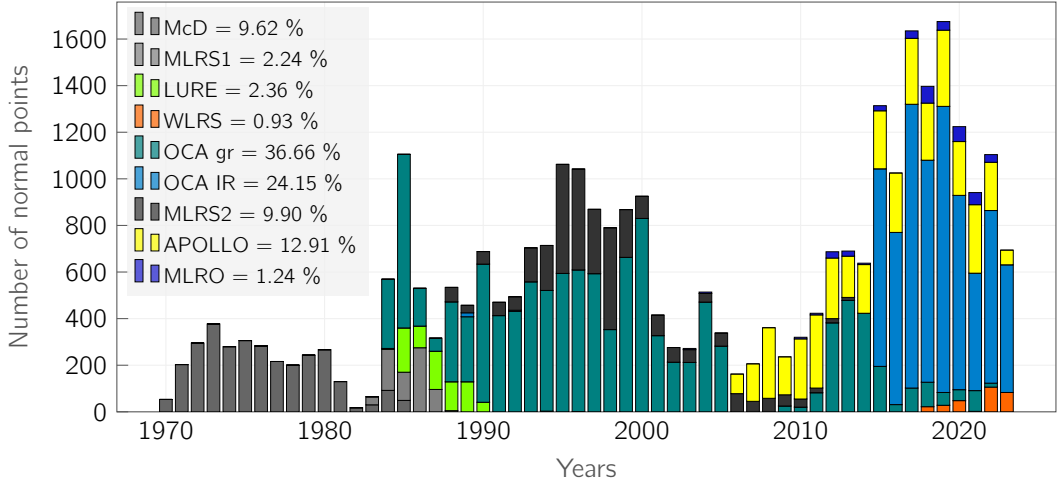


Figure 1: Distribution of NPs over 53 years for the various observatories in different colours. The legend shows the percentage of NPs of the individual observatories in relation to the sum of all NPs.

along with an increased number of NP measurements per night, gives the motivation for determining the Earth Orientation Parameters (EOPs) from LLR data.

2. EARTH ORIENTATION PARAMETER FROM LLR DATA

The Earth Rotation Parameters (ERPs) are the individual parts describing the change in the Earth's rotation axis with respect to the Earth's surface via the terrestrial pole coordinates x_p and y_p . The Earth rotation phase $\Delta UT1$ and the Length of Day (LOD) refer to the rotation of the Earth about its axis. The ERPs together with the celestial pole offsets, as corrections to the conventional precession-nutation model [Mathews et.al. (2002)], define the EOPs. In the LLR analysis these EOPs are needed for the transformation between the body-fixed reference system, the International Terrestrial Reference System (ITRS), and the inertial Barycentric Celestial Reference System (BCRS), which is the basic system in the LLR analysis. The transformation to the intermediate Geocentric Celestial Reference System (GCRS) is defined by

$$\mathbf{r}_{GCRS} = \mathbf{Q}(dt) \mathbf{R}(dt) \mathbf{W}(dt) \mathbf{r}_{ITRS}, \quad (1)$$

where $\mathbf{W}(dt)$ includes the terrestrial pole coordinates x_p and y_p and $\mathbf{R}(dt)$ the Earth rotation phase $\Delta UT1$. $\mathbf{Q}(dt)$, represented here according to the Fukushima–Williams parametrisation via precession and nutation [Fukushima (2003), Williams (1994)], contains the coefficients of the nutation series. As Eq. (1) is included in the LLR analysis model, the various parameters of the formula can be estimated directly in the least-squares adjustment of the LLR data together with other parameters of the Earth-Moon system. A more detailed description of the EOP determination from LLR data is given in Biskupek (2015) and Singh et.al. (2022).

A different approach to determine the ERPs from LLR data is given by Dickey et.al. (1985), Müller (1991), and Pavlov (2019), where the variation of longitude $\Delta UT0$ can be determined by

$$\Delta UT0 = \Delta UT1 + \frac{(x_p \sin(\lambda) + y_p \cos(\lambda)) \tan(\phi)}{15 \times 1.002737909}, \quad (2)$$

as combination of $\Delta UT1$ and the terrestrial pole coordinates x_p , y_p , with the observatories longitude λ and latitude ϕ [Chapront-Touze et.al. (2000)]. The variation of latitude VOL is given by

$$VOL = x_p \cos \lambda - y_p \sin \lambda. \quad (3)$$

VOL and $\Delta UT0$ are determined from the post-fit residuals of the least-squares adjustment of LLR data. The disadvantage of this approach is that the correlations between VOL , $\Delta UT0$, and the other parameters of the Earth-Moon system can not be investigated compared to the approach via Eq. (1). However, to better assess the results of the two approaches, they will be compared in a future study.

2.1 Earth rotation parameters

For the ERP results presented here, the LLR NPs were pre-analysed. Only nights where a minimum number of 15 NPs was reached were used for the determination of the ERPs. This condition was met for 519 nights for the time span 04.1984 – 05.2023. Each component of the ERPs, that is x_p , y_p , and $\Delta UT1$, was determined in a separate adjustment procedure. The IERS C04 series was used as the a-priori ERPs series. Its values have been fixed for the nights that were not considered in the fit, which helps to keep the LLR internal network closer to the ITRF.

The individual results for the differences of the ERP components to the a-priori series are given in Figure 2 (2a, 2c and 2e). The respective uncertainties are shown in Figure 2 (2b, 2d and 2f). Only the results after the year 2000 are shown in Figure 2, as the results improve from this point onwards compared to the results before 2000. The individual wrms of the uncertainties after 2000 results in 0.52 mas for x_p , 0.66 mas for y_p and 13.67 μ s for $\Delta UT1$. For the Earth rotation phase the uncertainties are given as two times the formal error from the least-square adjustment. Since correlations between $\Delta UT1$ and the polar coordinates are not taken into account by the separate adjustments, the given uncertainties might be too optimistic. For more details about the investigation of ERPs uncertainties, see Singh (2023). Compared to other space geodetic techniques like Very Long Baseline Interferometry (VLBI), Global Navigation Satellite System (GNSS) and Satellite Laser Ranging (SLR) the results from LLR are still worse, especially the pole coordinates. Nevertheless, when the LLR results become better in the future, a contribution as an independent technique could be considered in an inter-technique combination.

2.2 Nutation

In Eq. (1) all EOPs are needed for the transformation of station coordinates from the ITRS into the GCRS. The part of the nutation is included in $\mathbf{Q}(dt)$, represented according to the Fukushima–Williams parametrisation via precession and nutation [Fukushima (2003), Williams (1994)]. The IAU 2000 nutation model is described in the IERS Conventions 2010 [Petit & Luzum, (2010)] as a series for nutation in longitude $\Delta\psi$ and obliquity $\Delta\epsilon$, referred to the mean ecliptic of date:

$$\Delta\psi = \sum_{i=1}^n (A_i + A'_i t) \sin(ARG) + (A''_i + A'''_i t) \cos(ARG) \quad (4)$$

$$\Delta\epsilon = \sum_{i=1}^n (B_i + B'_i t) \cos(ARG) + (B''_i + B'''_i t) \sin(ARG) \quad (5)$$

with $ARG = \sum_j^5 N_j F_j$, N_j : multipliers, F_j : Delaunay parameters and time t measured in Julian centuries from epoch J2000. n gives the number of terms that compose the model: 678 lunisolar and 687 planetary terms with *in-phase* (first part of the sum in eqs. (4) and (5)) and *out-of-phase* (second part of the sum) coefficients. This series is based on the REN2000 nutation solution [Souchay et.al. (1999)] for the rigid Earth, which is convolved to the nutation model MHB2000 for the non-rigid Earth by the transfer function from Mathews et.al. (2002). This model is used as a-priori nutation model in the LLR analysis, where the non-time-dependent coefficients can be determined along with other parameters of the Earth-Moon system.

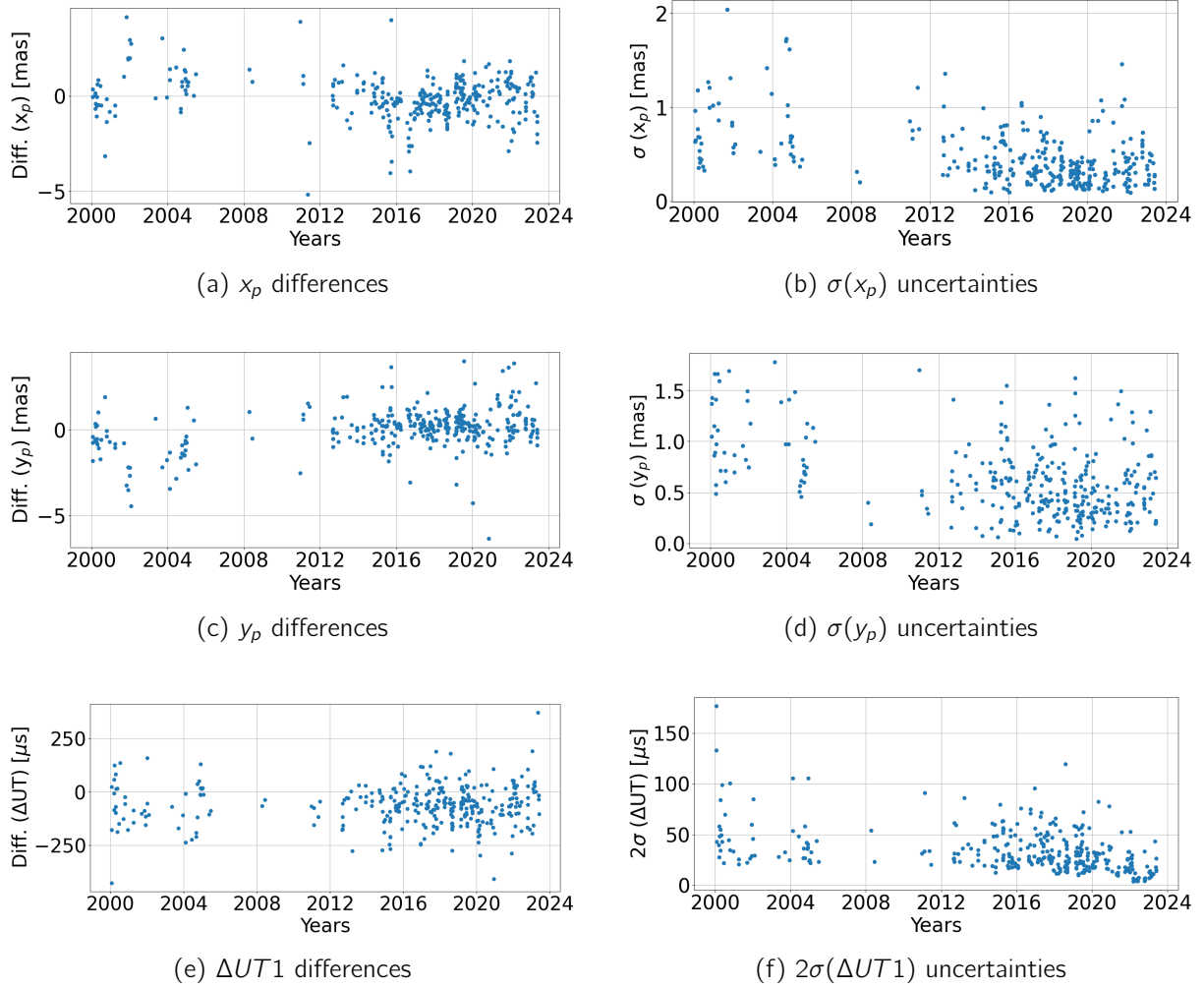


Figure 2: Results for the determination of ERPs from the NPs of all observatories. The left plots show the differences to the a-priori IERS C04 series and the right plots the respective uncertainties. For the pole coordinates the uncertainties are given as the formal errors of the least-squares adjustment, for $\Delta UT1$ as two times the formal errors.

In Table 1 are given the values from the LLR analysis for the periods with the largest contribution to the nutation angles. These periods are: 18.6-year, 182.62-day, 13.66-day, 9.3-year, and 365.26-day, sorted in order of their largest contribution. The values are given as differences to the a-priori model with uncertainties as three times the formal errors from the least-squares adjustment. The current results are compared with those from Hofmann et.al. (2018), where a shorter time span of NPs was used, which in particular means fewer NPs measured in the IR. Looking at the differences to the a-priori model, the 2023 results are smaller than the 2018 results in most cases. The uncertainties have improved by a factor of two. The largest improvement is for the 13.66-day period, where the benefit from IR OCA data and the associated more homogeneous observation of the lunar orbit is clearly visible. In addition, some changes in the ephemeris calculation procedure have improved the overall uncertainty of all parameters determined.

Table 1: Results from the determination of nutation coefficients as differences to the main periods of the MHB2000 model. Results are compared between a determination in 2018 (Hofmann et al., 2018) and the current results of 2023. All values are given in [mas].

period	results 2018	results 2023	period	results 2018	results 2023
$A_{18.6y}$	1.42 ± 0.18	0.79 ± 0.05	$A_{182.6d}$	0.51 ± 0.02	0.17 ± 0.05
$B_{18.6y}$	-0.18 ± 0.08	-0.20 ± 0.03	$B_{182.6d}$	-0.06 ± 0.01	0.19 ± 0.02
$A''_{18.6y}$	-0.68 ± 0.12	0.61 ± 0.05	$A''_{182.6d}$	-0.57 ± 0.02	0.73 ± 0.05
$B''_{18.6y}$	-0.06 ± 0.07	0.05 ± 0.02	$B''_{182.6d}$	-0.07 ± 0.01	0.04 ± 0.02
$A_{9.3y}$	-1.12 ± 0.12	0.23 ± 0.03	$A_{13.6d}$	1.49 ± 0.07	0.10 ± 0.03
$B_{9.3y}$	-0.27 ± 0.05	-0.04 ± 0.01	$B_{13.6d}$	-0.65 ± 0.03	0.01 ± 0.02
$A''_{9.3y}$	-1.55 ± 0.12	0.12 ± 0.03	$A''_{13.6d}$	-1.42 ± 0.10	-0.10 ± 0.03
$B''_{9.3y}$	0.17 ± 0.05	0.07 ± 0.01	$B''_{13.6d}$	0.27 ± 0.04	-0.11 ± 0.01
$A_{365.3d}$	1.05 ± 0.07	0.30 ± 0.06			
$B_{365.3d}$	-0.51 ± 0.03	-0.04 ± 0.03			
$A''_{365.3d}$	0.65 ± 0.05	0.28 ± 0.03			
$B''_{365.3d}$	0.04 ± 0.02	0.08 ± 0.02			

3. CONCLUSION

In the recent analysis 53 years of LLR data were analysed to determine Earth Orientation Parameters. The current best results are 0.52 mas for x_p , 0.66 mas for y_p and 13.67 μ s for $\Delta UT1$. However, the ERP uncertainties determined from LLR data might be too optimistic, because correlations between $\Delta UT1$ and the polar coordinates are not taken into account when determining the ERP components separately. Therefore as the next step, a determination of $\Delta UT0$ and VOL from the daily decomposition method for comparison with least-squares adjustment results will be done. In addition, $\Delta UT1$ and the pole coordinates will be determined together in the least-squares adjustment and analysed to find the best strategy for ERP determination from LLR data. It will also be further investigated, which parameters of the Earth-Moon system should be determined together with the ERPs. This will lead to a more realistic estimation of their uncertainties.

Compared to results for the nutation coefficients from the year 2018, the current differences to the a-priori MBH2000 model are smaller in most cases, and the uncertainties have improved by a factor of two. Here, the high number of IR NPs and the more homogeneous tracking of the lunar orbit are beneficial, especially for the 13.66-day nutation period.

With more IR data from the observatories OCA and WLRs, it is expected that the EOPs can be further improved. In future, a combined analysis of LLR and VLBI data for the EOP determination is planned.

Acknowledgments

We acknowledge with gratitude, that more than 53 years of processed LLR data have been obtained under the efforts of the personnel at McDonald Laser Ranging Station (MLRS), USA, Observatoire de la Côte d'Azur (OCA), France, Lure Observatory on Maui/Hawaii (LURE), USA, Apache Point Observatory Lunar Laser ranging Operation (APOLLO), USA, Matera Laser Ranging Observatory (MLRO), Italy and Geodetic Observatory Wettzell (WLRs), Germany. LLR data is collected, archived, and distributed under the auspices of the International Laser Ranging Service (ILRS) [Pearlman et.al. (2019)]. All LLR NPs used for these studies are available from the Crustal Dynamics Data Information System (CDDIS) at NASA's Archive for Space Geodesy Data,

USA, [Noll (2010)] at the website*. The IERS C04 EOP time series is available at the website †. We also acknowledge with thanks the funding by the Deutsche Forschungsgemeinschaft (DFG, German Research Foundation) under Germany's Excellence Strategy (EXC-2123 QuantumFrontiers - Project-ID 390837967).

4. REFERENCES

- Biskupek, L., 2015, "Bestimmung der Erdorientierung mit Lunar Laser Ranging", PhD thesis, Leibniz Universität Hannover, doi: 10.15488/4721.
- Biskupek, L., Müller, J., Hofmann, F., 2012, "Determination of Nutation Coefficients from Lunar Laser Ranging", In: Kenyon, S., Pacino, M.C., Marti, U., Sideris, M.G. (eds), *Geodesy for Planet Earth*, Int. Ass. Geod. Symp., vol 136., pp. 521–525, Springer, Berlin, Heidelberg, doi: 10.1007/978-3-642-20338-1_63.
- Biskupek, L., Müller, J., Torre, J.-M., 2021, "Benefit of New High-Precision LLR Data for the Determination of Relativistic Parameters", *Universe*, vol. 7, doi: 10.3390/universe7020034.
- Biskupek, L., Singh, V.V., Müller, J., Zhang, M., 2024, "Potential of Lunar Laser Ranging for the determination of Earth Orientation Parameters", In: Freymueller, J., Sanchez, L. (eds), *Gravity, Positioning and Reference Frames: Proceedings of Three IAG Symposia in Fall 2022*, Springer, Berlin, Heidelberg, in press.
- Chabé, J., Courde, C., Torre, J.-M., Bouquillon, S., Bourgoïn, A., Aïmar, M., Albanèse, D., Chauvineau, B., Mariey, H., Martinot-Lagarde, G., Maurice, N., Phung, D.-H., Samain, E., Viot, H., 2020, "Recent Progress in Lunar Laser Ranging at Grasse Laser Ranging Station", *Earth Sp. Sci.*, vol. 7, pp. e2019EA000, doi: 10.1029/2019EA000785.
- Chapront-Touzé, M., Chapront, J., Francou, G., 2000, "Determination of UT0 with LLR observations", In: *Proceedings of the Journées 1999 "Motion of Celestial Bodies, Astrometry and Astronomical Reference Frames"*, pp. 217–220.
- Cheng, Y.T., Liu, J.C., Zhu, Z., 2019, "Analyses of celestial pole offsets with VLBI, LLR, and optical observations", *A&A*, vol. 627, pp. A81, doi: 10.1051/0004-6361/201834785.
- Dickey, J.O., Newhall, X.X., Williams, J.G., 1985, "Earth Orientation From Lunar Laser Ranging and an Error Analysis of Polar Motion Services", *J. Geophys. Res.*, vol. 90, pp. 9353–9362.
- Eckl, J.J., Schreiber K.U., Schüler, T., 2019, "Lunar laser ranging utilizing a highly efficient solid-state detector in the near-IR", In: Prochazka, I., Sobolewski, R., James, R.B., Domokos, P., Gali, A. (eds), *Quant. Opt. Pho. Coun., International Society for Optics and Photonics*, vol. 11027, pp. 1102708, doi: 10.1117/12.2521133.
- Fukushima, T., 2003, "A New Precession Formula", *AJ*, vol. 126, pp. 494–534, doi: 10.1086/375641.
- Hofmann, F., Biskupek, L., Müller, J., 2018, "Contributions to reference systems from Lunar Laser Ranging using the lfe analysis model", *J. Geod.*, vol. 92, pp. 975–987, doi: 10.1007/s00190-018-1109-3.
- Hofmann, F., Müller, J., 2018, "Relativistic tests with lunar laser ranging", *Class. Quantum Grav.*, vol. 35, pp. 035, doi: 10.1088/1361-6382/aa8f7a.
- Mathews, P.M., Herring, T.A., Buffett, B.A., 2002, "Modeling of nutation and precession: New nutation series for nonrigid Earth and insights into the Earth's interior", *J. Geophys. Res.*, vol. 107, pp. ETG 3–1–ETG 3–30, doi: 10.1029/2001JB000390
- Müller, J., 1991, "Analyse von Lasermessungen zum Mond im Rahmen einer post-Newton'schen Theorie", PhD thesis, Technische Universität München, Deutsche Geodätische Kommission bei der Bayerischen Akademie der Wissenschaften, Reihe C, Nr. 383.
- Müller, J., Biskupek, L., Oberst, J., Schreiber, K.U., 2009, "Contribution of Lunar Laser Ranging to Realise Geodetic Reference System", In: Drewes, H. (ed), *Int. Ass. Geod. Sym.*, vol. 134,

*https://cdsis.nasa.gov/Data_and_Derived_Products/SLR/Lunar_laser_ranging_data.html

†<https://www.iers.org/IERS/EN/DataProducts/EarthOrientationData/eop.html>

- pp. 55–59, Springer, Berlin, Heidelberg, doi: 10.1007/978-3-642-00860-3.
- Noll C.E., 2010, “The crustal dynamics data information system: A resource to support scientific analysis using space geodesy”, *Adv. Space Res.*, vol. 45, pp. 1421–1440, doi: 10.1016/j.asr.2010.01.018.
- Pavlov, D.A., 2019, “Role of lunar laser ranging in realization of terrestrial, lunar, and ephemeris reference frames”, *J. Geod.*, vol. 94, pp. 5, doi: 10.1007/s00190-019-01333-y.
- Pavlov, D.A., Williams, J.G., Suvorkin, V.V., 2016, “Determining parameters of Moon's orbital and rotational motion from LLR observations using GRAIL and IERS-recommended models”, *Celest. Mech. Dyn. Astr.*, vol. 126, pp. 61–88, doi: 10.1007/s10569-016-9712-1.
- Pearlman M.R., Noll C.E., Pavlis E.C., Lemoine, F.G., Combrink, L., Degnan, J.J., Kirchner, G., Schreiber, U., 2019, “The ILRS: approaching 20 years and planning for the future”, *J. Geod.*, vol. 93, pp. 2161–2180, doi: 10.1007/s00190-019-01241-1.
- Petit, G., Luzum, B. (eds), 2010, “IERS Conventions 2010”, No. 36 in IERS Technical Note, Verlag des Bundesamtes für Kartographie und Geodäsie, Frankfurt am Main
- Singh, V.V., 2023, “Lunar Laser Ranging - Improved Modelling and Parameter Estimation”, PhD thesis, Leibniz Universität Hannover, doi: 10.15488/14298
- Singh, V.V., Biskupek, L., Müller, J., Zhang, M., 2022, “Earth rotation parameter estimation from LLR”, *Adv. Space Res.*, vol. 70, pp. 2383–2398, doi: 10.1016/j.asr.2022.07.038.
- Souchay, J., Loysel, B., Kinoshita, H., Folgueira, M., 1999, “Corrections and new developments in rigid earth nutation theory - III. Final tables “REN-2000” including crossed-nutation and spin-orbit coupling effects”, *A&AS*, vol. 135, pp. 111–131, doi: 10.1051/aas:1999446
- Viswanathan, V., Fienga, A., Minazzoli, O., Bernus, L., Laskar, J., Gastineau, M., 2018, “The new lunar ephemeris INPOP17a and its application to fundamental physics”, *Mon. Not. Roy. Astro. Soc.*, vol. 476, pp. 1877–1888, doi: 10.1093/mnras/sty096.
- Williams, J.G., 1994, “Contributions to the Earth's obliquity rate, precession, and nutation”, *AJ*, vol. 108, pp. 711–724, doi: 10.1086/117108.
- Williams, J.G., Boggs, D.H., Folkner, W.M., 2013, “DE430 Lunar Orbit, Physical Librations, and Surface Coordinates”, JPL Interoffice Memorandum IOM 335-JW,DB,WF-20080314-001, Jet Propulsion Laboratory, California Institute of Technology, Pasadena, California
- Williams, J.G., Turyshev, S.G., Boggs, D.H., 2012, “Lunar laser ranging tests of the equivalence principle”, *Class. Quantum Grav.*, vol. 29, pp. 184, doi: 10.1088/0264-9381/29/18/184004.
- Zhang, M., Müller, J., Biskupek, L., 2020, “Test of the equivalence principle for galaxy's dark matter by lunar laser ranging”, *Celest. Mech. Dyn. Astr.*, vol. 132, pp. 25, doi: 10.1007/s10569-020-09964-6.
- Zerhouni, W., Capitaine, N., 2009, “Celestial pole offsets from lunar laser ranging and comparison with VLBI”, *A&A*, vol. 507, pp. 1687–1695, doi: 10.1051/0004-6361/200912644.

PROSPECTS AND CAVEATS OF DETERMINING EARTH ORIENTATION PARAMETERS FROM LUNAR LASER RANGING DATA

D. Pavlov

St. Petersburg State University

ABSTRACT. Advances in lunar laser ranging (LLR) measurements make the technique capable of determining daily corrections to Earth orientation parameters, which was discussed in some recent works. One advantage of LLR over very large baseline interferometry (VLBI) is independence of clock offsets. In this work, the recent LLR data is analyzed and applied to EOP determination; also possible caveats are discussed: the effect of incorrect EOP to the formation of LLR normal point, and the LLR range error as a source of uncertainty of the determined EOP.

1. INTRODUCTION

Lunar laser ranging, among many of its applications, played an important role in the determination of the terrestrial pole and Universal time in 1970s and 1980s, see e.g. (Langley et al. 1981). Later came regular EOP determination via very long baseline interferometry (VLBI). Nowadays most used EOP series (IERS C04 and IERS Bulletin A) are constructed from VLBI, GNSS and SLR data, but no LLR data. (One exception is JPL KEOF series and its later extension, JPL EOP2*).

However, LLR has much improved since and achieved near-millimeter precision (Colmenares et al. 2023), also infrared LLR observations started, being less prone to atmospheric noise (Courde et al. 2017, Eckl et al. 2019). Also, the frequency of LLR observations has increased. Finally, LLR has some benefits over currently used EOP determination technologies: the Moon's orbit is more stable than the artificial satellites used in SLR and GNSS observations. Also, LLR observations do not suffer from daily clock offsets, like do GNSS and VLBI. All this suggests that LLR observations once again might be helpful in the for EOP determination (not replacing, but augmenting presently used observations).

Recent results of analysis of present LLR in regards to EOP determination can be found in e.g. (Pavlov 2020, Biskupek et al. 2022).

One night of LLR at one station allows to determine two daily (nightly) parameters of Earth rotation: UT0 and VOL, which are (apparent) corrections to station's longitude and latitude, respectively. UT0 and VOL are in linear relation with UT1 and terrestrial pole coordinates x_p , y_p (Chapront & Francou, 2009):

$$\begin{aligned} \text{UT0} &= \text{UT1} + \frac{(x_p \sin \lambda + y_p \cos \lambda) \tan \phi}{15 \times 1.002737909} \\ \text{VOL} &= x_p \cos \lambda - y_p \sin \lambda \end{aligned}$$

where λ and ϕ are the station's longitude and latitude, respectively, and 1.002737909 is the relative rate of mean solar time to sidereal time.

In this work, selected aspects of the technique are studied: effect of (real) EOP on formation

*<https://eop2-external.jpl.nasa.gov/>

of normal points, and effect of LLR range error on the accuracy of determined EOP.

2. PRESENT STATE OF LLR OBSERVATIONS PROCESSING

LLR solution used in this work is based on EPM lunar model and EPM lunar-planetary ephemeris (Pitjeva et al. 2022, Pavlov 2020, Pavlov et al. 2016) and all available LLR observations up until 2023 (including Grasse and Wettzell infrared observations made in the first quarter of 2023). The EOP series used was JPL EOP2. The statistics of postfit residuals is presented in Table 1.

Currently active stations are: Grasse (17 normal points in 2022 made with green laser, after which it ceased operations; 826 normal points in 2022 made with infrared laser), Apache Point (207 normal points in 2022), Matera (39), and Wettzell (106).

Table 1: Post-fit statistics of lunar solution. WRMS is one-way and given in cm.

Station	Timespan	Used	Rejected	WRMS
McDonald	1969–1985	3554	50	21.6
MLRS1	1983–1988	585	46	8.8
MLRS2	1988–2013	3272	381	3.6
Nauchny	1982–1984	25	0	11.1
Haleakala	1984–1990	747	23	5.3
Grasse (Ruby)	1984–1986	1109	79	16.8
Grasse (YAG)	1987–2005	8277	47	2.4
Grasse (MeO green)	2009–2022	2104	0	1.54
Grasse (infrared)	2015–2023	7407	7	1.21
Apache Point	2006–2022	3781	78	1.44
Matera	2003–2022	397	26	3.4
Wettzell	2018–2023	268	0	1.58

3. EFFECT OF $\Delta UT0$ AND VOL ON NORMAL POINT

LLR normal point is formed from raw LLR observations using the Herstmonceux algorithm or some more complicated scheme, e.g. (Colmenares et al, 2023). Any such scheme usually involves a polynomial trend to be fit to the series of residual differences of raw ranges—that is, the differences between the measured and model values of the two-way ranges. The observed value depends on the celestial coordinates of the station, which in turn depend on given (uncorrected) EOP values. In Fig. 1, residuals of raw (full-rate) data are shown; the data on the left was calculated with unmodified EOP, while the data on the right were calculated with 3 mas offset in station’s longitude ($UT0$), 1 mas in station’s latitude (VOL). Each of the two series of residuals have a square polynomial fit to it; this polynomial is subtracted before the normal point (marked black on the plots) is formed.

The difference between the left and right parts of Fig. 1 is shown at Fig. 2 (green line). It can be seen that perturbations in EOP introduce a linear trend in residuals. The equal linear trend appears between the two fitted polynomials (yellow line). Hence, the perturbations in EOP ($\Delta UT0$ and VOL) do not effectively change the resulting normal point. (The value of the polynomial in the given point and the model value of two-way range are added to the normal point in the end of the Herstmonceux algorithm.)

4. DETERMINING $\Delta UT0$ AND VOL FROM SERIES OR NORMAL POINTS

The detailed procedure can be found in (Pavlov, 2022); only the main points are reproduced here. Night with at least 10 normal points are selected; for each such night, corrections to station’s

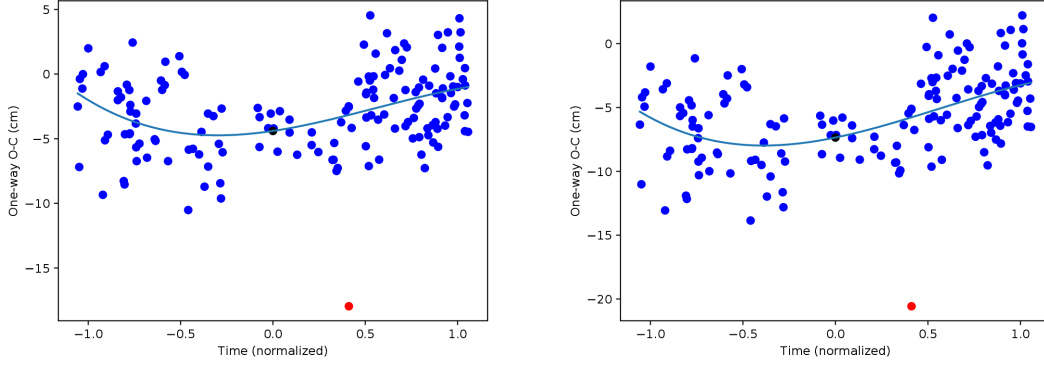


Figure 1: FRD data from Matera on Feb 8, 2018 (model delays subtracted). Left: with uncorrected EOP. Right: with modified EOP. (Black is the normal point, red is the raw range.)

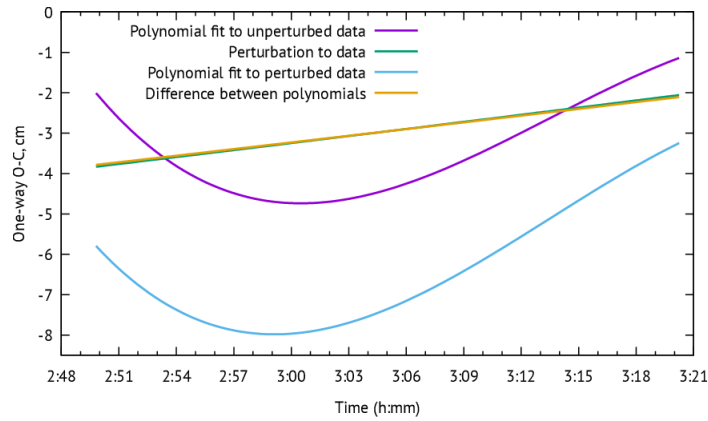


Figure 2: Polynomials fit to data and linear trend caused by EOP.

longitude and latitude, and also range error (Δ range) are made free parameters in the solution. Then, all parameters of lunar solution (including newly added ones) are fit to observations using least squares method. The determined values of corrections to station's longitude and latitude are negated Δ UT0 and VOL for this night.

Only nights starting from 2020 were studied in this work. On Fig. 3, the standard deviations (1σ) of the found EOPs are shown. For comparison, a similar experiment was done without determining Δ range; its results are on Fig. 4. While the results on Fig. 4 appear much more precise than on Fig. 3, it would be a mistake not to fit for Δ range. Each LLR session has some systematic error that comes from the delay of the signal in atmosphere. Fixing this error to zero would make the estimates of EOP uncertainties unfairly small (because EOP correlate with Δ range).

However, a compromise between Δ range and EOP uncertainties can be reached by making some reasonable claims on Δ range and using them in the least squares estimation. It should be safe to assume that Δ range has zero expected mean and the standard deviation of 2 cm. Under these assumptions, the EOP uncertainties are significantly better than without prior distribution on Δ range (Fig. 5).

Some Δ UT0 values were found to be outside their respective 3σ bounds, meaning that the initial EOP series were not in agreement with LLR measurements. Three such values were found since the beginning of 2020 (see Fig. 6) on the dates 13.12.2021, 06.01.2022, and 13.01.2022.

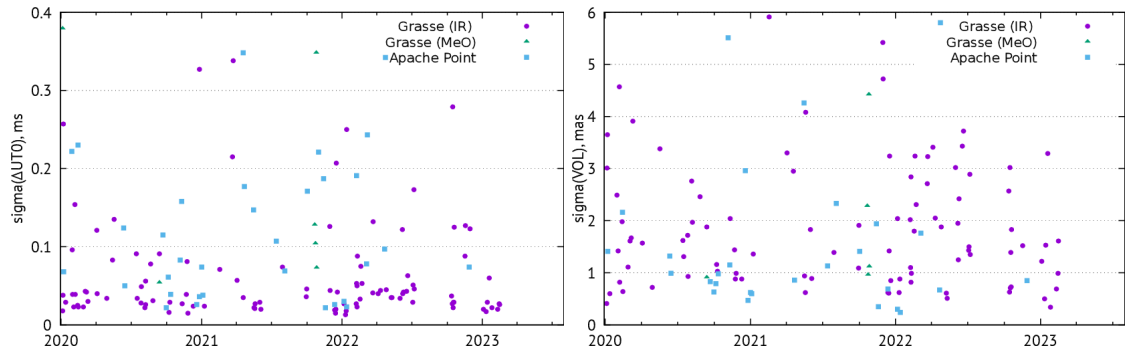


Figure 3: Accuracy of $\Delta UT0$ and VOL when also determining $\Delta range$

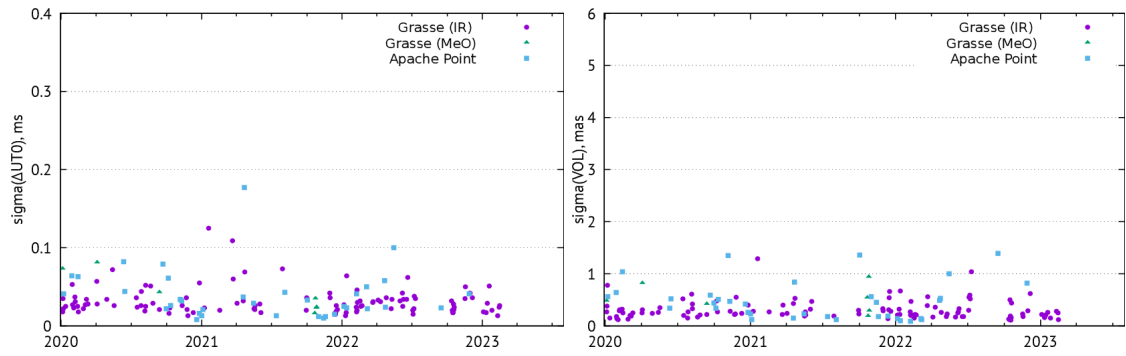


Figure 4: Accuracy of $\Delta UT0$ and VOL without determining $\Delta range$

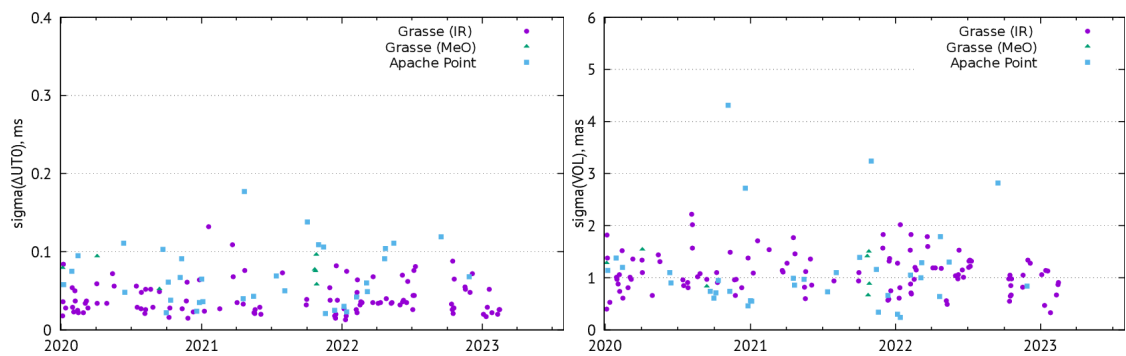


Figure 5: Accuracy of $\Delta UT0$ and VOL with a prior distribution on $\Delta range$

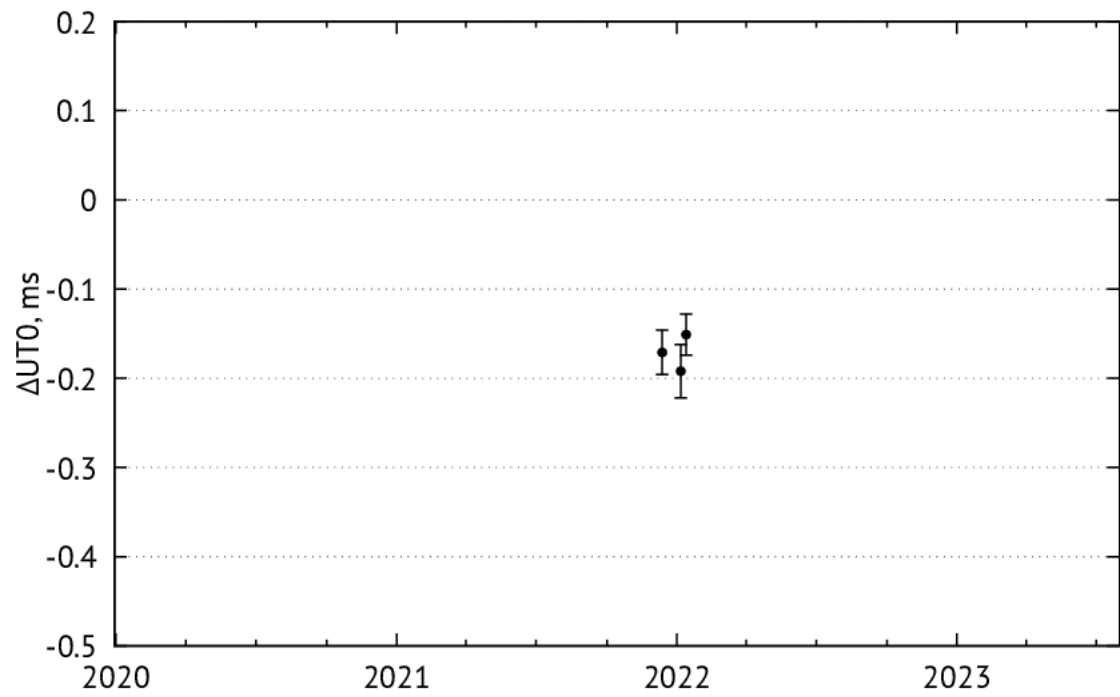


Figure 6: ΔUT0 outliers (outside 3σ)

5. CONCLUSION

In 2022, 48 $\Delta UT0$ values were found with $\sigma \leq 0.1$ ms, and 17 values with $\sigma \leq 0.04$ ms. 40 VOL values were found with $\sigma \leq 1.5$ mas, and 15 values with $\sigma \leq 1$ mas.

LLR can be useful for EOP determination once again after 1970-1980s.

Only two parameters ($\Delta UT0$ and VOL) can be determined at one night. (Except when two observatories work at the same night, which is rare.)

Errors in EOP do not bring any systematic error in the process of normal point calculation (besides the error that appears in the normal point itself).

Full dynamical solution must be obtained together with EOP to get more realistic error estimates. Daily range error should be included into the solution as well.

6. REFERENCES

- Biskupek, L., Singh, V.V., Müller, J., 2022. "Estimation of Earth Rotation Parameter UT1 from Lunar Laser Ranging Observations". In: Freymueller, J.T., Sánchez, L. (eds) *Geodesy for a Sustainable Earth. International Association of Geodesy Symposia*, vol 154. Springer, Cham, doi: 10.1007/1345_2022_178.
- Chapront, J., Francou, G., 2009. "Lunar laser ranging analysis: determination of UT0 and VOL". Tech. rep., Observatoire de Paris, ftp://cyrano-se.obspm.fr/pub/1_llr_analysis/3_fitted_parameters/doc7.pdf.
- Colmenares, N. R., Battat, J. B. R., Gonzales, D. P., Murphy Jr, T. W., Sabhlok, S., 2023. "Fifteen Years of Millimeter Accuracy Lunar Laser Ranging with APOLLO: Data Reduction and Calibration". *PASP* 135, 104503, doi: 10.1088/1538-3873/acf787.
- Courde, C., Torre, J.M., Samain, E., Martinot-Lagarde, G., Aimar, M., Albanese, D., Exertier, P., Fienga, A., Mariey, H., Metris, G., Viot, H., Viswanathan, V., 2017. "Lunar laser ranging in infrared at the Grasse laser station". *A&A* 602, A90, doi: 10.1051/0004-6361/201628590
- Eckl, J., Schreiber, U., Schüler, T., 2019. "Lunar laser ranging utilizing a highly efficient solid-state detector in the near-IR" *Quantum Optics and Photon Counting, Proceedings Volume 11027*, doi: 10.1117/12.2521133.
- Langley, R. B., King, R.W., Shapiro, I.I., 1981. "Earth rotation from lunar laser ranging". *J. Geophys. Res. (Solid Earth)*, 86(B12), doi: 10.1029/JB086iB12p11913
- Pavlov, D., 2020, "Role of lunar laser ranging in realization of terrestrial, lunar, and ephemeris reference frames". *J Geod* 94(5), doi: 10.1007/s00190-019-01333-y.
- Pavlov, D., Williams, G., Suvorkin, V., 2016, "Determining parameters of Moon's orbital and rotational motion from LLR observations using GRAIL and IERS-recommended models". *Celest. Mech. Dyn. Astr.* 126, doi: 10.1007/s10569-016-9712-1.
- Pitjeva, E., Pavlov, D., Aksim, D., Kan, M., 2022. "Planetary and lunar ephemeris EPM2021 and its significance for Solar system research". *Proc. IAU*, vol. 15 (S364), doi: 10.1017/S1743921321001447.

EXCITATIONS OF THE EARTH'S CHANDLER WOBBLE AND LENGTH OF DAY BY THE SOUTHERN OCEAN

E. NAGHIBI¹, C. Delizo-Salabit², S. KARABASOV³

¹ School of Architecture, Computing and Engineering, University of East London - UK

² Ernst & Young UK - UK

³ School of Engineering and Materials Science, Queen Mary University of London - UK
e.naghibi@uel.ac.uk, s.karabasov@qmul.ac.uk

ABSTRACT. In this paper, the effect of Southern Ocean on Chandler wobble and length of day excitations is investigated. To this end, the motion terms of excitations are calculated using the primitive equation ocean model, HYCOM (HYbrid Coordinate Ocean Model). The resulting excitations are analysed in time and frequency domains and compared to the previous studies for regional oceanic excitations of Chandler wobble and length of day. The excitations caused by the Southern Ocean are also compared with those caused by the global oceans in the same general circulation ocean model, HYCOM. Our results suggest that, amongst all oceanic regions, the Southern Ocean is a key contributor to both Chandler wobble and length of day excitations. The predicted excitations caused by the global oceans are also compared with geodetic observation of the Chandler wobble and length of day after subtraction of mass terms estimated from GRACE (Gravity Recovery and Climate Experiment) satellite gravimetry data.

1. INTRODUCTION

Geophysical sources of excitation for the Earth's polar motion and length of day in different time scales have always been an interesting question for geodynamicists. Starting with polar motion excitation at small time scales, ocean tides are reported to influence polar motion in sub-daily timescales [1, 2]. Angular momentum exchanges between the core and the mantle also affect polar motion at these timescales [1]. At intraseasonal timescales, most dominant excitation source is from atmospheric and oceanic processes, explaining roughly 65% and 71% of the observed excitation variance, between 1980 – 2000 and 1993 – 2000 respectively [3]. Forced annual wobble excitation is predominantly caused by seasonal shifting of air mass [4-6]. On the other hand, for the Chandler wobble excitation, ocean bottom pressure is the most significant mechanism [7], having 1.5 times more power than atmospheric surface pressure and 8 times more power than oceanic currents. The combined contribution of the atmospheric and oceanic processes account for 1.2 times the observed Chandler wobble from 1980 to 2000 [3] with atmospheric and ocean pressure variations being the most dominant mechanism. This highlights the significance of damping in Chandler wobble motion. Aoyama et al. [8] however noted that atmospheric wind and surface pressure were the dominant mechanisms in the same time period with wind being the main component. This is further supported by work done by Brzezinski et al. [9] which reported atmospheric wind and surface pressure contributing to 80% of the total excitation from atmospheric and oceanic processes in similar time periods.

Moving on to LOD excitations, at diurnal timescales, ocean tides are the predominant excitation mechanism providing up to 90% contribution [10]. Schindelegger et al. [11] discovered El Nino - Southern Oscillation to be the main perturbation for diurnal cycle characteristics in the troposphere. Atmospheric and oceanic processes cause 92% of the observed LOD variations in intraseasonal time scales from 1980 – 2000 and 1992 – 2000 [12]. Atmospheric processes sig-

nificantly dominate oceanic processes, with motion effects contributing more than the pressure. However,, ocean bottom pressure and currents are also shown to be effective in these time scale [13]. Effects of upper atmospheric winds (10hPa to 0.3hPa) were analysed at the same timescales and were shown to be weaker than lower atmospheric winds (ground to 10hPa), however, they still had a greater effect than ocean contributions. Rosen et al. [14], over a 2 - year sample, has also deduced that tropospheric and stratospheric winds can fully account for seasonal, nontidal variations in LOD. Leading up to seasonal timescales, ocean excitation contributions become more significant, with large scale variations in ocean water mass and water on land being responsible [18]. Lambeck & Hopgood [15] find that zonal wind and body tides dominate semi-annual timescales with the remaining 10% contribution coming from oceanic currents and hydrologic processes, especially associated with the Antarctic circumpolar current in the Southern Ocean. In interannual timescales [12] atmospheric and oceanic processes explain around 88% of observed variations, with atmospheric processes having a larger contribution than oceanic processes.

The Southern Ocean, embracing Antarctic Circumpolar Current (ACC),the strongest current on the Earth, is an important player in the climate system. Given the strength of currents in the Southern Ocean, the resulting angular momentum for this region is one of the key contributors in overall oceanic angular momentum. Hence, as suggested by previous articles [16-19], the Southern Ocean has a dominant role in the motion term of excitation for polar motion and length of day. In this paper, the general circulation ocean model, HYCOM, is deployed to investigate the regional effect of the Southern Ocean on the Earth's polar motion and length of day. As a high resolution general circulation model with realistic continent boundaries and bottom topography, multiple layers in depth and wind forcing adopted from general circulation atmospheric models, HYCOM is capable of predicting ocean dynamics with high fidelity [20]. The angular momentum calculated from HYCOM simulations have a very rich temporal variability, and hence, have a larger effect on the Earth dynamics than low fidelity ocean models, such as the quasi-geostrophic models [21, 22] and reduced-order ocean dynamics models [23, 24].

The paper is structured as follows: the governing equations for polar motion and length of day as well as HYCOM governing equations are presented in the methods section with typical HYCOM simulation results illustrated in the end of the section. Predicted values for angular momentum components and change in length of day for global oceans and the isolated region of the Southern Ocean are shown in the results section and conclusions are discussed in the last section.

2. METHODS

In this study, the polar motion and length of day excitation functions caused by oceanic angular momentum are calculated using the general circulation model, HYCOM.

2.1 Polar motion and length of day equations

Polar motion and length of day equations are given as

$$\begin{aligned} \frac{\dot{m}_1}{\sigma_0} + m_2 &= \frac{\Omega^2 c_{23} - \Omega \dot{c}_{13} + \Omega h_2 - \dot{h}_1}{\Omega^2 (C - A)} \frac{k_s}{k_s - k} = \phi_2 \\ \frac{\dot{m}_2}{\sigma_0} - m_1 &= -\frac{\Omega^2 c_{13} + \Omega \dot{c}_{23} + \Omega h_1 + \dot{h}_2}{\Omega^2 (C - A)} \frac{k_s}{k_s - k} = -\phi_1 \\ \dot{m}_3 &= \frac{-\Omega \dot{c}_{33} - \dot{h}_3}{\Omega C} \left(1 + \frac{4}{3} \frac{k}{k_s} \frac{C - A}{C}\right)^{-1} = \phi_3 \end{aligned} \quad (1)$$

where m_1 and m_2 are polar motion and m_3 is the length of day component, Ω is the Earth's spin rate, k is the Love number, k_s is the secular Love number and σ_0 is the Chandler frequency. h_i are relative angular momentum components, c_{ij} are the perturbations of the Earth's moment of inertia with A and C as the main components and ϕ_i are the excitation function componets [25].

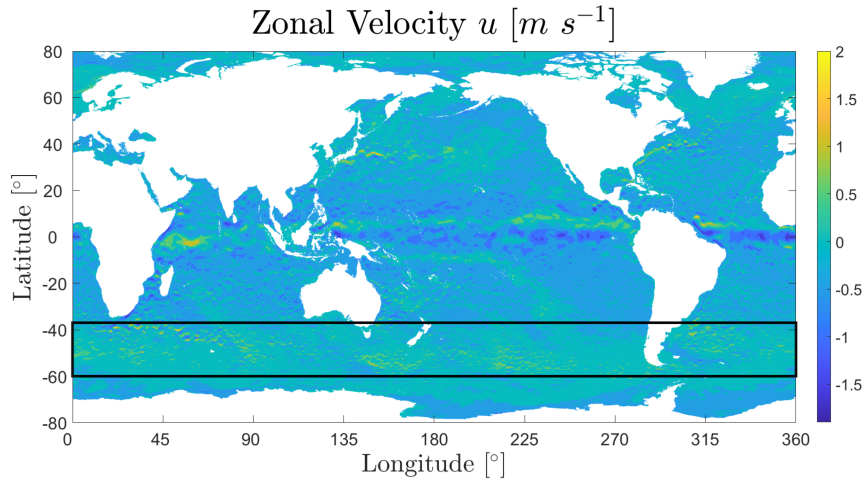


Figure 1: Instantaneous zonal velocity distribution in HYCOM simulations for the top isopycnal layer. The Southern Ocean region is displayed in a rectangular window.

2.2 HYCOM governing equations

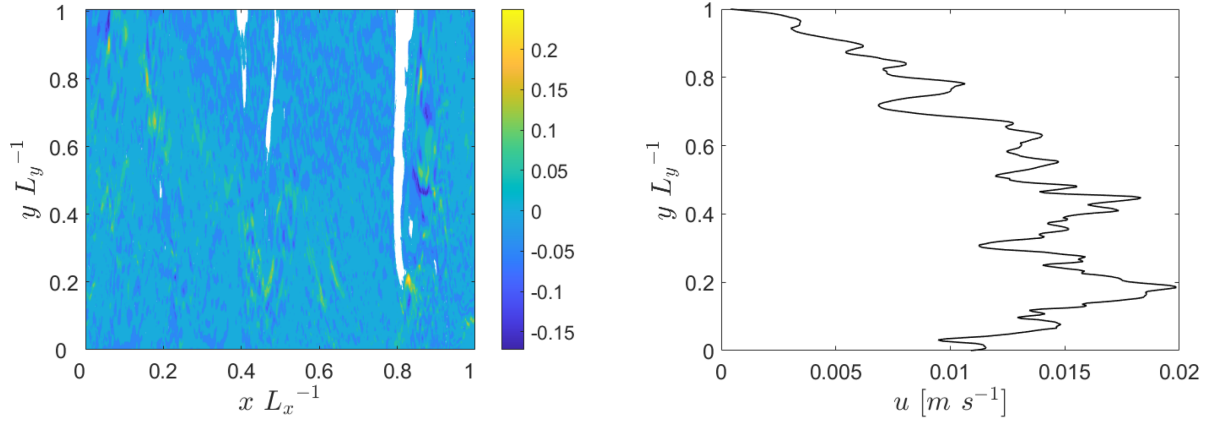


Figure 2: Time and layer averaged zonal velocity distribution (left); time, layer and zonally-averaged zonal velocity profile vs meridional coordinate (right) for the Southern Ocean region in HYCOM simulations.

To calculate oceanic excitation of polar motion and length of day, we use solutions from a general ocean circulation HYCOM (HYbrid Coordinate Ocean Model). The model simulation results are downloaded from the HYCOM data portal (hycom.org), where they had been interpolated to z-level coordinates. HYCOM governing equations consist of the conservation laws for momentum, temperature, salinity and mass, as well as the equation of state:

$$\begin{aligned}
 \frac{\partial \mathbf{v}}{\partial t} + (\mathbf{v} \cdot \nabla) \mathbf{v} + 2\boldsymbol{\omega} \times \mathbf{v} &= -\frac{\nabla P}{\rho} + \frac{\nabla \cdot \boldsymbol{\tau}}{\rho}, \\
 \frac{\partial T}{\partial t} + \nabla \cdot (T\mathbf{v}) &= \nabla \cdot (\kappa \nabla T) + F^T, \\
 \frac{\partial S}{\partial t} + \nabla \cdot (S\mathbf{v}) &= \nabla \cdot (\kappa \nabla S) + F^S, \\
 \nabla \cdot \mathbf{v} &= 0, \\
 \rho &= \rho(T, S, P),
 \end{aligned} \tag{2}$$

where $\mathbf{v} = (u, v, w)$ is the velocity vector, $\boldsymbol{\omega}$ is the Earth's angular velocity vector, P is pressure, and $\boldsymbol{\tau}$ is a stress tensor including viscosity. T and S are temperature and salinity while F^T and F^S

are the corresponding source terms in their conservation equations, κ is diffusivity tensor and ρ is the density. The horizontal resolution in HYCOM is 1/12 degree in the longitude and latitude and the model includes 41 isopycnal layers. The hybrid coordinate is isopycnal in the open, stratified ocean while it reforms to terrain-following coordinates in shallow coastal regions and to z-level coordinates in the mixed layer and unstratified seas. The atmospheric wind forcing in HYCOM is time-dependent and is generated by atmospheric general circulation models such as NAVGEM (Navy Global Environmental Model) [20].

Typical ocean simulation results by HYCOM are illustrated in figures 2-4. Figures 2 and 3 show instantaneous distributions of zonal and meridional velocity components in HYCOM simulations with the Southern Ocean region depicted in a rectangular box. Figure 2 displays time and layer averaged distribution of zonal velocity in the Southern Ocean region as well as its zonally averaged profile versus the meridional coordinate. Similarly, in figure 4 time and layer average distribution of meridional velocity is shown in the Southern Ocean region as well as its meridionally averaged profile versus the zonal coordinate. Time averaging is performed in the 5-year period from December 2013 to December 2018 based on 10-day sampled snapshots.

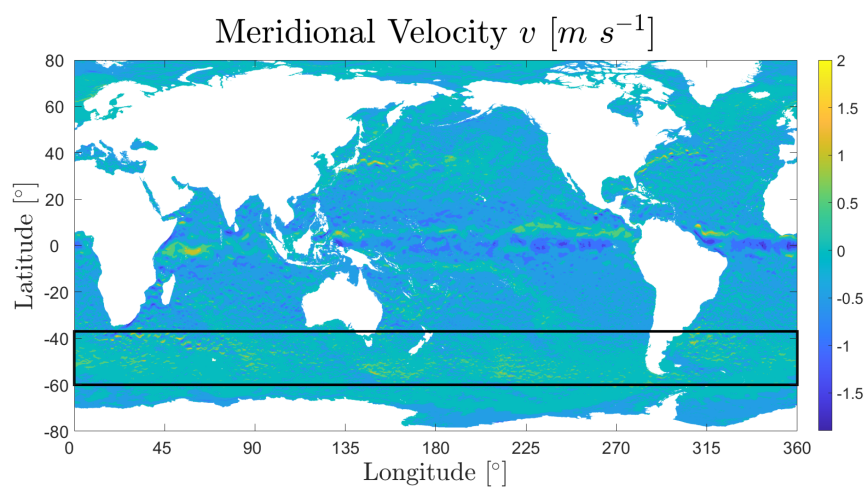


Figure 3: Instantaneous meridional velocity distribution in HYCOM simulations for the top isopycnal layer. The Southern Ocean region is displayed in a rectangular window.

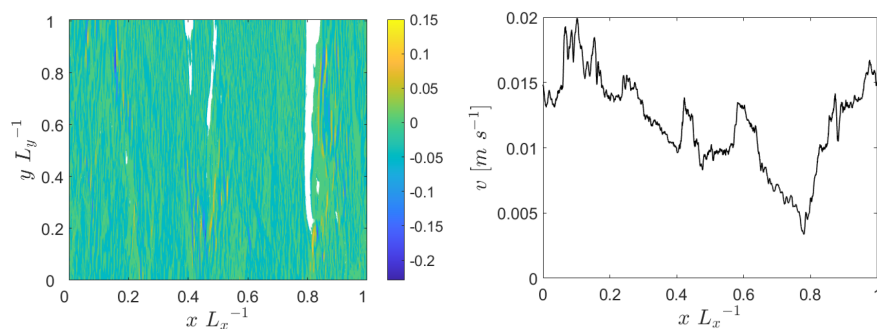


Figure 4: Time and layer averaged meridional velocity distribution (top); time, layer and meridionally-averaged meridional velocity profile vs zonal coordinate (bottom) for the Southern Ocean region in HYCOM simulations.

3. RESULTS

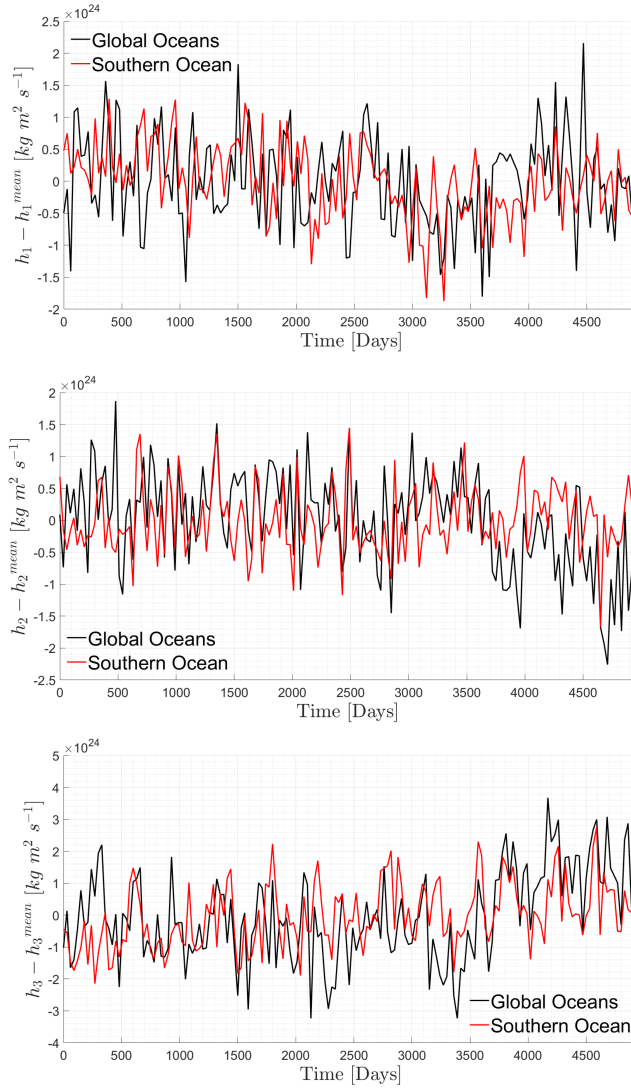


Figure 5: Relative angular momentum components h_1 (top), h_2 (middle) and h_3 (bottom) calculated from the velocity field of the Southern Ocean and global oceans in HYCOM simulations.

Figure 5 shows angular momentum components resulting from velocity field in HYCOM simulations in the period September 2002 to June 2016, sampled every 30 days. Angular momentum fluctuations are calculated for global oceans and the isolated region of the Southern Ocean and plotted after subtracting the average values in time. As observed in this figure, in contrast to other ocean regions such as North Atlantic and North Pacific [21,22], the fluctuations order of magnitude is the same for the Southern Ocean region and global oceans. This highlights the significant contribution of the Southern Ocean currents in the excitation of polar motion and length of day. Figure 6 shows the change in length of day resulting from angular momentum in the Southern Ocean and global oceans in both time and frequency domains. To analyse the contribution of the Southern Ocean in the excitation of length of day, the correlation factors between the two time series are compared in the original case and after apply low-pass, band-pass and high-pass filters on the signals. In all cases, correlation factors are higher than 0.49 and the highest correlation is observed when a band-pass filter with cut-off frequencies corresponding to 90 days and 400 days are applied

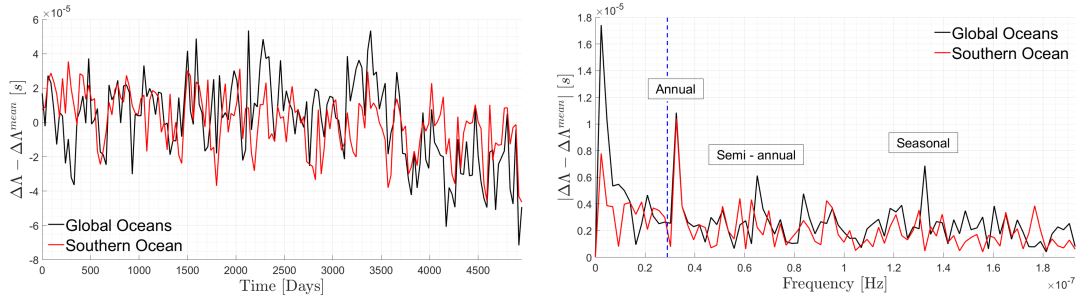


Figure 6: Change in length of day resulting from the Southern Ocean and global oceans angular momentum in HYCOM simulations in time (top) and frequency (bottom) domains. In the bottom panel, the spectral peaks corresponding to seasonal, semi-annual and annual frequencies are labeled accordingly and the frequency of the dashed line corresponds to 400 days.

on the signals as shown in figure 7. Figure 8 compares length of day fluctuations caused by global

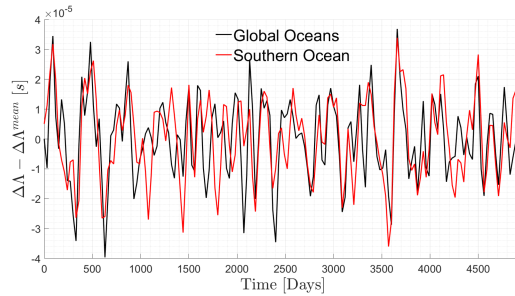


Figure 7: Change in length of day resulting from the Southern Ocean and global oceans angular momentum in HYCOM simulations after applying a band pass filter with cut-off frequencies corresponding to 90 and 400 days.

oceans with geodetic observations after subtracting the mass term both in time and frequency domains. Geodetic observations for length of day are obtained from IERS portal and the mass term coefficient (C20) is calculated by CNES (French National Centre for Space Studies) using gravimetric Earth observation satellite mission, GRACE (Gravity Recovery A Climate Experiment). The predicted change in length of day by HYCOM simulations is an order of magnitude smaller than the geodetic observations and this can be explained by the dominant effect of atmospheric angular momentum in the excitation of length of day. To examine cross-correlation between the two time series, low-pass, band-pass and high-pass filters were applied on the signals and only in case of a band-pass filter with cut-off frequencies of 90 and 400 days, the correlation factor of 0.2 was observed.

4. CONCLUSION

In this paper, oceanic excitation of length of day and polar motion are investigated using a high-resolution general circulation ocean model. To this end, oceanic angular momentum components are calculated and compared between the Global Oceans and the isolated region of the Southern Ocean. The comparison shows that the Southern ocean has a dominant contribution in oceanic excitation of polar motion and length of day, supporting previous notions by Wahr [19] and Lambeck and Hopgood [16]. Strong correlation between Southern ocean and global oceans is observed in

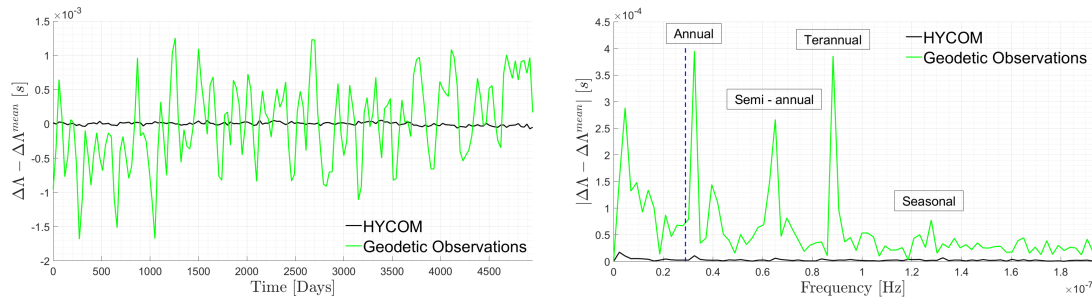


Figure 8: Comparison of length of day fluctuations caused by global oceans in HYCOM simulations with geodetic observations after subtracting the mass term, in time (top) and frequency (bottom) domains.

the original time series as well as window-filtered signals with highest correlation in case of band pass filtering with cut-off frequencies corresponding to 90 and 400 days. Excitations from Global oceans have correlation with geodetic observations for motion term when the same band-pass filter is applied i.e. in seasonal or interseasonal scales which agrees with previous studies. One of the important findings of this work is that even when the excitation terms are carefully reconstructed from the high-resolution ocean models, they are not sufficient to explain the geodetic observations. Hence, the future work will concentrate on including the atmospheric angular momentum in the suggested modelling framework.

5. REFERENCES

- [1] Seitz, F. and Schmidt, M., 2005. Atmospheric and oceanic contributions to Chandler wobble excitation determined by wavelet filtering. *Journal of Geophysical Research: Solid Earth*, 110(B11).
- [2] Chao, B.F., Ray, R.D., Gipson, J.M., Egbert, G.D. and Ma, C., 1996. Diurnal/semidiurnal polar motion excited by oceanic tidal angular momentum. *Journal of Geophysical Research: Solid Earth*, 101(B9), pp.20151-20163. Vancouver
- [3] Gross, R.S., Fukumori, I. and Menemenlis, D., 2003. Atmospheric and oceanic excitation of the Earth's wobbles during 1980–2000. *Journal of Geophysical Research: Solid Earth*, 108(B8).
- [4] Dicke, R.H., 1961. *The Rotation of the Earth (A geophysical discussion)*.
- [5] Nastula, J., Salstein, D.A. and Gross, R., 2014. Regional multi-fluid-based geophysical excitation of polar motion. In *Earth on the Edge: Science for a Sustainable Planet* (pp. 467-472). Springer, Berlin, Heidelberg.
- [6] McCarthy, D.D. and Luzum, B.J., 1991. Prediction of Earth orientation. *Bulletin géodésique*, 65(1), pp.18-21.
- [7] Gross, R.S., 2000. The excitation of the Chandler wobble. *Geophysical Research Letters*, 27(15), pp.2329-2332.
- [8] Aoyama, Y. and Naito, I., 2001. Atmospheric excitation of the Chandler wobble, 1983–1998. *Journal of Geophysical Research: Solid Earth*, 106(B5), pp.8941-8954.
- [9] Brzeziński, A. and Nastula, J., 2002. Oceanic excitation of the Chandler wobble. *Advances in Space Research*, 30(2), pp.195-200.
- [10] Gross, R.S., 2007. Earth rotation variations-long period. *Treatise on geophysics*, 3, pp.239-294.
- [11] Schindelegger, M., Salstein, D., Einöspigel, D. and Mayerhofer, C., 2017. Diurnal atmosphere-ocean signals in Earth's rotation rate and a possible modulation through ENSO. *Geophysical Research Letters*, 44(6), pp.2755-2762.

- [12] Gross, R.S., Fukumori, I., Menemenlis, D. and Gegout, P., 2004. Atmospheric and oceanic excitation of length of day variations during 1980–2000. *Journal of Geophysical Research: Solid Earth*, 109(B1).
- [13] Johnson, T.J., Wilson, C.R. and Chao, B.F., 1999. Oceanic angular momentum variability estimated from the Parallel Ocean Climate Model, 1988–1998. *Journal of Geophysical Research: Solid Earth*, 104(B11), pp.25183-25195.
- [14] Rosen, R.D. and Salstein, D.A., 1985. Contribution of stratospheric winds to annual and semiannual fluctuations in atmospheric angular momentum and the length of day. *Journal of Geophysical Research: Atmospheres*, 90(D5), pp.8033-8041.
- [15] Dill, R., Dobslaw, H. and Thomas, M., 2019. Improved 90-day Earth orientation predictions from angular momentum forecasts of atmosphere, ocean, and terrestrial hydrosphere. *Journal of Geodesy*, 93(3), pp.287-295.
- [16] Lambeck, K. and Hopgood, P., 1981. The Earth's rotation and atmospheric circulation, from 1963 to 1973. *Geophysical Journal International*, 64(1), pp.67-89.
- [17] Ma J., Zhou Y.H., Liao D.C., Chen J.L., 2009. Excitation of Chandler wobble by Pacific, Indian and Atlantic Oceans from 1980 to 2005, *Chinese Journal of Astronomy and Astrophysics*, 33(4), 410–420.
- [18] Nastula J., Gross R.S., Salstein D.A., 2012. Oceanic excitation of polar motion: identification of specific oceanic areas important for polar motion excitation, *Journal of Geodynamics.*, 62, 16–23.
- [19] Wahr J.M., 1983. The effects of the atmosphere and oceans on the Earth's wobble and on the seasonal variations in the length of day – II. Results, *Geophysical Journal International*, 74(2), 451–487.
- [20] Wallcraft, A.J., Metzger, E.J. and Carroll, S.N., 2009. Software design description for the HYbrid Coordinate Ocean Model (HYCOM) version 2.2. Naval Research Laboratory, pp.13-15.
- [21] Naghibi, S.E., Jalali, M.A., Karabasov, S.A. and Alam, M.R., 2017. Excitation of the Earth's Chandler wobble by a turbulent oceanic double-gyre. *Geophysical Journal International*, 209(1), pp.509-516.
- [22] Naghibi, S.E. and Karabasov, S.A., 2020. Excitation of the Earth's Chandler wobble by the North Atlantic double-gyre. *Astrometry, Earth Rotation, and Reference Systems in the GAIA era*, pp.237-242.
- [23] Naghibi, S.E., Karabasov, S.A., Jalali, M.A. and Sadati, S.H., 2019. Fast spectral solutions of the double-gyre problem in a turbulent flow regime. *Applied Mathematical Modelling*, 66, pp.745-767.
- [24] Naghibi, S.E., Karabasov, S.A. and Kamenkovich, I., 2023. Zonal jets in the Southern Ocean: A semi-analytical model based on scale separation. *Ocean Modelling*, 183, p.102198.
- [25] Gross, R.S., 2007. Earth rotation variations-long period. *Treatise on geophysics*, 3, pp.239-294.

EFFECT OF THE TIDAL MASS REDISTRIBUTION ON THE EARTH SECULAR CHANGES IN LENGTH OF DAY

A. ESCAPA¹, T. BAENAS², J. M. FERRÁNDIZ³

¹ Universidad de León, Dept. Ingeniería Aeroespacial, León - Spain - alberto.escapa@unileon.es

² Centro Universitario de la Defensa, Dept. Ciencias e Informática, Murcia - Spain

³ Universidad de Alicante, Dept. Matemática Aplicada, Alicante - Spain

ABSTRACT. We study the Earth secular changes of the length of day due to tidal mass redistribution (Baenas et al. 2021, A&A 648, A89). The problem is worked out within a Hamiltonian framework for a two-layer deformable Earth model including dissipative effects at the core–mantle boundary. That canonical approach makes possible to derive in a unified way the effects of the tidal redistribution potential for all the aspects of Earth rotation like precession, nutation, and length of day. We obtain the analytical expressions that allow the computation of the secular changes of length of day for different Earth rheological and oceanic models by means of frequency–dependent Love number formalism. Their evaluation for the Love number sets given by IERS Conventions (2010) —solid Earth— and Williams & Boggs (2016) —oceans— provides an increase of 2.418 ms/cy in the length of day, in very good agreement with recent observational values.

1. INTRODUCTION

In the last years we have investigated the contributions of the redistribution tidal potential to the Earth rotation (Baenas et al. 2019, 2020, and 2021). That redistribution arises as a consequence of the tidal action of the Moon and the Sun: it generates an Earth mass redistribution that, in turn, gives rise to an additional term of the gravitational potential of the Earth —the redistribution tidal potential. This mass redistribution depends on the Earth structure; with a very significant role of the frequency–dependent Love numbers describing the solid and oceanic tides.

The redistribution tidal potential contributes to all the facets of Earth rotation. In particular, to the precession and nutation of the Earth that were previously tackled within the Hamiltonian framework of the rotation of the non-rigid Earth. Such framework provided consistent analytical formulae that can be evaluated for different Earth parameters and rheological models like, e.g., Love number sets (Baenas et al. 2019, 2020).

Here, we summarize the extension of the above formulation to study the secular variation of the Earth’s rotation rate due to tidal redistribution effects. This topic has been comprehensively addressed in Baenas et al. (2021), so we refer to the reader to that work to find further details on its notations, fundamentals, and derivations.

The Earth’s rotation rate is defined in terms of the z component —relative to a certain system linked to the Earth— of the angular velocity of the Earth, ω_z . Alternatively, one can introduce the length of day (LOD) as $\text{LOD} = 2\pi\dot{\theta}/\omega_z$, with $\dot{\theta}$ the Earth’s rotation angle (ERA).

Hence, any change in ω_z translates into a change in LOD. Denoting such changes with a δ we have (Bizouard 2020)

$$\delta\text{LOD} = -\overline{\text{LOD}} \frac{\delta\omega_z}{\omega_E}, \quad (1)$$

where ω_E is the nominal mean angular velocity of the Earth —one mean solar day— and $\overline{\text{LOD}}$ is the mean length of day, $\overline{\text{LOD}} = 2\pi\dot{\theta}/\omega_E$. For a secular angular acceleration of the Earth about its

spin axis, Eq. (1) entails that the secular changes in the LOD time rate are given by

$$\delta \left(\frac{d\text{LOD}}{dt} \right) = -\frac{\overline{\text{LOD}}}{\omega_E} \delta \left(\frac{d\omega_z}{dt} \right). \quad (2)$$

Observationally, the tidal part of the LOD rate is about 2.3 ± 0.1 ms/cy (Stepheson et al. 2016), including a contribution from the atmospheric tides that amounts to -0.1 ms/cy (Ray et al. 1999). There are other significant contributions to the LOD rate of non-tidal origin related to changes of the Earth’s inertia matrix, e.g., glacial isostatic adjustment (GIA), and other physical mechanisms (Gross 2015).

The main goal of our study is to derive an analytical expression for the secular LOD rate that takes into account the tidal contribution. That expression will depend on the perturbing bodies causing the tides, i.e., the Moon and the Sun, through their physical characteristics and ephemerides, as well as of the Earth’s own response characterized by the Earth model (rheology, layers, etc.).

Authors	LOD rate (ms/cy)	Mass redistribution	Earth model	Analytical
Getino & Ferrándiz (1991)	2.10	AE	1L	Yes
Krasinsky (1999)	2.13	AE	1L	Yes
Ray et al. (1999)	2.38	OT	1L (atm.)	No
Lambert & Mathews (2008)	2.34	AE+OT	2L	No
Mathews & Lambert (2009)	2.50	AE+OT	2L	No
Williams & Boggs (2016)	2.40	AE+OT	2L	Yes

Table 1: Some researches on the tidal secular deceleration for different Earth models

In Table 1 we have displayed a summary of other works that have also computed the tidal secular deceleration. Most of them used a torque–approach, but Getino & Ferrándiz (1991) —as this work, and not always providing analytical formulae (Analytical column in Table 1). The employed structure of the Earth is also different: earlier studies took one layer models (1L), whereas the later ones also include a fluid core (2L).

Besides, in some works the tidal mass redistribution was reduced to the anelasticity (AE) of the solid part, albeit others incorporate the direct effects due to oceans tides (OT), or estimate the effect of the atmosphere (Ray et al. 1999).

Mathews & Lambert (2009) and Williams & Boggs (2016) considered the most complete model —two–layer Earth with coupled core–mantle in the secular evolution, although the underlying oceanic model is different (CSR4.0 versus FES2004, respectively), as well as the frequency dependence of the Love numbers. The formalisms were also different: SOS (Sasao et al. 1980) approach versus direct torque approach.

As we will show in the next section, our Earth model (Baenas et al. 2021) is quite close to that of Williams & Boggs (2016), but the theory is constructed from a Hamiltonian approach, in such a way that we can consistently derive other effects of the tidal mass redistribution on the Earth rotation.

2. METHOD

Our baseline Earth model consists of a two–layer structure with a deformable mantle and a fluid core. The gravitational interaction of the Moon and the Sun —responsible of the tides— is described from the orbital functions $B_{i;p}$, $C_{i;p}$, and $D_{i;p}$ defined in Kinoshita (1977). They are

computed from some lunar and Sun ephemerides, e.g., ELP 2000 (Chapront-Touzé & Chapront 1983) or VSOP82 (Bretagnon 1982).

The mass redistribution —response of the Earth to the Moon and the Sun gravitational action— is characterized by introducing the Love number formalism with frequency dependence per tide both for the solid and oceanic tides. Love numbers are, in fact, complex functions of the frequency defined as

$$\bar{k}_{2m,j} = |\bar{k}_{2m,j}| e^{i\epsilon_{2m,j}}, m = 0, 1, 2, \quad (3)$$

where m indicates the zonal, diurnal, or semidiurnal band and j refers to the orbital frequency of the Moon and the Sun motions inducing the mass redistribution (Baenas et al. 2019).

In our approach the Love numbers are inputs, derived from some rheological models of the Earth. In particular, in this work we consider for the solid Earth deformation the values given in IERS Conventions (2010) that take into account anelasticity, rotation, ellipticity, and ocean load, as well as the set provided in Williams & Boggs (2016) for the direct contribution of the oceans based on the FES2004 ocean tide model (Lyard et al. 2006).

Our Earth model also incorporates a dissipative torque, \mathbf{N}_d , of viscous and electromagnetic nature at the core–mantle boundary (CMB). The physical characterization of that torque follows Sasao et al. (1980), who defined it in terms of the differences between the angular velocity of the mantle and that of the core $\delta\boldsymbol{\omega}$, as well as three coupling constants. Namely, in a certain system linked to the Earth, we have

$$\mathbf{N}_d = \begin{pmatrix} -R & R' & 0 \\ -R' & -R & 0 \\ 0 & 0 & -R^* \end{pmatrix} \delta\boldsymbol{\omega}. \quad (4)$$

In the study of the Earth tidal secular deceleration, the relevant contribution of \mathbf{N}_d is that of its third component $-R^*\delta\omega_3$. It governs the degree of coupling of the core and mantle according to the fixed time scale T of the secular evolution, through a time–averaged effective polar moment of inertia $C_{\text{eff}}(T)$ as described in Baenas et al. (2021). Its expression is given by

$$\frac{1}{C_{\text{eff}}(T)} = \frac{1}{C} \left(1 + \frac{C_c^2}{C} \frac{1 - e^{-\frac{CR^*T}{C_m C_c}}}{R^*T} \right), \quad (5)$$

where C , C_m , and C_c are the polar principal moments of inertia of the whole Earth, the mantle, and the core.

Usually, two different scenarios are considered. When $T \rightarrow 0^+$, the evolution of the mantle and the core is decoupled (e.g., Yoder et al. 1981 or Wahr et al. 1981) and $C_{\text{eff}}(T) \rightarrow C_m$. For $T \rightarrow +\infty$, the evolution of the mantle and the core is totally coupled (e.g., Mathews & Lambert 2009 or Williams & Boggs 2016) moving as one single deformable layer with $C_{\text{eff}}(T) \rightarrow C$.

All the above features are implemented within a Hamiltonian framework (Baenas et al. 2021). The procedure is direct, but involved. Its main steps consist of introducing a canonical set of variables —Andoyer–like variables (Getino 1995); formulating the rotational kinetic energy of the model through the sum of that of the mantle and that of the core; and constructing the expression for the redistribution tidal potential (Baenas et al. 2019). In addition, since there is a dissipative torque \mathbf{N}_d , it is necessary to construct its associated generalized forces.

Then, it is possible to form the equations of motion and solve them with the aid of a canonical perturbation method (e.g., Hori 1971 or Baenas et al. 2017), providing an analytical expression for the tidal part of the LOD secular rate. It is also possible to extend this approach to tackle the

periodic variations of LOD.

3. RESULTS

By doing so (Baenas et al. 2021), we derive a formula for computing the secular angular deceleration

$$\delta \left(\frac{d\omega_z}{dt} \right) = -\omega_E \frac{C}{C_{\text{eff}}(T)} \sum_{p,q=M,S} f_q k_p \sum_{\substack{i,j;\tau,\epsilon \in \mathcal{I} \\ m=1,2}} |\bar{k}_{2m,j}| T_{ijpq,m}^{(\omega_z)} \sin \varepsilon_{2m,j}. \quad (6)$$

It is given in terms of the following dependencies:

- A combination $T_{ijpq,m}^{(\omega_z)}$ related to Kinoshita orbital functions $B_{i;p}$, $C_{i;p}$, and $D_{i;p}$, which can be computed from ephemerides
- Love number sets $\bar{k}_{2m,j}$ (Eq. 3) as given from some input rheological Earth model for solid and oceanic tides
- The time-averaged effective polar inertia moment $C_{\text{eff}}(T)$ (Eq. 5)
- Model parameters k_p and f_p involving the masses and semi-major axis of the perturbers' orbit, as well as some Earth constants like its dynamical ellipticity, equatorial radius, etc.

The analytical character of Eq. (6) allows isolating the effects of the several features entering in our model. For example, it is possible to evaluate the differences between the decoupled $C_{\text{eff}}(T) = C_m$ and totally coupled $C_{\text{eff}}(T) = C$ cases—or intermediate situations—or to compute the contributions associated with each frequency band or with solid and oceanic tides, as well as the sensitivity of Earth secular changes in the LOD to different Love numbers sets.

In Tables 2 and 3 we present some of these calculations. For all of them we employed the orbital functions $B_{i;p}$, $C_{i;p}$, and $D_{i;p}$ derived in Kinoshita (1977); the solid Earth Love numbers given in IERS Conventions (2010); the set for the direct contribution of the oceans provided in Williams & Boggs (2016); and the remaining parameters like C_c/C_m , k_p , and f_p as those appearing in Baenas et al. (2021).

Case	Solid tides (IERS 2010)	Ocean tides (WB2016)	Total (ms/cy)
Tot. coupled	0.108	2.310	2.418
Decoupled	0.122	2.607	2.729

Table 2: Contributions to the tidal part of the LOD rate for totally coupled/decoupled cases and solid/oceanic Love numbers models

In Table 2 the differences between the decoupled and totally coupled cases, and the contributions from the solid and oceanic tides, are displayed. The oceanic tides are the main contributors to the tidal part of the LOD rate, since they are the dominant source of dissipation. They enter our model through the imaginary part of the ocean Love number set $\bar{k}_{2m,j}$.

It can also be concluded that, for this secular effect, the totally coupled core–mantle case fits well with the observational evidence for the tidal part LOD rate—without considering the effect of the atmosphere—which is about 2.4 ± 0.1 ms/cy, as indicated in Section 1.

In Table 3 we show the contributions per frequency band or harmonic contribution of the re-distribution tidal potential, keeping also those of the solid and oceanic tides, for a totally coupled

Potential	Solid tides (IERS 2010)	Ocean tides (WB2016)	Total (mas/cy)
Tesseral ($m = 1$)	-0.004	0.352	0.348
Sectorial ($m = 2$)	0.112	1.959	2.071
Total	0.108	2.310	2.418

Table 3: Contributions to the tidal part of the LOD rate per tidal band and solid/oceanic Love numbers models

core–mantle model. There is no contribution of the zonal terms. As can be viewed, the most important frequency band for the tidal part of the LOD rate is the semidiurnal band, which corresponds to the sectorial terms of the redistribution potential.

Our numerical results presented in Tables 2 and 3 are in very good agreement, in addition to observational evidences, with those of Williams & Boggs (2016), despite the quite different theoretical approaches to the problem. It confirms the validity of both researches.

In contrast, the results present significant differences with respect to those of Lambert & Mathews (2008) and Mathews & Lambert (2009). The source of the discrepancies is uncertain (Baenas et al. 2021), since such works do not provide analytical expressions to the tidal LOD secular rate. They might be due to the use of different underlying models, particularly of the oceanic Love number set, to some flaw in their developments, or to some combination of both factors.

In this regard, analytical approaches allow a straightforward application to different Earth rheological and oceanic models, since they provide literal formulae. So, a change in Love number sets for both the solid Earth and the oceans, as that scheduled in the next IERS Conventions update, can be directly incorporated into these frameworks, determining their contribution to the rotation of the Earth due to the tidal redistribution of mass.

Furthermore, the Hamiltonian formalism offers the additional advantage that all the effects of the redistribution tidal potential are worked out from the same Hamiltonian function, so its contribution to precession, nutation, and secular changes in LOD necessarily remains consistent.

Acknowledgements

This work has been partially supported by the Spanish projects PID2020-119383GB-I00 funded by Ministerio de Ciencia e Innovación (MCIN/AEI/10.13039/501100011033/) and PROMETEO /2021/030 funded by Generalitat Valenciana.

4. REFERENCES

- Baenas, T., Escapa, A., Ferrándiz, J.M., Getino, J., 2017, “Application of first-order canonical perturbation method with dissipative Hori-like kernel”, *Int. J. Nonlin. Mech.* 90, pp. 11–20, doi: 10.1016/j.ijnonlinmec.2016.12.017
- Baenas, T., Escapa, A., Ferrándiz, J.M., 2019, “Precession of the non-rigid Earth: Effect of the mass redistribution”, *A&A* 626, A58, doi: 10.1051/0004-6361/201935472
- Baenas, T., Escapa, A., Ferrándiz, J.M., 2020, “Nutation of the non-rigid Earth: Effect of the mass redistribution”, *A&A* 643, A159, doi: 10.1051/0004-6361/202038946
- Baenas, T., Escapa, A., Ferrándiz, J.M., 2021, “Secular changes in length of day: Effect of the mass redistribution”, *A&A* 648, A89, doi: 10.1051/0004-6361/202140356
- Bizouard, C., 2020, “Geophysical Modelling of the Polar Motion”, *De Gruyter Studies in Mathematical Physics* 31, De Gruyter, doi: 10.1515/9783110298093

- Bretagnon, P., 1982, "Théorie du mouvement de l'ensemble des planètes. Solution VSOP82", *Astron. Astrophys.* 114, pp. 278–288
- Chapront-Touzé, M., Chapront, J., 1983, "The lunar ephemeris ELP 2000", *Astron. Astrophys.* 124, pp. 50–62
- Getino, J., 1995, "Forced nutations of a rigid mantle-liquid core Earth model in canonical formulation", *Geophys. J. Int.* 122, pp. 803–814, doi: 10.1111/j.1365-246X.1995.tb06839.x
- Getino, J., Ferrándiz, J.M., 1991, "A Hamiltonian theory for an elastic earth: Secular rotational acceleration", *Celest. Mech. Dyn. Astr.* 52, pp. 381–396, doi: 10.1007/BF00048453
- Gross, R. S., 2015, "Earth rotation variations — long period", in *Treatise on Geophysics* (second edition) 3, pp. 215–261, doi: 10.1016/B978-0-444-53802-4.00059-2
- Hori, G. H., 1971, "Theory of general perturbation for non-canonical systems", *Publ. Astr. Soc. Japan* 23, pp. 567–587
- IERS Conventions (2010), 2010, Gerard Petit and Brian Luzum (eds.), IERS Technical Note; No. 36
- Kinoshita, H., 1977, "Theory of the rotation of the rigid Earth", *Celest. Mech.* 15, pp. 277–326 doi: 10.1007/BF01228425
- Krasinsky, G.A., 1999, "Tidal effects in the Earth–Moon system and the earth's rotation", *Celest. Mech. Dyn. Astr.* 75, pp. 39–66, doi: 10.1023/A:1008381000993
- Lambert, S.B., Mathews, P.M., 2008, "Second-order torque on the tidal redistribution and the Earth's rotation", *A&A* 481, pp. 883–884, doi: 10.1051/0004-6361:20054516e
- Lyard, F., Lefevre, F., Letellier, T., Francis, O., 2006, "Modelling the global ocean tides: modern insights from FES2004", *Ocean Dyn.* 56, pp. 394–415, doi: 10.1007/s10236-006-0086-x
- Mathews, P.M., Lambert, S.B., 2009, "Effect of mantle and ocean tides on the Earth's rotation rate", *A&A* 493, pp. 325–330, doi: 10.1051/0004-6361:200810343
- Ray, R.D., Bills, B.G., Chao, B.F., 1999, "Lunar and solar torques on the oceanic tides", *J. Geophys. Res.* 104, pp. 17653–17659, doi: 10.1029/1999JB900165
- Sasao, T., Okubo, S., Saito, M., 1980, "A simple theory on the dynamical effects of a stratified fluid core upon nutational motion of the Earth", *Proc. Symp. IAU 78*, pp. 165–183, doi: 10.1017/S0074180900032009
- Stephenson, F.R., Morrison, L.V., Hohenkerk, C.Y., 2016, "Measurement of the Earth's rotation: 720 BC to AD 2015", *Proc. R. Soc. A.*, 472:20160404, doi: 10.1098/rspa.2016.0404
- Wahr, J.M., Sasao, T., Smith, M.L., 1981, "Effect of the fluid core on changes in the length of day due to long period tides", *Geophys. J. R. Astron. Soc.* 64, pp. 635–650, doi: 10.1111/j.1365-246X.1981.tb02688.x
- Williams, J.G., Boggs, D.H., 2016, "Secular tidal changes in lunar orbit and Earth rotation", *Celest. Mech. Dyn. Astr.* 126, pp. 89–129, doi: 10.1007/s10569-016-9702-3
- Yoder, C.F., Williams, J.G., Parke, M.E., 1981, "Tidal variations of Earth rotation", *J. Geophys. Res.* 86, pp. 881–891, doi: 10.1029/JB086iB02p00881

RECENT IMPROVEMENTS TO THE IERS RAPID SERVICE / PREDICTION CENTER COMBINED EOP SOLUTION

M. DAVIS¹, S. BYRAM¹, N. STAMATAKOS¹

¹ U.S. Naval Observatory - USA - maria.a.davis33.civ@us.navy.mil

ABSTRACT. The International Earth Rotation and Reference Systems Service (IERS) Rapid Service / Prediction Center (RS/PC) is responsible for producing Earth Orientation Parameters (EOPs) from a combination of techniques that include Very Long Baseline Interferometry (VLBI), Global Navigation Satellite System (GNSS), Satellite Laser Ranging (SLR), Atmospheric Angular Momentum (AAM), and UTGPS. The RS/PC is committed to producing high-quality EOPs in a low-latency environment to support international geodesy. With this in mind, the RS/PC has made several updates to the combined solution since the last Journées meeting, along with a future development plan to improve the robustness and accuracy of our combined EOP products. These updates include redundancy in observational contributions and modifications to the software that allow for more agile development in the future.

1. BRIEF OVERVIEW OF THE IERS RS/PC EOP COMBINATION

The IERS Rapid Service / Prediction Center (RS/PC) is responsible for disseminating a daily Earth Orientation Parameters (EOP) solution using a combination of observed and modeled data from a variety of techniques (Table 1) to the international community. The RS/PC products contain a combined solution for Polar Motion $-x$ and $-y$, UT1–UTC, Celestial Pole Offsets (dX , dY or $d\psi$, $d\epsilon$), and a calculated length of day (LOD) from the combined UT1–UTC solution. Each contributor in Table 1 is carefully curated to support the larger combined-solution. For example, the primary contributor to the Polar Motion combination is the International GNSS Service (IGS). While the IGS Finals (International GNSS Service 2024a) has a latency of up to 3 weeks, this data also provides a highly-accurate solution that strongly influences Polar Motion. Conversely, the IGS Ultra rapids (International GNSS Service 2024b) have a low-latency of less than 1 day, but in exchange provide a slightly less accurate estimate of Polar Motion.

The UT1–UTC combined-solution is primarily determined from the International VLBI Service for Geodesy and Astrometry (IVS). In the way IGS creates an understanding of Polar Motion behavior from the low- to high-latency, the IVS also produces high-accuracy 24-hour “Rapid” observations that typically take 2-3 weeks to process and analyze (International VLBI Service for Geodesy and Astrometry 2024b). The IVS also sponsors low-latency 1-hour “Intensive” UT1–UTC observations with a lower-accuracy, but can be processed and analyzed in less than 1 day (International VLBI Service for Geodesy and Astrometry 2024a).

While IGS primarily supports Polar Motion, and the IVS primarily supports UT1–UTC, other techniques also contribute to the respective EOP combination (Table 1). However, 24-hr VLBI observing sessions are the only technique able to observe Celestial Pole Offsets (CPOs), dX and dY .

For each parameter, the available data is combined using a weighted smoothing cubic-spline. Only data present at the time of the RS/PC combined-solution will determine the daily EOP solution. Therefore, high-quality, low-latency data is critical in determining a high-quality 0-day EOP solution. In other words, low-latency observations that are also low-quality can significantly impact the 0-day solution, particularly for UT1–UTC. This concept is explained in Figure 1, where

Table 1: Techniques used in the RS/PC daily combination and Bulletin A EOP products, listed by Analysis Center (AC). Diversity in techniques, in addition to high-accuracy, low-latency observations are critical to generating high-quality daily EOPs.

Technique	Contributor	Latency*	Product	EOP
GNSS (IGS)	IGS Finals	≤ 21.5 days	IGS Combination	PM x,y
	IGS Rapids	29 hrs		PM x,y , UT1-UTC [†]
	IGS Ultra rapids	17 hrs		
VLBI (IVS + 1 VLBA)	GSFC VLBI AC	22 hrs	1hr Intensives	UT1-UTC
	USNO VLBI AC			
	GSI VLBI AC	9 hrs	24hr R1/R4	PM x,y , UT1-UTC, dX, dY
	GSFC VLBI AC	~ 2 weeks		
	USNO VLBI AC			
	IAA VLBI AC	N/A		
	IVS Combination AC	2-3 weeks		
SLR	ILRS	2.5 – 7 days	Series A	PM x,y
UTGPS	USNO GPS AC	17 hrs	Derived from IGS Ultra rapid	UT1-UTC
AAM	NOAA	17 hrs	Analysis + 7.5 days predictions	UT1-UTC [†]
	U.S. Navy			

* Latency is defined as from the observation mid-point to the time of RS/PC combination.

[†] Integrated LOD

two versions of a combined UT1-UTC solution are shown. The solid, horizontal line represents the combined EOP solution for a given day, while the faded dashed line demonstrates how the combined EOP solution could be affected if a low-latency observation with low-accuracy (faded hexagon) is

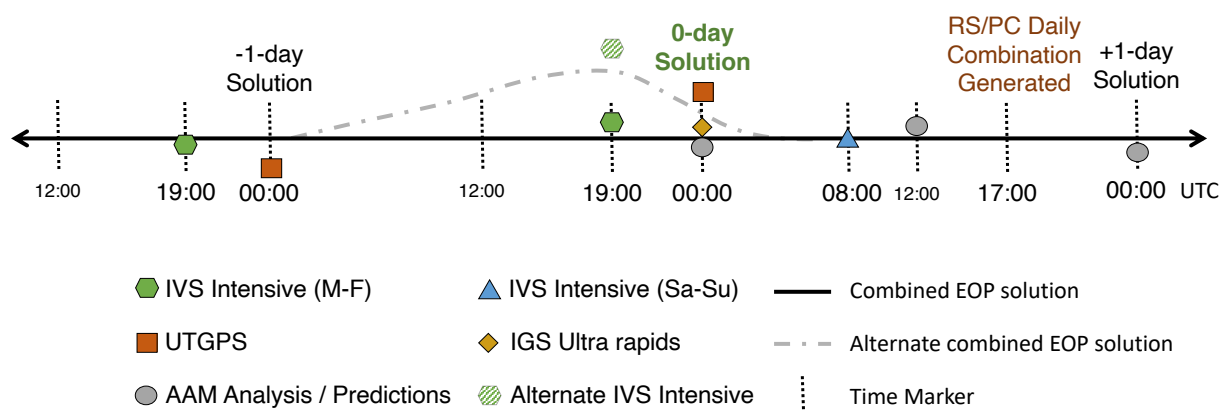


Figure 1: Sketch of RS/PC data contributors for UT1-UTC combined 0-day solution. The alternate marker and alternate combined solution show a scenario where a low-latency observation (e.g., Alternate IVS Intensive) reports a significantly different UT1-UTC value; the local combined-solution, including the UT1-UTC 0-day solution, would be reported in our daily products with a different UT1-UTC value.

included in the combination. An additional challenge with low-latency data is determining how close to “truth” a given input is. Typically, validation for low-latency observations cannot occur for up to 2-3 weeks, once higher-accuracy observations have been fully processed and integrated into the RS/PC combination. For UT1–UTC, “truth” cannot be determined until a 24 hour IVS Rapid observation has been analyzed and integrated into the combination. If the original low-latency observation falls between (is \gtrsim 12 hours from) the more precise IVS Rapid observations, the uncertainty of the local “truth” becomes increasingly difficult to determine.

1.1 Products generated by the RS/PC

While the IERS Earth Orientation Center produces a more stable EOP product because it is delayed by 30 days (C04/Bulletin B) (IERS Earth Orientation Center 2024a; IERS Earth Orientation Center 2024b), the IERS Rapid Service / Prediction Center (RS/PC) combination supports geodetic applications and research that requires EOPs to be updated daily. These products are generated on a daily and weekly basis, and while the recent EOPs will fluctuate as more observational data becomes available, the RS/PC products are able to generate a dynamic, low-latency EOP combination to support daily requirements. The RS/PC generates a rapid EOP combination each day by 17:30 UTC, and weekly EOP products each Thursday before 20:00 UTC (Table 2).

Table 2: The RS/PC publishes updated Earth Orientation Parameters daily and weekly, in addition to quarterly and annual updates to deltaT data and predictions. The presence of “2000A” in the title of a *.data or *.daily file indicates the Celestial Pole Offsets (CPOs) are calculated in dX and dY , while the absence of “2000A” indicates CPOs are calculated in $d\Psi$ and $d\epsilon$. All files in this table can be found on the RS/PC website, <https://maia.usno.navy.mil/ser7>.

File	Description	Publishing Schedule
finals[2000A].all	2 Jan 1973 (MJD 41684) \rightarrow $\langle \text{day}_{\text{BulletinA}} \rangle + 373$ days	
finals[2000A].data	1 Jan 1992 (MJD 48622) \rightarrow $\langle \text{day}_{\text{BulletinA}} \rangle + 373$ days	
Bulletin A (ser7.dat)	$\langle \text{day}_{\text{BulletinA}} \rangle - 7$ days & 365 days predictions (PM, UT1–UTC) - Latest updates to CPOs - Human readable + announcements	Thursdays by 20:00 UTC (typically by 18:30 UTC)
mark3.out	$\langle \text{day}_{\text{BulletinA}} \rangle - 85$ days \rightarrow $\langle \text{day}_{\text{BulletinA}} \rangle + 90$ days - Only PM-x, PM-y, and UT1–UTC	
gpsrapid.out	1 May 1992 \rightarrow $\langle \text{day}_{\text{BulletinA}} \rangle + 15$ days	
finals[2000A].daily.extended	2 Jan 1973 (MJD 41684) \rightarrow $\langle \text{today} \rangle + 373$ days	Daily by 17:30 UTC
finals[2000A].daily	$\langle \text{today} \rangle - 90 \rightarrow \langle \text{today} \rangle + 90$ days	
gpsrapid.daily	$\langle \text{today} \rangle - 90 \rightarrow \langle \text{today} \rangle + 15$ days	
deltat.data	deltaT values on 1st of each month since Feb 1973	Quarterly
deltat.preds	deltaT predictions on beginning of quarter for 10 years	Annually
historic_deltat.data	deltaT values every half year from 1657 to 1984.5	—

The RS/PC began publishing finals[2000A].daily.extended (Table 2) in March 2021, which provides the benefit of a long-term time-series (beginning in 1973) along with daily updates to combined and predicted EOPs. This relatively new product can now replace ad-hoc files users were creating using finals[2000A].all and finals[2000A].daily to meet their needs.

For those interested in deltaT values, the RS/PC publishes an updated file, “deltat.data”, approximately every 3 months containing a deltaT value for the 1st of each month since 1973. A static “historic_deltat.data” file reports deltaT values for every 6 months from 1657 to 1984.5, and “deltat.preds” is published annually providing 10 years of predictions.

2. RECENT UPDATES TO THE COMBINATION

There have been many improvements to the RS/PC combination in the last 4 years including streamlining the combination software to make it more dynamic, easier to update, and generally more robust. Furthermore, the RS/PC website returned in January 2022, and is now more resilient and user friendly. Prior to the current website, the RS/PC offered a “primary” and “backup” website. However, the burden was on the user to determine which server had provided the primary solution on a given day. With the current configuration, there is a single website (<https://maia.usno.navy.mil/ser7/>) where a user will receive the most up-to-date RS/PC EOP solution; redundant solutions are now handled on the backend to reduce user confusion. In a continued effort to support user needs, the RS/PC no longer publishes daily products (Table 2) using any updated data-contributions intended for the Bulletin A products on Thursdays. Instead, the daily products are published with the available contributor’s data at 17:00 UTC, and the Bulletin A products are published with any additional data from contributors provided after the daily; “finals[2000A].daily.extended” and “finals[2000A].all” will contain the same combination epochs on Thursdays once the Bulletin A products are published, while “finals[2000A].all” will potentially contain a slightly more updated solution. One of the most critical updates made to our publication process is the implementation of manual publication, where the daily RS/PC combination is not published without a manual review and approval. This procedure helps to ensure the RS/PC is producing the best combined EOP solution possible with the available data.

The RS/PC continually works to improve the redundancy and robustness of observational input data included in the combination. One such improvement has been the addition of the Very Long Baseline Array’s (VLBA) Mauna Kea antenna. Mauna Kea (Mk) participates in 1 hour Intensive observations with Wettzell (Wz), as a substitute for Kokee (Kk) or Ishioka (Is) when the latter are unable to observe. Recently, Mk has replaced Is in the weekend Intensives while Is continues to observe in VGOS. Mk continues to participate in IVS Intensives as an important contributor to the UT1–UTC combined solution.

Another relatively recent improvement to the combination has been to implement individual systematic corrections for VLBI observations. Prior to this update, the RS/PC was only able to apply a single systematic correction per analysis center data file. For example, the USNO VLBI Analysis Center (AC) provides a single file for all VLBI Intensive observations it analyses. Previously, the RS/PC was only able to generate a single characterization for all of the baselines; characterizing each unique baseline (e.g., Kk–Wz) is now managed individually. By characterizing the residuals (i.e., $residual_{session-type} = EOP_{session-type} - EOP_{C04}$) of each session-type or baseline, the RS/PC is able to better integrate new baselines into the combination, particularly if they have significantly different systematic characteristics than the dominant baseline (i.e., the baseline with the majority of observations in a given analysis file). This in turn creates the opportunity to integrate new session-types into the combination, previously ignored due to this constraint.

2.1 Integrating VLBI VGOS Intensives

One such new session-type recently integrated into the RS/PC combination is the VGOS-INT-A series analyzed by the NASA Goddard Space Flight Center (GSFC) AC; a VGOS Intensive utilizing VGOS Kokee and Wettzell (K2–Ws) antennas. This Intensive series underwent more rigorous analysis prior to being integrated into the combination, as VGOS is a new observation methodology within the VLBI community. While the UT1–UTC observations generally behaved similarly to the S/X Kk–Wz Intensive series, the relationship between the series’ residual ($UT1 - UTC_{K2-Ws} - UT1 - UTC_{RS/PCFinals}$) and reported error was skewed (Figure 2a). While Kk–Wz slightly overestimates the accuracy of its observations, K2–Ws significantly overestimates the accuracy of its observations (Figure 2). However, GSFC AC was able to correct a large portion of the overestimation (Figure 2b) by applying a model to account for previously ignored physical parameters, such as atmospheric turbulence (Gipson et al., 2023). While the error appears to

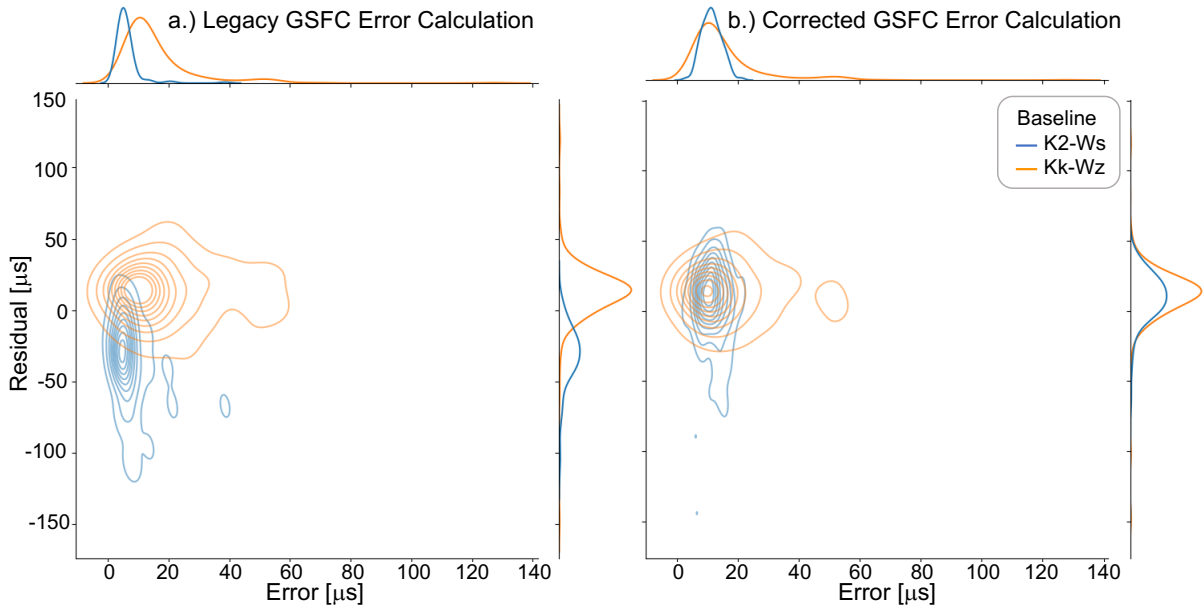


Figure 2: The RS/PC initially found that a) the reported error of the VGOS K2-Ws (Kokee to Wettzell South) baseline was significantly overestimating the accuracy of the observation. This relationship was corrected enough to use in the RS/PC combination after b) GSFC AC applied a model accounting for physical parameters such as atmospheric turbulence.

continue to be overestimated, the discrepancy between the Intensive residual and the associated error is sufficiently small enough to use in the RS/PC combination. The additional VLBI Intensive, K2-Ws baseline, continues to report UT1–UTC values within 1σ of the Kk–Wz baseline from GSFC AC and USNO AC, adding resiliency to the combined UT1–UTC solution.

2.2 Transitioning to the ITRF2020

The RS/PC combination aligned to the International Terrestrial Reference Frame 2020 (ITRF2020) (Altamimi et al., 2023) via the 20C04 on 29 June 2023, 3 months after the initial transition date of 30 March 2023. The transition to align RS/PC products with ITRF2020 was delayed when an initial discrepancy was identified between 20Finals and 20C04 (i.e., $residual_{2020}$) in Polar Motion, showing a significant increase in the standard deviation of residuals, and an offset of the $residual_{2020}$ preceding the end of the ITRF2020 time-series. Similar characteristics were present when comparing the 20C04 to 20JPL-SPACE, but not present when comparing 20Finals to 20JPL-SPACE (Jet Propulsion Lab (JPL) 2024). This issue was quickly corrected by the IERS Earth Orientation Center once notified.

The RS/PC also reached out to the IERS International Terrestrial Reference System (ITRS) Center concerned about an uncharacterized signal in UT1–UTC from the EOP file associated with the ITRF2020 (ITRF2020_EOP-F1.DAT). Figure 3 demonstrates the relationship between the IVS Combination Center UT1–UTC aligned to the ITRF 2020 (IVS20) and the 20C04, ITRF2020, 20JPL-SPACE, and 14Finals. The moving medians show the ITRF2020 and 20JPL-SPACE to be out of alignment with the IVS20, but in very good alignment with 20C04 and 14Finals. The origin of the discrepancy was found in the alignment of the 20JPL-SPACE to ITRF2020 rather than 20C04 to IVS20. While both methods should yield a very similar result, the ITRS identified an error (International Terrestrial Reference Frame 2024) in one of the contributions to the ITRF2020 UT1–UTC EOP file, resulting in the misalignment of 20JPL-SPACE UT1–UTC by nearly $40\mu s$ by

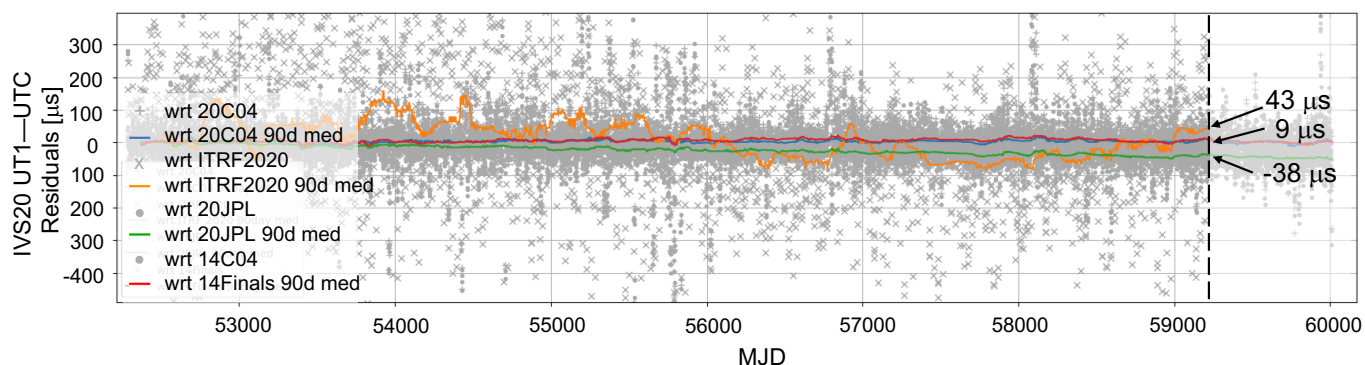


Figure 3: Residuals of the IVS20 UT1–UTC with respect to 20C04, ITRF2020, 20JPL-SPACE, and 14Finals. The solid lines show a moving median with a 90 day window.

the end of the ITRF2020 time-series.

2.3 A modest proposal for future ITRF transitions

Transitioning to a new ITRF within the geodetic community is challenging. The RS/PC goes through a multi-step transition process to maintain consistency between the contributed data sets while each of the contributors first align to the latest ITRF, and then again when the C04 aligns to the ITRF. As each contributing Analysis Center transitions to the latest ITRF (i.e., ITRF2020), the RS/PC must re-calculate systematic corrections for all products used from that Analysis Center, and then re-calculate corrections a second time once the C04 transitions to the new ITRF. Once the RS/PC has aligned to the latest C04 (i.e., 20C04), the combination (Finals) is then considered fully transitioned to the latest ITRF (20Finals).

We propose the following to improve this process for future ITRF transitions: the IERS creates a process that outlines the transition procedure for each of the primary stakeholders (i.e., ITRF, C04, and Finals) under IERS. Within this process a communication procedure is established to identify when the IERS Directing Board, stakeholders, and larger community are notified of transition *progress* or when an *error* has been identified. A standardized evaluation methodology is established to identify any errors in the respective EOP products, and then reviewed based on a predetermined process prior to publication.

3. CONCLUDING REMARKS

The RS/PC continues to innovate our EOP combination software and combination methodology in an effort to improve the accuracy and increase robustness of our low-latency EOP products, thereby better serving the international geodetic community. Any questions regarding our products may be directed toward the RS/PC group email address, eopcp @ us.navy.mil.

4. REFERENCES

- Altamimi, Z. et al. (2023). *ITRF2020 [Data set]*. IERS ITRS Center Hosted by IGN and IPGP. DOI: <https://doi.org/10.18715/IPGP.2023.LDVIOBNL>. URL: https://itrf.ign.fr/ftp/pub/itrf/itrf2020/ITRF2020_EOP-F1.DAT.
- Gibson, J. et al. (June 2023). "Operational KOKEE12M-WETTZ13S VGOS Intensives". In: *26th European VLBI Group for Geodesy Astronomy*. Bad Kötzting. Germany.

A REVISED VALUE OF THE EARTH DYNAMICAL ELLIPTICITY

H_{IAU2006}

A. ESCAPA¹, T. BAENAS², J. M. FERRÁNDIZ³

¹ Universidad de León, Dept. Ingeniería Aeroespacial, León - Spain - alberto.escapa@unileon.es

² Centro Universitario de la Defensa, Dept. Ciencias e Informática, Murcia - Spain

³ Universidad de Alicante, Dept. Matemática Aplicada, Alicante - Spain

ABSTRACT. We recompute the Earth dynamical ellipticity H from the value given in IAU 2006 precession. The methodology consists of obtaining H from the first-order lunisolar precession, once accounted the main higher order precession contributions. By means of a Hamiltonian approach we complete the precession parts due to the second order terms stemming from the Earth's non-rigidity, in the perturbation theory sense, and to the redistribution of mass of tidal origin. Our treatment also allows specifying unambiguously the tidal system in which H is given, recommending its zero-frequency value. This is indispensable for achieving consistency among the different constants used in Astrodynamics, Astronomy, Geodesy, etc., and collected in the numerical standards.

1. INTRODUCTION

The Earth dynamical ellipticity H is defined as

$$H = \frac{2C - (A + B)}{2C}, \quad (1)$$

A , B , and C being the Earth principal moments of inertia. It governs the magnitude of the torque, alternatively the potential energy, exerted by the external bodies (e.g., Kinoshita, 1977). Hence, it plays a key role in the study of the Earth precession and nutation motions. Each precession-nutation theory leads to a different value of H depending on the employed observations and the underlying theoretical constructions, as shown in Table 1. In addition, the dynamical ellipticity is a

H	Uncertainty (ppm)	Source
0.0032737 634	–	Williams (1994)
0.0032737 548	–	Souchay et al. (1999)
0.0032737 674	–	Roosbeek & Dehant(1998)
0.0032737 949	0.4	Mathews et al. (2002) (IAU2000)
0.0032737 804	0.1	Fukushima (2003)
0.0032737 9448	–	Capitaine et al. (2003) (IAU2006)
0.0032737 96	–	Ferrándiz et al. (2004)
0.0032737 95	0.3	IERS Conventions 2010
0.0032738 0001	–	Baenas et al. (2017)

Table 1: Values of the Earth dynamical ellipticity for different precession or nutation models.

central parameter for constructing a fundamental system of geodetic constants. In fact, H is the

only parameter which enables to derive the principal moment of inertia (Burša, 1995). Such role is based on the expression

$$\frac{CH}{Ma_0^2} = J_2, \quad (2)$$

where J_2 is the Earth Stokes parameter, a_0 a length scale parameter, and M the mass of the Earth.

Therefore, H as determined from precession-nutation must adhere to the same conventions used for other geodetic constants, e.g., the same tidal system. In this sense, the parameter values can be (e.g., Groten, 2000; see also Mäkinen, 2021):

- Tide-free: all tidal effects have been removed;
- Zero-frequency: the indirect tidal distortion is included, but not the direct distortion;
- Mean tide: direct and indirect permanent tidal distortions are included.

There is no mention about the tidal system used in IAU2006 and other determinations of H , with very few exceptions like, for example, Williams (1994), Marchenko & Schwintzer (2003), or Escapa et al. (2020).

The XVIII General Assembly (1983) of the International Association of Geodesy (IAG) resolved (Res. 161) that the indirect effect due to the permanent yielding of the Earth be not removed (zero-tide). This question is relevant from a practical point of view, since the difference between the tide-free and zero values of H is about 25 ppm (Escapa et al., 2021).

Within this context, our objective is to provide a revised value of H from H_{IAU2006} based on:

1. Using the procedure by Capitaine et al. (2003), based on Kinoshita & Souchay (1990) —also in Williams (1994)—, but completing it with recent second order terms computations of the precession of the non-rigid Earth (Baenas et al., 2017, 2019);
2. Making explicit in the computations in which tidal system the dynamical ellipticity value is provided.

2. METHOD

The derivation of H_{IAU2006} consists of obtaining H from the first-order lunisolar precession p'_A through (Kinoshita & Souchay, 1990)

$$p'_A = p'_M + p'_S = 2H \left(\frac{m_M}{m_M + m_E} \frac{n_M^2}{\omega_E} M_0 + \frac{m_S}{m_S + m_M + m_E} \frac{n_S^2}{\omega_E} S_0 \right) \cos \epsilon_A = H \alpha_{\text{orb}}. \quad (3)$$

The numerical value of α_{orb} is obtained from orbital ephemeris, whereas that of the first-order lunisolar precession is determined from the observed, or estimated, value of the general precession in longitude p_A with

$$p_A = p'_A + \delta p, \quad (4)$$

where δp are the complementary terms to be added to p'_A .

In particular, we accounted for terms in δp of the second order and arising from the non-rigidity of the Earth, all the remaining parts of δp being basically the same as in Capitaine et al. (2003). The theoretical contributions have been derived in a consistent way using the framework of the Hamiltonian theory of the non-rigid Earth that provides analytical formulae to perform the calculations.

We considered two kind of contributions: second-order effects in the perturbation sense and redistribution mass effects. The lunisolar second order contributions were computed in Baenas et al. (2017), and that is the only theoretical derivation that incorporates the effects of the Earth's non-rigidity on the precession, i.e., they are absent in IAU 2006 precession. The redistribution contributions have been derived with Love number sets from IERS Conventions (2010) and Williams & Boggs' (2016) direct oceanic tides (Baenas et al 2019). The systematic approach to the former terms makes possible to introduce in a clear way the tidal system used for calculating H , i.e., zero-frequency or tide-free.

3. RESULTS

With the proposed method (Escapa et al., 2023), we recomputed the value of H with the observed $p_A = 5028.79619$ as/cy from IAU 2006 and the parts of δp related to geodesic precession, J_2 and planetary tilt, planetary first order, and lunisolar J_4 as given in Capitaine et al. (2003). Such contributions are not affected by the non-rigidity of the Earth within our order of approximation.

Our derived values for the second order terms were $\delta p = -55.29$ mas/cy for the lunisolar second order (Baenas et al., 2017) and $\delta p = -43.95$ mas/cy for the tidal mass redistribution (Baenas et al., 2017). The used tidal system depends on whether p_A has been corrected or not with the contributions due to the permanent tide. If it is not compensated, we have a zero-frequency value; whereas if we consider $p_A - \delta p_{S,pt}$ we get a tide free-value. From our computations we got $\delta p_{S,pt} = 136.60$ mas/cy. That process led to the numerical values displayed in Table 2.

H	Relative change wrt $H_{IAU2006}$ (ppm)	Tidal system
0.0032737 9448 (IAU2006)	0	Not available
0.0032738 1488	+6.23	Zero-frequency
0.0032737 2616	-20.87	Tide-free

Table 2: Revised value of the Earth dynamical ellipticity with the tidal system.

In accordance with Resolution 161 of XVIII IAG GA, we recommend to provide H with the revised value in the zero-frequency convention, as follows

$$H_{\text{revised}}^{\text{zf}} = 0.00327381488. \quad (5)$$

Acknowledgements

This work has been partially supported by the Spanish projects PID2020-119383GB-I00 funded by Ministerio de Ciencia e Innovación (MCIN/AEI/10.13039/501100011033/) and PROMETEO /2021/030 funded by Generalitat Valenciana.

4. REFERENCES

- Baenas, T., Ferrándiz, J.M., Escapa, A., Getino, J., Navarro, J.F., 2017, "Contributions of the Elasticity to the Precession of a Two-Layer Earth Model", AJ 153, 11pp, doi: 10.3847/1538-3881/153/2/79
- Baenas, T., Escapa, A., Ferrándiz, J.M., 2019, "Precession of the non-rigid Earth: Effect of the mass redistribution", A&A 626, A58, doi: 10.1051/0004-6361/201935472

- Burša, M., 1995, "Primary and derived parameters of common relevance of Astronomy, Geodesy, and Geodynamics", *Earth Moon Planets* 69, pp. 51–63, doi: 10.1007/BF00627769
- Capitaine, N., Wallace, P.T., Chapront, J., 2003, "Expressions for IAU 2000 precession quantities", *A&A* 412, pp. 567–586, doi: 10.1051/0004-6361:20031539
- Escapa, A., Baenas, T., Ferrándiz, J.M., 2020, "On the permanent tide and the Earth dynamical ellipticity", 22nd EGU General Assembly, doi: 10.5194/egusphere-egu2020-21410
- Escapa, A., Baenas, T., Ferrándiz, J.M., 2021, "On the Earth dynamical ellipticity", Scientific Assembly of the International Association of Geodesy (IAG) (Beijing 2021)
- Escapa, A., Baenas, T., Ferrándiz, J.M., 2023, "A revised value of the Earth's dynamical ellipticity", XXVIII General Assembly of the International Union of Geodesy and Geophysics (IUGG) (Berlin 2023), doi: 10.57757/IUGG23-2626
- Ferrándiz, J.M., Navarro, J.F., Escapa, A., Getino, J., 2004, "Precession of the Nonrigid Earth: Effect of the Fluid Outer Core", *AJ* 128, pp. 1407–1411, doi: 10.1086/422738
- Fukushima, T., 2003, "A New Precession Formula", *AJ* 126, pp. 494–534, doi: 10.1086/375641
- Groten, E., 2000, "Parameters of Common Relevance of Astronomy, Geodesy, and Geodynamics", *J. Geod.* 74, pp. 134–140, doi: 10.1007/s00190-000-0134-0
- IERS Conventions (2010), 2010, Gerard Petit and Brian Luzum (eds.), IERS Technical Note; No. 36
- Kinoshita, H., 1977, "Theory of the Rotation of the Rigid Earth", *Celest. Mech.* 15, pp. 277–326 doi: 10.1007/BF01228425
- Kinoshita, H., Souchay, J., 1990, "The Theory of the Nutation for the Rigid Earth Model at the Second Order", *Celest. Mech. Dyn. Astr.* 48, pp. 187–265, doi: 10.1007/BF02524332
- Mäkinen, J., 2021, "The permanent tide and the International Height Reference Frame IHRF", *J. Geod.* 95, 19pp, doi: 10.1007/s00190-021-01541-5
- Marchenko, A., Schwintzer, P., 2003, "Estimation of the Earth's tensor of inertia from recent global gravity field solutions", *J. Geod.* 76, pp. 495–509, doi: 10.1007/s00190-002-0280-7
- Mathews, P.M., Herring, T.A., Buffet, B.A., 2002, "Modeling of nutation and precession: New nutation series for nonrigid Earth and insights into the Earth's interior", *J. Geophys. Res. (Solid Earth)* 107(B4), 26pp, doi: 10.1029/2001JB000390
- Roosbeek, F., Dehant, V., 1998, "RDAN97: An analytical development of rigid Earth nutation series using the torque approach", *Celest. Mech. Dyn. Astr.* 70, pp. 215–253, doi: 10.1023/A:1008350710849
- Souchay, J., Loysel, B., Kinoshita, H., Folgueira, M., 1999, "Corrections and new developments in rigid earth nutation theory. III. Final tables "REN-2000" including crossed-nutation and spin-orbit coupling effects", *A&A* 135, pp. 111–131, doi: 10.1051/aas:1999446
- Williams, J., 1994, "Contribution to the Earth's Obliquity Rate, Precession, and Nutation", *AJ* 108, pp. 711–724, doi: 10.1086/117108
- Williams, J.G., Boggs, D.H., 2016, "Secular tidal changes in lunar orbit and Earth rotation", *Celest. Mech. Dyn. Astr.* 126, pp. 89–129, doi: 10.1007/s10569-016-9702-3

Session I

REFERENCE SYSTEMS : SPACE AND TIME

HOW TO ESTABLISH A GEODESY AND TIME REFERENCE IN SPACE?

A. SCHLICHT¹, S. MARZ², P. VOLLMAIR³

¹ FESG, Technical University of Munich - Germany - anja.schlicht@tum.de

² IAPG, Technical University of Munich - Germany - s.marz@tum.de

² IAPG, Technical University of Munich - Germany - peter.vollmair@tum.de

ABSTRACT. The Terrestrial Reference Frame is based on measurements of different space geodetic techniques, such as Satellite Laser Ranging (SLR), Very Long Baseline Interferometry (VLBI), Doppler Orbitography and Radiopositioning Integrated by Satellite (DORIS) and Global Navigation Satellite Systems (GNSS). A combination of these techniques at observation level with estimating as many common parameters as possible, would be the ultimate goal. The biggest problem is to control many different systematic errors in each measurement type. While the planned ESA mission GENESIS will allow the study of these systematic errors, a concept has to be developed which uses the synergy between different ranging techniques in an optimal way. We present our first simulation studies about how a Geodesy and Time Reference In Space (GETRIS) should look like, how we optimally combine the different techniques, and how the ranging geometry may be expanded. We explain why it is important to use GNSS as a backbone for such a task. Our analysis is based on a study of the synergy of ranging techniques and an optimization of the three pillars of orbit determination: instrumentation, geometry, and modelling.

1. INTRODUCTION

DORIS, GNSS, SLR and VLBI are the currently used geodetic space techniques which contribute to the International Terrestrial Reference Frame (ITRF). The combination of these techniques is not yet done at observation level, but predominantly analyzed individually and further combined at a much higher processing state. On the one side, each technique has its own main focus where it contributes most to the definition of the ITRF. On the other side, each technique has its weak points, as different estimation parameters absorb different systematic effects of the measurements. The Global Geodetic Observing System (GGOS) has set the goal to define a highly accurate, long-term stable and reproducible reference frame for monitoring of the global change. Therefore, the integration and consistent combination of the space geodetic techniques is indispensable, as well as the full characterization of systematic effects influencing the individual measurement technique.

Analyzing the four space geodetic techniques in more detail, it stands out that most of them do one-way ranging with microwave (MW) frequencies. Only SLR is a two-way technique working in the optical frequency domain. With an optimal case for the combination of the techniques in mind, we first have to analyse the pros and cons of each ranging method. Based on that, we can develop a strategy where the biggest synergy out of their combination can be achieved. Comparing optical and microwave signals propagating through the atmosphere, the advantage of using optical frequencies is the accuracy in modelling the troposphere, as only the slow varying hydrostatic part causes delays. The microwave frequencies are influenced by the wet part, too, which shows much more variability on short time scales and its handling in troposphere models is therefore more demanding. Another part of the atmosphere is influencing the microwave signals, namely the ionosphere, but its footprints can be minimized by using two frequencies. The biggest

advantage of using MW signals is their non-dependency on the weather, while clouds make ranging in the optical impossible. The biggest advantage of optical ranging is the capability of doing regular calibrations on short distances, at least on ground. This has the consequence that biases can be kept small and their long-term variations can be eliminated from the data sets.

In principle one can perform ranging in one-way, two-way or dual one-way mode. While one-way techniques have the advantage of connecting multiple observers and transmitters at the same epoch, the connectivity per epoch in two-way measurements is limited. This benefit is connected with a decrease in precision as for example a 360° receiver is disturbed by other sources, like multipath or phase center variations. In geodesy all one-way techniques measure ranges or are interferometric methods, so two entities are involved and their clocks have to be synchronized. For two-way measurements only one clock is involved and with a dual one-way measurement clock synchronization is inherently given.

In summary, we can characterize optical two-way techniques as sporadic but highly accurate in modelling and instrumentation, and one-way MW techniques as very precise, allowing favourable geometries (if not interferometric) at any time. How should a system look like which makes the best out of the available techniques? Clearly, the backbone of such a constellation should allow for building-up a nearly perfect observation geometry, which is not limited by weather conditions. This argument makes GNSS the basis for such a system and the other techniques the supporting technologies. The geometry of GNSS can be further enhanced by connecting the GNSS satellites with each other by inter-satellite links (ISL). As all techniques should share as many common parameters as possible, we aim at a collocation of all techniques on ground and in space. SLR brings in the advantages of the optical measurement, the calibration capability and the high accuracy in troposphere modelling. As all SLR stations have GNSS receivers, the collocation comes without additional costs. We combine a one-way and a two-way technique which makes it necessary to calibrate a pseudorange/phase measurement where time transfer is equally mandatory. Then range, time and troposphere delays decorrelate totally. SLR can take that part, too. T2L2 on Jason 2 has already shown the capability to synchronize clocks better than the stability of the on-board DORIS oscillator what CLT on Tiangong (Geng et al., 2024) is already performing and ELT on ACES (Cacciapuotti et al., 2020) will demonstrate. To exploit the collocation on this topic, costs are incurred as a common clock is needed for SLR and the GNSS receiver. This feature is rare at SLR stations. Leute et al. (2018) have shown that in the case of a common clock the GNSS receivers of two stations can be calibrated via the Jason2 satellite by the optical links.

The support from VLBI as an interferometric technique has the advantage of measuring differences in an extraordinary precision and further relating the satellite orbits to the International Celestial Reference Frame (ICRF). Especially deficiencies in precise orbit determination (POD) will show-up in this case. DORIS is a MW tracking technique, which is limited to low Earth orbiters and therefore cannot be collocated in space on GNSS satellites even though the number of collocated sites with other techniques on ground grows. A combination with SLR can be achieved directly. With the LEO satellite carrying a GNSS receiver an indirect way of contributing can be realized.

Comparing our discussion so far with the planned ESA mission GENESIS (Delva et al., 2023) some limitations of this mission can be recognized for fulfilling the task of tightening space geodetic techniques together and determining systematic errors in each technique. GENESIS will bring a LEO satellite in orbit which carries a GNSS receiver, a DORIS receiver with an ultra stable oscillator, a VLBI beacon and will have retroreflectors on board. In this mission DORIS takes the part of the backbone with indirect support of GNSS, with its precise clocks. As DORIS does not deliver range, but Doppler measurements, the collocation with SLR on ground will not be so effective and not many stations have this ability. GENESIS will be the first mission having a VLBI beacon on-board together with the other ranging techniques and that will bring the whole support discussed with that technique. GENESIS will also be a technological demonstrator mission for the collocation of space geodetic techniques.

On the ground station side, a big step still needs to be taken towards the GETRIS concept, as at least some stations distributed around the world require collocation of instruments for each technique together with usage of a common clock. Simulations are necessary to illustrate the potential of the concept, but we are by far not able to show all the features. As an initial analysis, we started with the demonstration of how GNSS satellites should be connected by inter-satellite links and how optical links support the tightening to Earth. In the next sections we will introduce these studies and summarize their outcome.

2. SIMULATION STUDIES

In principle two different kind of simulation studies are necessary to demonstrate how we can exploit such a constellation and where we should start to develop new strategies in the combination. The first are global simulations which show an overall performance of individual stages of expansion. Here the focus is on orbit and clock modelling and in total the product of the ITRF. The second kind are local studies, where the focus is on atmosphere modelling and errors in connecting the instruments on ground stations to a common clock. For the second kind of study we have started with a different combination of techniques. Such a discussion is better to be held on a combination of optical and MW techniques, where both are very accurate.

For this we choose Atomic Clock Ensemble in Space (ACES) mission with collocated dual one-way MW ranging and two-way and one-way optical ranging. This ESA mission has the main focus on fundamental physics and time synchronization with collocated high-precise space geodetic observation techniques in space and on ground. Since ACES will not start until 2025, we have simulated this observation geometry in Vollmair et al. (2023) and evaluated different scenarios. One of the challenges of this work was to adequately separate the so-called Bermuda Triangle of space geodesy (Figure 1). This term refers to the strong correlation between range, troposphere and time. Inaccurate modelling of just one of these parameters will lead to inaccurate determination of the others, even if the other parameters are well modelled. It can be shown that the spatial collocation of microwave-based and optical observation techniques significantly reduces the correlation of the three main parameters and thus significantly increases their determinability. The ground calibration and the almost non-existent influence of the wet part of the troposphere on the optical observations make this observation technique an advantageous complement to the microwave system. In addition to spatial collocation, collocation also takes place in parameter space in the sense of a common satellite orbit. This allows the clock parameters to be separated from the other parameters.

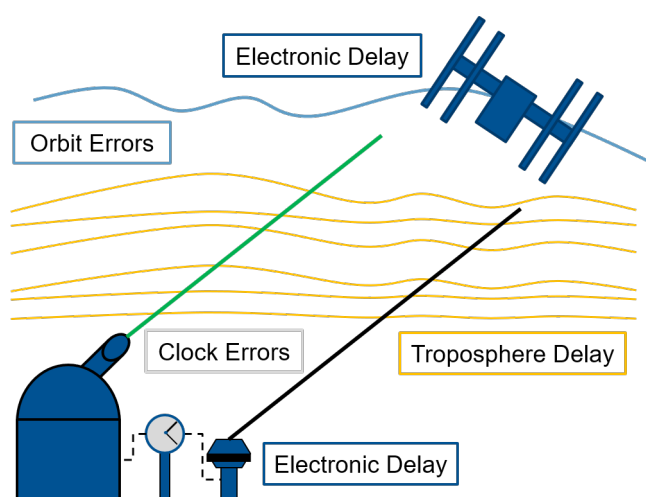


Figure 1: Bermuda triangle of space geodesy.

If this approach is followed consistently, the next step will be to extend the collocation in parameter space. Even though the microwave and optical observations have different atmospheric delays, both signals pass through the same tropospheric region at almost the same time. This can theoretically be used to define a common troposphere for these two observation techniques. This extends the collocation of the parameter space and further reduces the correlation of the different parameters. In the presentation "Collocation of high-precision geodetic observation methods for time synchronisation in context of the ACES-Mission: a simulation study" by Vollmair et al. (2023) it was shown that the time parameters can be significantly better decorrelated and thus determined by collocation of the troposphere. An increase in the number of observation techniques was also investigated in this presentation. Recent developments in the electronic components of SLR systems also allow an extension of the observation techniques. In addition to the conventional optical detectors at 532 nm, high-precision detectors with a sensitivity of 1064 nm can now be used. This almost doubles the number of available optical observations and contributes significantly to the stabilisation of the entire observation system. The extended collocation in parameter space through a common troposphere, as well as the additional optical measurements, ensure a significant increase in the accuracy of the determination of the time parameters.

The studies, which belong to the first category, focus only on orbit determination and clock synchronization with a small network of ground stations. As we already mentioned, GNSS is the best backbone for a GETRIS concept, as at each measurement epoch multiple links between satellites and ground stations can be established. The geometrical configuration can be enhanced by inter-satellite links (ISL). In Schlicht et al. (2020) we analysed different connecting schemes for inter-satellite ranging between Galileo satellites. The simulation strategy was to simulate errors and noise in GNSS as good as possible. Starting with simulation studies it is not possible to totally rebuild reality as most systematic and modelling errors are not known today, but you have to focus on the main contributors of systematic effects. In GNSS we took the multipath effects observed in a receiver as the main source of systematic errors. In fact we used known patterns of phase center variations and got the orbit accuracy in the expected range. In the local studies we recognized that an error in this size is coming from the fluctuations in the troposphere, so in further studies we should use such an error source. In global simulation studies we introduce an atmosphere modelling error for MW frequencies by simulating with the Vienna Mapping Function and using the Global Mapping Function in the estimation. We worked with the Galileo satellite constellation and we consequently took the Galileo ground segment of 16 stations as a base. As we wanted to analyse if the ISLs allow for better orbit modelling, we introduced a modelling error by using a box-wing model for the satellites with 10% error in the optical parameters. The orbit modelling capability is tested by analyzing how many empirical parameters of ECOM type can be estimated in the process of POD. ISL was simulated with accuracy and precision of some millimeters at 60s integration time with a range and orbit dependent contribution and additional coloured noise. This corresponds to a moderate optical link achievable with reasonable effort. In this first study the main focus was on the differences in link scenarios. We compared the so called "any-to-any" ranging with different possibilities of forming ring scenarios which only break at some point in time. The benefit of ranging between any two satellites in view is so much more attractive, that we further kept this scenario.

In Marz et al. (2021) we implemented an optical ground-space link, which we called "optical two-way link" (OTWL). While the accuracy we took for these measurements is comparable to SLR, it made simulations much easier as the same link type as for ISL can be used. In this study we also analyzed in more detail which solar radiation pressure parameters can be estimated and which impact this has on the orbit modelling. In this paper we also showed how simulation results should be interpreted as the benefit of a simulation study is exactly the total control of all parameters on orbit determination. The best possible orbit, a fit of exact positions of the satellite with the orbit model, demonstrates the modelling error influencing the POD. A discussion of the formal errors relates the different scenarios simulated to each other in respect to geometry and white

noise contribution. The final adjusted orbit has an error related to all the contributions mentioned before and the systematic errors and coloured noise in the measurement. This full control allows a discussion of why which error contribution of a measurement system can be balanced by another technique.

An indication for the internal consistency of our simulations is the result, that for GNSS without ISL the estimation of more parameters than the usual ECOM2 model does not bring any benefit (Figure2). This is also what is observed in real data and shows that the main error contributions may be captured. The orbit accuracy with ISL improved by a similar amount as supporting GNSS by OTWL, which is interesting as we included a delay modelling error of half the difference between two models. Even the combination of all three techniques improves the orbit even further, as ISL fixes the relative orbits of the satellite to each other but not to ground. Here optical ground links can show their capability (Figure 2).

Two further studies analyse the integration of geosynchronous (GSO) satellites into the constellation (Marz et al., 2023a) and analyse the clocks in all the simulated scenarios (Marz et al., 2023b). The first paper illustrates, that the high performance in orbit determination can be achieved also for GSO satellites if they are integrated into the ISL system. In the latter paper we showed that OTWL has a high performance in synchronizing space and ground clocks while it is the task of ISL to do the same between satellite clocks. With such a constellation we would be prepared to distribute highly stable clock signals around the world and into space. Making it usable at every ground station, up to the GSO orbit and to the moon.

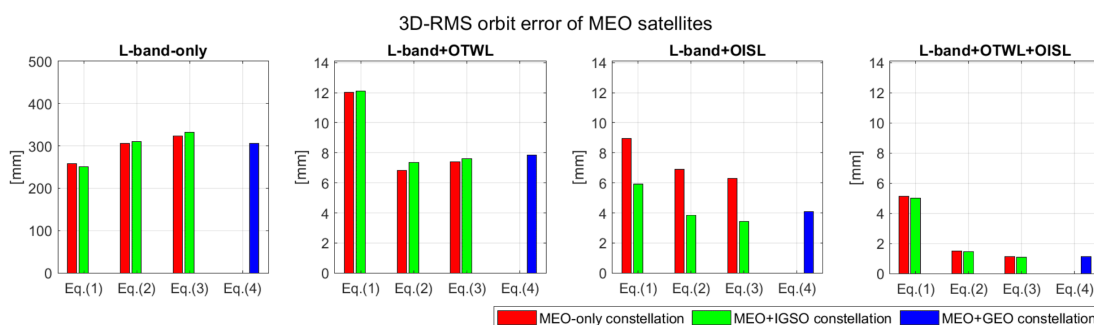


Figure 2: The figure shows the rms of orbit errors of Galileo satellites (MEO) in different constellations. The red bars represent results within a normal Galileo constellation, the green bars represent results where additional inclined geosynchronous satellites expand the constellation, and blue bars show the orbit errors of MEOs in a constellation with geostationary satellites. Each graph represents a different combination of measurement techniques. Only L-band measurements on the left to the combination of L-band, OTWL and ISL on the right. Within the figures different empirical models were used in POD. Eq1 represents the normal ECOM2 model. In Eq2 the parameters for an error once per revolution in B was exchanged by terms three-times per revolution. While in Eq3 the full spectrum of analysed frequency for the MEO orbit was estimated: once, three-times and five-times per revolution in B direction. While all MEO and IGSO satellites we simulated, were in yaw-steering mode, this is not true for GEO satellites which are in orbit normal mode. For these satellites the coordinate system and the estimated parameters have to be changed. The case study according to Eq4 takes Eq3 for the MEOs but a different one for the GEO satellites. In yaw-steering mode sine and cosine parameters were estimated while we analysed that it is the best to estimate once per revolution sine, twice per revolution cosine, three-times sine and four-times sine parameters in D direction, once per revolution sine and twice cosine in Y direction and once cosine, twice sine, three-times cosine, and four-times sine in B.

3. CONCLUSION

Even though we will have to go a long way to get to an understanding of how geodesy should handle the combination of all space geodetic techniques to use the synergy hidden in these diverse measurement techniques, we at least started with the most comparable observation techniques: GNSS and an optical link to ground with the capability to do ranging and time transfer. We want to explicitly mention it here, as it has not been studied directly. The benefit of the optical ranging is only exploited if the optical method supports the one-way technique in ranging and time transfer. Only then we are able to separate range, clock and troposphere delays as analysed in the local simulations.

For the global simulations we wanted to start with the best possible observation geometry: we analysed inter-satellite links first and came to the conclusion, that for geodesy that link scheduling is most efficient, which allows an estimation of the bias parameters through the "any-to-any" scenario. For the inter-satellite links and for the ground links we took a ranging accuracy and precision (despite troposphere modelling) of some millimeters and achieved an orbit accuracy of some millimeters. One may think that this is logical and it does not need simulations for that. But we exactly showed, that this is absolutely not true. We can achieve the ultimate performance only if we also enhance our modelling capacity. In our case, estimating more and the right solar radiation parameters and combining the two supporting techniques with GNSS (Figure 2). GNSS is still necessary, as it is the backbone that can connect many entities at the same epoch by distributing the high accuracy of the optical links within the system.

Future work towards further steps will be to also exploit the synergies with the other listed techniques that ultimately will bring us to a Geodesy and Time Reference in space, the GETRIS concept.

4. REFERENCES

- Cacciapuoti, L., Armano, M., Much, R., Sy, O., Helm, A., Hess, M.P., Kehrer, J., SKoller, S., Niedermaier, T., Esnault, F.X., Massonnet, D., Goujon, D., Pittet, J., Rochat, P., Liu, S., Schaefer, W., Schwall, T., Prochazka, I., Schlicht, A., Schreiber, U., Delva, P., Guerlin, C., Laurent, P., le Poncin-Lafitte, C., Lilley, M., Savalle, E., Wolf, P., Meynadier, F., Salomon, C., 2020, "Testing gravity with cold-atom clocks in space: The ACES mission", *The European Physical Journal D*, 74 (8), DOI: 10.1140/epjd/e2020-10167-7.
- Delva, P., Altamimi, Z., Blazquez, A., Blossfeld, M., Böhm, J., Bonnefond, P., Boy, J.P., Bruinsma, S., Bury, G., Chatzinikos, M., Couhert, A., Courde, C., Dach, R., Dehant, V., Dell'Agnello, S., Elgered, G., Enderle, W., Exertier, P., Glaser, S., Haas, R., Huang, W., Hugentobler, U., Jäggi, A., Karatekin, O., Lemoine, F.G., Le Poncin-Lafitte, C., Lunz, S., Männel, B., Mercier, F., Métivier, L., Meyssignac, B., Müller, J., Nothnagel, A., Perosanz, F., Rietbroek, R., Rothacher, M., Schuh, H., Sert, H., Sosnica, K., Testani, P., Ventura-Traveset, J., Wautelet, G., Zajdel, R., 2023, "GENESIS: co-location of geodetic techniques in space", *Earth, Planets and Space*, 75(1), <https://doi.org/10.1186/s40623-022-01752-w>.
- Exertier, P., Samain, E., Martin, N., Courde, C., Laas-Bourez, M., Foussard, C., Guillemot, P., 2014, "Time Transfer by Laser Link: Data analysis and validation to the ps level", *Advances in Space Research*, 54(11), pp. 2371-2385, <https://doi.org/10.1016/j.asr.2014.08.015>.
- Geng, R., Wu, Z., Huang, Y., Cheng, Z., Yu, R., Tang, K., Zhang, H., Meng, W., Deng, H., Long, M., Qin, S. Zhang, Z., 2024, "A complete analysis of the link uncertainty budget for pulsed laser time transfer on China space station", *Advances in Space Research*, 73(5), 2548-2566, <https://doi.org/10.1016/j.asr.2023.12.022>.

- Leute, J., Petit, G., Exertier, P., Samain, E., Rovera, D. Urich, P., 2018 "High accuracy continuous time transfer with GPS IPPP and T2L2" 2018 European Frequency and Time Forum (EFTF), Turin, Italy, 2018, pp. 249-252, doi: 10.1109/EFTF.2018.8409043.
- Marz,S., Schlicht, A., Hugentobler, U., 2023a, "Geosynchronous satellites expanding a future GNSS satellite constellation: A precise orbit determination study", *Advances in Space Research*, 71: 624.
<https://doi.org/10.1016/j.asr.2022.11.009>.
- Marz,S., Schlicht, A., Hugentobler, U., 2023b, "Toward a Geodesy and Time Reference in Space (GETRIS): A Study of Apparent Satellite Clocks of a Future GNSS Satellite Constellation", *Geosciences*, 13, 173. <https://doi.org/10.3390/geosciences13060173>.
- Marz, S., Schlicht, A., Hugentobler, U., 2021, "Galileo precise orbit determination with optical two-way links (OTWL): a continuous wave laser ranging and time transfer concept", *Journal of Geodesy*, 95, 85, <https://doi.org/10.1007/s00190-021-01534-4>.
- Schlicht, A., Marz, S., Stetter, M., Hugentobler, U., Schäfer, W.,2020, "Galileo POD using optical inter-satellite links: A simulation study", *Advances in Space Research*, 60, 1558-1570.
- Vollmair, P., Schlicht, A., Hugentobler, U., 2023, "Colocation in Time and Space of High-Precision Two-Way Optical and Microwave Observations for Calibration of a Microwave Ranging Link—The ACES Mission Case". *Remote Sens.* 15, 4897. <https://doi.org/10.3390/rs1520489>

INTRODUCTION OF FREQUENCY-DEPENDENT TIDAL MODELS IN LUNAR EHPIMERIDES

D. BAGUET¹, N. RAMBAUX¹, A. FIENGA², A. BRIAUD², H. HUSSMANN³, M. GASTINEAU¹, X. HU⁴, J. LASKAR¹, A. MÉMIN², A. STARK³

¹ IMCCE, Observatoire de Paris, PSL, Sorbonne Université, France - daniel.baguet@obspm.fr

² Université Côte d'Azur, Observatoire de la Côte d'Azur, CNRS, IRD, Géoazur, France

³ Institute of Planetary Research, German Aerospace Center (DLR), Germany

⁴ Institute of Geodesy and Geoinformation Science, Technical University of Berlin, Germany

ABSTRACT. The tidal deformation of the Moon affects its orbit and rotation through the modification of the gravitational potential and the dissipation due to viscosity. In current ephemeris, the lunar tidal deformation for degree-2 harmonics is described with a tidal Love number independent of the frequency of the tidal forcing and with a unique time delay characterizing the lag of the tidal bulge due to the viscosity. However, the tidal Love number depends on the forcing frequency and the unique time delay model is correctly describing the dissipation only for the monthly terms. Therefore, we introduce in INPOP the tidal distortion coefficients as Fourier series. This allows to take into account the frequency dependency. We compare the time delay and the series formulations by looking at the impact on the lunar orbit and rotation. We show that the series need to have about five hundred terms in order to reduce the effect due to the serie truncation.

1. INTRODUCTION

Since the start of the Artemis program, interest in lunar studies has been renewed. In particular, the probing of the inner structure of the Moon is a challenging research field and can help us to understand how it formed. The Moon is affected by tides, mainly exerted by the Earth and the Sun, that deform its shape and create a bulge. Studies of lunar tides are crucial to reveal its inner structure. Indeed, the amplitude and orientation of the tidal deformation strongly depends on the density and the rheology inside the Moon (e.g. Williams & Boggs, 2015; Briaud et al., 2023a). Recent results based on thermodynamical and tidal constraints highlight that the core may be composed of a solid inner part with a radius of 258 ± 40 km and a fluid outer part with a radius of 365 ± 15 km (Briaud et al., 2023b).

The Lunar Laser Ranging (LLR) experiment measures the Earth-Moon distance with an accuracy of around two centimeters and the Moon's librations at a one milliarcsecond accuracy (Viswanathan et al., 2018). The ephemeris INPOP of the Paris Observatory is a solution of a joint numerical integration of the planetary orbits and of the lunar orbit and rotation, which is fitted, among others, to the LLR data. The tidal Love number k_2 quantifies the amplitude of the response of the gravitational potential for degree-2 harmonics due to the tidal deformation. The tidal dissipation due to the viscosity inside the Moon can be quantified by a time delay parameter. This time delay represents the shift of the tidal bulge with respect to the Earth-Moon direction due to the dissipation. The tidal Love number, as well as the dissipation inside the Moon depend on the period of the tidal forcing. The value of k_2 of the Moon for the dominant monthly term has been determined by the GRAIL mission and is $k_2 = 0.02405 \pm 0.00018$ (Konopliv et al., 2013). In INPOP, the tidal deformation accounts for a Love number independent of the forcing frequency and a unique time delay (Viswanathan et al., 2018). However, such a formulation is adequate to characterize only the contribution of the main tidal forcing at one month. The formulation in

Fourier series of the distortion coefficients of the degree-2 harmonics of the gravitational potential by Williams & Boggs (2015) allows to describe the tidal deformation by taking into account the frequency dependency of the tidal forcing. Therefore, we introduce in INPOP the formulation of the distortion coefficients as Fourier series in order to test the impact of the variation of the Love number and of the dissipation on libration measurements.

2. METHOD

In the case of elastic lunar tides, the deformation of the Moon is instantaneous and the tidal bulge is oriented in the Earth-Moon direction. However, in the case of visco-elastic deformation, the tidal bulge is shifted with respect to the Earth-Moon direction. In order to take into account this shift, in current ephemerides, the distortion coefficients of the degree-two harmonics of the gravitational potential are computed with the time delay model. In the visco-elastic case, the tidal Love number is complex and noted k_2^* . Its real and imaginary parts can be written as:

$$\text{Re}(k_2^*) = |k_2^*| \sqrt{1 - 1/Q^2}, \quad (1)$$

$$\text{Im}(k_2^*) = -\frac{|k_2^*|}{Q}, \quad (2)$$

where Q is a dissipation factor. In the time-delay model, the dissipation factor is linked to the time delay parameter τ through the relation

$$Q = \frac{1}{\sin(f\tau)}, \quad (3)$$

where f is the frequency of the tidal forcing.

Figure 1 shows the variation of the Love number with respect to the period of the tidal forcing. The left and right diagrams are showing respectively the variation of the real and imaginary part respectively. The blue curves show the variation for the time delay model, using the values of the unique Love number and time-delay parameter of INPOP19a which are $|k_2^*| = 0.023559$ and $\tau = 0.094$ days (Fienga et al., 2019). The red curves show the variation from a solution computed from a lunar interior model (Briaud et al., 2023a)* consistent with currently available observational constraints. The solution has been computed with the version ALMA3 of the ALMA code (Spada & Boschi, 2006; Melini et al. 2022) In this model, the inner structure of the Moon is composed of five layers, and has been chosen so that its values for the real and imaginary parts of the Love number for the dominant period at around 27.212 days do not deviate more than 1% of the values of the time delay model computed with the parameters of INPOP19a. The time delay model provides a good description of the deformation and dissipation for the dominant terms of the tidal forcing with a monthly period but does not allow to reproduce a variation of the complex Love number with respect to the period of the forcing that is similar as in the solutions computed from lunar interior models.

The tidal contribution in the moment of inertial I_{tides} is related to the gravitational potential through the relation:

$$I_{tides} = MR^2 \begin{pmatrix} \frac{1}{3}\Delta C_{20} - 2\Delta C_{22} & -2\Delta S_{22} & -\Delta C_{21} \\ -2\Delta S_{22} & \frac{1}{3}\Delta C_{20} + 2\Delta C_{22} & -\Delta S_{21} \\ -\Delta C_{21} & -\Delta S_{21} & -\frac{2}{3}\Delta C_{20} \end{pmatrix} \quad (4)$$

where ΔC_{2m} and ΔS_{2m} (with $m = 0, 1$ or 2), are the distortion coefficients of the gravitational potential for degree-two harmonics, M is the mass of the Moon and R its radius. Williams & Boggs

*Data available on request.

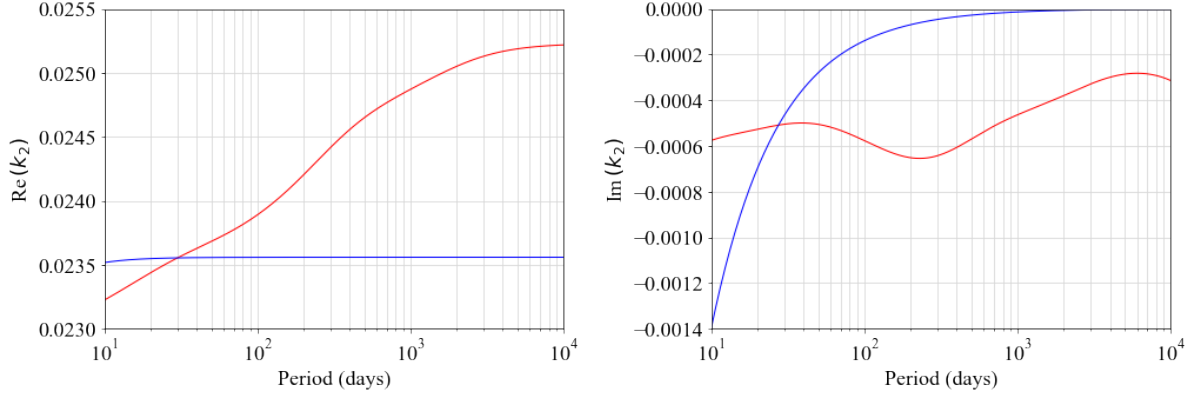


Figure 1: **Left:** Variation of the real part of the tidal Love number with respect to the period of the tidal forcing. **Right:** Variation of the imaginary part of the tidal Love number with respect to the period of the tidal forcing. The blue curve is for the solution of the time delay model and the red curve is for a solution computed from a lunar interior model.

(2015) provided a Fourier series formulation of the distortion coefficients:

$$\Delta C_{2m}(t) = \sum_q C_{2mq} \left(\operatorname{Re}\{k_2^*(P_q)\} \cos \zeta_q(t) - \operatorname{Im}\{k_2^*(P_q)\} \sin \zeta_q(t) \right), \quad (5)$$

$$\Delta S_{2m}(t) = \sum_q S_{2mq} \left(\operatorname{Re}\{k_2^*(P_q)\} \cos \zeta_q(t) - \operatorname{Im}\{k_2^*(P_q)\} \sin \zeta_q(t) \right), \quad (6)$$

where C_{2mq} and S_{2mq} are amplitudes, P_q is the period of the forcing term and $\zeta_q(t)$ is an argument evolving accordingly to the period P_q . The distortion coefficient $\Delta S_{20}(t)$ is always equal to zero. The advantage of such a formulation is that it allows to separate the different periods of the tidal forcing and to associate for each term its corresponding Love number. We include in INPOP the computation of the distortion coefficients with the formulation in Fourier series, as an alternative to the computation with the time delay model.

3. RESULTS

Firstly, we compare the solution of INPOP19a (Fienga et al., 2019) with our solution obtained with the Fourier series formulation of the distortion coefficients of equations (5) and (6). To do so, we compute the real and imaginary parts of the tidal Love number with the equations (1-3). The equation (3) allows to obtain a solution of k_2^* which corresponds to the solution of the time delay model. We used the same value of the time delay than in INPOP19a, which is $\tau = 0.094$ days. Figure 2 shows the residual for the distance to the retroreflector Apollo 11 (A11) between the solution of INPOP19a and the solution of the version of INPOP with the distortion coefficients computed in Fourier series. The Fourier series contain the terms presented in Williams & Boggs (2015). The amplitude of the residual reach two meters, which is well above the observational accuracy of two centimeters provided by the LLR data.

The terms of the series computed by Williams & Boggs (2015) are based on the ephemerides DE of JPL. We computed the terms of the series based on the solution of INPOP19a. In order to do so, we used the Paris Lunar Ephemeris (ELP) which is a semi-analytical representation of the lunar orbit. The last version of ELP is called ELP/MPP02 and has been fitted to DE405 (Chapront & Francou, 2003). We fit the secular parameters of the Moon of ELP to the solution of INPOP19a. Figure 3 shows the residual of the longitude of the Moon in spherical coordinates

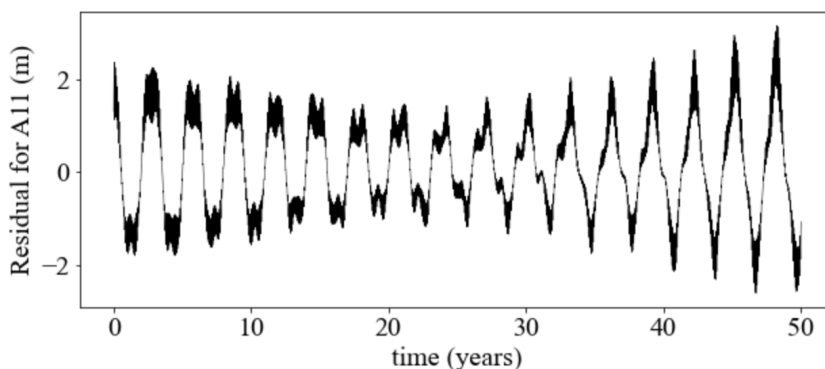


Figure 2: Residual of the distance to the retroreflector A11 with respect to the solution of INPOP19a, in the case where the Fourier series contain the terms of Williams & Boggs (2015).

between the solution of INPOP19a and the solution of ELP. The slope of the residual for the case of ELP fitted to DE405 is eliminated thanks to the fit of the secular parameters. However, the difference induced on the distance to the retroreflector by this latter solution with respect to the solution with the series of Williams & Boggs (2015) is only at the submillimeter level.

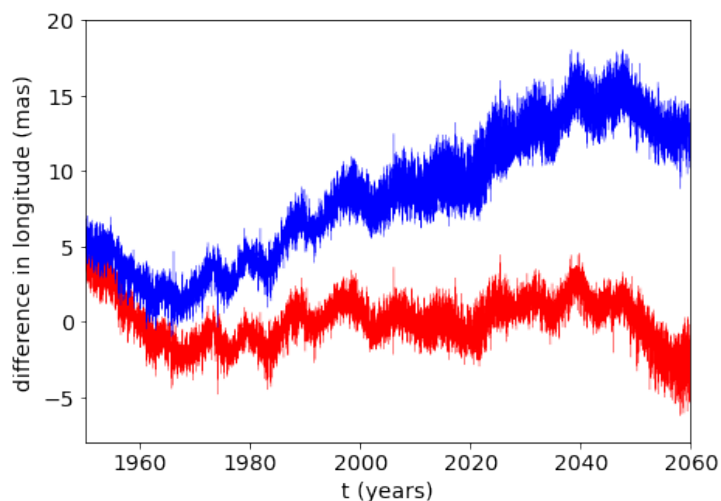


Figure 3: Residual of the longitude of the Moon in spherical coordinates with respect to the solution of INPOP19a. The blue and red curves are for the cases with the secular parameters fitted respectively to DE405 and INPOP19a.

The amplitude of the residual in Figure 2 is mainly due to the truncation of the series. Figure 4 shows the residual for different cases with different number of terms in the series. We need to include around five hundred terms in the Fourier series of each distortion coefficient in order to have a residual on the distance to the retroreflectors that is at the level of the accuracy of the Lunar Laser ranging data.

Now that we have reduced the residual due to the truncation of the series, we introduce, in the Fourier series of the distortion coefficients, the solution of the Love number represented with the red curves of Figure 1 computed from a lunar interior model. Then, we compute a new solution of the orbit and rotation of the Moon that we compare to the solution of INPOP19a. The residual of this comparison for the proper rotation of the Moon is represented in Figure 5. It shows that the effect on the proper rotation of the Moon introduced by the variation of the Love number according to a solution from a lunar interior model is much more important than the effect of the

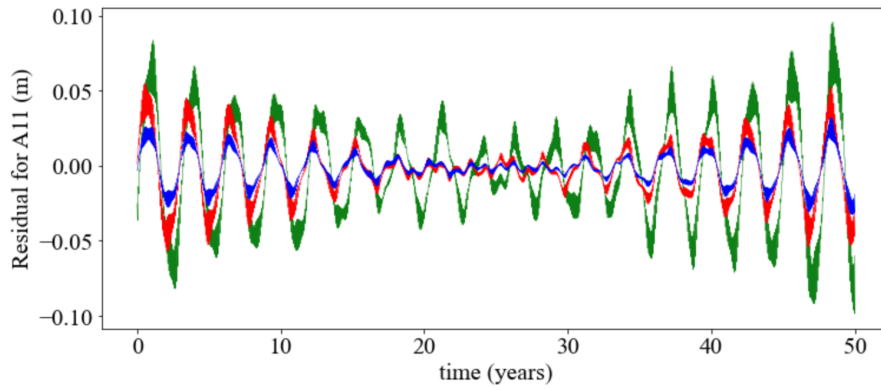


Figure 4: Residual of the distance to the retroreflector A11 with respect to the solution of INPOP19a. The green, red and blue curves are respectively for the cases with one hundred terms, two hundred terms and five hundred terms.

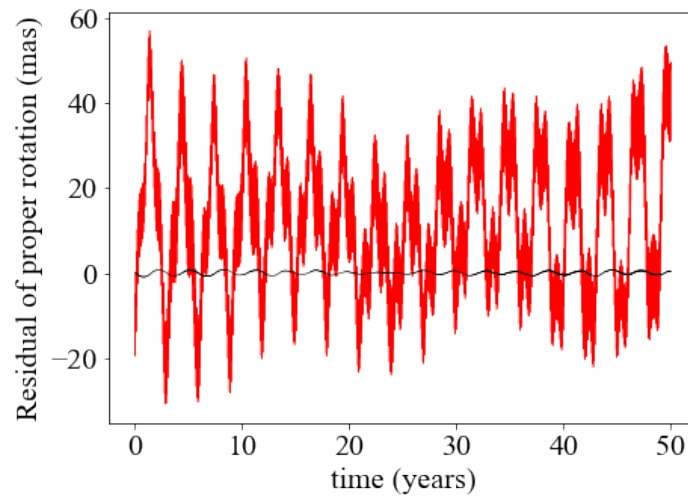


Figure 5: Residual of the lunar proper rotation with respect to the solution of INPOP19a. The black curve shows the residual only due to the effect of the truncation of the Fourier series and the red curve shows the residual due to the effect of the variation of the complex tidal Love number according to a solution from a lunar interior model

truncation of the Fourier series, which is just below 1 mas. For the red curve, the frequency analysis shows that the difference in the amplitude of the proper mode at 1056.21 days has an important contribution in the residual and reaches 22 mas. Among the terms of the tidal forcing, the one at 1095 days is the most significant, with a contribution of 24 mas. The one at 365 days is also important, with a contribution of 9 mas. Several terms at around 27 days have a contribution of about 10 mas, and the term in 18.6 years has an effect of 6 mas.

4. CONCLUSION

We introduced in the ephemerides INPOP, the formulation in Fourier series of the distortion coefficients of Williams & Boggs (2015). We have fitted secular parameters of ELP to the solution of INPOP19a. From this solution of ELP fitted to INPOP19a, we have computed the terms of the Fourier series of the distortion coefficients. We find that the difference induced by this last solution of the series with respect to those of Williams & Boggs (2015) is at the submillimeter level and is negligible. We have shown that we need to add up about five hundred terms in the series in

order to reduce the residual of the distance to the retroreflectors to the level of the observational accuracy. We were able to introduce the Love number variation with respect to the period of the tidal forcing according to lunar interior models, which causes much greater variations than the error due to truncation of the series. In future work we will test several solutions of Love number variation provided by interior models in order to test which models are able to absorb the residuals.

This work has been funded by the French National Research Agency (ANR), France and by the German Research Foundation (DFG), Germany joined project ANR-19-CE31-0026.

5. REFERENCES

- Briaud, A., Fienga, A., Melini, D., Rambaux, N., Mémin, A., Spada, G., Saliby, C., Hussmann, H., Stark, A., Viswanathan, V., Baguet, D., 2023a, "Constraints on the lunar core viscosity from tidal deformation", *Icarus* 394, 115426.
- Briaud, A., Ganino, C., Fienga, A., Mémin, A., Rambaux, N., 2023b, "The lunar solid inner core and the mantle overturn", *Nature* 617, 743.
- Chapront, J., Francou, G., 2003, "The lunar theory ELP revisited. Introduction of new planetary perturbations", *A&A* 404, 735.
- Fienga, A., Deram, P., Viswanathan, V., Di Ruscio, A., Bernus, L., Durante, D., Gastineau, M., Laskar, J., 2019, "INPOP19a planetary ephemerides", *Notes scientifiques et techniques de l'Institut de Mécanique Céleste*, S109.
- Konopliv, A. S., Park, R. S., Yuan, D.-N., Asmar, S. W., Watkins, M. M., Williams, J. G., Fahnestock, E., Kruizinga, G., Paik, M., Strelakov, D., Harvey, N., Smith, D. E., Zuber, M. T., 2013, "The JPL lunar gravity field to spherical harmonic degree 660 from the GRAIL Primary Mission", *J. Geophys. Res. Planets*, 118 (7), 1415-1434.
- Melini, D., Saliby, C., Spada, G., 2022, "On computing viscoelastic Love numbers for general planetary models: the ALMA³ code", *Geophys. J. Int.* 231 (3), 1502–1517.
- Spada, G., Boschi, L., 2006, "Using the Post-Widder formula to compute the Earth's viscoelastic love numbers", *Geophys. J. Int.* 166 (1), 309–321.
- Viswanathan, V., Fienga, A., Minazzoli, O., Bernus, L., Laskar, J., Gastineau, M., 2018, "The new lunar ephemeris INPOP17a and its application to fundamental physics", *MNRAS* 476, 1877.
- Williams, J. G., Boggs, D. H., 2015, "Tides on the Moon: Theory and determination of dissipation", *J. Geophys. Res. Planets*, 120 (4), 689-724.

RADIO SOURCES WITH LARGE CHANGES IN THE APPARENT COORDINATES

A. Osetrova¹, O. Titov², A. Melnikov³

¹ St Petersburg University - Russia - gelaosetrova@gmail.com

² Geoscience Australia - Australia - oleg.titov@ga.gov.au

³ The Institute of Applied Astronomy of the Russian Academy of Sciences - Russia - aem@iaaras.ru

ABSTRACT. The ICRF3 was officially adopted in 2018, and by that date the positions of the most unstable radio sources are believed to vary within 2-3 mas. However, we recently found some radio sources that expose extremely large positional instability (up to 130 mas) on the time interval from 3 to 30 years. This is far beyond of usually expected instability, therefore it attracts so much attention. Herewith, we conducted a systematic search of similar objects using the time series of radio source coordinates between 1993 and 2023 and developed special criteria. We identified 37 objects with the positional change exceeding 10 mas. They could be sorted in three types of instability:

1. steady apparent proper motion (6 objects),
2. "step" or "peak" at the position time series (13 objects),
3. "bouncing" first and last points (18 objects).

1. INTRODUCTION

The International Celestial Reference system (ICRS) is the current standard celestial reference system adopted by the International Astronomical Union (IAU) with its origin in the Solar System barycentre. ICRS is the quasi-inertial reference system allowing acceleration of the origin, but the rotation of the reference axis is not permitted. Thus, the acceleration of the Solar System barycentre due to the Galaxy rotation could be incorporated to the reduction model.

The International Celestial Reference Frame is a realization of the ICRS using extragalactic radio sources observed in radio frequencies (2.3 and 8.4 GHz) as reference points. These radio sources have neither physical proper motion, no parallax due to a large cosmological distance to the Earth's observer. ICRF is supposed to be a catalogue of highly accurate coordinates of radio sources evenly distributed around the sky. The most recent version of the ICRF (known as ICRF3) was adopted in 2018 (Charlot et al., 2020). ICRF3 comprises coordinates of 4536 extragalactic objects (at X-band), 303 of which are used to define the directions of the ICRS fundamental axes ("defining" sources). The formal error of the coordinates of the most observed radio sources reaches 6 μas , however, due to some positional instability in apparent position the "floor", or inflated, error is about 30 μas . The major reason is variability of the intrinsic structure of the extragalactic radio sources (Marcaide et al., 1985; Kellermann et al., 2004; Titov, 2007). Motion of relativistic jet with respect to the central core could cause a displacement of phase centre as detected by the interferometer. In addition, this displacement depends on the baseline length and orientation with respect to the core-jet (Charlot, 1990). Therefore, a radio source with extended structure may display some positional variations even at stable state. Such astrometrically unstable radio sources are treated as 'arc' parameters and their positions are to be estimated for each observational experiment. So far, the astrometrically unstable radio sources were known to

change the positions within 2–3 mas, and no large displacement in the radio source coordinates were found during preparation of the ICRF3.

Soon after ICRF3 was released, four radio sources (3C48, CTA21 1144+352, 1328+254) were found to show large positional shifts of 20–130 mas on the time scale 3–30 years (Titov et al., 2022). It occurs that, the coordinates of these sources as they were published in ICRF3, are not reliable. For instance, figure 1 depicts the large-scale shift (130 mas) in coordinates of 1328+254 in both components happened between 2014 and 2017. Its ICRF3 coordinate was based on three points before the break and one point after the break (2017). As a result it does not coincide neither with position of the radio source before the breaks, nor with position after the break. The optical Gaia DR3 position (Gaia Collaboration, 2023) is close to the post-shift radio position.

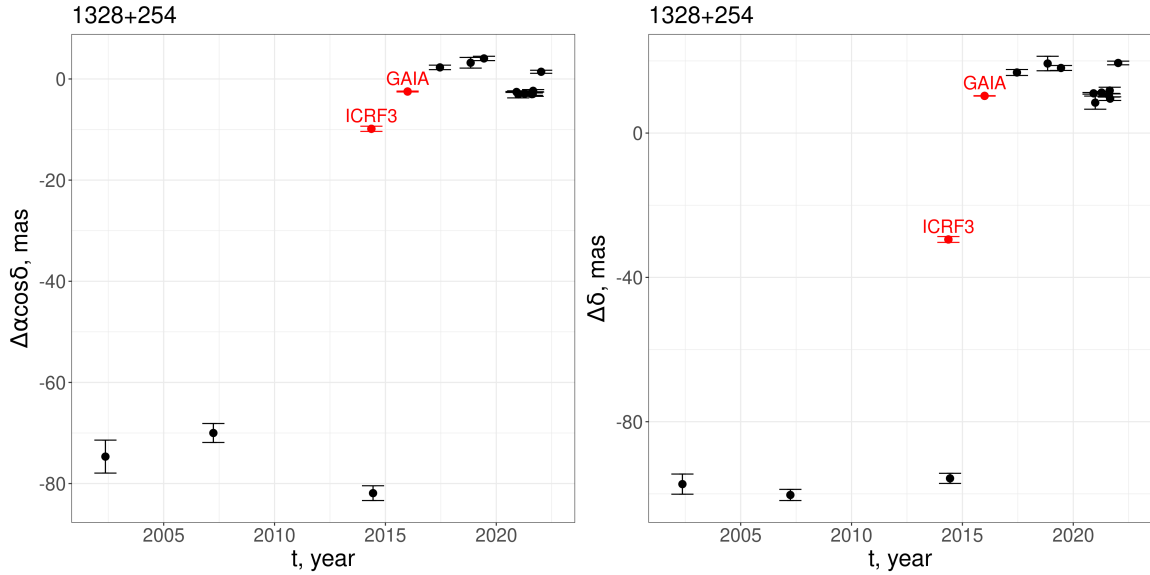


Figure 1: Shift of coordinates of 1328+254 in right ascension (left panel) and declination (right panel), ICRF3 and GAIA DR3 position are shown in red colour.

This sudden change of the astrometric position may cause a serious problem with processing of the geodetic VLBI experiments because the standard procedures are not designed to accommodate positional variations with so large magnitude. Therefore, the primary goal of our paper is searching for the objects with large astrometric instability using the time series of radio source coordinates obtained with geodetic VLBI observations in 1993–2023.

2. OBSERVATION AND DATA ANALYSIS

We used all geodetic VLBI observations organised by the International VLBI Service (IVS) (Nothnagel, et al., 2017) in 1993–2023 to estimate time series of daily radio source coordinates. In total, 4472 daily experiments were used and 4530 radio sources were studied. We added seven custom experiments run by the Institute of Applied Astronomy (IAA RAS) in Saint-Petersburg (Russia) using three radio telescopes Quasar VLBI network Svetloe (Sv), Badary (Bd), Zelenchukskaya (Zc) in Russia (Shuigina et al., 2019), Yebes40M (Yb), Seshan25 (Sh) and Wark30M (Wa). These experiments mostly focused on monitoring of some unstable radio sources listed in Table 1.

VLBI data were processed with OCCAM 6.3 software. For this solution we used a novel method that includes a preliminary calibration of the wet troposphere delays, gradients, and the clock phase instabilities. These stochastic parameters were calibrated with the least squares collocation for each

observational epoch and recorded to the data file similar to the ionosphere delay. On the second iteration, the wet troposphere parameters were not estimated, and the clock phase instabilities approximated by quadratic polynoms. As a result, we applied the plain least squares method for processing of all 24-hour experiments. Apart from the clock phase parameters, EOP, station, and radio source coordinates are included to the parametrical model.

Date DD-MM-YY	Radio telescopes
27-06-2020	Bd-Sv-Zc-Sh-Yb
28-11-2020	Bd-Sv-Zc-Yb
26-12-2020	Bd-Sv-Zc-Sh-Yb
20-03-2021	Bd-Sv-Zc-Sh
27-03-2021	Bd-Sv-Zc-Sh-Wa
10-04-2021	Bd-Sv-Zc-Sh
28-08-2021	Bd-Sv-Zc

Table 1: The list of the VLBI sessions of the RU-A project

3. SELECTION PROCEDURE

We estimated the corrections to the ICRF3 positions for both components, right ascension and declination, and their standard deviations: $\Delta\alpha^*(t) \pm \sigma_{\Delta\alpha^*}$ ($\Delta\alpha^* = \Delta\alpha \cos \delta$), $\Delta\delta(t) \pm \sigma_{\Delta\delta}$. Then, the weighted root-mean-squares (WRMS) values $\psi_{\Delta\alpha^*}$ and $\psi_{\Delta\delta}$ for each component time series $\Delta\alpha^*$ and $\Delta\delta$ were calculated. Finally, we found the total positional correction ψ as follows:

$$\psi = \sqrt{\psi_{\Delta\alpha^*}^2 + \psi_{\Delta\delta}^2} \quad (1)$$

This parameter ψ reflects the range of scatter of the daily estimates of the radio source position with respect to the catalogue value. It could be used as a statistical criterion for selection the radio sources with high astrometric instability. The histogram on Fig. 2 shows the parameter ψ distribution for the 1580 radio sources with at least 100 observations. The statistics was fitted by the Rayleigh distribution $f(x) = \frac{x}{\sigma_\psi^2} \exp(-\frac{x}{2\sigma_\psi^2})$, with scatter parameter $\sigma_\psi = 0.212 \pm 0.002$ mas.

The mathematical expectation of the value X equal to $E_X = \sqrt{2}\sigma\Gamma(1 + \frac{1}{2}) = \sigma\sqrt{\frac{\pi}{2}}$, was found to be $E_\psi \approx 0.27$ mas. It matches to the mean value of ψ , $\bar{\psi} = 0.27$ mas. We have chosen the statistical threshold $C_\psi = 3E_\psi \approx 0.8$ mas to separate "stable" and "unstable" radio sources and extended it to the whole sample of ψ for 4450 radio sources with more than one observations.

Based on this criterion we have pre-selected 627 of 4450 objects with $\psi \geq C_\psi$ as potentially unstable.

4. THREE TYPES OF INSTABILITY

For most of the 627 pre-selected objects with $C_\psi \geq 3\sigma_\psi$, the displayed high scatter of the daily position variations could be considered as a random noise without any feature. Only 37 radio sources show a sign of instability with conditions:

$$|\Delta\alpha_i^* - \Delta\alpha_j^*| \geq 3\sqrt{\sigma_{\Delta\alpha_i^*}^2 + \sigma_{\Delta\alpha_j^*}^2} \quad (2)$$

$$|\Delta\delta_i - \Delta\delta_j| \geq 3\sqrt{\sigma_{\Delta\delta_i}^2 + \sigma_{\Delta\delta_j}^2} \quad (3)$$

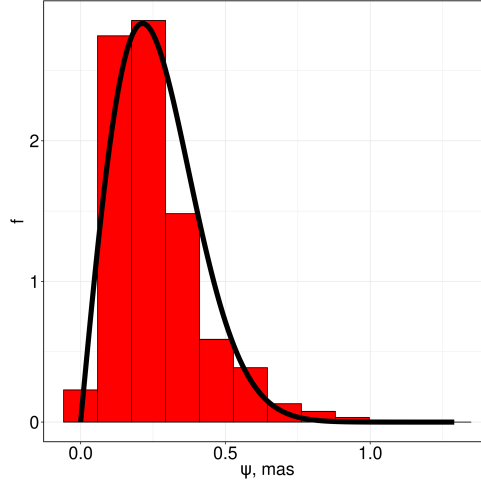


Figure 2: Distribution of ψ for 1580 radio sources.

They were sorted in three types as follows:

1. steady apparent proper motion (PM) (6 objects),
2. "step" or "peak" (SP) (13 objects),
3. "bouncing" first or last point (BP) (18 objects).

4.1 Instability of the "proper motion" type

The apparent proper motion of the radio sources is known for years. It is caused by the radio source intrinsic structure (motion of the jetted substance, appearance of new components, variability of flux density) rather than the relative motion of extragalactic objects with respect to the Solar system observer (as for the stars inside the Galaxy). This apparent proper motion could be approximated by linear or, sometimes, quadratic polynomials, or, may even change its sign. In the most extreme cases, positional evolution of the radio source position is modeled by a piecewise linear function. We used weighted least squares method (WLSM) to estimate the apparent (linear or quadratic) proper motion, where the weights of each single value $\Delta\alpha_j, \Delta\delta_j$ are inversely proportional to the squared formal error, i.e. $\sim \frac{1}{\sigma_{\Delta\alpha_j}^2}, \sim \frac{1}{\sigma_{\Delta\delta_j}^2}$.

We consider that the linear or quadratic models is valid, if three conditions are met:

1. the proper motion magnitude exceeds the 3σ level;
2. R-squared (R^2) is more than 80%;

R^2 shows how well observed outcomes are replicated by the model (Glantz et al., 1990; Chicco et al., 2021). The most general definition of R^2 is given by:

$$R^2 = 1 - \frac{SS_{res}}{SS_{tot}}$$

SS_{res} — residual sum of squares, in case of WLSM $SS_{res} = \sum w_{y_i} (y_i - \hat{y}_i)^2$.

SS_{tot} — total sum of squares, in case of WLSM $SS_{tot} = \sum w_{y_i} (y_i - \frac{1}{\sum w_{y_i}} \sum y_i w_{y_i})^2$. y_i is observed value, \hat{y}_i — estimated by WLSM, w_{y_i} — weight for y_i .

In the ideal scenario when $y_i = \hat{y}_i$, the $R^2 = 1$. This equality indicates the perfect fitting, whereas the meaning of $R^2 \geq 0.8$ is considered to be good enough.

3. Eq (2) or (3) where i, j are two "extreme" points.

Radio source 0350+177 (Fig 3) is a perfect example of the proper motion type instability. It constitutes proper motion of -4.1 ± 1.3 mas/year on right ascension. This leads to the RA change by 40 mas over the 10-year interval of observations. At the same time, the shift in declination of 75–100 mas between two sets of data is detected, and we classified this type of instability as the "step" type. Therefore, this radio source displays two different categories of instability for the two positional components. It should be noted that the ICRF3 position of 0350+177 is based on observations during 2017, i.e. before the "break".

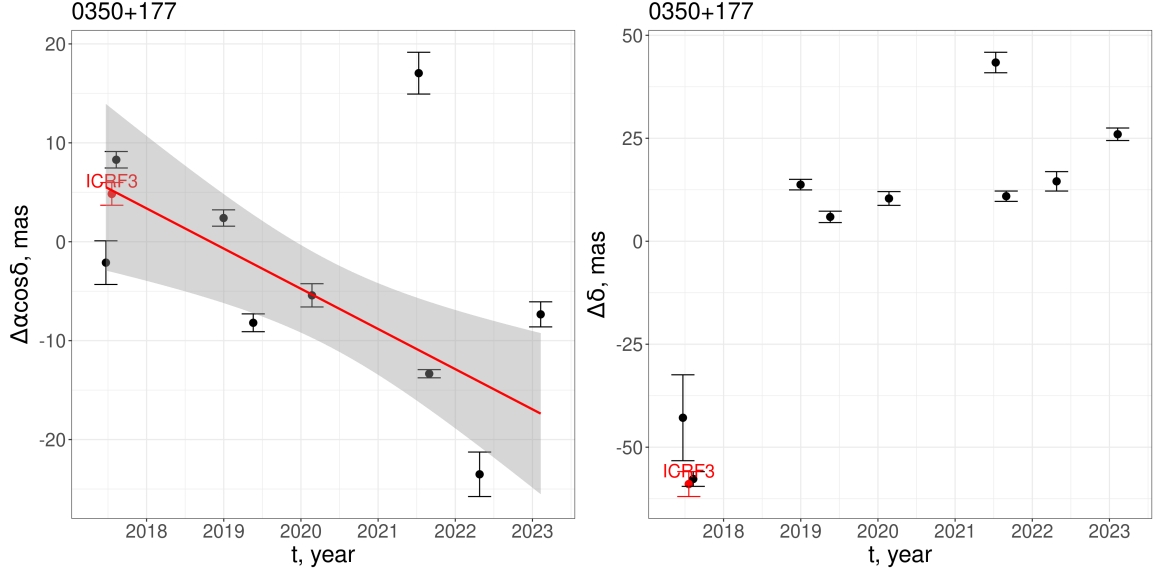


Figure 3: Radio source 0350+177, proper motion on right ascension is -4.1 ± 1.3 mas/year.

4.2 "Step" and "peak" type instabilities

To describe the two following types of instabilities we used terms "step" and "peak" just due to our visual impression. We are aware that the results from one or two VLBI experiments may be affected by many reasons — hardware malfunction, fake signal, low signal-to-noise, etc. Therefore, identification of these two types of instabilities at 2 or 3 points looks dodgy. Nevertheless, some radio sources shows such a large shift on very short time scale that it can not be ignored.

To identify these radio sources we developed a new algorithm based on the comparison of three parameters ψ_1, ψ_2, ψ_3 . We define $\psi_1(i)$ as ψ (Eq. 1) which is calculated for all points from the time series without i -th point ($j = 1, 2 \dots i - 1, i + 1 \dots n$). Parameter $\psi_2(i)$ is calculated using the points for j from the 1 to i -th points, and $\psi_3(i)$ is calculated using the points for j from i -th to n .

If one point on the graph (for example i -th point) lies far from the others, then two inequalities should be satisfied: the parameter $\psi_1(i)$ is less than C_ψ (in contrast, for all other points $\psi_1 > C_\psi$), and $\psi_2(i) > \psi_3(i)$. Thus, one could define the location of the peak (at the i -th point in our case). Finally, we need to check the statistical significance of the difference between $(i - 1)$ -th and i -th points by 3σ criteria. The equations (2 and 3) should be used for calculation of the difference between the total correction for $(i - 1)$ -th and i -th points.

4.2.1 "Step" type instability

The radio sources with the "step" type instability show a discontinuity of the first kind, when the left and right limits are not equal. At the visualization of the coordinate changes a "step" could be seen. It is important that both subsets (before and after the break) of data should be made of at least two points with 10 or more delays for each epoch to reduce the effect of random errors.

The outstanding example of this type of instability is the above-mentioned radio source 1328+254 (Fig. 1). Between 2014 and 2017 there was a huge shift in positions along the both components, with total amplitude of about 130 mas. Following the discussion above, it is not clear whether the ICRF3 position of 1328+254 refers to any physical feature. Therefore, the formal "radio – optical" offset between the 1328+524 Gaia and ICRF3 positions may not make sense. However, it may be feasible to analyse the "radio – optical" offsets for the two sets of radio coordinates separately.

4.2.2 "Peak" type instability

Some objects demonstrate an unusual variability in the position time series that could be treated as "peak" directed up or down along the coordinate time series. For example, radio source 1450+641 (Fig. 4) displays very specific evolution in its right ascension between 2018 and 2020 year. It was a developing "motion" in right ascension during the three years with a total shift of about 30 mas. Suddenly, in 14 days after reaching the maximum the position of the radio source came back to its starting point (near the ICRF3 catalogue position) forming a visual peak in the right ascension time series. This is not followed by any noticeable evolution in the declination component. Since this pattern was formed by three points we are confident about this effect, though, of course, a proper explanation of this quick evolution needs to be developed.

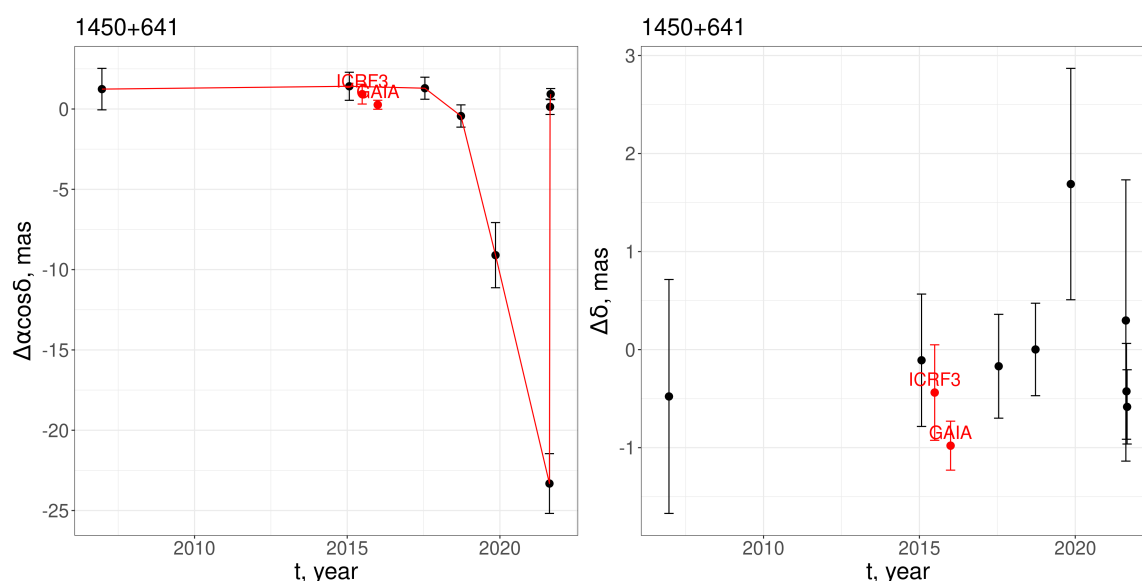


Figure 4: Radio source 1450+641, example of the "peak" type instability.

4.3 "Bouncing" first or last point

This category refers to the time series in which the first or last point lies far enough ("bounced") from all others. Of course, it can be caused by observation error for the single epoch experiment, therefore, this instability should be considered as "conditional" and needs an additional verification. An example of the instability may be radio source 1524-136. The coordinates of 1524-136 in ICRF2 and ICRF3 are different on more than 100 mas (Gordon et al., 2016). The ICRF2 coordinate of 1524-136 (Fey et al., 2015) is based on a single experiment in 1997 with 17 group delays. The ICRF3 coordinate of 1524-136 is based on three experiments in 2014–2017, whereas the experiment

from 1997 was excluded due to statistical inconsistency with the more recent experiments.

For the identification of the objects of this type we used the same statistical parameter ψ . The following conditions were to be met:

1. If the first point is bouncing, then the conditions are $\psi_1(1) = \min(\psi_1)$ and $\psi_2(2) > \psi_3(2)$, and if the last point is bouncing, then $\psi_1(n) = \min(\psi_1)$ and $\psi_2(n-1) > \psi_3(n-1)$.
2. The number of observations of bouncing first or last point is at least 10.
3. The shift of the positional time series is significant (Eqs 2 and 3).

Another example of this type instability is radio source 1518+046 (Fig. 5). It shows a large shift between the first (1995) and the second (2015) experiments of about 15 mas on right ascension and 23 mas on declination. The total shift is about 27.5 ± 3.8 mas exceeds the combined 3σ value and may be treated as reliable.

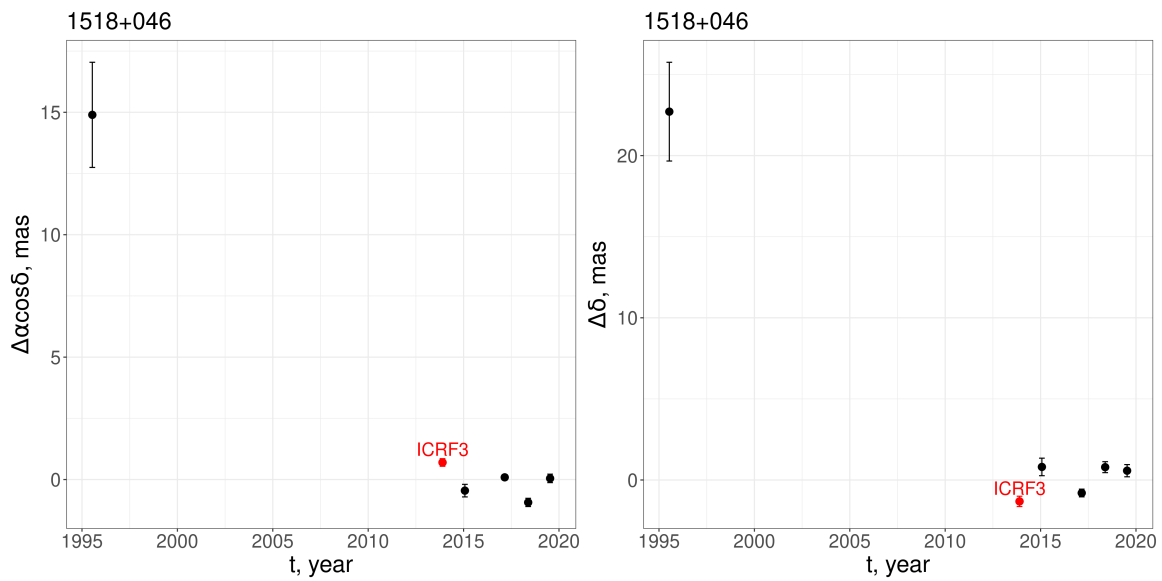


Figure 5: Radio source 1518+046.

5. CONCLUSION AND SUMMARY

We compiled a list of 37 radio sources with large change in coordinates between 1993 and 2023 (Table 2). In the context of the next ICRF catalogue preparation, these radio sources should be treated as astrometrically unstable objects.

source	inst.type	RA (ICRF3)	DE(ICRF3)	$\mu_{\alpha\cos\delta}$ mas/year	μ_{δ} mas/year	$\Delta\alpha\cos\delta$ mas	$\Delta\delta$ mas
0116+082	BP	01 19 01.27	+08 29 54.70			-1.8 ± 0.6	9.7 ± 1.1
0336+539	BP	03 40 06.49	+54 05 38.78				7.0 ± 1.2
0732+237	BP	07 35 59.92	+23 41 02.87			8.5 ± 1.8	5.8 ± 1.6
0959-443	BP	10 01 59.91	-44 38 00.60				-19.3 ± 2.2
1505-496	BP	15 08 38.94	-49 53 02.31				-5.2 ± 0.9
1506+591*	BP	15 07 47.39	+58 57 27.65				-7.8 ± 1.3
1518+046	BP	15 21 14.42	+04 30 21.64			-14.8 ± 2.2	-23.5 ± 3.1
1524-136	BP	15 26 59.44	-13 51 00.26			30.7 ± 1.5	-99.0 ± 2.5
1645+174	BP	16 47 41.84	+17 20 11.86				12.9 ± 2.3
1755+626	BP	17 55 48.44	+62 36 44.19			-54.0 ± 4.8	-87.3 ± 3.5
1814+349	BP	18 16 23.90	+34 57 45.75			5.5 ± 1.2	
1943+546	BP	19 44 31.51	+54 48 07.06			-7.0 ± 0.8	
2311-452	BP	23 14 09.38	-44 55 49.24			0.4 ± 0.1	-5.5 ± 0.4
0233+434*	SP	02 37 01.21	+43 42 04.19			-33.4 ± 3.9	
0622+147	SP	06 25 45.92	+14 40 19.74				-6.1 ± 1.1
0932-281	SP	09 35 11.50	-28 20 31.53			-17.8 ± 2.9	-26.3 ± 7.2
0958+559*	SP	10 01 57.80	+55 40 47.24			-20.4 ± 1.1	15.5 ± 1.1
1117+146	SP	11 20 27.81	+14 20 54.97			13.2 ± 3.3	-15.8 ± 3.2
1305+770	SP	13 07 05.25	+76 49 18.17			-10.2 ± 2.1	
1328+254	SP	13 30 37.70	+25 09 10.94			85.1 ± 1.8	115.0 ± 2.4
1334-179*	SP	13 37 39.78	-12 57 24.69			-41.9 ± 11.7	
1421+122	SP	14 23 30.10	+11 59 51.25			-15.4 ± 2.9	7.3 ± 2.2
1503-091	SP	15 06 03.03	-09 19 12.06			-11.8 ± 1.4	
1740-517	SP	17 44 25.45	-51 44 43.74			-6.2 ± 0.8	-13.0 ± 1.3
1825-055	SP	18 28 40.15	-05 30 50.86				-6.3 ± 1.7
1829+290	SP	18 31 14.86	+29 07 10.29			14.7 ± 2.5	
2105-212	SP	21 08 29.34	-21 01 38.19			-37.2 ± 3.4	
2304+377	SP	23 07 00.99	+38 02 42.23			9.1 ± 1.3	-4.6 ± 1.0
2358+406	SP	00 00 53.08	+40 54 01.81			-3.5 ± 1.1	12.4 ± 1.2
3C48	SP	01 37 41.30	+33 09 35.13			-7.2 ± 2.3	-58.1 ± 4.2
CTA21	SP	03 18 57.80	+16 28 32.68			10.2 ± 0.9	-33.5 ± 1.5
0200+304	PM	02 03 45.36	+30 41 29.11	-0.45 ± 0.10		-12.7 ± 1.9	
0350+177	PM/SP	03 52 52.92	+17 54 36.73	-4.09 ± 1.27		8.8 ± 2.3	101.1 ± 3.1
0423-163	PM	04 25 53.57	-16 12 40.24	0.36 ± 0.12		8.4 ± 2.1	11.8 ± 3.6
0711+356	PM	07 14 24.82	+35 34 39.80	0.08 ± 0.02	-0.20 ± 0.05	1.5 ± 0.3	-9.2 ± 0.7
0956-256*	PM	09 58 23.28	-25 56 15.47	-23.1 ± 1.3	38.1 ± 11.6	-48.4 ± 6.6	80.4 ± 10.1
1144+352	PM	11 47 22.13	+35 01 07.53	-0.77 ± 0.10	0.50 ± 0.07	-20.7 ± 0.4	13.7 ± 0.5

Table 2: List of 37 astrometrically unstable radio sources. Column 1: Source name; Column 2: type of instability – step or peak (SP), bouncing first or last point (BP), proper motion (PM). Columns 3 and 4: ICRF3 right ascension and declination. Coordinates of the non-ICRF3 radio sources (marked with *) are aus2022b solution (<https://cddis.nasa.gov/archive/vlbi/ivproducts/crf/>). Columns 5 and 6: proper motion on RA and DE, respectively. Columns 7 and 8: total difference in positions on RA and Dec over the observation period.

6. REFERENCES

- Charlot, P., et al. 2020, “The third realization of the International Celestial Reference Frame by very long baseline interferometry”, *A&A*, vol. 644, doi: 10.1051/0004-6361/202038368.
- Charlot P., 1990, “Radio-source structure in astrometric and geodetic very long baseline interferometry”, *AJ*, vol. 99, pp. 1309, doi:10.1086/115419.
- Chicco D, Warrens MJ, Jurman G, 2021. “The coefficient of determination R-squared is more informative than SMAPE, MAE, MAPE, MSE and RMSE in regression analysis evaluation”. *PeerJ Comput Sci.*, doi: 10.7717/peerj-cs.623
- Fey, A., et al. 2015, “The second realization of the International Celestial Reference Frame by very long baseline interferometry”, *AJ*, vol. 150, doi: 10.1088/0004-6256/150/2/58.
- Gaia Collaboration, A. Vallenari, A. G. A. Brown, T. Prusti, et al., 2023, “Gaia Data Re-

- lease 3 Summary of the content and survey properties”, *A&A* , vol. 674, doi: 10.1051/0004-6361/202243940.
- Glantz, Stanton A.; Slinker, B. K., 1990, “Primer of Applied Regression and Analysis of Variance”, McGraw-Hill, ISBN 978-0-07-023407-9.
- Gordon, D., et al., 2016. “Second epoch VLBA calibrator survey observations: VCS-II”, *AJ* , vol. 151, 154. doi: 10.3847/0004-6256/151/6/154.
- Kardashev N. S., 1986, “Cosmological proper motion”, *Soviet Astronomy*, vol. 30., pp. 501-503.
- Kellermann K. I., Lister M. N., Homan D. C., et al., 2004, “Sub-milliarcsecond imaging of quasars and active galactic nuclei. III. Kinematics of parsec-scale radio jets ”, *AJ* , vol. 609, pp. 539-563, 10.1086/421289.
- Marcaide J., Bartel N., Gorenstein M., et al, 1985, “Quasar 4C39.25 is not contracting ”, *Nature*, vol. 314, pp. 424, doi: 10.1038/314424a0.
- Nothnagel A., Artz T., Behrend D., Malkin Z., 2017, “International VLBI Service for Geodesy and Astrometry — delivering high-quality products and embarking on observations of the next generation”, *Journal of Geodesy*, vol. 91(7), pp. 711–721, doi:10.1007/s00190-016-0950-5.
- Titov, O., Frey, S., et al , 2022, “Unprecedented change in the position of four radio sources”, *Monthly Notices of the Royal Astronomical Society*, vol. 512, Issue 1, pp. 874–883, <https://doi.org/10.1093/mnras/stac038>
- Titov O. A., 2007, “Apparent proper motion of radio sources from geodetic VLBI data” , *Astronomy Letters*, vol. 33, pp. 481–487, doi: 10.1134/S1063773707070055.
- Shuigina N., Ivanov D., Ipatov A., et. al., 2019, “Russian VLBI network “Quasar” Current status and outlook” ,*Geodesy and Geodynamics*, vol. 10(2), pp. 150-156, doi: 10.1016/j.geog.2018.09.008.

A PROPOSAL FOR USING VERY LONG BASELINE INTERFEROMETER OBSERVATIONS TO IMPROVE LUNAR EPHEMERIDES

J.L. HILTON¹, V.V. MAKAROV², G.H.KAPLAN³, G.S. HENNESSEY⁴

¹ U.S. Naval Observatory (retired) - United States - jms.l.hilton@gmail.com

² U.S. Naval Observatory - United States - valeri.v.makarov.civ@us.navy.mil

³ U.S. Naval Observatory (contractor) - United States - george.h.kaplan.ctr@us.navy.mil

⁴ U.S. Naval Observatory - United States - gregory.s.hennessey.civ@us.navy.mil

ABSTRACT. Future activity on the lunar surface will require numerous radio transmitters situated there. These transmitters present an opportunity to re-introduce the use of Very Long Baseline Interferometry (VLBI) in the construction of lunar ephemerides. For the past fifty years precision lunar ephemerides have been constructed using solely lunar laser ranging (LLR), because it is at least an order of magnitude more accurate than any other currently available data type. LLR, however, provides only range data. Reliance on range alone results in large covariance values between several parameters of the ephemeris solution. VLBI plane-of-sky positions are complimentary to LLR ranges. The reduction process for analyzing near-field VLBI observations is well developed. Relative VLBI observations of the Apollo Surface Experiments Packages (ALSEP) demonstrated that it can provide more accurate lunar libration angles than from LLR alone. Past proposals to establish lunar VLBI beacons were made for this reason.

1. INTRODUCTION

King (1975) and King, Counselmann, & Shapiro (1976) established the viability of using relative Very Long Baseline Interferometry, VLBI, in lunar ephemerides. These experiments used the transmitters of the five Apollo Lunar Experiment Packages, ALSEP, left on the Moon as a part of the Apollo 12, 14, 15, 16, and 17* missions. This work established the relative positions of the ALSEP in lunar ephemerides with an uncertainty of 0.5 mas[†], a remarkable achievement for the time.

Slade *et al.* (1977) went on to report on work to improve the lunar ephemeris using observations of those ALSEP packages with respect to background quasars. The expected relative accuracy between an ALSEP package and nearby quasars was on the order of a few mas. Thus, the absolute positions of the quasars was the primary source of uncertainty at that time. This work came to an end on 30 September 1977 when the ALSEP packages were switched off (Bates, Lauderdale, & Kernaghan, 1979). The absence of active radio transmitters on the lunar surface brought to an end the ability to determine lunar positions from VLBI.

Since then, the lunar ephemeris has been determined solely from lunar laser ranging, LLR, data. LLR data are exclusively used because they are at least an order of magnitude more accurate than any other available data type. LLR, however, only provides a single observable parameter, range. Reliance on range alone results in large covariance values between some parameters in the ephemeris solution. For example, it is difficult to disentangle the Moon's position from its orientation.

Future lunar activity will require numerous radio transmitters on the lunar surface. These transmitters present an opportunity to re-introduce the inclusion of VLBI in the construction of

*The Apollo 14 and 15 ALSEP packages are colocated within a couple hundred meters of lunar laser retroreflectors.

[†]About 1 m at the Earth-Moon distance.

lunar ephemerides. The object of this contribution is to provide the rationale for its reintroduction. Section 2 examines LLR data and its weaknesses. Section 3 summarizes the details of the lunar ephemeris model. Section 4 examines VLBI data and how it may improve our knowledge of the lunar location and orientation ephemerides.

2. LUNAR LASER RANGING (LLR)

Lunar ephemerides have been constructed using solely LLR observations since shortly the first retroreflector was installed on the lunar surface by the Apollo 11 astronauts in 1969. The RMS fit of the early LLR observations (~ 1970 – 1980) to the lunar ephemeris is about 20 cm (Park *et al.* 2021). Improvements to both the hardware required for LLR and the atmospheric delay model have steadily reduced the RMS fit of observations since then. Recent observations, approximately the last decade and a half, have an RMS in the DE440 ephemeris of 1.3 cm.

2.1 LLR compared to stellar occultation

The next most accurate available data type for lunar ephemerides, stellar occultations, is also one-dimensional and has an uncertainty of about 0.1 s (Nather & Evans 1970). The derived uncertainty for the lunar position from an occultation by a point source is about 100 m. The primary source of uncertainty is the location of the apparent lunar limb, which depends on knowledge of both lunar topography and orientation. Nather & Evans estimate that the uncertainty in timing could be reduced to about 1–2 ms. Other sources of uncertainty such as diffraction, scintillation, and the apparent diameter of the occulted object would also need to be included. The uncertainty would be reduced to ~ 1 m, assuming the apparent limb can be well enough characterized. Thus, stellar occultation observations would remain at least two orders of magnitude less accurate than LLR observations.

Stellar occultation's strength is that these data give a one-dimensional, plane-of-sky position, complimentary to LLR ranges. The uncertainty in the lunar longitude from LLR alone is ~ 3 m and increases a few meters per decade squared. This estimate is arrived at from comparison of the positions in three modern ephemerides, DE430, DE440, and INPOP21a (Hilton, 2022 private communication). The uncertainty arises from LLR not providing an absolute position for the Moon within the ICRS and the stochastic increase in its semi-major axis arising from its tidal interaction with Earth. Thus, much improved occultation data should just be accurate enough to reduce the uncertainty in the lunar longitude.

2.2 LLR weaknesses

LLR data have some weaknesses as well.

- LLR produces only a single observable: the distance from the observer to the retroreflector.
- Retroreflector acquisition is accomplished using visual offset from a landmark. This method limits observations to phase angles where the landmark is visible.
- Both the laser pulse and timing its return require accuracies on the order of 10 ps to determine the distance with a centimeter level of uncertainty.
- The present uncertainty arising from atmospheric delay is about a millimeter (Hulley & Pavlis, 2006).
- The mean return from a single pulse is less than one photon[‡] (Murphy, 2013).

[‡]Temperature gradients within the retroreflectors affect their shape reducing the number of returned photons and reducing the effectiveness of LLR at phase angles around full Moon. The arrays have over the years become coated with electrostatically levitated dust reducing the reflectivity by as much as 90%.

- The plane of the retroreflector arrays are usually *not* perpendicular to the travel direction of the laser beam due to the extended areas of the retroreflector arrays and lunar libration. The difference between the extreme points of an array can be more than 10 cm.

The last two items require that the LLR observable is a normal point assembled over several minutes from a number of individual returns. A new generation of retroreflectors will shortly begin deployment on the lunar surface. These next generation devices will be more compact and constructed of lower expansion materials. Thus, data acquired using the new retroreflectors will have significantly reduced uncertainties arising from their structure.

3. THE LUNAR EPHEMERIS MODEL

A complex model is required to achieve the current accuracy of the lunar ephemeris. The structure and rheology of the Moon as well as the perturbations by external bodies must be included. Table 1 summarizes the model elements required to produce a state-of-the-art ephemeris. Pavlov *et al.* (2016), for example, required approximately 210 parameters of which 1/3 to 1/2 are estimated in the solution.

Interaction	Magnitude
Solar perturbations	3699 km
Jupiter perturbations	1.06 km
Venus perturbations	0.73 km
Earth J_2	0.46 km
Mars and Saturn perturbations	100 m
Lorentz contraction	0.95 m
Lunar J_2 and C_{22}	0.2 m
Tidal dissipation	38 mm yr ⁻¹
Solar potential	6 cm
Time transformation	5 cm
Other relativity	5 cm
Large asteroid perturbations	several mm
Solar radiation pressure	4 mm
Earth C_{22}	0.5 mm

Table 1: Effects required to construct a state-of-the-art lunar ephemeris. Sources: Williams & Dickey (2003) and Murphy (2013)

One result of fitting such a large number of parameters with a single one-dimensional data type is a number of high covariances between parameter subsets. Figure 1 is an example for a lunar ephemeris from Viswanathan (2017). In this case, 112 parameters are adjusted. The components of the Earth-Moon initial state vector, the lunar gravity field coefficients, and the orientation of the lunar axes of the principal moments of inertia all have large covariances. There are lower, but not insignificant covariances between the locations of the retroreflectors and the gravity field coefficients, principal moments of inertia, and state vector. These latter covariances are particularly large for parameters modeling the Apollo 15 retroreflector, the array used most often[§] for LLR data acquisition.

[§]The Apollo 15 retroreflector array was used for almost 76% of the normal points from 16 March 1970 through 18 Dec. 2012 (Williams *et al.*, 2013). Data through March 2020 this array still accounted for almost 66% of the total (Williams & Boggs, 2020).

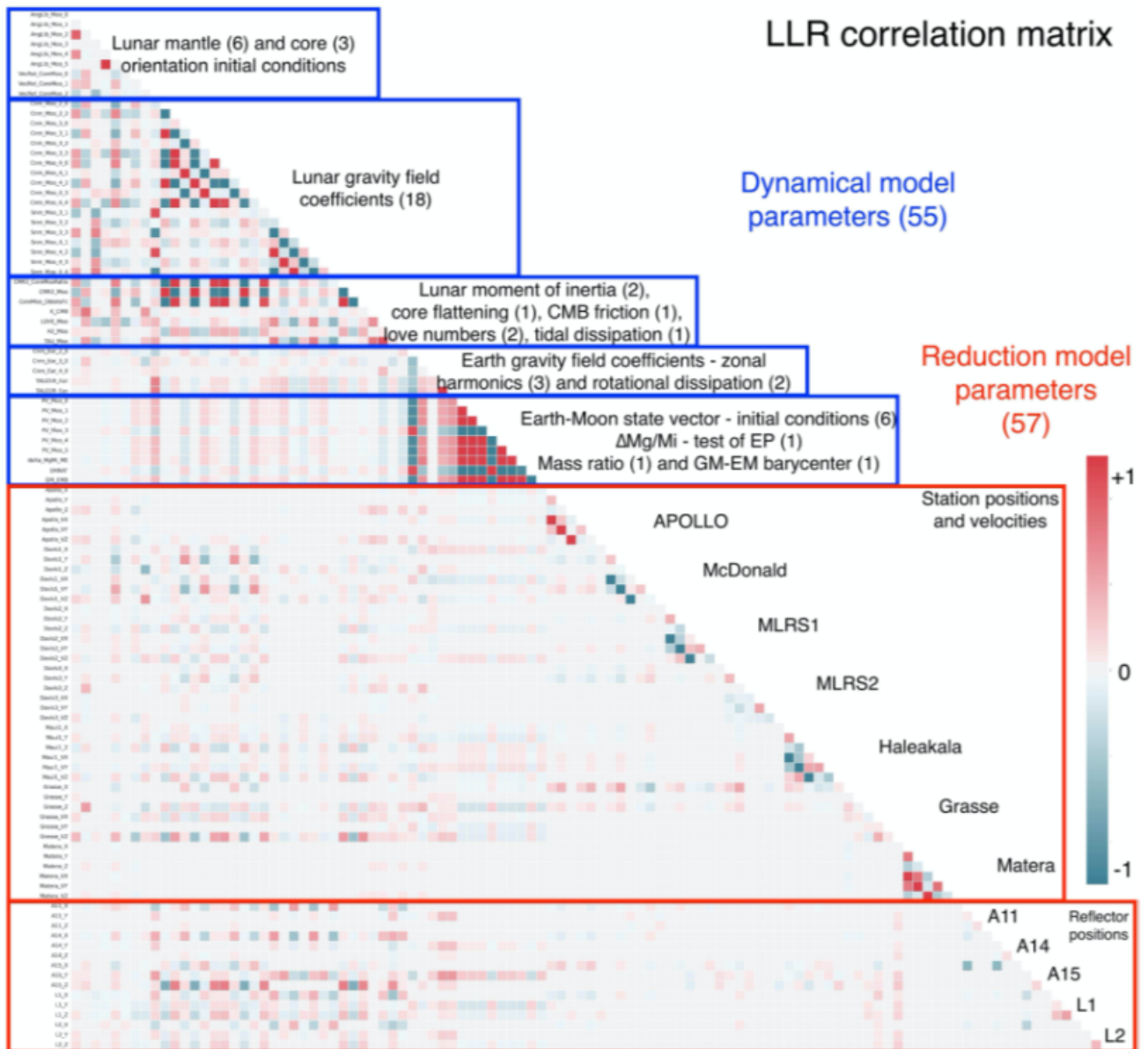


Figure 1: A non-numerical example covariance matrix from Viswanathan (2017).

3.1 Lunar orientation

Two widely used systems are used to describe the orientation of the lunar surface: First, there is the mean Earth-mean pole of rotation (ME) system. Here the x -axis points in the mean direction towards Earth, the z -axis is the mean pole of rotation, and the y -axis completes a right-handed Cartesian coordinate system. Recent publications, *e.g.* Williams *et al.* (2013) and Park *et al.* (2021) have adopted the DE421 (Williams *et al.*, 2008) ME system as the practical realization of that system; effectively anchoring it to the lunar surface. Second, there is the principal moments of inertia (PA) system where the x -axis points along the mean least moment of inertia axis, the z -axis points the along the mean greatest moment of inertia axis, and the y -axis points the along the mean intermediate moment of inertia axis in the direction that completes a right-handed Cartesian coordinate system. Because the Moon is not a rigid body the locations of the PA axes are a function of the lunar model orientation and must be determined in the ephemeris solution. The difference between the orientations of the ME and PA axes are represented by a set of small rotations about the x -, y -, and z -axes. The rotation around the x -axis is less than an arcsecond, while the rotations around the y - and z -axes are both slightly more than an arcminute. The exact values of the rotations are parameters solved for in the ephemeris solution.

The apparent disk seen by an Earth-based observer is not constant but librates over time. The total apparent libration of the Moon is complex. It contains physical and optical components. The physical libration arises from the non-constant lunar rotation in response to torques and is often distributed as a lunar orientation ephemeris. Optical libration arises variation in the lunar rate of orbital motion, the obliquity of the lunar equator to its orbital plane, and diurnal changes of geometric perspective of the Earth-based observer. It is much larger than the physical libration. LLR data must also account for the geometric perspective of the retroreflector array on the lunar surface. Thus, it contains a composite of lunar position and orientation that is likely degenerate for a solution using solely range data.

The variation in range, δr , between a retroreflector array and a lunar laser ranging station arising from libration is, to second order,

$$\delta r \approx R \left(\phi \sin \theta - \frac{\phi^2}{2} \cos \theta \right) \quad (1)$$

where R is the lunar radius, θ is the angular distance along the great circle passing through the retroreflector and the center of the apparent lunar disk, and ϕ is the component of libration along θ . Table 2 shows the values of θ and azimuth for each of the arrays. The Apollo 11 and 14 arrays are located near the equator, and thus have little sensitivity to rotation about the y -axis. The Apollo 15 array is near the prime meridian, so it has little sensitivity to rotation about the z -axis. Lunkhods 1 and 2 arrays are located at azimuths close to being perpendicular to each other, and each is approximately equally sensitive to rotations about the y - and z -axes[¶]. They are also both closer to the limb than any of the Apollo arrays, so they are more sensitive to rotation about these two axes. Rotation around the x -axis is essentially in the plane-of-the-sky so LLR is almost completely insensitive to the component of libration around this axis^{||}.

4. VERY LONG BASELINE INTERFEROMETRY (VLBI)

VLBI can produce two-dimensional plane-of-sky data complimentary to LLR ranges. The accuracy of absolute VLBI derived positions is limited by the 0.22 mas total mean uncertainty in the locations of the quasars used to define the International Celestial Reference Frame (Charlot *et al.*

[¶]The difference between the ME and PA systems is small enough that it makes no qualitative difference which one is used here.

^{||}There is a small amount of sensitivity to rotation about the x -axis arising from motion of the x -axis about the center of the apparent disk arising from libration about the y - and z -axes.

Retroreflector Array	Distance from Center		Azimuth (deg)
	Lunacentric, θ (deg.)	Apparent (radii)	
Apollo 11	23.5	0.40	88
Apollo 14	17.8	0.31	282
Apollo 15	26.4	0.44	7
Lunokhod 1	39.5	0.64	324
Lunokhod 2	50.0	0.77	47

Table 2: Azimuth and distance of the retroreflector arrays from the center of the apparent disk. Source: Williams, Boggs & Folkner (2013)

2021). This translates to a linear uncertainty of about 40 cm, at the semi-major axis distance of the Moon. Thus, absolute VLBI data are more than an order of magnitude less accurate than LLR data. But it is still useful because of its complimentary nature and the ability to make relative simultaneous measurements of multiple transmitters:

- VLBI would address uncertainty in lunar a direct, two-dimensional absolute position more accurately than occultation data. It would also provide a complimentary observation to LLR of the increase in semi-major axis from tidal friction in the form of the change in observed longitude arising from the change in the mean motion.
- Observation of the *relative* positions of multiple Moon-based transmitters would allow the determination of the lunar orientation less dependent on the location of the lunar center of mass. The apparent change of a location for a rotation about either the y - or z -axis is proportional the cosine of the lunacentric angle between the transmitter and the center of the apparent disk. A rotation of $1''$ at the distance of the lunar semi-major axis results in an apparent displacement of about 4.5 mas for a transmitter at the center of the apparent disk.
- Similarly, a rotation of the Moon about the x -axis of $1''$ at the distance of the lunar semi-major axis results in an apparent displacement of about 4.5 mas at the limb. Thus, VLBI provides sensitivity to the component of libration about the x -axis. The sensitivity is proportional to the apparent distance of the radio transmitter from the center of the lunar disk. Table 2 shows the apparent distances in lunar radii for the five retroreflector arrays. A transmitter colocated with these arrays would yield apparent displacements ranging from about 1.4 mas for Apollo 14 to 3.5 mas for Lunokhod 1 for a $1''$ rotation about the x -axis.
- VLBI transmitter acquisition is a non-visual process. Thus, obtaining VLBI data is not limited by phase angle. This property also may reduce parameter covariances arising because the phase restrictions have periods similar to the synodic month.

The problem for obtaining lunar VLBI data is that the technique requires an active radio transmitter in a band accessible to VLBI receivers. A transmitter does not have to be powerful; a 1 W omnidirectional transmitter on the lunar surface would provide a several Jansky signal at Earth's surface. Eubanks (2018) proposed constructing and installing 1 mW special purpose transmitters. These transmitters would be powered with Americium-241 batteries, which could last for decades, and would be hardened to survive the lunar day-night cycle.

A transmitter need not be dedicated to VLBI. Previous experiments (King, 1975; King, Counselmann, & Shapiro (1976); and Slade *et al.*, 1977) made use of the radio transmitters that were

a part of the ALSEP packages^{**}. The software King used to reduce those data is publicly available as part of the Planetary Ephemeris Program (PEP)^{††} (Chandler *et al.*, 2021). These results are over 45 years old, so a thorough review will be required.

Groups, such as Duev *et al.* (2012) have more recently addressed the modification of VLBI analysis required to observe near-field sources. Zhou *et al.* (2022) validated Duev *et al.*'s method in the vicinity of the Moon; using it to navigate the Chang'E-5 spacecraft. Thus, an alternative exists if the older analysis methods are too crude to meet modern requirements.

5. REFERENCES

- Bates, J.R., Lauderdale, W.W., & Kernaghan, H., 1979, "ALSEP Termination Report," NASA RP-1036.
- Chandler, J.F., Battat, J.B.R., Murphy, T.W., Reardon, D., Reasenberg, R.D., & Shapiro, I.I., 2021, "The Planetary Ephemeris Program: Capability, comparison, and open source availability," *A&A* 162, 78.
- Charlot, P., Jacobs, C.S., Gordon, D., Lambert, S., de Witt, A., Böhm, J., Fey, A.L., Heinkelmann, R., Skurikhina, E., Titov, O., Arias, E.F., Bolotin, S., Bourda, G., Ma, C., Malkin, Z., Nothnagel, A., Mayer, D., MacMillan, D.S., Nilsson, T., & Gaume, R., 2021, "The third realization of the International Celestial Reference Frame by very long baseline interferometry," *A&A* , 644, A159.
- Duev, D.A., Molera Calvés, G., Pogrebenko, S.V., Gurvits, L.I., Cimó, G., & Bocanegra Bahamon, T.M., 2012, "Spacecraft VLBI and Doppler tracking: Algorithms and implementation," *A&A* , 541, A43.
- Eubanks, T.M., 2018, "Milliwatt lunar VLBI beacons: Surviving the lunar night," Survive the lunar night workshop 2018, (LPI contrib. No, 2106).
- Hulley, G. & Pavlis, E.C., 2006, "Improvement of current refraction modeling in Satellite Laser Ranging (SLR) by ray tracing through meteorological data," *J. Geophys. Res.* , 112, 2006JB004834.
- King, R.W., Jr., 1975, Precision selenodesy via differential very-long-baseline interferometry, PhD thesis, Massachusetts Institute of Technology.
- King, R.W., Jr., Counselmann, C.C., III, & Shapiro, I.I., 1976, "Lunar dynamics and selenodesy: Results from analysis of VLBI and laser data," *J. Geophys. Res.* , 81, pp. 6251-6256.
- Murphy, T.W., 2013, "Lunar-laser ranging: The millimeter challenge," *Rep. Prog. Phys.*, 76, 076901.
- Nather, R.E. & Evans, D.S., 1970, "Photoelectric measurement of lunar occultations. I. The process," *AJ* , 75, pp. 575-582.
- Park, R.S., Folkner, W.M., Williams, J.G., & Boggs, D.H., 2021, "The JPL planetary and lunar ephemerides DE440 and DE441," *AJ* , 161, 105.
- Pavlov, D.A., Williams, J.G., & Suvorkin, V.V., 2016, "Determining parameters of Moon's orbital and rotational motion from LLR observations using GRAIL and IERS-recommended models," *Celest. Mech. Dyn. Astr.* , 126, pp.61-88.
- Slade, M.A., Preston, R.A., Harris, A.W., Skjerve, L.J., & Spitzmesser, D.J., 1977, "ALSEP-quasar differential VLBI," *The Moon*, 17, pp. 133-147.
- Viswanathan, V., 2017, Improving the dynamical model of the Moon using lunar laser ranging (LLR) and spacecraft data, PhD thesis, Université Paris.

^{**}Bates, Lauderdale, & Kernaghan (1979) state that the ALSEP transmitters were left in a state that would allow them to be switched on if sent the activation code. Thus, it might be possible to revive the ALSEP transmitters provided: the activation code is still available, the electronics are still functioning, and the radioisotope thermoelectric generators are still able to provide sufficient power.

^{††}PEP's test suite also includes an example lunar VLBI data reduction.

- Williams, J.G. & Dickey, J.O., 2003, "Lunar geophysics, geodesy, & dynamics," in Proceedings from the science sessions and full proceedings CD-ROM of the 13th international lunar laser ranging workshop, R. Noomen, S. Klosco, C. Noll, & M. Pearlman eds., NASA/CP-2003-212248.
- Williams, J.G. & Boggs, D.H., 2020, "The JPL lunar laser ranging model 2020," JPL Interoffice Memorandum, IOM 335N-20-01.
- Williams, J.G., Boggs, D.H., & Folkner, W.M., 2008, "DE421 Lunar Orbit, Physical Librations, and Surface Coordinates," JPL Interoffice Memorandum, IOM 335-JW,DB,WF-20080314-00.
- Williams, J.G., Boggs, D.H., & Folkner, W.M., 2013, "DE430 Lunar Orbit, Physical Librations, and Surface Coordinates," JPL Interoffice Memorandum, IOM 335-JW,DB,WF-20130722-016.
- Zhou, W.L., Song, S.L., Hu, X., Zhang, Z.B., Li, P.J., Jiang, J., Li, W., Jin, X.L., & Jiao, G.Q., 2022, "Tropospheric delay correctin of VLBI Stations for the real-time trajectory determination of the Chang'E-5 spacecraft," *Radio Sci.*, 57, e2022RS007440.

LOOKING FOR A LUNAR REFERENCE TIMESCALE

P. DEFRAIGNE¹, F. MEYNADIER², P. TAVELLA²

¹ Royal Observatory of Belgium - Belgium - p.defraigne@oma.be

² Bureau International des Poids et Mesures

ABSTRACT. Multiple space missions to the Moon are currently being planned by space agencies and industrials. Positioning, Navigation and Timing (PNT) are expected to rely on lunar equivalents of terrestrial GNSS, which relies on clock comparisons and the existence of a common reference timescale. This triggers the need to define such a reference timescale, and to identify how to implement it in a way that will allow, like on the Earth, effective synchronisation of the clocks involved as well as realization and dissemination of this reference timescale. In a first step, we have to define a Lunar time scale, associated with the Lunar Reference System in a relativistic frame, while keeping the link with our Earth-based time scales, in particular the Terrestrial Time TT and UTC, its realization corrected for leap seconds. We explore some aspects of these questions while taking part to an inter-agency work about the interoperability of systems in cis-lunar environment (LunaNet proposal), which covers many physical and technological aspects of the cooperation between operators of Moon space missions. In this talk we will present the current status on this topic from the viewpoint of timescales and clock proper times.

BIPM is willing to help for the definition and the realization of time scale and the connection with the UTC. It is also of great importance that other International organizations can be involved. IAU defines space time reference frames, while communication on the Moon may involve the ITU for the allocation of frequency band and related spectrum issues. quickest and largest involvement of the national and international partners working on Moon missions will allow a fast and sound definition of the necessary conventions that will then support all the mission developments.

1. CONTEXT

This work has been triggered by requests from space agencies who are seeking how to define a common framework for their space missions around the Moon. So far each lunar mission carried more or less its own space and time reference system with it. The level at which these reference frames were connected to the Moon's surface (for spatial reference frame) and to the mission control timescale (for time reference frame) was adapted to the nature of the mission on a case-by-case basis. The renewed interest for lunar and cislunar environment and the multiplication of projects calls for a new approach to this matter: spacecrafts belonging to different entities might offer interoperable services for navigation, timing, and data transfer for example. This requires defining a common set of references. A proposed framework for this is the LunaNet Interoperability Specification* (LNIS, Israel et al., 2020), which is currently developed by NASA and ESA.

This paper represents the status of the author's proposal during the "Journées des systèmes de Références 2023". A lot of exchanges happened during these Journées, which oriented subsequent discussions.

2. GNSS Time Interoperability

Determining a position thanks to Global Navigation Satellite Systems consists in determining

*https://www3.nasa.gov/sites/default/files/atoms/files/lunanet_interoperability_specification_version_4.pdf

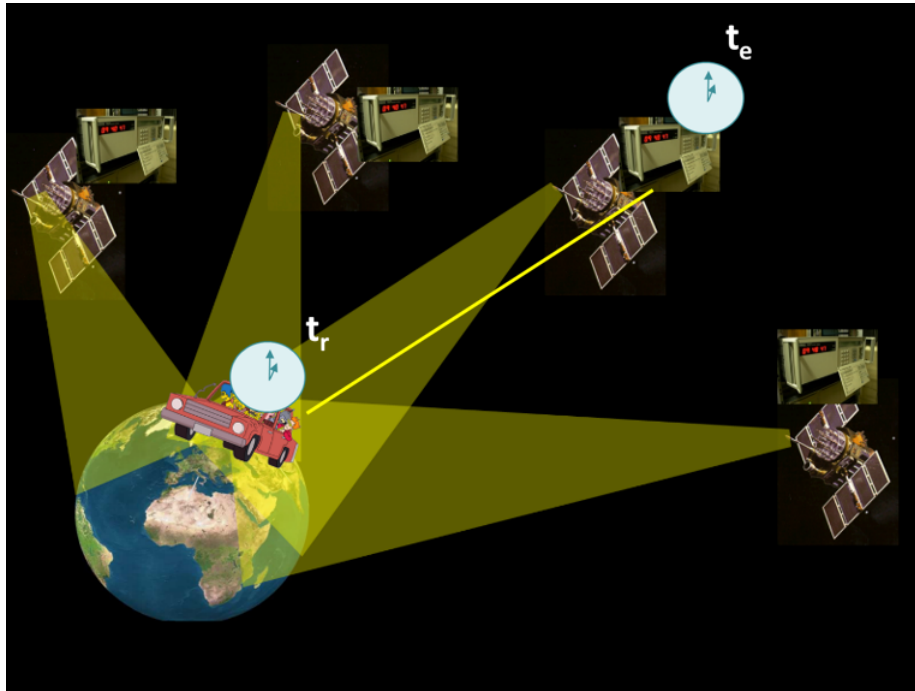


Figure 1: Multi-constellation GNSS positioning

the distance between the receiver and each visible satellite, whose position in the sky is known, and then solve the system of equations (one equation per satellite, 4 unknowns for time and space coordinates of the receiver). Neglecting atmospheric delays, this corresponds to

$$\begin{cases} P^{\text{sat}.1} = |x_{\text{sat}.1} - x_r| + c(t_{\text{rec}} - \text{ref}) - c(t_{\text{sat}.1} - \text{ref}) + \text{errors} \\ \dots \\ P^{\text{sat}.n} = |x_{\text{sat}.n} - x_r| + c(t_{\text{rec}} - \text{ref}) - c(t_{\text{sat}.n} - \text{ref}) + \text{errors} \end{cases} \quad (1)$$

Where $P^{\text{sat}.n}$ is the measured observable, $x_{\text{sat}.n}$ is the 3-dimensional position of satellite, x_r is the 3-dimensional position of the receiver (their difference being the pseudo-range), c is the speed of light, t_{rec} is the time at the receiver, t_{sat} is the time at the satellite, and ref the reference timescale, common to all satellites (this is usually achieved partly by steering or periodically synchronising the onboard clocks, and partly by providing known clock biases data in the navigation message).

Errors on time determination directly translate in errors in pseudoranges, e.g. a 1 ns error on time difference will induce an error of the order of ~ 30 cm on position.

When satellites belong to different constellations, it can no longer be assumed that ref is common to all satellites, and the difference between reference system times becomes an additional unknown. It can be either determined by using redundant equations (if more than 5 satellites are available), or extracted from external information sources. In the latter case, in theory if N constellations are used then $N(N-1)/2$ inter-constellation biases need to be determined. Using a common reference, e.g. UTC on Earth, reduces this need.

This problem is already studied for Earth-based GNSS, but will arise more sharply in cislunar environment where the number of satellites per constellation is expected to be lower : having to determine position from a small number of satellites all belonging to different constellations on Earth is exceptional and edge-case, but may be much more common on the Moon. It is therefore crucial that the system reference time scales remain close one another, which requires technically that a reference is defined, with a physical realization made available so that each system can steer

its own reference on it.

3. A common timing reference on the Moon

In this section we will first detail requirements on a reference time to be defined for cislunar activities. We then remind the coordinate time differences that exist between the Earth and Moon reference frames, we discuss the possible realizations, of these coordinate times and then make a proposal for a Lunar Reference Time.

3.1 Requirements for a Timing Reference

The list of desirable properties for a lunar timescale was found to be as follows:

- It should be associated with the Lunar Reference System in a relativistic frame
- A physical realization should be available so that all satellites, system times, user clocks, can be steered on this reference.
- It must be possible to maintain this physical realization on the Earth, as long as there are no clocks on the Moon.
- This reference should be connected to UTC, as *UTC produced by the BIPM, based on TAI, is the only recommended time scale for international reference* (Resolution 2 of the 26th CGPM in 2018).
- The difference with respect to UTC should be measurable and predictable (to an extent that still needs to be determined).

These are meant to ensure that the defined timescale is practical and well defined with respect to the other timescales. A major hurdle is the fact that relativity is far from negligible in this context. Although the targeted positioning performance should be lower than the one currently achieved on Earth with full GNSS constellations, it will definitely require careful integration of relativistic effects, the main one being the differential gravitational redshift in the vicinity of the Moon.

3.2 Coordinate time scales

It should be noted at this point that the general issue of determining relativistic timescales at arbitrary points of the Solar System has already been covered by the IAU 1991 recommendations, and their clarifications in 2000 (Soffel et al., 2003). They define the Barycentric Celestial Reference System (BCRS) as a global coordinate system, and the Geocentric Celestial Reference System (GCRS) as a local (terrestrial) one. Furthermore, doing so provides also a general way to define a local coordinate system for each body of the solar system, hence a Luni-Centric Reference System (LCRS).

Figure 2 provides a tentative schema of the current timescales defined on Earth and at the barycentre of our Solar System, and what would be their equivalent for the Moon.

TCB (resp. TCG) is the timescale associated to the BCRS (resp. GCRS), and TCL could be the equivalent of TCG for the lunar local system (LCRS). On the Earth surface, Terrestrial Time (TT) is a scaled timescale, meaning that it is defined with respect to TCG with a fixed, conventional frequency ratio L_G . Its purpose is to account for the effect of the geopotential and provide a convenient timescale to realize on the surface, i.e. where the clocks actually are. TDB has also been defined as a scaled version of TCB, so that the difference between TDB and TT contains only periodic terms and remains lower than 2 milliseconds.

The Temps Atomique International (TAI), which is the basis for Universal Coordinated Time (UTC), is a realization of TT : this timescale is calculated *a posteriori* every month by the BIPM, by

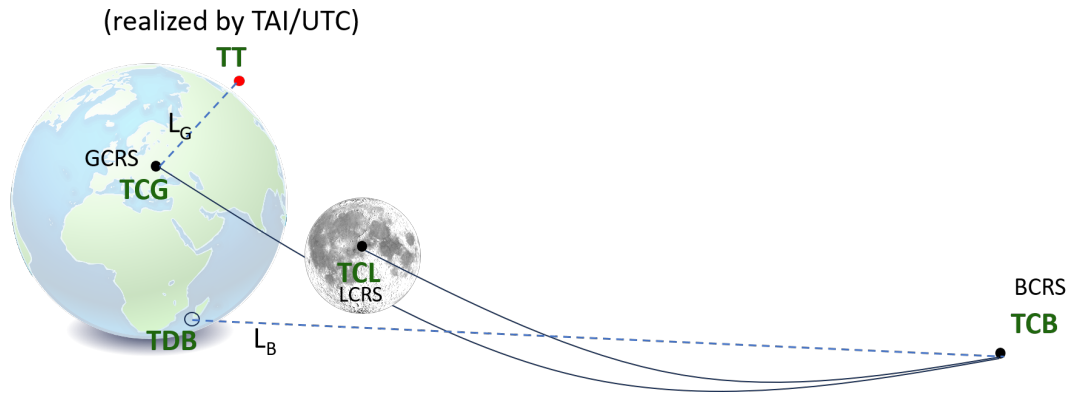


Figure 2: A brief reminder about Coordinate time scales defined by the IAU, and their relations (full line corresponding to 4-dimensional transformations, while dashed lines are for linear transformations)

comparing around 450 atomic clocks around the world (Échelle Atomique Libre or EAL) and steer it using a dozen of primary and secondary frequency standards, i.e. cold atoms atomic fountains. As these standards are situated at different geopotential heights, there is a residual effect that has to be corrected for them to tick at the same rate, but the first order effect is identical and it is therefore convenient to choose a common frequency close to the “natural” one.

The difference between the coordinate time (TCG) for the CGRS and the coordinate time (TCL) at the center of the LCRS can be computed from their differences to the TCB, as in the IAU conventions, considering also that the Earth-Moon system is in free fall around the Sun. The general form of such estimate over two years is represented on figure 3. We observe a linear term of $\simeq -1.5\mu\text{s}/\text{d}$, plus some additional periodic terms with the main period corresponding to the orbital period of the Moon around Earth.

It is tempting to define a similar “Lunar Time” (LT) time scale, following the same principle as TT, and providing a useful time reference for clocks on the Moon. This would require defining a reference equipotential close to the Moon surface, and fixing an associated scaling factor from TCL to LT. The difference between the scaled coordinate time scales LT and TT would have the same periodic terms as shown in Figure 3, but with a linear term of $\simeq 57\mu\text{s}/\text{d}$. The magnitude of these frequency differences is clearly a non-negligible effect for most navigational purposes.

3.3 Consequences on the practical realization of a lunar timescale

In practice, the only clock data you can play with are clock comparisons. These clocks can be co-located or remotely distributed. Ideal clocks tick their proper time, and all we can do to synchronise them (within a certain synchronisation convention) is to perform time transfers between clocks and apply some frequency correction to each clock to align them on a common reference.

Some orders of magnitude arise from the simple models we studied:

- Close to the Moon surface, two clocks at rest will exhibit a frequency offset proportional to their altitude with a factor $\simeq 1.8 \times 10^{-17}/\text{m}$ (about 5 times less than the corresponding effect on Earth).
- Comparing a clock on the Moon surface to a clock on the Earth surface, we will see a difference of $\simeq 57\mu\text{s}/\text{d}$ as mentioned previously, plus the periodic terms with magnitudes of the order of $0.5 \mu\text{s}$.

In addition, except the primary frequency standard which directly realise the definition of the second, all other clocks have their own drift (not always constant) with respect to the ideal time

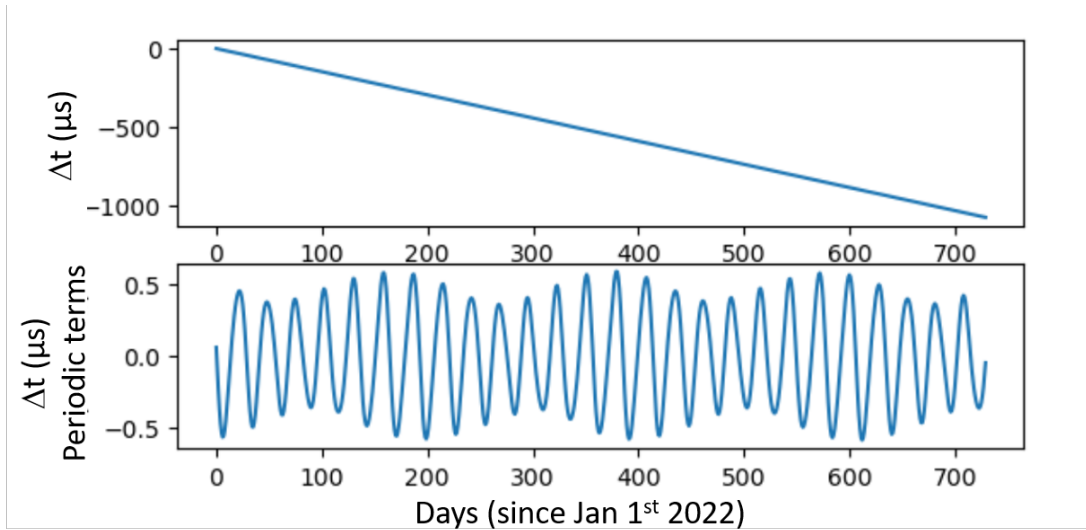


Figure 3: Top: differences between TCL and TCG over two years. Bottom: differences between TCL and TCG after removing the linear drift.

scale ticking the SI second. This drift can be corrected by a frequency offset to align the clock on the reference, and this correction can be achieved either physically (e.g. by using a microphase stepper) or in post-processing, by adding a correction when comparing it to other clocks. It is therefore largely conventional to decide where to introduce the frequency corrections, but it may also be linked to practical issues when such a correction has to be disseminated. When comparing two clocks, it is usually preferred that the bulk of the time difference is already removed, and that the comparison output stays small. As an example, the difference between the proper time of a GNSS clock in orbit around the Earth and a clock on the geoid is mainly a linear drift of $\simeq 38\mu\text{s}/\text{d}$, to which are added the clock own frequency bias and variations. In order to keep only small differences between these clocks and the GNSS reference time (which is close to UTC), their onboard frequency is adjusted to remove the frequency bias with respect to the GNSS reference time scale. The first correction certainly corrects for the main relativistic effect, while further corrections will compensate possible clock deterministic effects, depending on the clock stability.

3.4 A proposal

We suggest to define Lunar Time (LT) such that $LT = TCL + \Delta f(t - t_0)$, with Δf being the linear term between TCL and TT. In this option, the difference between LT and TT would be only periodic terms, averaging to 0 over a to-be-defined period. The origin t_0 would be anytime where the periodic terms equal zero, and there would be no long-term divergence between LT and TT. Practically, this means that the clocks in the vicinity of Moon surface should have their average frequency aligned on $f(\text{UTC})$. There is no need to fix a value for the Δf as all clocks would be steered on UTC, using Earth-Moon communication. This is similar to what we do on Earth for clocks on board GNSS satellites, as mentioned in previous section.

Alternately, we could introduce a conventional term that embeds this frequency difference, e.g. $LT = TCL + L_L(t - t_0)$ with L_L being determined by theory and fixed by convention, so that the Lunar Time ticks the SI second on a given selenoid (L_L would then be the Moon-equivalent of the L_G scaling factor between TCG and TT for the Earth). Clocks in the vicinity of the Moon surface would then have their average frequency aligned on LT, and would have a frequency bias with respect to UTC of $\Delta f - L_L$.

Both options would require numerical corrections for the periodic terms, to be calculated from

ephemeris for any link between the Moon and the Earth. It remains to be seen how far the agreement between the various ephemeris would go, and how often they would have to be updated. In our view, the first solution would allow LT to stay always close to UTC i.e. within the amplitude of the periodic terms. For some future users on the Moon requiring moderate precision lower than about $0.5 \mu\text{s}$, any clock realizing LT would directly serve as a proxy of UTC. On the opposite, the second solution would mean that LT drifts away from UTC quite rapidly, and it would require fixing a time scale origin t_0 for LT, as well as a value for L_L . Furthermore, a value for Δf should be fixed as well, especially as long as there is no clock on the Moon, and only UTC (or more precisely some realization of UTC, named UTC(k)) can serve today for a realization of LT. For any practical purpose that involves interaction with earth-based clocks, a correction for the difference LT-UTC should be considered in particular there would be no direct interoperability with Earth's GNSS which are aligned on UTC. It would however be more tightly connected to the Lunar Celestial Reference system.

4. CONCLUSION

This talk took place at a very early stage of reflection on this issue. It is clear that, rigorously speaking, there is no way to define a coordinate time where clocks on Earth and in cislunar environment can remain synchronized. However we will have to eventually find a practical approach that will be close enough to allow PNT services to operate around the Moon, and possibly around other bodies of the Solar System, while keeping a useful link with the references (which, so far, are Earth-bound). More work is needed to further understand the issues, and some of it has been sparked by the discussions during these Journées.

5. REFERENCES

- Israel, D.J., et al., 2020, "Lunanet: a flexible and extensible lunar exploration communications and navigation infrastructure.", 2020 IEEE Aerospace Conference, pages 1–14
- Soffel, M., et al., 2003, "The IAU 2000 resolutions for astrometry, celestial mechanics, and metrology in the relativistic framework: Explanatory supplement. ", AJ , 126(6):2687, doi: 10.1086/378162

THE CARTOGRAPHIC LUNAR REFERENCE FRAME

B. Archinal¹, A. Conrad², T. Duxbury³, D. Hestroffer⁴, L. Jorda⁵, R. Kirk¹, S. Klioner⁶, J.-L. Margot⁷, J. Oberst⁸, F. Paganelli⁹, J. Ping¹⁰, K. Seidelmann¹¹, D. Tholen¹², I. Williams¹³

¹ U. S. Geological Survey, Astrogeology Science Center, USA, barchinal@usgs.gov

² Large Binocular Telescope Observatory, USA, aconrad@lbto.org

³ George Mason University, USA, tduxbury@gmu.edu

⁴ PSL IMCCE, Observatoire de Paris, Univ. PSL, CNRS, France, hestro@imcce.fr

⁵ Laboratoire d'Astrophysique de Marseille, France, laurent.jorda@lam.fr

⁶ Technische Universität Dresden, Lohrmann Observatory, Germany, Sergei.Klioner@tu-dresden.de

⁷ University of California, USA, jlm@epss.ucla.edu

⁸ DLR Berlin Adlershof, Germany, juergen.oberst@dlr.de

⁹ National Radio Astronomy Observatory, USA, fpaganel@nrao.edu

¹⁰ National Astronomical Observatories of CAS, China, jsping@bao.ac.cn

¹¹ University of Virginia, USA, pks6n@virginia.edu

¹² University of Hawaii, USA, tholen@ifa.hawaii.edu

¹³ Queen Mary University of London, UK, I.P.Williams@qmul.ac.uk

Abstract. We describe how lunar cartographic coordinates are currently determined internationally, based on recommendations of the International Astronomical Union (IAU) Working Group on Cartographic Coordinates and Rotational Elements. Currently, a mean Earth/polar axis (ME) system-based frame and ephemeris (JPL DE 421 ME) is used for that purpose. Recently, there has been some discussion that a lunar principal axis system-based frame should be used instead. We describe how that would be a major change to how lunar data are currently acquired, and how data and mapping products are created and archived, searched for, accessed, and used, and our concerns that such a change would cause significant problems. Existing lunar data, data products, papers, and databases could need to be converted, or substantial confusion could result due to the ~ 1 km difference between systems, perhaps resulting in navigation or safety issues. The publication and dissemination of any proposal(s) to change systems is encouraged, as are comments on a comparatively much smaller update to the current ME frame proposed here.

1. Introduction

We describe here, and give our rationale for questioning, recent discussions to make a fundamental change to how coordinates are defined on the Moon that would alter feature coordinates at roughly the kilometer level. The Lunar Reference System, Lunar Reference Frame (LRF), and lunar orientation model currently used internationally for lunar mapping have been recommended for use by the IAU Working Group on Cartographic Coordinates and Rotational Elements (WGC-CRE) [Davies et al., 1980; Archinal et al., 2011 and 2017], of which we are the members. The current recommendation is to use a ME system-based frame (defined below) to define the orientation and therefore the cartographic frame for the Moon. As described below, the ME system has been used for essentially all lunar mapping since the 18th century. The adoption of this system and the currently used frame are a standards success story that is literally foundational (both

practically and following the spatial data infrastructure definition [Laura et al., 2017]) to all lunar mapping, with little to no known confusion as to which system lunar cartographic products are in. We have heard anecdotally that many users are not even aware that an alternate system exists. Both the NASA Artemis III SDT report [NASA, 2020], the NASA LEAG-MAPSIT LCDP SAT report [LEAG-MAPSIT SAT, 2021], and a white paper produced by the NASA Lunar Exploration Analysis Group [Archinal et al., 2023d] have endorsed the continued use of the ME system for lunar mapping and included recommendations for making minor updates to the specific ME frame that is currently used.

Several groups, including the U. S. National Geospatial-Intelligence Agency (NGA), NASA, and ESA, are considering whether to use the principal axis (PA) system-based reference frame (again, defined below) for lunar mapping as part of their work to develop a lunar reference system [Garner, 2023]. Informal meetings were held to discuss this topic on June 7 and July 19, 2023. So far, however, other than being PA system-based, there does not appear to be a specific published proposal outlining the modalities on how any new frame would be created, updated, or used for cartographic purposes, nor what the benefits, if any, such a change will support.

Using a PA system-based frame for cartography would be of great concern, as nearly all lunar cartographic data and products are currently in an ME frame. Switching between systems would necessitate at some point, either soon or whenever used in the future, converting the needed lunar data and related documentation. Users would need to take caution and be aware that all scientific papers and lunar databases that cite the locations of features on the Moon would include out-of-date coordinates.

Here we briefly describe the two different systems, the relevant frames in those systems, and some of the many issues that would arise if there were a need to use and/or convert data and products from an ME to a PA frame. Many lunar missions, data sources, and massive amounts of data involved would need to be considered, including the steps that would be needed to change frames. Confusion would also result when data and products exist for some time, if not forever (such as in published scientific papers at least), in two different frames, and there would be increased difficulty in processing or using lunar data.

Separately, we also consider the Artemis III SDT report, the LEAG-MAPSIT LCDP SAT report, and the LEAG white paper recommendations to make (comparatively minor) updates to the existing recommended ME frame. This paper follows up on earlier abstracts and presentations made by the WGCCRE on this topic [Archinal et al., 2023a, b, and c].

2. Background

The terms “coordinate system” and “coordinate frame” are often used interchangeably but in this situation have specific meanings. We forego giving a detailed explanation, but briefly, a coordinate system is an overall concept, including theory and conventions to form an idealized coordinate model. A coordinate frame is a specific realization of a system, e.g., a solution that, using data, defines point coordinates. Two different systems have long been in use for the Moon. These are the Mean Earth/polar axis (ME, sometimes MER for Mean Earth/Rotation) and the Principal Axis (PA) systems. In brief, ME is defined by having 0° longitude in the mean direction of the Earth and an equator defined by the mean direction of the lunar pole, whereas PA is defined by the axes of the principal moments of inertia of the Moon (e.g., see Archinal, et al., [2018]). Since the Moon is not truly a synchronously rotating triaxial ellipsoid, the PA and ME rotation axes do not coincide. The axes of the two systems differ by about 1 km at the lunar surface [LRO Project and LGCWG, 2008].

Since the 18th century, the ME system has been used for lunar mapping [Davies and Colvin, 2000], while the PA coordinate system has been used specially for dynamical studies in areas such as gravity field determination and lunar laser ranging (LLR). The difference between the ME and

PA systems/frames has a maximum of 875 meters with components in both longitude and latitude. The difference varies depending on location but is usually at least several hundred meters. The WGCCRE has recommended the use of the ME system for cartography since its initial report [Davies et al., 1980]. More recently, the Lunar Reconnaissance Orbiter (LRO) mission and the Lunar Geodesy and Cartography Working Group (LGCWG) [LRO Project and LGCWG, 2008] recommended the use of the JPL DE 421 ephemeris, rotated into the ME system and therefore an ME frame, as the basis for mapping. However, for specific applications internal to the LRO Instrument Science Operation Centers (SOCs) or elsewhere, the Principal Axis (PA) lunar reference system was allowed. This allowance came with the requirement for all SOC products to be archived in the Planetary Data System (PDS) be converted to the ME system prior to transmission to the PDS [LRO Project and LGCWG, 2008]. The LGCWG included representatives from NASA, ESA, China, India, Japan, and the UK. The WGCCRE accepted their input and made the same recommendation [Archinal et al., 2011 and 2018]. To our knowledge the ME system and frame as recommended by the LRO mission, the LGCWG, and the WGCCRE is in use by all space agencies worldwide for lunar mapping. We are unaware of any published issues with using the ME frame for such mapping.

During the June 7, 2023, meeting some questions were raised regarding the relative accuracy of any PA frame vs. a ME frame. As explained above, these systems and their associated frames serve two different purposes, so any claim that one is more accurate than the other is an unmerited comparison. Still, it should be made clear that the frames such as those associated with the currently recommended and used JPL Lunar Laser Ranging (LLR) solutions and ephemerides are exactly the same internally, since the PA and ME frames differ only by a global rotation. Distances and angles measured in those frames are invariant to each other. The global rotation was derived to satisfy the need for the ME (cartographic) frame to be initially referenced to the mean direction of the Earth and mean pole of the Moon. Successive updates to the ME frame, such as that associated with the JPL DE 440 LLR solution and ephemeris [Park et al., 2021] incorporate a no-net rotation (from the DE 421 ME frame) condition so that changes in lunar surface coordinates are minimized. This process is similar to that used for updating the International Terrestrial Reference Frame (<https://www.iers.org/IERS/EN/DataProducts/ITRF/itrf.html>), in order to minimize changes in coordinates for the Earth. Successive PA frames (currently) have no such condition imposed so coordinates of lunar features will have larger changes. Due to the no-net rotation condition, the RMS difference between the DE 421 and DE 440 LLR ME frames is 9 cm, while the RMS difference between the old and new PA frames (which do not have such a condition enforced) is 29 cm. It should be noted that Laurenti, et al. [2022] advocated using a PA frame for purposes related to a “lunar radio navigation system”, making the point that orbit propagation should, of course, normally be done in a PA frame, since lunar gravity field data are derived in the PA system. However, it was also noted that positions in an ME frame will be needed for use with cartographic products.

3. Issues with changing the cartographic system

The use of a PA rather than a ME system-based frame for cartography could necessitate making significant changes to all existing lunar mapping data, data products, and lunar databases, thus introducing confusion in their use. Here we briefly highlight some (but not all) of the major issues involved.

Technically, it might be possible to relabel existing datasets with new coordinates to account for this shift. However, current lunar datasets are massive. For example, 65 percent of the NASA Planetary Data System holdings are LRO data [Petro and Banks, 2023]. That dataset is a few petabytes in size, including millions of images and billions of lidar measurements. The LRO Camera system alone has provided approximately 3.5 million images and 1.5 petabytes of data

(personal comm., e-mail of 2023 April 24 from Trent Hare), and this does not account for other U.S. and international lunar missions. Since the frame difference is a 3-axis rotation, mapping products cannot simply be made by shifting pixels, but would have to be individually reprojected and resampled. Such an effort would be huge, and in many cases difficult or impossible, as the originators of many mapping products either are no longer available or would not have the resources to recreate and document these products. Products such as digital terrain models would lose some level of accuracy and precision during resampling, so would either have to be recreated or have versions kept in both frames to allow for analysis at full resolution. The scale of such conversion work is so large that it would likely take a substantial effort just to estimate what associated personnel, software, and funding would be needed to make it happen.

A perhaps bigger issue is the resulting confusion over which system/frame a cartographic product will be in. There are few datasets or cartographic products in a PA frame. The only product known to us is a particular LRO LOLA Gridded Data Record Shape Map, the file, LDEM_64_PA.IMG, a 16 pixels/degree (1.895 km/pixel) lunar shape model in a PA system-frame, available from the PDS (https://ode.rsl.wustl.edu/moon/pagehelp/Content/Missions_Instruments/LRO/LOLA/GDR/GDRDEM.htm). (There may be some maps that have been made of the lunar gravity field in the PA frame, but the current resolution of such fields is less than the difference between the two systems). As recommended by the LCDP SAT report [LEAG-MAPSIT SAT (2021); Finding 4], which system and frame is in use for any lunar mapping product should be documented. However currently, users confidently assume that their data and/or products are in an ME system, if not specifically the currently recommended ME frame. When such products start to be placed in a PA frame, users will always be required to check carefully which frame their data is in. Otherwise, there will be an increased likelihood that confusion could result in using incorrect coordinates for attempting landings and doing surface operations (including for search and rescue), resulting in serious or even catastrophic situations.

Finally, an open question is whether any “new” standard will be accepted by others. The reports of the WGCCRE recommend that as reference frames are updated the change should be as small as needed [Archinal et al., 2018, p. 7]. A switch from using the ME to the PA frame for cartography by the groups previously cited as considering such a change (NGA, NASA, and ESA, or components of those organizations) would not seem to meet that recommendation. Individual space agencies, including all of those represented on the LGCWG, have accepted the use of the ME frame for cartography, may or may not wish to change. So once started, the use of both systems for cartography could continue indefinitely. This too could result in navigation and safety issues.

Given these issues and the lack of any published material outlining the benefits supporting such a change, we argue that a ME system-based frame should continue to be used for cartographic purposes. PA system-based frames can continue to be used for dynamical purposes, and the relationships between these frames should continue to be derived or defined. If, perhaps, there is a strong desire to use only one system, it should be feasible to convert any desired gravity field to the current ME-based frame and use it to do orbital calculations in that frame. Changing one or a few gravity field models would likely engender far less effort and cause far less confusion than converting millions of lunar data products, billions of data records, and all existing lunar databases and published papers containing lunar coordinates information.

4. Further issues to consider

Next, we consider the comparatively less serious and much smaller in effect topic of making minor updates to the current cartographic LRF recommendations. The Moon is one of few bodies in the Solar System without a specific longitude-defining surface feature. After many years of discussion, it may be time to finally use a LLR solution to define the LRF, following long-standing

IAU and WGCCRE recommendations [ibid.]. Currently, a particular LLR solution is already the underlying basis for the DE421 ME frame, and the coordinates of such a solution define the frame by default. So, such a solution and future improved solutions could instead serve to directly define the frame in the ME system, and in practice would match in a no-net rotation sense to the existing recommended DE421 ME frame. This would formally separate the definition and recommendation of the body fixed lunar reference frame (including the direction of the lunar prime meridian) from that of a lunar orientation model alone.

Separately, the cartographic lunar orientation model could now be specified by using the JPL DE440 ephemeris in the ME frame [Parks et al., 2021]. The new JPL solutions use substantially more available data and improved modeling compared to the previous (2008) DE421 solution. Differences from the previous model are < 1 meter during the period 1900–2050. See e.g., Figure 1 in Archinal et al. [2023a]. Differences in the underlying LLR solutions are < 1.5 meters. Such differences are unlikely to be noticeable in the positioning of data products except at the highest current levels of accuracy. This update would nevertheless help to prepare for the best future accuracy, by reducing one source of error.

The current JPL products are the most likely data sources for updating the lunar frames (both ME and PA) in the near term. Eventually, updates would need to consider LLR solutions and ephemerides from other sources, possibly in some sort of combined solutions.

5. Recommendations

If serious consideration is being given to proposing that lunar mapping be done in a PA system-based frame rather than with a ME system-based frame as currently, it would be useful to see a published proposal describing the modalities so that the WGCCRE and the international lunar community could consider it. It would be useful to know which PA frame would be used and how it would be updated. It would also be useful to hear about the benefits of such a change relative to the significant problems it would cause (as partially discussed above). Given the near universal use of a ME system-based frame currently for mapping, various groups should be asked to consider such a proposal and provide input. This could include the various U.S. organizations that may be involved, international space agencies, and various international organizations, such as the International Astronomical Union, the International Association of Geodesy, and the International Planetary Data Alliance. In addition, as previously recommended by the WGCCRE [Paganelli et al., 2020] and others, an international group, perhaps similar to the LGCWG, or an international lunar SDI working group (e.g., see Hunter et al. [2023]) should be formed to coordinate lunar coordinate system and mapping issues. Feedback would also be useful on the value of making the described minor updates to the existing ME system LRF. A recommendation to update the existing ME frame definition is something the WGCCRE hopes to decide on and likely publish by the end of this year.

Acknowledgments

Archinal has received funding via the NASA-USGS Planetary Spatial Data Infrastructure Inter-agency Agreement. We appreciate the important work of Park et al. [2021] in providing improved lunar ephemerides and frames.

6. References

Archinal, B. A., A'Hearn, M. F., Bowell, E., Conrad, A., Consolmagno, G. J., Courtin, R., Fukushima, T., Hestroffer, D., Hilton, J. L., Krasinsky, G. A., Neumann, G., Oberst, J., Seidelmann, P. K., Stooke, P., Tholen, D. J., Thomas, P. C., and Williams, I. P., 2011, "Report of the IAU Working Group on Cartographic Coordinates and Rotational Elements: 2009," *Celest.*

- Mech. Dyn. Astr. , 109, no. 2, February, pp. 101-135, <https://doi.org/10.1007/s10569-010-9320-4>.
- Archinal, B. A., Acton, C. H., A'Hearn, M. F., Conrad, A., Consolmagno, G. J., Duxbury, T., Hestroffer, D., Hilton, J. L., Kirk, R., Klioner, S. A., McCarthy, D., Meech, K., Oberst, J., Ping, J., Seidelmann, P. K., Tholen, D. J., Thomas, P. C., and Williams, I. P., 2018, "Report of the IAU Working Group on Cartographic Coordinates and Rotational Elements: 2015," *Celest. Mech. Dyn. Astr.* , 130:22, <https://doi.org/10.1007/s10569-017-9805-5>.
- Archinal, B., and the IAU Working Group on Cartographic Coordinates and Rotational Elements, 2023a, "Considerations On Updating the Lunar Reference Frame," 54th Lunar and Planetary Science Conference, March 13-17, The Woodlands, TX. Abstract #2305, <https://www.hou.usra.edu/meetings/lpsc2023/pdf/2305.pdf>. Poster available at <https://lpsc2023.ipostersessions.com/default.aspx?s=68-FA-6C-24-D5-C1-58-83-3A-BB-25-67-C9-C2-97-A6>.
- Archinal, B., and the IAU Working Group on Cartographic Coordinates and Rotational Elements, 2023b, "Updating the Lunar Reference Frame," European Geosciences Union General Assembly 2023, April 23-28, Vienna, Austria. Abstract #EGU23-9136, <https://meetingorganizer.copernicus.org/EGU23/EGU23-9136.html>.
- Archinal, B., and the IAU Working Group on Cartographic Coordinates and Rotational Elements, 2023c, "Lunar Reference Frame Considerations," 6th Planetary Data Workshop, June 26-28, Flagstaff, AZ, <https://www.hou.usra.edu/meetings/planetdata2023/>. Abstract #7095. Available at <https://www.hou.usra.edu/meetings/planetdata2023/pdf/7095.pdf>.
- Archinal, B., Fassett, C., Gaddis, L., Hare, T., Malaret, E., Ostrach, L., and Park, R., 2023d, "Continued Use of the Mean Earth Coordinate System for the Moon," a white paper produced at the request of the NASA Lunar Exploration Analysis Group. Available as https://www.lpi.usra.edu/leag/reports/ME-White-Paper_Final.pdf.
- Davies, M. E., Abalakin, V. K., Cross, C. A., Duncombe, R. L., Masursky, H., Morando, B., Owen, T. C., Seidelmann, P. K., Sinclair, A. T., Wilkins, G. A., and Tjuflin, Y. S., 1980, "Report of the IAU Working Group on Cartographic Coordinates and Rotational Elements of the Planets and Satellites," *Celest. Mech.* 22, pp. 205-230, <https://adsabs.harvard.edu/full/1980CeMec..22..205D>.
- Davies, M. E., and Colvin, T. R., 2000, "Lunar coordinates in the regions of the Apollo landers," *J. Geophys. Res.* , 105, no. E8, pp. 20,277-20,280, August 25, <https://doi.org/10.1029/1999JE001165>.
- Garner, T., 2023, "Developing a Lunar Reference System for Navigation Safety," ION ITM, <https://www.ion.org/itm/abstracts.cfm?paperID=10769>.
- Hunter, M. A., Laura, J. R., Archinal, B.A., Keszthelyi, L., Stopar, J.D., Beyer, R.A., Petro, N. E., and Lawrence, S. J., 2023, "Lunar Spatial Data Infrastructure and Proposed Standards to Support the Mapping Community," Lunar Surface Science Workshop Virtual Session 20: Geological Mapping to Support Artemis Strategic Decisions, August 16-17. Available at <https://www.hou.usra.edu/meetings/lunarsurface20/pdf/5010.pdf>.
- Laura, J. R., Hare, T. M., Gaddis, L. R., Ferguson, R. L., Skinner, J. A., Hagerty, J. J., and Archinal, B. A., 2017, "Towards a Planetary Spatial Data Infrastructure," *ISPRS Int. J. Geo-Inf.* 2017, 6, 181. Available from <http://www.mdpi.com/2220-9964/6/6/181/pdf>.
- Laurenti, M., Stallo, C., Bellardo, V., Marty, J.-C., Giordano, P., Zoccarato, P., Schoenemann, E., Swinden, R., and Traveset, J. V., 2022, "Reference Frames Analysis for Lunar Radio Navigation System," ION ITM, 606, <https://doi.org/10.33012/2022.18170>.
- LEAG-MAPSIT SAT, 2021, "Final Report of the Lunar Critical Data Products Specific Action Team," Available as https://www.lpi.usra.edu/mapsit/reports/leag_mapsit_report_2022-01-11.pdf.

- LRO Project and LGCWG, 2008, "A Standardized Lunar Coordinate System for the Lunar Reconnaissance Orbiter and Lunar Datasets," Version 5, October 1, <http://lunar.gsfc.nasa.gov/library/LunCoordWhitePaper-10-08.pdf>.
- NASA, 2020, "Artemis III Science Definition Team report," NASA/SP-20205009602, <https://www.nasa.gov/sites/default/files/atoms/files/artemis-iii-science-definition-report-12042020c.pdf>.
- Paganelli, F., Archinal, B. A., Acton, C. H., Conrad, A., Duxbury, T. C., Hestroffer, D., Hilton, J. L., Jorda, L., Kirk, R. L., Klioner, S. A., Margot, J.-L., Oberst, J., Ping, J., Seidelmann, P. K., Tholen, D. J., and Williams, I. P., 2020, "The Need for Recommendations in Support of Planetary Bodies Cartographic Coordinates and Rotational Elements Standards," submitted to the Planetary Science and Astrobiology Decadal Survey White Paper 2023-2032, <https://is.gd/WGCCRE2020wp>.
- Park, R. S., Folkner, W. M., Williams, J. G., and Boggs, D. H., 2021, "The JPL Planetary and Lunar Ephemerides DE440 and DE441," *AJ* 161(3), 105, <https://doi.org/10.3847/1538-3881/abd414>.
- Petro, N. E., and Banks, M. E., 2023, "The Lunar Reconnaissance Orbiter and her Data: Paving the Way for Artemis III and Beyond," oral presentation by Banks, LSSW Workshop, April 4, Abstract #2015, <https://www.hou.usra.edu/meetings/Artemis.III.2023/pdf/2015.pdf>.

LUNAR DECLINATION ANGLE WITH GLOBAL GREAT EARTHQUAKES

H. Hu¹, K. Tang²

¹ Yunnan Observatory, Chinese Academy of Science, Kunming 650216 - P.R. China - huhui@mail.ynao.ac.cn

² Shanghai Astronomical Observatory, Chinese Academy of Science, Shanghai 200030 - P.R. China

ABSTRACT. In this paper, $M \geq 7.0$ earthquakes occurred in the world during the period of 1900 to 2011.6, namely, six 18.6 year cycles, are selected. According to plate tectonics, these earthquakes are divided into 13 research region, and their relationship with the lunar declination angle is analyzed. The research results show that any seismic activity period of each research region corresponds to a certain interval of lunar declination angle. These provide a scientific basis for the future mid-to-long-term earthquake trend prediction in each research region. It is worth further study.

1. INTRODUCTION

The moon is the closest celestial body to the earth. Therefore, people have always attached great importance to the study of the moon. The changes in the tidal force of the sun and the moon are widely used at home and abroad as an important factor in studies of seismic activity, and different analysis methods are used to discuss the relationship between the tidal force of the sun and the moon and earthquakes from various angles. More and more analyses show that the earthquake occurrence is related to the combined changes in tidal force of the sun and the moon. Some use the tidal force of the sun and the moon to study the triggering mechanism of a certain area or an earthquake (Tsuruoka et al. 1995, Heaton 1982, Palumbo 1986, Rydelek et al. 1992, Gao et al. 1981). Some even use the loading and unloading effects of the sun and moon tidal forces on faults to make medium-shore earthquake predictions. However, these studies mainly involve only such as the month tide, semi-month tide, diurnal tide and semi diurnal tide etc. short-period term astronomical factors, and the scope of the research is generally an earthquake or earthquakes in a certain area. Luan Juqing and his grandfather summed up the Yangtze and Yellow River'correspond regions of the lunar declination by observing the sky, and used it for long-term weather forecasting and earthquake prediction (Luan 1988). Some authors analyzed from different angles, and obtained the lunar declination angle is an important astronomical factor affecting natural disasters (Yang et al. 2014).

The so-called lunar declination angle is the obliquity of the moon's orbit (moon's path) to the equator. The moon's orbit around the earth is called the moon's path, which intersects the ecliptic at two points. The point where the moon moves on the moon's path from the south of the ecliptic to the north of the ecliptic is called the ascending node, and the opposite point is called the descending node. The angle of intersections between the moon's path and the ecliptic varies between $4^{\circ}57'$ and $5^{\circ}19'$, with an average value of about $5^{\circ}9'$. Because the gravitational force of the sun on the moon, the line of the two intersection points (the line of intersection) moves westward along the direction opposite to the direction of the ecliptic and the moon. As a result, the moon does not return to its original position after making a full circle. The phenomenon that the intersection line moves westward is called the intersection retreat. The line of intersection

moves $19^{\circ}21'$ every year, completing a period in about 18.6 years, which causes changes in the declination and declination angle of the moon. When the lunar ascending node coincides with the vernal equinox, the ecliptic is located between the moon's path and the equator, and the intersection angle between the moon's path and the equator is the sum of the ecliptic-equator intersection angle and the ecliptic-moon's path intersection angle; when the lunar descending node coincides with the autumnal equinox, the moon's path is located between the equator and the ecliptic. The angle between the moon's path and the equator is the difference between the ecliptic-equator intersection angle and the ecliptic-moon's path intersection. Therefore, the lunar declination angle (that is, the angle of intersection between the moon's path and the equator) varies from 28.60° (that is, $23.45^{\circ} + 5.15^{\circ}$) to 18.30° (that is, $23.45^{\circ} - 5.15^{\circ}$), and the change period is about 18.6 years. It is the lunar declination angle that controls the latitude range of the moon at the point of direct radiation on the earth's surface. Therefore, this paper focuses on the influence of lunar declination angle on global great earthquakes by calculating the lunar declination angle.

Because the change cycle of the lunar declination angle is 18.6 year. In order to ensure the reliability and accuracy of the analysis results, this paper selects six consecutive 18.6 year cycles (i.e. from 1900.0 to 2011.6) of global $M \geq 7.0$ earthquakes, and according to the fact that global earthquakes are mainly distributed on plate boundaries and the distribution of plates, we divide global earthquakes into 13 research region for such research (see Figure 1).

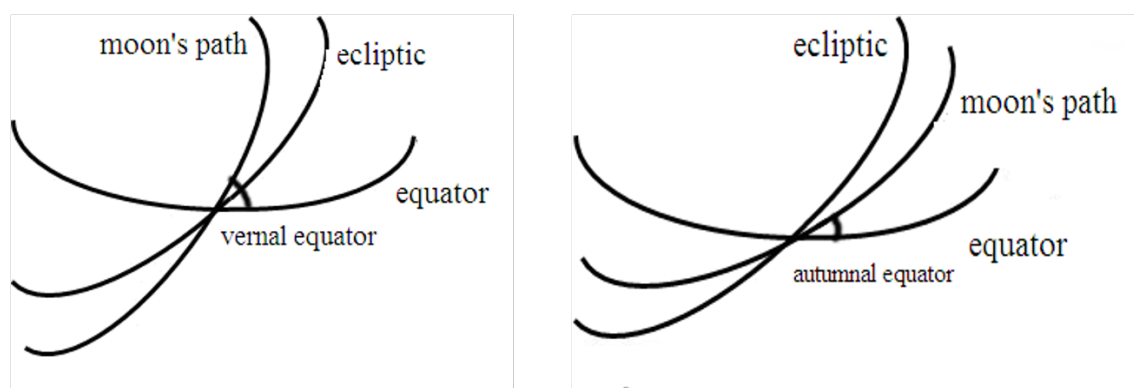


Figure 1: Schematic diagram of when lunar ascending node coincides with the vernal equinox and autumnal equinox respectively.

2. INTRODUCTION TO DATA AND RESEARCH METHODS

2.1 Earthquake data

According to Engdahl's research, the catalogue of $M \geq 7.0$ earthquakes since 1900.0 is complete and reliable. Therefore in this paper the seismic data of 1900.0-2000.0 used is taken from the catalogue of earthquakes he compiled (Engdahl et al., 2002), latter part is taken from the advanced national seismic system network of the United States *. During the period of 1900.0-2011.6 (August 2011), there were 1728 earthquakes with $M \geq 7.0$ in the world.

2.2 Research methods

In this paper, the method of analyzing the lunar declination angle and random data is used to study the correlation between the lunar declination angle and $M \geq 7.0$ earthquakes. Because the moon is perturbed by many celestial bodies, its orbital changes are extremely complicated, so the

*<http://earthquake.usgs.gov/earthquakes/search>

numerical integration can only be used (Van Flandern and Pulkkinen, 1979). Here are only a few calculation formulas related to the analysis:

$$\begin{aligned} f_1 &= \frac{NK}{20.6}, \\ f_2 &= \frac{N(20.6-K)}{20.6}, \end{aligned} \quad (1)$$

$$\chi^2 = \frac{(n-f_1)^2}{f_1} + \frac{(N-n-f_2)^2}{f_2}. \quad (2)$$

Equation (1) is to calculate the expected frequency f_1 and f_2 of the earthquake for active period and inactive period of each studied region. K is the length of the active period, the units of K and 20.6 are degrees, and N is the total number of samples in the study region. Equation (2) is to calculate the χ^2 , that is, the sum of the squares of the deviations of the active and inactive periods from their expected values is calculated (Bendat and Piersol 1971).

3. CORRELATION ANALYSIS

According to the above method, calculation, statistics and analysis were carried out according to 13 study regions (see Figure 2). The results are shown in Table 1. According to the χ^2 test theory, under degree of freedom is equal to 1, if $\chi^2 \geq 3.841$, there is a significant level of 95%, and the uniform distribution null hypothesis be rejected, that is, the periodicity of the earthquake concentrated in the above active period is received. The analysis results show that the values of χ^2 listed in Table 1 are all greater than 3.841, so the seismic activity in each study region has a period of 18.6 years. The interval of strong seismic activities is associated with a closed interval of the lunar declination angle in the Table 1.

Since the ascending node of the moon is receding westward on the ecliptic, the lunar declination angle is constantly decreasing. When the lunar declination angle decreases to its minimum value of 18.3, it begins to gradually increase again until 28.6. It gradually decreases again, so the total range of the lunar declination angle is $(28.6 - 18.3) \times 2 = 20.6^\circ$, and so on, with 18.6 years a cycle. For study region 1st, its active period starts from 28.4° and gradually decreases to 23.2°. This activity period ends. When the lunar declination angle decreases to 18.3°, it enters another period of activity, so The active period length of study region 1 $K = (28.4 - 23.2) + (28.3 - 18.3) = 15.1^\circ$. The closed interval of some seismic active periods passes through the minimum value of the lunar declination angle (indicated by min in the Table 1), such as he closed interval of study region 2nd, 5th, 7th, and the 10th study region not only passed the minimum point of the moon's declination angle, but also passes the maximum value of the lunar declination angle (indicated by max).

From Figure 2, we can see that, except for the 1st, 2nd, and 3rd research regions, the remaining 10 research regions all belong to the Pacific Rim seismic zone, so most of the world's earthquakes occur in the Pacific Rim seismic zone. In addition, from Table 1 it can also be seen that when the lunar declination angle increases from 20.7° to 22.1°, only the 2nd study region is not in the seismic activity period; and when the lunar declination angle increases from 18.3° to 20.7°, only the 2nd and 12th study regions is not in the seismically active period; and when the lunar declination angle increases from 25.0° to 25.8°, only the 2nd and 4th study regions are not in the seismically active period. Similarly, when the lunar declination angle decreases from 27.9° to 24.0°, only the 2nd, 3rd, and 12th study regions are not in the seismically active period. It can be seen that this time is the global earthquake-prone period; the rest of the period is the relatively quiet period of earthquakes.

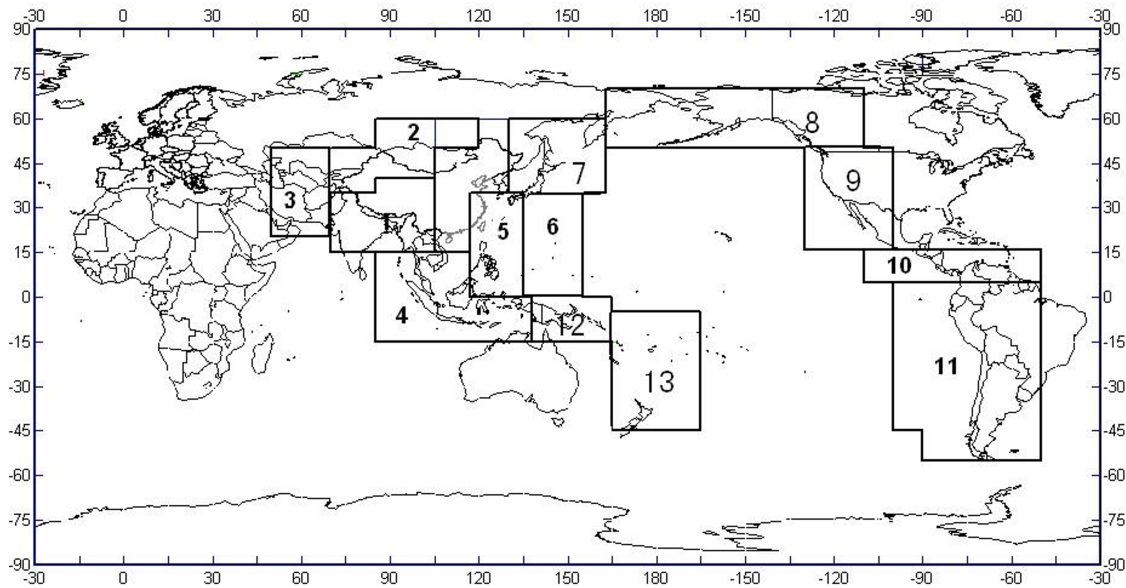


Figure 2: The studied region of 18.6 years recurrence of the great earthquakes in the world.

Table 1: Statistic results of seismic recurrence of 18.6 years of the principal seismic regions in the whole world.

No.	studies region	total	seismic active interval		
			sample	$\alpha(^{\circ})$	χ^2
1	Himalayas and its region	52	49	[28.4 – 23.2, 18.3 – 28.3]	15.0557
2	Mt. Tianshan and Baikal	48	41	[24.0 – <i>min</i> – 28.1]	5.7709
3	Eastern Alps plate	21	12	[18.3 – 25.8]	6.9958
4	Malay Peninsula - Sunda Islands	145	125	[28.2 – 24.0, 18.3 – 28.4]	5.9606
5	Weslern Philipping sea plate	200	169	[28.4 – <i>min</i> – 22.1, 27.9 – 28.4]	5.2289
6	Eastern Philipping sea plate	64	59	[28.2 – 20.4, 18.3 – 28.4]	7.6886
7	Kamchatka- Northeast Japan	204	165	[27.9 – <i>min</i> – 25.8]	7.6262
8	Aleutian - Alaska	90	89	[28.4 – <i>min</i> – 28.3]	6.1455
9	Western United States -North Mexico	51	47	[28.4 – 24.0, 18.9 – 28.1]	6.1008
10	Central America - Caribbean	74	76	[28.4 – <i>min</i> – <i>max</i> – 26.3]	3.9027
11	West of southern America	183	118	[19.7 – <i>min</i> – 22.1, 25.0 – 28.4]	10.0567
12	New Guinea - Solomon	153	110	[27.6 – 19.7, 20.5 – 28.4]	4.2512
13	New Hebrides - Kermadek	268	237	[28.4 – 18.9, 18.3 – 28.1]	5.0179
Total		1553			

4. CONCLUSION

The influence of the moon on the earth is mainly the tidal force. Although the mass of the sun is 27 million times that of the moon, the distance between the moon and the earth is only 1/390 of the distance between the sun and the earth, so the tidal force of the moon is 2.25 times that of the sun (Peng and Lu 1983). The tidal force of the sun and the moon not only causes the sea water on the earth's surface to generate tides, but also deforms the surface and interior of the elastic earth. The internal deformation will cause the redistribution of materials, thus changing the original gravity field of the earth (Melchior, 1978; Fang, 1984). Studies have showed that besides the semidiurnal tide, the diurnal tide and the semilunar tide, there are also 18.6 year lunar node tides, there are also 18.6 year lunar node tides in the moon tides. It is a long cycle tide, and also the longest cycle in the moon movement and the

main nutation cycle of the earth's movement. Studies have proved that the semidiurnal, diurnal tide and semilunar tides play a triggering role in the earthquakes occurrence in some areas (Heaton 1982; Ding. et al., 1983). However, this lunar node tide may not be triggered in the earthquakes occurrence, but participates in the energy accumulation and preparation of earthquakes in the seismic zone by slowly adjusting the Earth's gravity field. It is a cumulative effect increased the accumulation of energy in the seismic zone. Therefore, the influence of the lunar declination angle on the global great earthquake is actually the influence of the lunar node tide. Only the most direct quantity reflecting the change of the lunar node tide is the lunar declination angle. Accordingly, this paper analyzes the correlation between the lunar declination angle and the global great earthquake by calculating the lunar declination angle. It is the lunar declination angle that controls the latitude range of the moon's direct point on the earth's surface. The maximum of the lunar declination angle is 28.6° , so there are no or very few earthquakes in the polar and high latitude regions. The astronomical factor can be calculated and predicted in advance. Therefore, the conclusions drawn by this article can provide a scientific basis for the future mid-to-long-term earthquake trend prediction in each research region. It is worth further study.

5. REFERENCES

- Bendat, J.S., Piersol, A.G., 2011, "Random data: analysis and measurement procedures", John Wiley & Sons.
- Engdahl, E.R., 2002, "Global seismicity: 1900-1999", International handbook of earthquake and engineering seismology, pp.665-690.
- Ding, Z.Y., Jia, J.K., Wang, R., 1983, "Seismic triggering effect of tidal stress", Tectonophysics, 93(3-4), pp.319-335.
- Fang, J., 1984, "Solid Earth Tides", Science Press.
- Gao, X.-M., Yin, Z.-S., Wano, W.-Z., Huang, L.-J., Li, J., 1981, "Triggering of earthquakes by the tidal stress tensor", Acta Seismologica Sinica, 3(3), pp.264-275.
- Heaton, T.H., 1982, "Tidal triggering of earthquakes", Bulletin of the Seismological Society of America, 72(6A), pp.2181-2200.
- Luan, J.Q., 1988, "Motion of celestial object and long-term prediction of weather and earthquakes", Beijing Normal University Press.
- Melchior, P., 1983, "The tides of the planet Earth", Oxford.
- Palumbo, A., 1986, "Lunar and solar tidal components in the occurrence of earthquakes in Italy", Geophysical Journal International, 84(1), pp.93-99.
- Peng, G.B., Lu, W., 1983, "The fourth type of natural factors in climate", Science Press.
- Rydelek, P.A., Sacks, I.S., Scarpa, R., 1992, "On tidal triggering of earthquakes at Campi Flegrei, Italy", Geophysical journal international, 109(1), pp.125-137.
- Tsuruoka, H., Ohtake, M., Sato, H., 1995, "Statistical test of the tidal triggering of earthquakes: contribution of the ocean tide loading effect", Geophysical Journal International, 122(1), pp.183-194.
- YANG, D.-H., YANG, X.-X., 2014, "The relation between ice sheets melting and low temperature in Northern Hemisphere", Progress in Geophysics, 29(2), pp.610-615.
- Van Flandern, T.C., Pulkkinen, K.F., 1979, "Low-precision formulae for planetary positions", The Astrophysical Journal Supplement Series, 41, pp.391-411.

VLBI ASTROMETRY OF RADIO STARS TO LINK RADIO AND OPTICAL CELESTIAL REFERENCE FRAMES

J. Zhang^{1,2}, B. Zhang¹

¹ Shanghai Astronomical Observatory, Chinese Academy of Sciences, 80 Nandan Road, Shanghai 200030, People's Republic of China - zb@shao.ac.cn

² University of Chinese Academy of Sciences, No.19 (A) Yuquan Rd, Shijingshan, Beijing 100049, People's Republic of China

ABSTRACT. The *Gaia* Celestial Reference Frame (*Gaia*-CRF) is aligned to the International Celestial Reference Frame (ICRF) at the faint end ($G > 13$) using quasars, but at the bright end ($G < 13$), there are no available quasars for the alignment. Very Long Baseline Interferometry (VLBI) measurements of radio stars can play a role as an independent assessment at the bright end. Currently, the number of available radio stars (< 100) is much smaller than the number of quasars (thousands), so the focus is on increasing the number of available radio stars. We have observed several stars with conventional five-parameter VLBI astrometry, and more observations are ongoing. Considering that the conventional observing strategy is high-cost, we also propose to observe with a new double-epoch strategy which according to our simulation is $\sim 30\%$ more efficient for CRF link.

1. MOTIVATION

In the era of multi-wavelength astronomy, establishing a celestial reference frame consistent at different wavelengths is a fundamental and important issue. ICRF3 is based on VLBI measurements of extragalactic radio sources, whose position accuracy achieves a level of $\sim 30 \mu\text{as}$ for the best-measured sources (Charlot et al., 2020). In the optical band, *Gaia*-CRF3, defined by quasar-like sources, is aligned to ICRF3 with an accuracy of $\sim 7 \mu\text{as}$ (Gaia Collaboration et al., 2022).

However, there is a systematic rotation of *Gaia* astrometric data between the bright end ($G < 13$) and the faint end ($G > 13$), likely caused by a deficiency in the astrometric instrument calibration model (Lindgren 2020). Radio stars can be detected in both radio and optical bands, and VLBI astrometry of radio stars can give an independent estimation of this systematic rotation. There have been several related works, for example, Lindgren (2020), Bobylev (2022), and Lunz et al. (2023). However, because the number of available radio stars is small (< 100), the estimated rotation parameters are not quite reliable. Therefore, the key is to increase the number of available radio stars. It is worth emphasizing that VLBI observations as close to the *Gaia* reference epoch will contribute more to the estimation of the orientation parameters, therefore it is important to carry out the observations in the most recent years with an efficient observing strategy.

2. DOUBLE-EPOCH OBSERVING STRATEGY

The double-epoch strategy is to observe each radio star for only two epochs, approximately separated by an integer number of years, so that two individual positions can be obtained. The purpose of the integer-year time interval is to cancel out parallactic offsets, so an unbiased proper motion measurement can be obtained. Along with the *Gaia* counterparts, the positions and proper motions can contribute to the estimation of orientation ($\boldsymbol{\varepsilon} = [\varepsilon_X, \varepsilon_Y, \varepsilon_Z]'$) and spin ($\boldsymbol{\omega} = [\omega_X, \omega_Y, \omega_Z]'$)

parameters between two CRFs.

2.1 Simulation for strategy assessment

The double-epoch strategy is assessed and compared with the conventional five-parameter and single-epoch strategies through simulation. The costs of different strategies are kept the same so that they can be compared with each other: 120 epochs in total, 120 stars \times 1 epoch, 60 stars \times 2 epochs, and 20 stars \times 6 epochs for single-epoch, double-epoch, and five-parameter strategies respectively. The epochs of simulated VLBI measurements are between 2023.5 to 2024.5, and the position uncertainties of VLBI measurements are set to be $50 \mu\text{as}$, while *Gaia* DR3 uncertainties are used for optical counterparts.

Results of the simulation are shown in Table 1, which show: (1) the double epoch strategy performs better than the other two strategies ($\sim 30\%$ better than the five-parameter strategy); (2) improvement of the uniformity of sky distribution by adding samples located in the deep-southern sky is helpful to make the uncertainties of CRF link parameters on the three axes more even; (3) Adding 60 new stars with the double-epoch strategy to the “real” data under the specified conditions obtains 25% and 71% lower uncertainties in orientation and spin parameters respectively.

Strategy	dataset	χ_{red}^2	$\sigma_\epsilon (\mu\text{as})$			$\sigma_\omega (\mu\text{as yr}^{-1})$		
			X	Y	Z	X	Y	Z
single-epoch	All	1.080	352.9	458.5	486.8	44.5	57.7	61.7
five-parameter	All	1.032	121.1	156.3	149.2	16.5	21.3	20.7
double-epoch	All	1.080	82.6	101.7	96.3	11.0	13.6	13.1
double-epoch	North	1.084	82.8	117.2	86.6	11.0	15.5	11.7
five-parameter	Real	-	53.0	92.2	41.2	22.5	26.3	25.3
mix	All+Real	1.040	40.2	65.1	33.5	6.0	9.2	6.3

Table 1: Comparison between different observing strategies and datasets. “All” denote the whole simulated dataset, “North” denote the dataset without deep-southern stars, “Real” denote only real data used, and “All+Real” denote combining simulated and real data. χ_{red}^2 denote the reduced chi-square of the solution. σ_ϵ and σ_ω are formal uncertainties of orientation and spin parameters of the solution respectively.

2.2 Practical observing epoch scheduling

The strategy is designed not to be affected by parallax, however, the time interval between the two epochs is practically difficult to be exactly an integer number of years, which will bring parallactic displacement. This displacement is corrected by an offset calculated from *Gaia* parallax ϖ_{Gaia} . Suppose there exists a bias between ϖ_{Gaia} and the “true” parallax ϖ_{true} , the displacement would not be perfectly corrected. This will affect the independence of the CRF link, and reduce the accuracy of the position and proper motion of the radio star.

The trend of the impact of the possible parallax bias with time depends on positions in the sky. For stars far from the Ecliptic, the impact does not vary much with time; While for stars close to the Ecliptic, it changes significantly with time. Two examples are given in Figure 1, showing the impact on position (c_p) and proper motion (c_μ) for two positions in the sky. c_p is a function of position and epoch, while c_μ is in addition related to the time interval between epochs: how long and how exact it is close to an integer number of years. In most cases, for the minimization of the impact of the possible parallax bias, it is advised to choose a pair of epochs with a lower c_p , and extend the time interval between epochs and tightening constraints on observation dates to reduce c_μ .

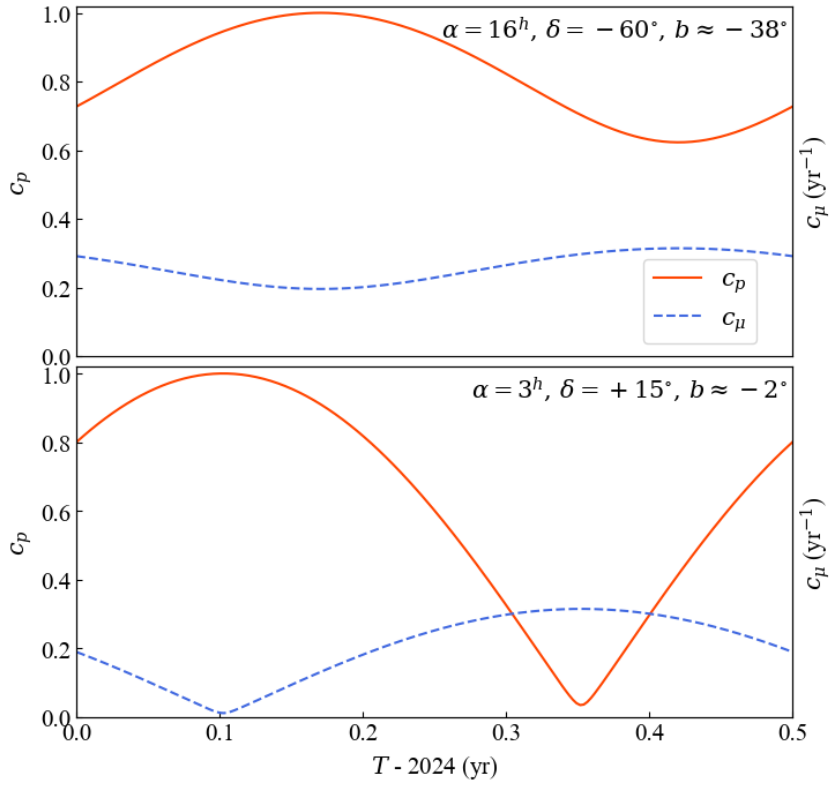


Figure 1: The impact of the possible parallax bias on position c_p and proper motion c_μ as function of epoch T .

3. OBSERVATIONS

Over 20 radio stars, including both old and new ones, have been confirmed detectable through the European VLBI Network (EVN) and the Australian Long Baseline Array (LBA) snap-shot observations. Then two Very Long Baseline Array (VLBA) pilot projects for 5 stars were carried out using the conventional five-parameter strategy, in which the result of one project was published in Chen et al. (2023). Two projects are ongoing: a VLBA project (five-parameter strategy) for 11 stars, and an LBA project (double-epoch strategy) for 5 stars. There will be more observations to come, and the number of detectable radio stars is likely to increase with more and more radio surveys and new fast-developing facilities.

4. REFERENCES

- Bobylev, V. V., 2022, “Link between the Optical and Radio Frames from Gaia DR3 Data and VLBI Measurements”, *Astronomy Letters* 48(12), pp. 790-797, doi: 10.1134/S1063773722110032.
- Charlot, P., Jacobs, C. S., Gordon, D., et al., 2020, “The third realization of the International Celestial Reference Frame by very long baseline interferometry”, *A&A* 644, A159, doi: 10.1051/0004-6361/202038368.
- Chen, W., Zhang, B., Zhang, J., et al., 2023, “VLBI Astrometry of radio stars to link radio and optical celestial reference frames. I. HD 199178 & AR Lacertae”, *MNRAS* 524(4), pp. 5357-5367, doi: 10.1093/mnras/stad1214.
- Gaia Collaboration et al., 2022, “Gaia Early Data Release 3. The celestial reference frame (Gaia-

- CRF3)", A&A 667, A148, doi: 10.1051/0004-6361/202243483.
- Lindegren, L., 2020, "The Gaia reference frame for bright sources examined using VLBI observations of radio stars", A&A 633, A1, doi: 10.1051/0004-6361/201936161.
- Lunz, S., Anderson, J. M., Xu, M. H., et al., 2023, "Enhancing the alignment of the optically bright Gaia reference frame with respect to the International Celestial Reference System", A&A 676, A11, doi: 10.1051/0004-6361/202040266.

SESSION II

Time: Measurement, Transfer, Dissemination

TAKING THE LEAP: THE MOVE TO CONTINUOUS UTC

A. J. KOPF¹

¹ U.S. Naval Observatory - United States - andrew.j.kopf.civ@us.navy.mil

ABSTRACT. The irregular rotation of the Earth causes challenges in timekeeping. The imprecise observed solar time (UT1) routinely drifts from International Atomic Time (TAI), the latter being the foundation of the international timekeeping standard Coordinated Universal Time (UTC). As a result, the leap second was introduced in 1972 to keep UTC and UT1 within 0.9 seconds of each other. This process has become a regular occurrence, applied 27 times in the last 50 years. In 2022, the General Conference on Weights and Measures (CGPM) passed a resolution recommending the move to continuous UTC by 2035. Once in effect, UTC and UT1 would diverge, as UTC would mirror Terrestrial Time (TT) by a constant time offset, including a large initial offset to help UTC remain continuous for an extended period. This summary details emerging challenges and potential solutions in the astronomical community, including those in observation and almanac data.

1. LEAP SECONDS

Introduced in 1972, the leap second serves to keep the observed solar time (UT1) and Coordinated Universal Time (UTC) at approximately the same time, to within less than one second. Due to the routine drift of UT1 from atomic time, this process has become a regular occurrence, as 27 leap seconds have been added to UTC since their inception just over 50 years ago. The predictability of these is a constant challenge, as they occur at highly irregular intervals, due to Earth's climate and geological variability. When a leap second is needed, the decision is made roughly six months in advance by the International Earth Rotation Service (IERS), which provides regular monitoring of the UT1-UTC discrepancy.

Leap seconds are not without controversy. Services that utilize precise timekeeping can face significant disruption, particularly in digital infrastructure. Leap seconds create discontinuities that risk causing serious malfunctions in digital infrastructure including the GNSS systems, telecommunications, and energy transmission systems. Operators of digital networks have developed and applied different methods to incorporate the leap seconds, which do not follow any agreed standard. These include spreading out the leap second over multiple hours or adding it in at non-standard times. The implementation of these different uncoordinated methods threatens resilience of the synchronization capabilities that underpin critical national and international infrastructures. It can also lead to confusion that puts at risk the recognition of UTC as the unique reference time scale.

To add to the challenges and controversy, recent observations of the rotation rate of the Earth indicate the possible need for the first ever negative leap second in the coming years, an adjustment which has never before been foreseen or tested.

In 2022, the General Conference on Weights and Measures (CGPM) passed a resolution recommending the maximum value of UT1-UTC be increased by 2035, effectively creating a near-continuous UTC system. It directed the BIPM to consult with the ITU and other organizations to propose a new maximum value for UT1-UTC that would ensure continuity for at least a century. This proposal, including its implementation plan, would then be reviewed by the CGPM in enough time to allow for a final vote on an official resolution presented at the 2026 meeting of the CGPM.

2. IMPLICATIONS OF CONTINUOUS UTC

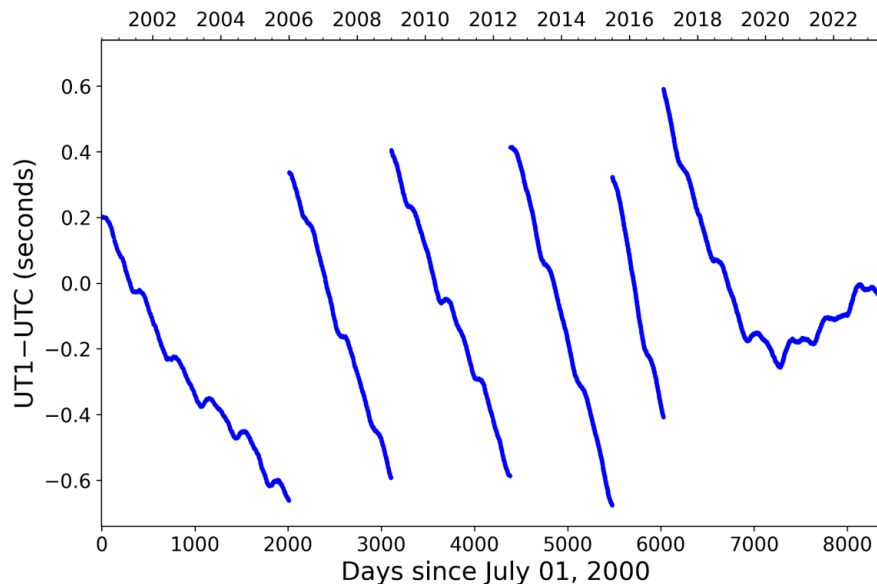


Figure 1: The IERS tracking of UT1-UTC since 2000. Leap seconds appear as discontinuities.

With a continuous UTC system apparently on the way, the remainder of this discussion shall focus on the implications of changing to such a system, particularly within the astronomical community.

First, and perhaps most importantly, the community will have to break a widely-held practice that UT1 and UTC are the same and therefore interchangeable. In many applications that don't deal with precise timekeeping, this has been a safe assumption due to the negligible error of less than a second. It is likely that many users are not even aware that there are two kinds of Universal Time. As a result, more user education and explicit instruction will be needed from the international community following this change.

Telescopic observation is another area where this adjustment will have immediate impact. It is fortunate that most, if not all, major observatories and astronomical applications that require UT1 with high precision already use the internet, GPS, or Beidou to satisfy their needs. These institutions and applications will be unaffected by the change in definition. However, any existing astronomy software or application that until now has assumed UT1 and UTC to be essentially equivalent may require changes. This will be particularly prevalent in the academic and amateur communities. Some software upgrades may be required to accommodate more digits when UT1-UTC becomes greater than a second. If addressed well ahead of time, it is likely that these items can be resolved without major issue.

Almanacs will present a more substantive challenge. In somewhat a parallel of the previous topic, the almanacs produced by the Nautical Almanac Office at the US Naval Observatory already do not use UTC in the data tables, nor in the computation of the ephemerides, so change is not absolutely required. The new definition would actually be useful for data based on Terrestrial Time (TT), as it would now hold a constant offset from the redefined UTC. However, sticking to the status quo puts significant burden on the user to be able to convert between the two systems. Furthermore, due to the advanced publication of these resources, any conversion done either for the tables or by the user would be based on predictions of UT1-UTC from about two years prior, and would pose challenges to maintaining accuracy. Digital formats could adapt in real time, but existing requirements for physical publications inhibit a fully real-time capability.

In support of all the above, IERS predictions and observations of UT1-UTC may gain increased

significance. There will likely be a demand for more real-time dissemination of the observed data, and new tools to aid in the conversion between the two soon-to-be-separated systems.

3. CONCLUSION

Ultimately, the international community will have a choice to make as it moves to this new definition for UTC and its relationship to UT1. The responsibility for smooth and practical incorporation will fall on the policy makers, and ultimately two options will govern the response to each of these challenges above.

Option 1 - "They Can Handle It" - Make sure any references to UT are clarified to be either UT1 or UTC, and then provide significant educational resources to users as to how to convert between the two systems for their own uses.

Option 2 - "We Can Handle It" - Change UT tabulations in printed or digital references to be based on UTC, use UT1-UTC projected values to compute relevant data, and provide regular corrections as either updates to digital tools or follow-ons to printed materials generated in advance based on earlier predictions.

This summary does not seek to impose a decision on which path to take, but concludes by noting that each situation may be unique, and that a one-size-fits-all model may not be applicable. It will be an ongoing challenge as this change to the UTC system is advanced to adequately prepare for its incorporation into this wide variety of applications.

4. REFERENCES

General Conference on Weights and Measures, 2022, "On the use and future development of UTC", 27th CGPM, Resolution 4, doi:10.59161/CGPM2022RES4E.

Kaplan, G.H., 2005, "The IAU Resolutions on Astronomical Reference Systems, Time Scales, and Earth Rotation Models: Explanation and Implementation", US Naval Observatory, Circular 179, <https://doi.org/10.48550/arXiv.astro-ph/0602086>.

TIME AND FREQUENCY TRANSFERS IN OPTICAL SPACETIME

A. BOURGOIN^{1,†}, P. TEYSSANDIER¹, P. TORTORA², and M. ZANNONI²

¹ SYRTE, Observatoire de Paris, PSL Research University, CNRS, Sorbonne Université, UPMC, Univ. Paris 6, 61 avenue de l'Observatoire, 75014 Paris - France

² Dipartimento di Ingegneria Industriale, Alma Mater Studiorum - Università di Bologna, Via Fontanelle 40, 47121 Forlì - Italy

ABSTRACT. Determining the travel time of light signals as a function of the reception time and the locations of the emitter and the receiver is of prime importance in laser ranging to satellites and Moon, very long baseline interferometry, radio occultation experiments, etc. We show how the time transfer function methodology already developed for light travelling through empty space can be extended to light signals propagating through a flowing, non-dispersive medium. We briefly present some applications to the calculation of radio occultation phenomena and tropospheric delays.

1. INTRODUCTION

Given the level of accuracy achieved in a number of space or astronomical techniques—the millimeter for satellite laser ranging (SLR), the centimeter for lunar laser ranging (LLR), the microarcsecond for very long baseline interferometry (VLBI), the decimeter for the range and the micrometer per second for the range-rate of current space probes (e.g., BepiColombo, JUICE, etc.)—we cannot content ourselves with describing the propagation of light in a vacuum. It is necessary to take into account the physical properties of the medium through which the light travels. For astro-geodetic techniques (SLR, LLR, GNSS, VLBI,...), the main optical medium is the Earth's atmosphere. In radio experiments during an occultation event, the optical medium is the atmosphere of a distant planetary body. When performing clock comparisons in metrology, the main optical medium is either the Earth's atmosphere for free space optical links or a fiber.

In this paper, we summarize some of the results obtained in Bourgoin 2020 and Bourgoin *et al.* 2021, making it possible to model time and frequency transfers for light rays crossing a moving, non-dispersive optical medium. It has been shown that such light rays are null geodesics of an *optical metric* involving the refractive index of the medium (see, e.g., Gordon 1923, Synge 1960). Using this property, it is possible to extend the formalism of time transfer functions already developed for light rays travelling through an empty space (see Le Poncin-Lafitte *et al.* 2004 and Refs. therein). The time transfer function corresponding to a quasi-Minkowskian light ray is obtained in the form of a series whose each term is given by an integral taken along a straight line. The integrals giving the first and second order terms are explicitly written in the case where the influence of the gravitational field can be neglected and the optical medium is a stationary flow of matter with a refractive index independent of time. With a view to applications to radio occultation phenomena, the quasi-Minkowskian time transfer function is explicitly calculated at the lowest order with respect to the refractivity for a spherically symmetric, rotating perfect fluid in hydrostatic equilibrium. The analytical result is compared with a numerical integration of the relativistic equations of light rays.

2. NOTATIONS AND CONVENTIONS

Throughout this work, c denotes the speed of light in a vacuum. Greek letters are used for

[†]adrien.bourgoin AT obspm.fr

indices running from 0 to 3, Latin letters for indices running from 1 to 3. Spacetime is assumed to be covered by a global quasi-Cartesian coordinate system $(x^\alpha) = (x^0, x^1, x^2, x^3)$, where $x^0 = ct$, t having the dimension of a time and x^1, x^2, x^3 the dimension of a length. For the sake of brevity, we use a 3-dimensional vector-like notation for any ordered triple: \vec{a} stands for (a^1, a^2, a^3) , also denoted by (a^i) . With this convention, the local coordinates of a point-event x are generally denoted by (ct, \vec{x}) .

The Lorentzian metric describing the gravitational field and determining the proper time of the observers is denoted by g and is called the *physical metric*. The signature adopted for g is $(+, -, -, -)$.

According to Einstein's convention on repeated indices, expressions like $u^\mu v_\mu$ and $a^i b_i$ stand for $\sum_{\mu=0}^3 u^\mu v_\mu$ and $\sum_{i=1}^3 a^i b_i$, respectively.

Any 4-vector is denoted by a bold letter. The scalar product $g(\mathbf{u}, \mathbf{v})$ of two 4-vectors \mathbf{u} and \mathbf{v} is denoted by $\mathbf{u} \cdot \mathbf{v}$: in the coordinate system (x^α) , $\mathbf{u} \cdot \mathbf{v} = g_{\mu\nu} u^\mu v^\nu = u^\mu v_\mu$, where u^μ , v^μ and $g_{\mu\nu}$ are the components of \mathbf{u} , \mathbf{v} and the metric tensor g , respectively; $v_\mu = g_{\mu\nu} v^\nu$.

Given two triples \vec{a} and \vec{b} , $\vec{a} \cdot \vec{b}$ stands for the Euclidean scalar product $\delta_{ij} a^i b^j$, where δ_{ij} is the Kronecker symbol; $\vec{a} \times \vec{b}$ is the triple obtained by the rule giving the exterior product of two vectors of the ordinary Euclidean 3-space. The notation $\|\vec{a}\|$ stands for the Euclidean norm of \vec{a} : $\|\vec{a}\| = (\vec{a} \cdot \vec{a})^{1/2}$.

A quantity f evaluated at point-event x is often noted $(f)_x$ instead of $f(x)$; x is generally omitted when there exists no ambiguity. The partial derivative $\partial f / \partial x^\mu$ is often denoted by $f_{,\mu}$.

3. RELATIVISTIC GEOMETRICAL OPTICS

In this section, we recall some fundamental results of the approximation of geometrical optics within the framework of metric theories of gravity (see e.g., Synge 1960 and Refs. therein; see also Bourgoïn 2020 and Refs. therein).

3.1 Physical properties of the optical medium

Let us denote by \mathcal{D}_{ext} the region of spacetime outside the bodies generating the gravitational field. We assume that a bounded domain \mathcal{M} , included in \mathcal{D}_{ext} , is filled by a transparent medium that is linear, isotropic and non-dispersive, the region $\mathcal{V} = \mathcal{D}_{\text{ext}} - \mathcal{M}$ being a vacuum. The optical properties of the medium are characterized by two scalar functions: the permittivity $\epsilon(x)$ and the permeability $\mu(x)$. On \mathcal{V} , these functions reduce to their vacuum values, namely ϵ_0 and μ_0 , which are linked by the well-known relation $c = (\epsilon_0 \mu_0)^{-1/2}$. The refractive index of the optical medium is the function defined by

$$n(x) = c \sqrt{\epsilon(x) \mu(x)}. \quad (1)$$

We have of course $n(x) = 1$ when $x \in \mathcal{V}$.

Furthermore, we assume that the fluid elements are not colliding, which means that their worldlines form a congruence of timelike curves. The unit 4-velocity vector of a particle of the fluid passing through a point-event x is denoted by $\mathbf{w}(x)$; \mathbf{w} is a vector field on \mathcal{M} . Its components are denoted by w^μ .

3.2 Light propagating through the optical medium

Within the geometrical optics approximation, an electromagnetic wave is described by a set of functions of the type

$$\psi(x) = \mathcal{A}(x) e^{i\mathcal{S}(x)}, \quad (2)$$

where \mathcal{A} is the *amplitude* varying slowly at the scale of the wavelength of the signal and \mathcal{S} is the *phase* (or *eikonal*), changing much faster than the amplitude. The wavelength is assumed to be

much smaller than the spacetime curvature. The *wave-covector* is the covariant vector defined by

$$k_\mu = \partial_\mu \mathcal{S}. \quad (3)$$

Maxwell's equations treated within the geometrical optics approximation imply that the phase satisfies on \mathcal{M} an *eikonal equation*, namely

$$\bar{g}^{\mu\nu} \partial_\mu \mathcal{S} \partial_\nu \mathcal{S} = 0, \quad (4)$$

where

$$\bar{g}^{\mu\nu} = g^{\mu\nu} + (n^2 - 1)w^\mu w^\nu, \quad (5)$$

the quantities $g^{\mu\nu}$ being the contravariant components of the metric tensor g .

The light rays are defined as the characteristic curves of the eikonal equation (4). This equation can be considered as the Jacobi equation associated with the Hamilton function

$$\mathcal{H} = \frac{1}{2} \bar{g}^{\mu\nu} k_\mu k_\nu, \quad (6)$$

where x^μ and k_ν are regarded as a set of independent canonical variables. The light rays travelling through \mathcal{M} are thus the curves $x^\mu = x^\mu(\lambda)$ which are solutions to the canonical equations

$$\frac{dx^\mu}{d\lambda} = \{\mathcal{H}, x^\mu\}, \quad \frac{dk_\alpha}{d\lambda} = \{\mathcal{H}, k_\alpha\}, \quad (7)$$

where $\{f, h\}$ denotes the Poisson bracket of the functions $f(x^\mu, k_\nu)$ and $h(x^\mu, k_\nu)$, namely

$$\{f, h\} = \frac{\partial f}{\partial k_\nu} \frac{\partial h}{\partial x^\nu} - \frac{\partial f}{\partial x^\nu} \frac{\partial h}{\partial k_\nu}. \quad (8)$$

The ray-tracing equations thus read as:

$$\begin{cases} \frac{dx^\mu}{d\lambda} = k^\mu + (n^2 - 1)(\mathbf{k} \cdot \mathbf{w})w^\mu, \\ \frac{dk_\alpha}{d\lambda} = -\frac{1}{2} g^{\mu\nu, \alpha} k_\mu k_\nu - (n^2 - 1)(\mathbf{k} \cdot \mathbf{w})k_\nu w^\nu_{, \alpha} - n n_{, \alpha} (\mathbf{k} \cdot \mathbf{w})^2, \end{cases} \quad (9a)$$

$$\quad (9b)$$

where \mathbf{k} denotes the 4-vector whose components are given by

$$k^\mu = g^{\mu\nu} k_\nu. \quad (10)$$

It was shown in Gordon 1923 that the light rays obeying these equations are null geodesics of the *optical metric* \bar{g} whose components $\bar{g}_{\mu\nu}$ are such that $\bar{g}^{\mu\alpha} \bar{g}_{\alpha\nu} = \delta^\mu_\nu$, i.e.

$$\bar{g}_{\mu\nu} = g_{\mu\nu} - \left(1 - \frac{1}{n^2}\right) w_\mu w_\nu. \quad (11)$$

This property explains why it is possible to extend the method allowing the determination of the time and frequency transfers for light signals travelling through a vacuum to light signals crossing a moving, non-dispersive medium (see Sect. 4).

3.3 Doppler effect

Let \mathcal{O}_A and \mathcal{O}_B be two observers whose world-lines \mathcal{L}_A and \mathcal{L}_B intersect the phase hypersurface $\mathcal{S}(x) = \text{const.}$ at points-events x_A and x_B , respectively. Denote by ν_A and ν_B the frequencies of the wave respectively measured by \mathcal{O}_A and \mathcal{O}_B . It can be shown that the ratio $(\nu_B)_{x_B}/(\nu_A)_{x_A}$ is given by (see e.g., Synge 1960)

$$\frac{(\nu_B)_{x_B}}{(\nu_A)_{x_A}} = \frac{(\mathbf{k} \cdot \mathbf{u}_B)_{x_B}}{(\mathbf{k} \cdot \mathbf{u}_A)_{x_A}}, \quad (12)$$

where \mathbf{u}_A and \mathbf{u}_B are the unit 4-velocities of \mathcal{O}_A and \mathcal{O}_B , respectively.

Putting

$$(l_i)_{x_A} = \left(\frac{k_i}{k_0} \right)_{x_A}, \quad (l_i)_{x_B} = \left(\frac{k_i}{k_0} \right)_{x_B}, \quad (13)$$

it is easily seen that Eq. (12) can be written in the form

$$\frac{(\nu_B)_{x_B}}{(\nu_A)_{x_A}} = \frac{(u^0)_{x_B} (k_0)_{x_B} (1 + \beta^i l_i)_{x_B}}{(u^0)_{x_A} (k_0)_{x_A} (1 + \beta^i l_i)_{x_A}}, \quad (14)$$

where $(\beta^i)_{x_A}$ (resp. $(\beta^i)_{x_B}$) is the i -th component of the coordinate velocity of \mathcal{O}_A (resp. \mathcal{O}_B) divided by c :

$$(\beta^i)_{x_A} = \frac{1}{c} \left(\frac{dx^i}{dt} \right)_{x_A}, \quad (\beta^i)_{x_B} = \frac{1}{c} \left(\frac{dx^i}{dt} \right)_{x_B}, \quad (15)$$

and

$$(u^0)_{x_A} = \sqrt{(g_{00} + 2g_{0i}\beta^i + g_{ij}\beta^i\beta^j)_{x_A}}, \quad (u^0)_{x_B} = \sqrt{(g_{00} + 2g_{0i}\beta^i + g_{ij}\beta^i\beta^j)_{x_B}}. \quad (16)$$

4. USING TIME TRANSFER FUNCTIONS: A BRIEF OVERVIEW

In this section, we recall some fundamental results concerning the time transfer function formalism (see e.g., Teyssandier and Le Poncin 2008 and Refs. therein; see also Linet and Teyssandier 2016 and Refs. therein).

4.1 Time transfer functions: definition and relation with the Doppler effect

The phase function \mathcal{S} is constant along a light ray. Indeed, Eqs. (3), (9a) and (4) imply that $d\mathcal{S}/d\lambda = k_\mu dx^\mu/d\lambda = \bar{g}^{\mu\nu} k_\mu k_\nu = 0$. So we have

$$\mathcal{S}(ct_A, \vec{x}_A) = \mathcal{S}(ct_B, \vec{x}_B) \quad (17)$$

for a light ray emitted at point-event (ct_A, \vec{x}_A) and received at point-event (ct_B, \vec{x}_B) . This equality implies that Eqs. (12) and (14) hold when points-events x_A and x_B are connected by a light ray.

Equation (17) implies also that there exists a functional relation between the light travel time $t_B - t_A$ and \vec{x}_A , t_B and \vec{x}_B . More precisely, given the time of reception t_B , the position \vec{x}_A of the emitter and the position \vec{x}_B of the receiver, there exists a family of light rays $\{\mathcal{G}^{[\sigma]}(\vec{x}_A, t_B, \vec{x}_B)\}$ originating from a point-event of spatial location \vec{x}_A and received at point-event x_B . Denoting by $t_A^{[\sigma]}$ the time of emission of the ray $\mathcal{G}^{[\sigma]}(\vec{x}_A, t_B, \vec{x}_B)$, we can write

$$t_B - t_A^{[\sigma]} = \mathcal{T}_r^{[\sigma]}(\vec{x}_A, t_B, \vec{x}_B), \quad (18)$$

where $\mathcal{T}_r^{[\sigma]}(\vec{x}_A, t_B, \vec{x}_B)$ will be called the *reception time transfer function* associated with the light ray $\mathcal{G}^{[\sigma]}(\vec{x}_A, t_B, \vec{x}_B)$. Of course, a family of *emission time transfer functions* can also be defined, but we do not use it here.

Substituting for $t_A^{[\sigma]}$ from Eq. (18) into Eq. (17), we get an equation satisfied whatever \vec{x}_A , t_B , and \vec{x}_B , namely

$$\mathcal{S}(ct_B, \vec{x}_B) - \mathcal{S}(ct_B - c\mathcal{T}_r^{[\sigma]}(\vec{x}_A, t_B, \vec{x}_B), \vec{x}_A) = 0. \quad (19)$$

Differentiating this equality with respect to x_A^i , x_B^i , and t_B , we find the relations

$$\left(l_i^{[\sigma]} \right)_{x_A^{[\sigma]}} = \left(\frac{k_i^{[\sigma]}}{k_0^{[\sigma]}} \right)_{x_A^{[\sigma]}} = c \left(\frac{\partial \mathcal{T}^{[\sigma]}}{\partial x_A^i} \right)_{(\vec{x}_A, t_B, \vec{x}_B)}, \quad (20a)$$

$$\left(l_i^{[\sigma]} \right)_{x_B} = \left(\frac{k_i^{[\sigma]}}{k_0^{[\sigma]}} \right)_{x_B} = -c \left(\frac{\partial \mathcal{T}^{[\sigma]}}{\partial x_B^i} \right)_{(\vec{x}_A, t_B, \vec{x}_B)} \left[1 - \left(\frac{\partial \mathcal{T}^{[\sigma]}}{\partial t_B} \right)_{(\vec{x}_A, t_B, \vec{x}_B)} \right]^{-1}, \quad (20b)$$

$$\left(k_0^{[\sigma]} \right)_{x_B} = \left(k_0^{[\sigma]} \right)_{x_A^{[\sigma]}} \left[1 - \left(\frac{\partial \mathcal{T}^{[\sigma]}}{\partial t_B} \right)_{(\vec{x}_A, t_B, \vec{x}_B)} \right], \quad (20c)$$

where $x_A^{[\sigma]} = (ct_A^{[\sigma]}, \vec{x}_A)$.

Equations (14), (16) and (20) show that the Doppler shift can be expressed in terms of the derivatives of the reception time transfer function when the motions of the emitter and the receiver are known.

4.2 Quasi-Minkowskian light rays

It is easily deduced from Eqs. (3), (4), (18) and (20) that given t_B and \vec{x}_B , each time transfer function $\mathcal{T}_r^{[\sigma]}(\vec{x}, t_B, \vec{x}_B)$ satisfies a partial differential equation as follows (see Teyssandier and Le Poncin 2008, and Refs. therein):

$$\begin{aligned} & \bar{g}^{00} \left(ct_B - c\mathcal{T}_r^{[\sigma]}(\vec{x}, t_B, \vec{x}_B), \vec{x} \right) + 2c\bar{g}^{0i} \left(ct_B - c\mathcal{T}_r^{[\sigma]}(\vec{x}, t_B, \vec{x}_B), \vec{x} \right) \left(\frac{\partial \mathcal{T}_r^{[\sigma]}}{\partial x^i} \right)_{(\vec{x}, t_B, \vec{x}_B)} \\ & + c^2 \bar{g}^{ij} \left(ct_B - c\mathcal{T}_r^{[\sigma]}(\vec{x}, t_B, \vec{x}_B), \vec{x} \right) \left(\frac{\partial \mathcal{T}_r^{[\sigma]}}{\partial x^i} \frac{\partial \mathcal{T}_r^{[\sigma]}}{\partial x^j} \right)_{(\vec{x}, t_B, \vec{x}_B)} = 0. \end{aligned} \quad (21)$$

In the cases discussed below, the optical metric is considered as a small perturbation of the Minkowski metric depending on a dimensionless parameter ε . So it is assumed that each component $\bar{g}^{\mu\nu}$ admits an expansion as follows (Bourgoin 2020):

$$\bar{g}^{\mu\nu}(x; \varepsilon) = \eta^{\mu\nu} + \sum_{\ell=1}^{\infty} \kappa_{(\ell)}^{\mu\nu}(x; \varepsilon), \quad (22)$$

where

$$\eta^{\mu\nu} = \text{diag}(1, -1, -1, -1) \quad (23)$$

and $\kappa_{(\ell)}^{\mu\nu}(x; \varepsilon)$ denotes a term of order ε^ℓ , i.e. a term that can be written as

$$\kappa_{(\ell)}^{\mu\nu}(x; \varepsilon) = \varepsilon^\ell \hat{\kappa}_{(\ell)}^{\mu\nu}(x). \quad (24)$$

Accordingly, we restrict our attention to the configurations for which one of the paths $\mathcal{G}^{[\sigma]}(\vec{x}_A, t_B, \vec{x}_B)$ is a small perturbation of a null geodesic of Minkowski spacetime. Such a ray will be called a *quasi-Minkowskian light ray* and denoted by $\mathcal{G}^{[qM]}(\vec{x}_A, t_B, \vec{x}_B)$. The reception time transfer function associated with $\mathcal{G}^{[qM]}(\vec{x}_A, t_B, \vec{x}_B)$ will be called *quasi-Minkowskian reception time transfer function* and denoted by $\mathcal{T}_r^{[qM]}(\vec{x}_A, t_B, \vec{x}_B)$. It is consistent with Eq. (22) to suppose that $\mathcal{T}_r^{[qM]}(\vec{x}_A, t_B, \vec{x}_B)$ can be expanded as follows:

$$\mathcal{T}_r^{[qM]}(\vec{x}_A, t_B, \vec{x}_B) = \frac{R_{AB}}{c} + \frac{1}{c} \sum_{\ell=1}^{\infty} (\Delta_r)^{[qM]}_{(\ell)}(\vec{x}_A, t_B, \vec{x}_B; \varepsilon), \quad (25)$$

where

$$R_{AB} = \|\vec{x}_B - \vec{x}_A\| \quad (26)$$

and $(\Delta_r)_{(\ell)}^{[qM]}(\vec{x}_A, t_B, \vec{x}_B; \varepsilon)$ is a term of order ε^ℓ , i.e. a term which may be written as

$$(\Delta_r)_{(\ell)}^{[qM]}(\vec{x}_A, t_B, \vec{x}_B; \varepsilon) = \varepsilon^\ell (\hat{\Delta}_r)_{(\ell)}^{[qM]}(\vec{x}_A, t_B, \vec{x}_B). \quad (27)$$

It can be inferred from Eq. (21) that each quantity $(\Delta_r)_{(\ell)}^{[qM]}$ is given by an integral taken along the line of parametric equation $x = z(\lambda)$, with $z(\lambda)$ defined by

$$z^0(\lambda) = ct_B - \lambda R_{AB}, \quad \vec{z}(\lambda) = \vec{x}_B - \lambda(\vec{x}_B - \vec{x}_A), \quad (28)$$

(see Bourgoïn 2020 and Refs. therein). This fundamental result implies the uniqueness of the quasi-Minkowskian reception time transfer function.

5. APPLICATION TO RADIO OCCULTATION EXPERIMENTS

In order to illustrate the capabilities of the method explained above, we summarize in this section some of the results obtained in Bourgoïn *et al.* 2021 for radio occultations by planetary atmospheres. In this approach, the gravitational field is assumed to be negligible everywhere. Accordingly, the coordinates x^α are considered as Cartesian coordinates of a global inertial reference frame, so that the components of the physical metric are given by

$$g_{\mu\nu} = \eta_{\mu\nu}, \quad \eta_{\mu\nu} = \text{diag}(1, -1, -1, -1). \quad (29)$$

5.1 Case of a stationary optical spacetime

The refractive index n and the unit 4-velocity vector \mathbf{w} are assumed to be time-independent. The optical metric is then stationary. It follows from Eq. (9b) that k_0 is constant along each light ray. This property implies that the time transfer functions do not depend on t_B (see Eq. (20c)). Consequently, the reception and emission time transfer functions are identical. So we can drop the index “ r ” standing for “reception”. Furthermore, the refractive index is supposed to be very close to 1, which is equivalent to regarding as a very small quantity the refractivity $N(\vec{x})$ defined by

$$N(\vec{x}) = n(\vec{x}) - 1. \quad (30)$$

Noting that Eq. (29) implies that the exact expression of the quantities $\bar{g}^{\mu\nu}$ can be written as

$$\bar{g}^{\mu\nu} = \eta^{\mu\nu} + \kappa_{(1)}^{\mu\nu} + \kappa_{(2)}^{\mu\nu}, \quad (31)$$

where

$$\kappa_{(1)}^{\mu\nu} = 2Nw^\mu w^\nu, \quad \kappa_{(2)}^{\mu\nu} = N^2 w^\mu w^\nu, \quad (32)$$

and choosing a mean value of N as the perturbation parameter, $\kappa_{(1)}^{\mu\nu}$ and $\kappa_{(2)}^{\mu\nu}$ can be considered as first- and second-order perturbation terms, respectively. So the procedure outlined in the previous section can be applied.

In what follows, we suppose that the medium is rotating about a fixed axis with a constant rate $\vec{\omega}$, which means that its coordinate velocity divided by c is the triple

$$\vec{\xi}(\vec{x}) = \frac{\vec{\omega} \times \vec{x}}{c}. \quad (33)$$

The unit 4-velocity vector $\mathbf{w} = (w^0, \vec{w})$ of a particle of the medium at point x is therefore given by

$$w^0(\vec{x}) = \Gamma(\vec{x}), \quad \vec{w}(\vec{x}) = \Gamma(\vec{x}) \vec{\xi}(\vec{x}). \quad (34)$$

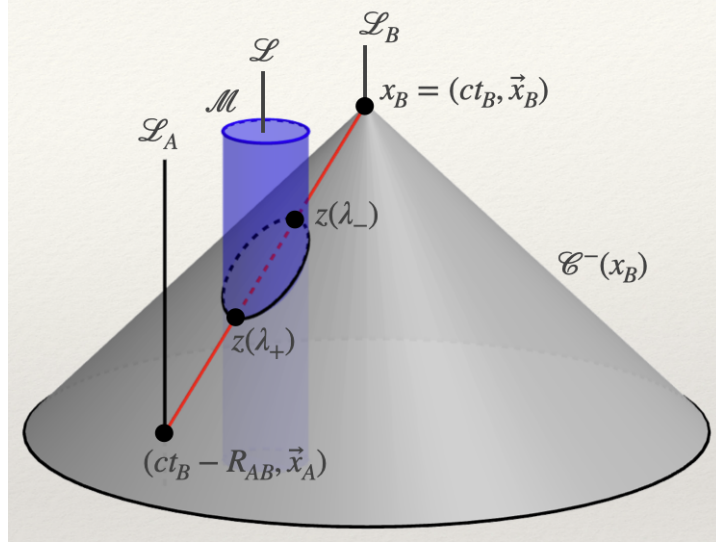


Figure 1: Spacetime diagram representing a radio occultation experiment. The atmosphere is confined in a time-like tube \mathcal{M} in blue. The integrals giving the perturbation terms involved in the quasi-Minkowskian time transfer function $\mathcal{T}^{[qM]}(\vec{x}_A, \vec{x}_B)$ are calculated along the red line joining the point-events $(ct_B - R_{AB}, \vec{x}_A)$ and (ct_B, \vec{x}_B) . This line is on $\mathcal{C}^-(x_B)$, the past light cone at x_B , and cuts the boundary of \mathcal{M} at $z(\lambda_-)$ and $z(\lambda_+)$ (cf. Sect. 5.1).

where $\Gamma(\vec{x})$ is the Lorentz factor:

$$\Gamma(\vec{x}) = \frac{1}{\sqrt{1 - \|\vec{\xi}(\vec{x})\|^2}}. \quad (35)$$

Let us put

$$\gamma_d = 1 + \delta_d, \quad (36)$$

where δ_d is the *light-dragging* coefficient defined as

$$\delta_d = \frac{\vec{\omega} \cdot (\vec{x}_A \times \vec{x}_B)}{cR_{AB}}. \quad (37)$$

Using the method outlined in subsection 4.2 leads to expressions as follow for the first two terms in the expansion of the quasi-Minkowskian delay function:

$$\Delta_{(1)}^{[qM]}(\vec{x}_A, \vec{x}_B) = \gamma_d^2 R_{AB} \int_{\lambda_-}^{\lambda_+} (\Gamma^2 N)_{\vec{z}(\lambda)} d\lambda, \quad (38a)$$

$$\begin{aligned} \Delta_{(2)}^{[qM]}(\vec{x}_A, \vec{x}_B) = & \frac{1}{2} \gamma_d^2 R_{AB} \int_{\lambda_-}^{\lambda_+} (\Gamma^2 N^2)_{\vec{z}(\lambda)} d\lambda + 2\gamma_d R_{AB} \int_{\lambda_-}^{\lambda_+} (\Gamma^2 N \xi^i)_{\vec{z}(\lambda)} \left(\frac{\partial \Delta_{(1)}^{[qM]}}{\partial x^i} \right)_{(\vec{z}(\lambda), \vec{x}_B)} d\lambda \\ & - \frac{1}{2} R_{AB} \int_{\lambda_-}^{\lambda_+} \delta^{ij} \left(\frac{\partial \Delta_{(1)}^{[qM]}}{\partial x^i} \frac{\partial \Delta_{(1)}^{[qM]}}{\partial x^j} \right)_{(\vec{z}(\lambda), \vec{x}_B)} d\lambda, \end{aligned} \quad (38b)$$

where λ_- and λ_+ are the values of λ corresponding to the intersection points of the line defined by Eqs. (28) and the boundary of the domain \mathcal{M} , with the convention that $\lambda_- \leq \lambda_+$ (see Fig. 1).

In most applications, the parameter γ_d is arbitrarily fixed to 1, thus neglecting the influence of the light-dragging on the time and/or frequency transfers. The erroneous estimates resulting of such a choice in some experiments or observations are briefly evoked in the conclusion.

5.2 Spherical symmetry

These results can be applied to a spherically symmetric perfect fluid surrounding a celestial body of radius R_0 . On the assumption of hydrostatic equilibrium, the refractivity N is a function of $r = \|\vec{x}\|$ which can be represented by a product of an exponential of scale height H for the pressure profile and a polynomial in powers of r describing the temperature profile, namely

$$N(r) = N_0 \exp\left(-\frac{r - R_0}{H}\right) \sum_{m=0}^d b_m r^m, \quad (39)$$

where $N_0 = N(R_0)$ and where b_m are constant polynomial coefficients, with d the degree of the polynomial expansion, the center of mass of the celestial body being chosen as the origin of spatial coordinates x^i .

Inserting Eq. (39) into Eq. (38a) yields for the quasi-Minkowskian time transfer function up to and including the first order in N_0 and δ_d :

$$\begin{aligned} \mathcal{T}^{[qM]}(\vec{x}_A, \vec{x}_B) &= \frac{R_{AB}}{c} + \frac{\sqrt{2\pi} H N_0}{c} (1 + 2\delta_d) \exp\left(-\frac{D_{AB} - R_0}{H}\right) \\ &\times \sum_{m=0}^{\infty} \frac{(2m-1)!!}{2^m} \left(\frac{H}{D_{AB}}\right)^{m-1/2} \sum_{n=0}^{m_d} Q_{m-n} \sum_{l=n}^d \frac{n!}{l!(n-l)!} b_l D_{AB}^l, \end{aligned} \quad (40)$$

where D_{AB} is the Euclidean distance from the origin of spatial coordinates to the line passing by \vec{x}_A and \vec{x}_B , namely

$$D_{AB} = \frac{\|\vec{x}_A \times \vec{x}_B\|}{R_{AB}}. \quad (41)$$

The numerical coefficients Q_m and the numbers m_d are defined in Bourgoïn *et al.* 2021. In the next subsection, we present a test of the validity of Eq. (40) by a direct comparison with a numerical solution to the canonical equations (9).

5.3 Numerical ray-tracing

A numerical integration of the canonical equations (9) for a steady rotating planetary atmosphere can be achieved using an approach proposed in Schinder *et al.* 2015. Assuming an atmosphere with a refractivity profile given by Eq. (39), we have considered light rays emitted by a spacecraft orbiting about a planet and received by an observer \mathcal{O}_B located at infinity. We considered a planet of radius $R_0 = 2574$ km (similar to Titan), having an atmosphere with $N_0 = 10^{-6}$ and a scale height $H = 20$ km (see Bourgoïn *et al.* 2021 for numerical values of b_m 's). We have taken into account the fact that because of refraction in \mathcal{M} , the initial direction of the ray must be iteratively corrected so that the ray can reach \mathcal{O}_B . The time and frequency transfers thus obtained were compared with their values inferred from Eq. (40) (see Fig. 2). To test the accuracy of the Eq. (40), we have consider a rapidly rotating atmosphere using $\|\vec{\omega}\| = 2\pi$ rad/s, which corresponds to $\Omega = 0.05$, where

$$\Omega = \frac{\|\vec{\omega}\| R_0}{c}. \quad (42)$$

Within the atmosphere, two different regions can clearly be noticed: (i) the region with $h > 150$ km and (ii) the region with $h < 150$ km, h being the altitude. Within region (i), the difference between numerical and analytical solutions (see *dashed curves*) is at the level of the numerical noise, meaning that Eq. (40) is indeed a precise solution to Eqs. (9) (for the refractivity profile (39)).

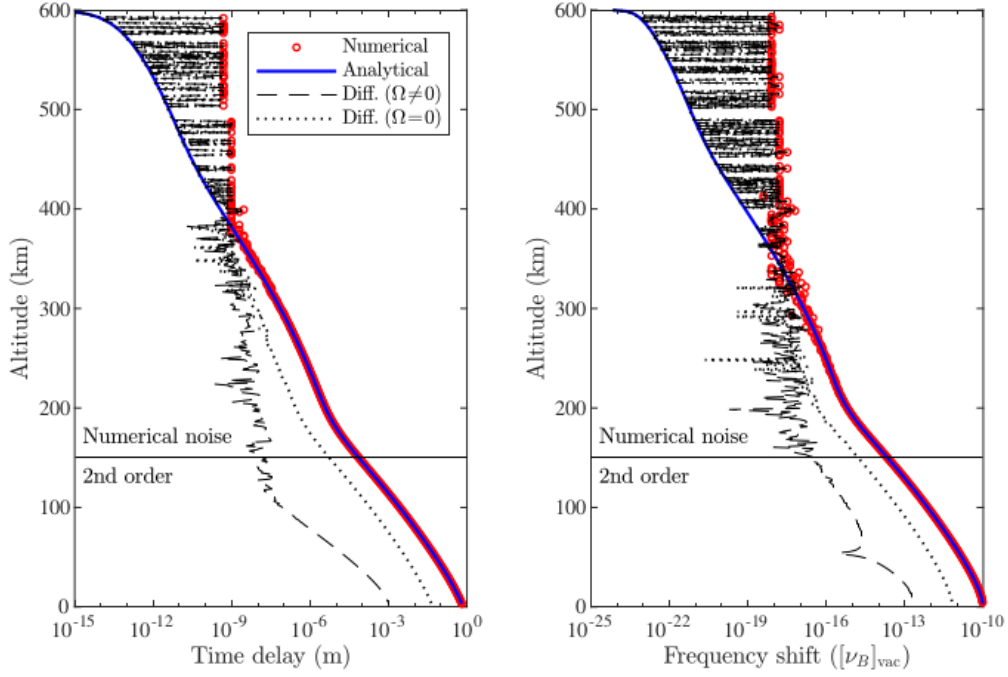


Figure 2: Evolution of the time delay (*left panel*) and frequency shift (*right panel*) with the altitude in a spherically symmetric atmosphere. Solutions of a numerical integration of the canonical equations for relativistic geometric optics are represented with *red circles*. Analytical predictions from the time transfer function formalism are the *blue curves*. The *dashed black curves* correspond to the difference between numerical and analytical results; the analytical formulation contains the light-dragging effect, namely $\Omega \neq 0$. The *dotted black curve* represent the difference between numerical and analytical results, while neglecting the light-dragging effect in Eq. (40), that is enforcing $\Omega = 0$.

Within region (ii), the precision of the analytical solution diminishes as the altitude decreases. Indeed, as mentioned previously in Sect. 5, solution (40) is a first order solution in refractivity. Therefore, since refractivity increases when altitude diminishes (cf. Eq. (39)), the neglected second order terms in refractivity render Eq. (40) less precise than for high altitudes where the refractivity stays small. Then, in region (ii), the difference between analytical and numerical solutions shows the contribution of the neglected second order terms in refractivity, namely the contribution from (38b), that was not considered to derive (40).

Figure 2 also makes visible the light-dragging contribution. Indeed, we computed from (40) a second analytical time transfer function corresponding to $\Omega = 0$ and $\delta_d = 0$. The difference between the numerical solution and this second analytical solution (see *dotted curves*) is significantly greater than the numerical noise level: the precision has decreased (by up to three orders of magnitude at 150 km altitude) comparatively to the analytical solution that includes the light-dragging. It is clear that the light-dragging effect must be taken into account in the case of a rapidly rotating atmosphere.

6. CONCLUSION

The methodology outlined here and discussed in more depth in Bourgoïn 2020 and Bourgoïn *et al.* 2021 offers an elegant framework for modelling the time and frequency transfers through a flowing, non-dispersive optical medium. This formalism allows an accurate estimate of the light-

dragging effect generated by the motion of the medium, which is at the threshold of visibility in many experiments. A direct application is a correct modelling of tropospheric delays in the processing of data provided by astro-geodetic techniques (SLR, LLR, GNSS, VLBI, etc.). Neglecting the light-dragging effect can indeed induce errors on the time delay at the level of 0.05 mm in GCRS reference frame and 3 mm in BCRS frame. Concerning the Doppler shift, the error could reach the level of $0.01 \mu\text{m/s}$ and $10 \mu\text{m/s}$ in GCRS and BCRS, respectively. Comparing with current data accuracies (see Sect. 1), it becomes clear that the light-dragging effect will need to be carefully modeled in the near future. As another example, the light-dragging by the zonal winds in Saturn's atmosphere must be taken into account in the processing of radio occultation data collected during the Cassini mission (Schinder *et al.* 2015).

To finish, we can mention that having an analytical description of how much time and frequency transfers are affected by the atmosphere enables one to easily assess errors related to thermodynamic profiles (see Bourgoïn *et al.* 2022). This last point is of a great interest in the context of radio occultation experiments, where the determination of error profiles usually requires *ad hoc* numerical procedures.

7. REFERENCES

- A. Bourgoïn, 2020, "General expansion of time transfer function in optical spacetime", Phys. Rev. D 101, 064035.
- A. Bourgoïn, M. Zannoni, L. Gomez Casajus, P. Tortora, and P. Teyssandier, 2021, "Relativistic modeling of atmospheric occultations with time transfer functions", A&A 648, A46.
- A. Bourgoïn, E. Gramigna, M. Zannoni, L. Gomez Casajus, and P. Tortora, 2022, "Determination of uncertainty profiles in neutral atmospheric properties measured by radio occultation experiments", Adv. in Space Research 70, 8.
- W. Gordon, 1923, "Zur Lichtfortpflanzung nach der Relativitätstheorie", Annalen der Physik, 377, 22 421-456.
- C. Le Poncin-Lafitte, B. Linet, and P. Teyssandier, 2004, "World function and time transfer: general post-Minkowskian expansions", Class. Quantum Grav. 21, 4463-4483.
- B. Linet and P. Teyssandier, 2016, "Time transfer functions in Schwarzschild-like metrics in the weak-field limit: A unified description of Shapiro and lensing effects", Phys. Rev. D 93, 044028.
- J. L. Synge, 1960, "Relativity: The General Theory", North-Holland Publishing Company, Amsterdam.
- P. J. Schinder, F. M. Flasar, E. A. Mourad, R. G. French, A. Anabtawi, E. Barbinis, A. J. Kliore, 2015, "A numerical technique for two-way radio-occultations by oblate axisymmetric atmospheres with zonal winds", Radio Science 50, 712-727.
- P. Teyssandier and C. Le Poncin-Lafitte, 2008, "General post-Minkowskian expansion of time transfer functions", Class. Quantum Grav. 25, 145020.

THE VLBI CORRELATOR AMBIGUITY AND THE RELATIVISTIC GROUP DELAY MODEL

O. TITOV

GEOSCIENCE AUSTRALIA - AUSTRALIA - oleg.titov@ga.gov.au

ABSTRACT. The conventional VLBI relativistic delay model refers to the time epoch when the signal passes one of two stations of an interferometer baseline. Before, 2002, this model was used as part of the correlation procedure. Since 2002, a new correlation procedure has been adopted in which the VLBI group delays refers to the time epoch of signal passage at the geocenter. A new alternative to the conventional VLBI model delay should be introduced to follow that change because the discrepancy between the two relativistic geometrical delay models is up to 6 ps for ground-based VLBI experiments. In addition, a miscalculation of the signal arrival moment to the geocentre or the "reference station" may cause a larger modelling error (up to 50 ps) which would directly affect the radio telescope positions with a corresponding formal error of 15 mm. This is particularly essential for upcoming geodetic VLBI observations as the final goal of 1-mm accuracy needs to be achieved.

1. INTRODUCTION

The Very Long Baseline Interferometry (VLBI) technique measures the difference between the arrival times of a signal from a distant radio source at two radio telescopes (Schuh and Behrend, 2012). The signal is recorded at each radio telescope together with time marks from independent hydrogen masers. Two radio telescopes are usually separated by a few hundred or thousand kilometres, the plane wave front passes the second telescope on one hundredth part of second later than the first one. This difference in the arrival time of the signal at both radio telescopes is called time delay

The time delay is measured during cross-correlation of the two independent records of the signals recorded at the both radio telescopes. There are two types of correlators (XF and FX) based on the order of the mathematical operations – cross-correlation (X) and Fourier transformation (F). Baseline-based correlators are designed as XF type correlators, and station-based correlators are FX type correlators. For the baseline-based XF-type MarkIII correlator used before 2002, the observables referred to the position of one of the two stations (station 1). For the station-based FX-type MarkIV correlator all observables for all baselines at one single multi-baseline scan are referred to the geocentre as a common reference point. All first-order and second-order effects of special relativity should be taken into account to achieve the 1-ps accuracy of the relativistic delay modeling.

One of the goals of the International VLBI Service activities is to achieve 1-mm accuracy from the analysis of a standard 24-hour geodetic VLBI experiment. The accuracy of the daily scale factor improved dramatically in 2002 when the MarkIII correlator was replaced by MarkIV correlator. However, so far this value varies about 3-4 mm despite further technological developments since 2002 (Titov and Krásná, 2018).

One possible reason for the lack of improvement in accuracy is the inconsistency between the VLBI observable group delays and the relativistic delay model developed in 1980s-90s, and published in the IERS Conventions 2010 (Petit and Luzum, 2010). The transition from the MarkIII to MarkIV correlator was not followed by any changes in the IERS Conventions model

that still refers to the epoch of the wavefront passage of station 1. Thus, it remains consistent with the XF-type correlators only while the consistency with the FX-correlator output needs to be investigated. We show here that an additional correction needs to be applied to make the output delay of the FX-correlator consistent with the IERS Conventions 2010 model (which is the XF-type style, on default). This conversion difference was called “subtle” (Whitney, 2000), however, in fact, it reaches 20 ns, which is quite significant. Brian Corey has developed a simple geometric approach under assumption of the finiteness of the speed of light to obtain this correction, but his final equation comprised a major term only, while several minor terms were not included (Corey, 2000). In this paper, we shall develop the correction using the Lorentz transformation to get the small but significant second order effects.

2. LORENZ TRANSFORMATION FOR GEODETIC VLBI

2.1 Lorentz transformation

Two radio telescopes located on the surface of the rotating Earth have their coordinates in the Geocentric Celestial Reference System (GCRS) co-moving with the Earth. Positions of the reference radio sources observed by the radio telescopes are presented in the Barycentric Celestial Reference System (BCRS). The transformation of the coordinates from BCRS to GCRS is based on the metric tensor of the Solar System at the first and second post-Newtonian level (e.g. Hellings, 1986; Kopeikin, 1990; Klioner, 1991; Soffel et al., 2017). A full analytical expression of the relativistic group delay model includes a lot of effects which are not detected. To present a simplified version of the delay let us start with the conventional Lorentz transformation

$$\begin{aligned} \mathbf{x}' &= \mathbf{x} + (\gamma - 1) \frac{(\mathbf{V} \cdot \mathbf{x})\mathbf{V}}{|\mathbf{V}|^2} - \gamma \mathbf{V} t \\ t' &= \gamma \left(t - \frac{(\mathbf{V} \cdot \mathbf{x})}{c^2} \right). \end{aligned} \quad (1)$$

where $\gamma = \left(\sqrt{1 - \frac{|\mathbf{V}|^2}{c^2}} \right)^{-1}$ is the so-called Lorentz “gamma-factor” .

Transformation (2) links the geocentric reference system $S'(x', t')$ that is moving with velocity \mathbf{V} around the Solar System Barycentre (SSB) and the barycentric reference system $S(x, t)$ located at the SSB. The time delay derived from (3) may be presented in the form (Titov and Krásná, 2018)

$$\tau_{g_0} = \frac{-\frac{(\mathbf{b} \cdot \mathbf{s})}{c} \left(1 - \frac{|\mathbf{V}|^2}{2c^2} \right) - \frac{(\mathbf{b} \cdot \mathbf{V})}{c^2} \left(1 + \frac{(\mathbf{s} \cdot \mathbf{V})}{2c} \right)}{1 + \frac{(\mathbf{s} \cdot \mathbf{V})}{c}} \quad (2)$$

Whether an astronomical instrument with a reference clock were placed in the Earth’s geocenter and the Solar gravitation were ignored, the equation (2) would be applied to reduction of the geodetic VLBI data. However, further complications will be discussed in two next subsections.

2.2 Space and time transformation with gravitational potential

The corresponding equation for the relativistic group delay includes the Solar gravitational potential at the geocenter of the Earth (Titov and Krásná, 2018)

$$\tau_{g_u} = \frac{-\frac{(\mathbf{b} \cdot \mathbf{s})}{c} \left(1 - \frac{2U}{c^2} - \frac{|\mathbf{V}|^2}{2c^2} \right) - \frac{(\mathbf{b} \cdot \mathbf{V})}{c^2} \left(1 + \frac{(\mathbf{s} \cdot \mathbf{V})}{2c} \right)}{1 + \frac{(\mathbf{s} \cdot \mathbf{V})}{c}} \quad (3)$$

The term proportional to $\frac{2U}{c^2}$ in (3) could be unified with the general relativity effect of the gravitational delay. Therefore, we will not include it into further analysis, however, we discuss it here as it is a part of the conventional geometric part of the relativistic delay model (Petit and Luzum, 2010).

2.3 Lorenz transformation referring to the epoch of first station

The physical clocks used for VLBI observations are located near the radio telescopes at the Earth surface rather than at the geocenter, and they follow all variations of the topocentric coordinates (e.g. due to the Earth tides) along with the 'host' radio telescopes. One of the two clocks is selected as "reference" clock, its time scale is treated as a perfect and all frequency and phase variations of the second clock are measured with respect to the "reference" one. Once the choice is made, the geocentric motion of the second ("no reference") clock is added to the relativistic group delay model. Then we consider the difference between barycentric coordinates of two radio telescopes, $\mathbf{r}_1(t_1)$ and $\mathbf{r}_2(t_2)$, measured at the two epochs t_1 and t_2 , to expand the vector $\mathbf{r}_2(t_2)$ as follows

$$\mathbf{r}_2(t_2) = \mathbf{r}_2(t_1) + \mathbf{w}_2(t_1)(t_2 - t_1) \quad (4)$$

where $\mathbf{w}_2 = \mathbf{w}_2(t_1)$ is the geocentric velocity of the second station at epoch t_1 .

Let's introduce a new geocentric reference frame $S'' = S''(x'', t'')$ with the reference epoch referred to station 1 in such way that two geocentric reference frames S'' and S' are linked by new transformation

$$\begin{aligned} \mathbf{x}'' &= \mathbf{x}' \\ t'' &= t' - \frac{(\mathbf{w}_2 \cdot \mathbf{x}')}{c^2} \end{aligned} \quad (5)$$

Transformation (5) could be easily combined with the Lorentz transformation (1)

$$\begin{aligned} \mathbf{x}'' &= \mathbf{x} + (\gamma - 1) \frac{(\mathbf{V} \cdot \mathbf{x})\mathbf{V}}{|\mathbf{V}|^2} - \gamma \mathbf{V} t \\ t'' &= \gamma \left(t - \frac{(\mathbf{V} \cdot \mathbf{x})}{c^2} \right) - \frac{(\mathbf{w}_2 \cdot \mathbf{x})}{c^2} - \\ &\quad - (\gamma - 1) \frac{(\mathbf{V} \cdot \mathbf{x})(\mathbf{V} \cdot \mathbf{w}_2)}{c^2 \cdot |\mathbf{V}|^2} + \gamma \frac{(\mathbf{V} \cdot \mathbf{w}_2)t}{c^2}. \end{aligned} \quad (6)$$

As both reference frames S'' and S' are geocentric, the time component is only changed due to transition from (1) to (6). Traditionally, authors proceed to the equation of the relativistic time delay (2) consistent with the XF-type correlator directly. Therefore, these two transformations (1) and (5) merged together and the difference between the delays (8) and (2) is lost. However, for the FX-type correlators this procedure must be separated into two steps to provide a proper relativistic conversion between the observables produced by the XF and FX correlators.

This equation could be converted to the form consistent with the conventional group delay model at 1-ps level after inclusion of the Solar gravitation term (3)

$$s'' = \frac{s \left(1 - \frac{2U}{c^2} - \frac{|\mathbf{V}|^2}{2c^2} - \frac{(\mathbf{V} \cdot \mathbf{w}_2)}{c^2} \right) + \frac{\mathbf{V}}{c} \left(1 + \frac{(\mathbf{V} \cdot \mathbf{s})}{2c} \right)}{1 + \frac{((\mathbf{V} + \mathbf{w}_2) \cdot \mathbf{s})}{c}} \quad (7)$$

Development of the time delay from (7) as $\tau = -\frac{(\mathbf{b} \cdot \mathbf{s}'')}{c}$ provides the conventional group delay model (8).

The conventional group delay model was finally adopted (Petit and Luzum, 2010).

$$\tau_g = \frac{-\frac{(\mathbf{b} \cdot \mathbf{s})}{c} \left(1 - \frac{2GM}{c^2 R} - \frac{|\mathbf{V}|^2}{2c^2} - \frac{(\mathbf{V} \cdot \mathbf{w}_2)}{c^2} \right) - \frac{(\mathbf{b} \cdot \mathbf{V})}{c^2} \left(1 + \frac{(\mathbf{s} \cdot \mathbf{V})}{2c} \right)}{1 + \frac{(\mathbf{s} \cdot (\mathbf{V} + \mathbf{w}_2))}{c}} \quad (8)$$

where \mathbf{b} is the vector of baseline $\mathbf{b} = \mathbf{r}_2 - \mathbf{r}_1$, \mathbf{s} is the barycentric unit vector of the radio source, \mathbf{V} is the barycentric velocity of the geocenter, \mathbf{w}_2 is the geocentric velocity of station 2, c is the speed of light, G is the gravitational constant, M is the mass of the Sun, and R is the geocentric distance to the Sun, and (\cdot) is the dot-product operator of two vectors. The reference epoch is the UTC epoch of the wavefront passage at the reference station. In accordance with the assumption, station 1 is treated as the reference station, the geocentric velocity of station 2 is presented in (1) explicitly. The modern revision (Soffel et al., 2017) is to add some smaller terms (less than 1 ps), but the analytical model (1) is still valid for the analysis of VLBI data.

Now it is obvious that this model is based on the modification of the Lorentz transformation (6) in which the transformation of time is presented in a non-standard way because our reference clocks are physically located at the Earth surface rather than at the geocenter.

Eq (2) misses the terms including the velocity of the second radio telescope in (8). At the 1 ps level of accuracy this difference $\delta\tau = \tau_g - \tau_{g_0}$ comprises five terms

$$\begin{aligned} \delta\tau = & \frac{2(\mathbf{b} \cdot \mathbf{s})U}{c^3} + \frac{(\mathbf{b} \cdot \mathbf{s})(\mathbf{w}_2 \cdot \mathbf{s})}{c^2} + \\ & + \frac{(\mathbf{b} \cdot \mathbf{s})(\mathbf{V} \cdot \mathbf{w}_2)}{c^3} + \frac{(\mathbf{b} \cdot \mathbf{V})(\mathbf{w}_2 \cdot \mathbf{s})}{c^3} - \\ & - \frac{2(\mathbf{b} \cdot \mathbf{s})(\mathbf{V} \cdot \mathbf{s})(\mathbf{w}_2 \cdot \mathbf{s})}{c^3} \end{aligned} \quad (9)$$

2.4 Correction to the reference epoch

The transition from the XF-type to FX-type correlators for processing geodetic VLBI data requires a corresponding revision of the relativistic group delay in the IERS Conventions to secure a match between the correlator output and the theoretic model. Alternatively, a special correction needs to be done at the final step of the post-correlation data processing. In Equation (9) we show in the four last terms the relativistic correction due to the time transformation from the epoch of the geocenter to the epoch of station 1. This correction is derived from the modified version of the Lorentz transformation in Equation (6). Missing of the three minor terms in Equation (9) can lead to a discrepancy of the group delay model at level of 6 ps for long baselines. This is, in particular, pertinent for the intensive experiments for rapid estimation of Universal Time, because a typical observational network consists of 2 or 3 radio telescopes separated by a long baseline (more than 7000 km). We would like to recommend this equation be applied for the post-processing analysis of VLBI data at the modern FX-correlators.

Another effect, though may be not directly linked to the first one, is the uncertainty of the time of signal registration for each telescope as measured by the local clock (hydrogen maser) at the reference station and extrapolated during the process of correlation. This effect also refers to the difference of the geocentric velocities of both radio telescopes, but it could be introduced as the extension of the clock instability model. The additional parameter describes how far the actual time of the signal arrival deviates from the time presented in the VLBI data file. The corresponding procedure to estimate the correction to the time of the signal registration for the case of XF-correlator is presented in (Titov, Melnikov, Lopez, 2020). The relativistic delay obtained with the FX-correlator should be free of the effect.

However, additional concern is about the definition of geocentre, if the FX-correlator is in use. Theoretically, the geocentre is defined as the centre of the Earth's mass (CM) which makes orbital

motion around the Solar System Barycentre (SSB). The barycentric velocity vector \mathbf{V} used in the relativistic equations has its origin in CM, and the imaginary reference clock should be “placed” exactly at CM. But VLBI, as a geometric technique, has its origin in the centre of figure (CF) (Lavalée, Blewitt, 2002; Blewitt, 2003). The discrepancy between the CM and CF may reach a centimeter level, therefore, the imaginary reference clock “measures” the arrival of signal to CF instead of CM. The corresponding uncertainty in the epoch of the signal arrival to the geocenter is up to 30 ps and out of control. This raises a question about a total additional error caused by using the FX-correlator for correlation of the geodetic VLBI data.

Acknowledgements

This paper was published with the permission of the CEO of the Geoscience Australia.

4. REFERENCES

- Schuh, H., Behrend, D., 2012, “VLBI: A fascinating technique for geodesy and astrometry”, *Journal of Geodynamics*, 61, pp. 68–80.
- Titov, O., Krásná, H., 2018, “Measurement of the solar system acceleration using the Earth scale factor”, *A&A*, 610, A36
- Petit, G., Luzum, B., 2010, *IERS Conventions 2010*, IERS Technical Notes 36, 2010
- Whitney, A., 2000, “How Do VLBI Correlators Work?” *Proc. of IVS 2000 General Meeting*, ed. by F. Takahashi, pp. 187–205.
- Corey, B., 2000, “Conversion from Mark IV to Mark III delays and rates”, *Memo of Massachusetts Institute of Technology, Haystack Observatory* (unpublished).
- Hellings, R.W., 1984, “RELATIVISTIC EFFECTS IN ASTRONOMICAL TIMING MEASUREMENTS”, *AJ*, 91, pp. 650–659.
- Kopeikin, S., 1990, “Theory of Relativity in Observational Radio Astronomy”, *Soviet Ast.*, 34, pp. 5–10.
- Klioner, S., 1991, “General Relativistic Model of VLBI Observables”, *Proc. of AGU Chapman Conference on Geodetic VLBI: Monitoring Global Change*, ed. by W. Carter, NOAA Technical Report, NOS 137 NGS 49, American Geophysical Union, Washington, D.C., pp. 188–202.
- Soffel, M., Kopeikin, S., Han, B., “Advanced relativistic VLBI model for geodesy”, *Journal of Geodesy*, 91, pp. 783–801.
- Titov, O., Melnikov, A., Lopez, Y., 2020, “Resolving VLBI correlator ambiguity in the time model improves precision of geodetic measurements”, *PASA*, 37, e050
- Lavalée, D., Blewitt, G., 2002, “Degree-1 Earth deformation from very long baseline interferometry measurements”, *Geoph Res Letters*, 29(20), 1967.
- Blewitt, G., 2003, “Self-consistency in reference frames, geocenter definition, and surface loading of the solid Earth”, *J. Geophys. Res.*, 108, 2103

Session III

General Relativity : Recent Highlights and tests in solar system

RECENT FINDINGS IN GROUND-BASED GRAVITATIONAL-WAVE DETECTORS

M. A. BIZOUARD¹ for the LIGO-Virgo-KAGRA collaboration

¹ Université de la Côte d'Azur, Observatoire de la Côte d'Azur, CNRS, ARTEMIS, Nice -

France - marianne.bizouard@oca.eu

ABSTRACT. Gravitational-wave astronomy has started less than a decade ago and has already yielded a wealth of fundamental results in astronomy and fundamental physics. We present an overview of the most recent results obtained by the LIGO-Virgo-KAGRA collaboration focusing on how gravitational waves emitted by compact binary coalescences can be used to study the content of the Universe, the standard model of cosmology and test the foundations of general relativity.

1. INTRODUCTION

A century after their prediction by Albert Einstein in his theory of general relativity, gravitational waves have been directly detected for the first time in 2015 by the two Michelson interferometers that form the Laser Interferometer Gravitational-wave Observatory (LIGO). LIGO (Aasi et al., 2015) along with Virgo (Acernese et al., 2015) in Europe and KAGRA (Akutsu et al., 2021) in Japan form an international network of ground-based gravitational-wave detectors that operate jointly to observe the Universe. More precisely they detect in the Herz-kiloHerz regime space-time perturbation generated by the path of gravitational waves through the Earth. Those waves are emitted by the most compact objects, black holes and neutron stars at cosmological distances, and travel at the speed of light without perturbation by the interstellar medium providing unique information about the dynamics of the source and its environment. Many phenomena involving compact objects emit gravitational waves: this is particularly the case when the core of a massive star ending its life starts to collapse forming a neutron star or a black hole. This is also the case of binary systems of two compact objects that coalesce until the final plunge; the orbit shrinks because of the gravitational-wave radiation. The last seconds of these ultra relativistic phenomena are what has been observed so far by the network of gravitational-wave detectors.

As of spring 2024, LIGO and Virgo have observed more than one hundred compact binary mergers including mainly two binary black holes, but also few binary neutron stars and mixed systems black hole - neutron star. As any revolution in science, the observation of the gravitational-wave emission opens many new opportunities: it is a new way to study the content of the Universe and especially to better understand how stellar-mass and intermediate-mass black holes are formed. For the first time general relativity can be tested in strong-field regime. It is interesting to note that a large fraction of alternative theories of general relativity have been ruled out by the discovery of GW170817, the merger of two neutron stars whose prompt electromagnetic counterpart had been observed less than two seconds after by gamma-ray-burst detectors. Thanks to the great sensitivity of the gravitational-wave detectors sources can be detected at cosmological distances and their redshifted properties allow to probe the standard model of cosmology with, for instance, a measure of the Hubble constant. Finally, gravitational waves are also the direct probe to test inflationary theories, as waves emitted during the early times of the Universe travel without any perturbation and form nowadays a stochastic background of primordial gravitational waves. All this requires a network of detectors whose sensitivity is regularly improved. In the next sections

we describe the current status of the network, describe the most interesting features of the latest catalog of gravitational-wave sources released by the LIGO-Virgo-KAGRA collaboration (LVK) and comment on the main results obtained in gravitational-wave astronomy.

2. THE NETWORK OF GRAVITATIONAL-WAVE DETECTORS

The network of ground-based gravitational-wave detectors is formed of two LIGO antennas in the USA, one in Washington State and the other one in Louisiana, the Virgo antenna in Italy and the KAGRA antenna in Japan. With arm lengths of 3 km for Virgo and KAGRA, and 4 km for LIGO, these detectors can measure a relative displacement of the interferometers' arm lengths of 10^{-18} m or smaller. We briefly describe the properties of these Michelson interferometers that can measure disturbances of spacetime created by merging binary neutron star and black holes systems millions to billions of light-years away.

Gravitational waves produce a transverse force on massive objects, a tidal force. Explained via general relativity it is more accurate to say that gravitational waves will deform the fabric of spacetime. Let us imagine a linearly polarized gravitational wave propagating in the z-direction, the fabric of space is stretched due to the strain created by the gravitational wave, but the distortion is not identical in all direction: while during half a period of the wave space is stretched out in one direction, it is squeezed in the orthogonal direction such that if one considers the arms of a Michelson interferometer, their length would be modified in a differential way such that the path of a gravitational wave would be detected as a small phase difference between the light in the two arms. The arms' length difference is directly proportional to the amplitude of the signal that scales inversely with the distance to the source. Because interferometers are sensitive to the amplitude of the signal (and not the square as for the electromagnetic emission), they can detect sources rather far away and an increase of sensitivity by a factor n multiplies the number of sources by a factor n^3 .

The current generation of gravitational-wave detectors (named Advanced LIGO, Advanced Virgo and KAGRA) include many features to enhance by many orders of magnitude their sensitivity. First, additional semi-transparent mirrors at the entrance of the arms form Fabry Perot cavities that increase the effective path of the light in the two arms before it gets recombined. With stabilized high-power lasers the interferometer can measure smaller distance displacements and achieve better sensitivity at high frequency. Furthermore more light circulating in the interferometer is possible by adding a mirror at the entrance of the interferometer to recycle the laser power. The interferometer operates such that virtually none of the light exits the interferometer dark port, and the bulk of the light returns towards the laser. However, currently the detectors are not operating with maximal laser power (~ 200 W) because of thermal effects in the optics, but in the current configuration several hundreds of kW are circulating in the Fabry Perot cavities. Figure 1 displays the optical layout of one LIGO detector.

There is one additional modification to the Michelson interferometer that further improves the sensitivity, by enlarging the frequency band range, thanks to another mirror between the beam-splitter and the detection photodiodes forming another Fabry-Perot cavity. This mirror allows the laser beam to acquire additional phase as it sends the light of one arm that contracts to the other one that is expanded. As this process is repeating over and over, signal recycling gives a substantial boost to interferometer sensitivity in a particular range of frequencies, and is implemented in all the main ground based interferometric detectors.

The large number of photons, whose arrival times are random (Poisson statistics) induce large radiation reaction noise (random motion due to transfer of momentum from the photons to the test mass). The low-frequency radiation reaction noise, plus the high frequency shot noise, combine to create the total quantum noise. At high frequencies the shot noise decreases with laser power, while at low frequencies radiation reaction noise increases with the power. One way to reduce quantum

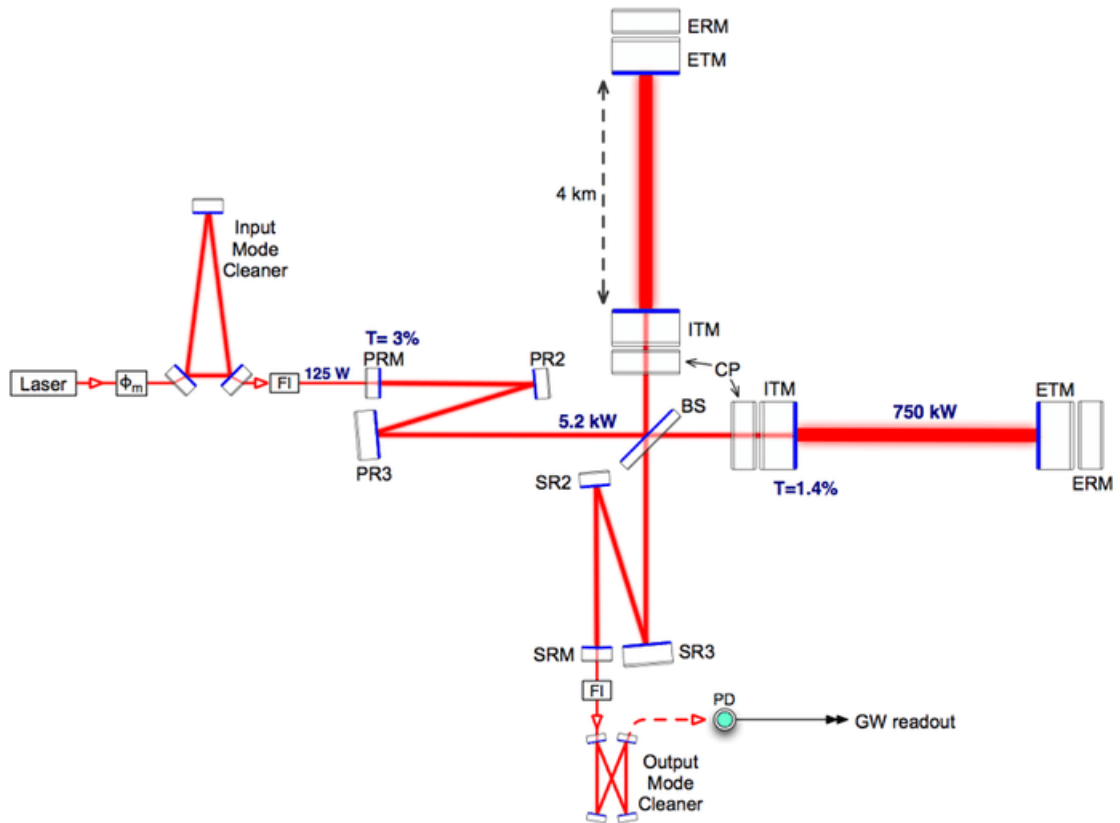


Figure 1: The Advanced LIGO optical layout. Figure from Aasi et al., 2015.

noise is to inject quantum states of the light in the interferometer. Squeezed light is a type of light in which the quantum fluctuations in one of the light's properties, such as its amplitude or phase, are reduced below the standard quantum limit. This reduction of noise was implemented by Advanced LIGO where squeezed light reduced the noise below the shot noise level for frequencies above 50 Hz by as much as 3 dB; Advanced Virgo has also achieved similar results. Advanced LIGO and Advanced Virgo are presently using a method called frequency dependent squeezing to reduce both the shot noise at high frequencies, and the radiation reaction noise at low frequencies. The use of quantum states of light is one of the ways that LIGO, Virgo and KAGRA plan to reduce their noise in the years to come. The other fundamental limiting noise comes from thermal motion of atoms in material that is at room temperature in LIGO and Virgo. The two main thermal noise sources are the wires suspending the mirrors in the last stage of the suspension, and the mirrors themselves, especially the coating material on the mirror surfaces. To reduce the thermal noise, two main ways are investigated: KAGRA sapphire test masses are enclosed into cryostat and cooled down at 20 K. LIGO and Virgo test masses are at room temperature but thermal noise in the wires is reduced by the use of fused silica and better mirror coatings that are in development.

Since 2015, the network of advanced detectors is jointly planning observation with periods for upgrading the detectors to improve their sensitivity as illustrated in Figure 2. During observing runs,

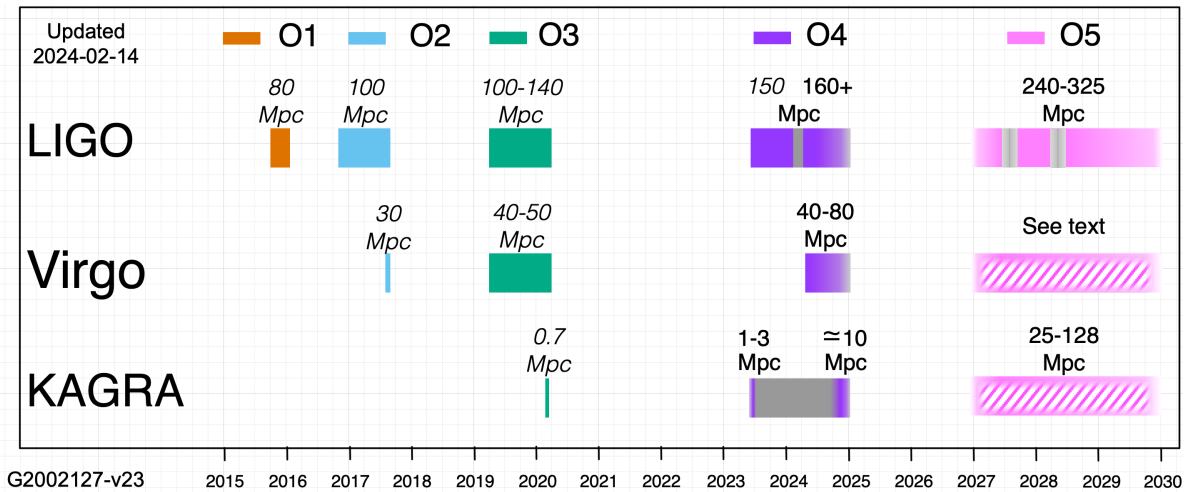


Figure 2: Observing plans of the network of gravitational-wave detectors LIGO, Virgo and KAGRA since 2015. The Virgo detector sensitivity for the fifth observing run O5 is not yet released. Figure from The LIGO-Virgo-KAGRA collaboration, 2024.

data recorded at each observatory are transferred within few a seconds latency to a few computing centers as they need to be coherently analyzed. Several pipelines are searching for compact binary coalescence of binary black holes, binary neutron stars and mixed systems as well as any coherent short duration (up to few seconds) transient signals. Gravitational-wave sources are detected and public alerts are generated and published over the Global Coordinate Network system with a latency of a few tens of seconds. These alerts provide information about the nature of the source, the probability the event could be due to noise, its most likely 3D location and some indication about a possible electromagnetic counterpart. This latter information is important for the follow-up by world-wide large instruments that search for an electromagnetic counterpart to a gravitational-wave signal, such as GW170817 (Abbott et al., 2017a), the first binary neutron star discovered thanks to its gravitational-wave emission as well as the prompt gamma emission that quickly followed. The afterglow emission of the kilonova has been detected 11 hours after by 1–m class telescopes (Abbott et al., 2017b).

The next important step are the offline searches that target not only transient gravitational-wave signals but also gravitational-wave continuous signals from isolated neutron stars and the stochastic gravitational-wave background resulting from the built-up of all gravitational-wave emission. These searches benefit from improved background rejection (many artefacts are present in the data) and better data calibration. Their sensitivity is improved compared to the low-latency signal detection searches and more refined information about the source parameters are determined.

For well modeled signals such compact binary coalescence all source parameters are estimated using Bayesian inference methods (Christensen and Meyer, 2022). This includes the individual masses and spins, the sky position, the luminosity distance, the polarization and inclination angles, the time and phase of coalescence. For non-compact binary sources, waveform reconstruction assuming generic waveform models is performed (Cornish and Littenberg, 2015).

The proprieties of all the gravitational-wave sources that are considered confidently detected are reported in a catalogue of gravitational-wave sources. The catalogue is regularly updated as explained in the next section. Because gravitational-wave detectors' improvements are challenging, it happens that not all four detectors of the network are observing during official observation runs. This has been for instance the case for KAGRA which joined the third observing run (O3) after LIGO and Virgo had to shutdown earlier than foreseen because of the pandemic in 2020. This is

also the case of Virgo that could not join the first part of the fourth observation run (O4) because its sensitivity and stability were not good enough compared to the LIGO detectors. Despite the fact that the accuracy of the source parameters estimation increases with the number of observing antennas (this is especially the case of the source sky localization), it is possible to detect confidently sources with one or two detectors.

2. THE GWTC-3 CATALOGUE

The third Gravitational-Wave Transient Catalog (GWTC-3) describes sources detected with Advanced LIGO and Advanced Virgo up to the end of their third observing run (O3). It includes all events from previous released catalogs (Abbott et al., 2023a). In total GWTC-3 contains 90 confident detections among which 35 new compact binary coalescences observed during the second half of O3 run between November 2019 and March 2020 by at least one search algorithms with a probability of astrophysical origin $p_{astro} > 0.5$. Of these, 18 were previously reported as low-latency public alerts, and 17 were found offline.

2.1 Population studies

Based upon estimates for the component masses, all sources are consistent with gravitational-wave signals from binary black holes or neutron star–black hole binaries, and none from binary neutron stars, which means that GW170817 and GW190425 are the only identified binary neutron stars mergers. The range of inferred component masses is similar to that found with previous catalogs, but the new candidates include the first confident observations of neutron star–black hole binaries GW200125 and GW200115. Overall, the number of detected events scales with the detectors' network sensitivity increase and the observation duration: 3 detections during the first observing run (O1), 11 in GWTC-1 catalogue after the second observing run (O2), 55 in GWTC-2.1 after the end of the first part of O3 and finally 90 at the end of O3. Some of the source parameters are accurately estimated; this is the case for the chirp mass ($\mathcal{M} = \frac{(m_1 m_2)^{3/5}}{(m_1 + m_2)^{1/5}}$ where m_1 and m_2 are the primary and secondary component mass). This is not the case for the individual spins which have often very wide posterior distributions. What is slightly better measured is χ_{eff} the mass-weighted spin projections onto the orbital angular momentum and the precession spin χ_p that quantifies the orbital precession of the binary. The chirp mass as function of the effective spin of the binary is given in Figure 3. Among the sources in GWTC-3, few have interesting features:

- GW190425 is likely the result of the merger of two neutron stars with components masses of $\sim 1.7 M_\odot$ and $\sim 1.5 M_\odot$ (Abbott et al., 2020a). Contrary to GW170817 no electromagnetic counterpart has been observed for this event. The prompt gamma-ray emission is collimated and only a small fraction of gamma-ray burst are detected. The isotropic afterglow emission has been missed because of the distance (156 Mpc) and the poor sky localization (8200 deg^2). This event was observed by only one LIGO detector. This shows the difficulty of multi-messenger astronomy and the importance of having a network of several detectors observing at the same time. One noteworthy aspect of GW190425 is the high mass of the resulting object after the neutron star merger. The total mass of the system is $\sim 3.4 M_\odot$, making the remnant object more massive than most known neutron stars.
- GW190814 components mass ($\sim 23.3 M_\odot$ and $\sim 2.6 M_\odot$) makes the system the most unequal mass ratio yet measured with gravitational waves and its secondary component is either the lightest black hole or the heaviest neutron star ever discovered in a double compact-object system (Abbott et al., 2020b). It might also be the first observed merger of a black hole with a neutron star.
- GW190521 is the most massive binary black hole merger ever observed with a gravitational-wave signal consistent with the merger of two black holes with masses of $\sim 85 M_\odot$ and

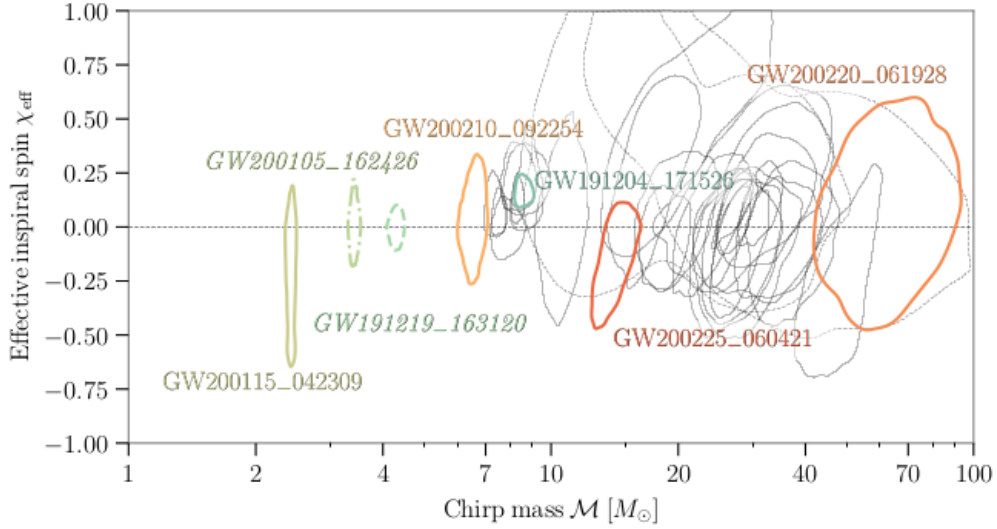


Figure 3: Credible-region contours (90%) in the plane of chirp mass \mathcal{M} and effective spin χ_{eff} for the 35 newest candidates of the GWTC-3 catalog. Figure from Abbott et al., 2023a.

$\sim 66 M_{\odot}$ at 90 % confidence level (Abbott et al., 2020c). What makes it very particular is the fact that the primary black hole mass lies within the gap produced by pulsational pair-instability supernova processes (PPIS), and has only a 0.3% probability of being below $65 M_{\odot}$ which is the lower bound of the PPIS mass gap. The remnant object with a mass of $\sim 142 M_{\odot}$ can be considered an intermediate mass black hole, the first evidence of their existence.

- Two neutron star - black hole mergers have been reported in GWTC-3. The source of GW200105 has component masses $\sim 8.9 M_{\odot}$ and $\sim 1.9 M_{\odot}$, whereas the source of GW200115 has component masses $\sim 5.7 M_{\odot}$ and $\sim 1.5 M_{\odot}$. Despite their large value, the secondary's mass is below the maximal mass of a neutron star with a high probability. After many binary black hole mergers, GW170817 and GW190425, the first observation of mixed systems completes the family of compact object binary systems (Abbott et al., 2021).

GW190814, GW190425 and few others events seem to indicate that the hypothetical mass gap between the heaviest neutron stars ($\sim 2.5 M_{\odot}$) and the lightest black holes ($\sim 5 M_{\odot}$ due to matter fallback accretion onto the newborn black hole) does not exist when all factors such as star's initial mass, rotation, and metallicity are considered (de Sá, 2022). With GW190521 and few other massive mergers, gravitational-wave observation seem also to indicate that the other mass gap between ~ 65 and $\sim 130 M_{\odot}$ is maybe populated by few massive black holes. However GW190521 itself has not permit to conclude if the primary component is the remnant of the collapse of a massive star at the end of its life or the result of a merger of two lighter black holes. In the latter case, this would mean that we have observed the merger of second generation black holes, the first hints of the hierarchical merger process that is privileged to explain how intermediate and super-massive black holes are created. A precise measurement of the component spins would help to estimate the fraction of mergers that are formed from an isolated system of massive stars that overcome a collapse into a black hole. For these systems one expects that the components have aligned their spin. In the case of a dynamical binary black hole formation in dense environment one could expect misaligned spins and thus orbits with precession. The large majority of GWTC-3 mergers do not show any precession. GW200129 is the only merger for which the spin component

in the orbital plane χ_p is not null at 90% confidence level.

The merger rate of the three families of binary systems is more and more precisely measured and the population of binary black hole merger shows that the rate as function of the redshift follows roughly the star formation rate redshift dependence. The primary component mass distribution of the GWTC-3 population is displayed in Figure 4.

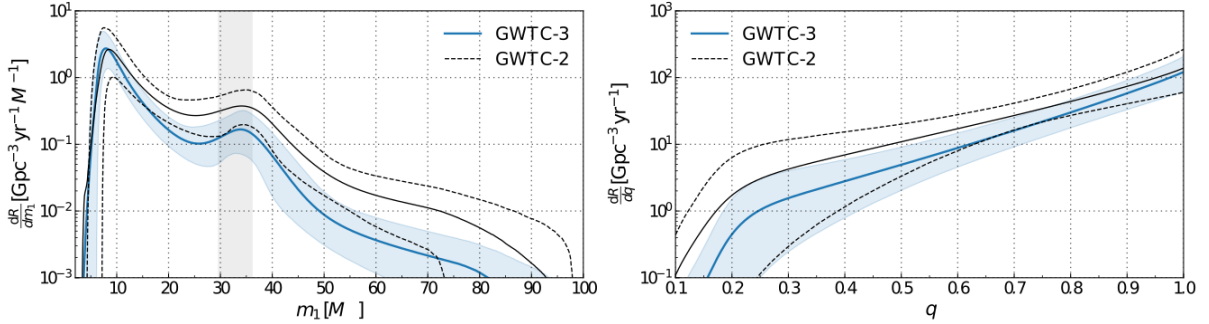


Figure 4: Merger rate as function of primary mass (left) or mass ratio (right) obtained from the GWTC-3 catalog. The solid blue curve shows the posterior population distribution with the shaded region showing the 90% credible interval. The black solid and dashed lines corresponds to the GWTC-2 catalog. Figure from Abbott et al., 2023b.

2.2 Cosmology with gravitational waves

The Hubble constant (H_0) represents the current rate of expansion of the Universe. Gravitational waves can provide a unique and independent way to measure the Hubble constant. The approach involves using standard sirens, which are astrophysical events that emit both gravitational waves and electromagnetic radiation, such as binary neutron star mergers or binary black hole mergers.

Gravitational-wave observations of the merger of two compact objects provide an estimate of the mass and spins of the binary component as well as the luminosity distance to the source. When the compact binary involves a neutron star, electromagnetic radiation, such as gamma-ray burst followed by a kilonova, is emitted. The joint detection of gravitational waves and electromagnetic signals allows for a more precise determination of the source's location in the sky. This helps to determine with small/medium field of view telescopes the host galaxy. Spectrometer measurements can then determine the redshift of the host galaxy. By combining the distance to the source, the redshift, and the speed of light, one can calculate the Hubble constant using the Hubble law: $H_0 = v/d$, where H_0 is the Hubble constant, v is the velocity (determined from the redshift), and d is the distance. This standard sirens method has been used to estimate the Hubble constant with gravitational-wave measurements of GW170817 ($70.0^{+12.0}_{-8.0} \text{ km s}^{-1} \text{ Mpc}^{-1}$) (Abbott et al., 2017c). Besides, an accurate measurement of the Hubble constant from standard siren GW cosmology also requires a robust peculiar velocity correction of the redshift of the host galaxy. For sources without an electromagnetic counterpart, such as binary black hole mergers (dark standard sirens), alternative techniques to infer the source redshift are considered (Abbott et al., 2023c): the first method include comparing the redshifted mass distribution to an astrophysically-motivated source mass distribution to extract the redshift. The second method associates each binary black hole merger with its probable host galaxy in the catalog GLADE+, statistically marginalizing over the redshifts of each event's potential hosts. Both methods have shortcomings and are impacted by assumptions either about the binary black hole source mass distribution or are affected by the rather large error box in the sky of the source location. This makes most of the binary black hole

sources, except the well-located source GW190814, rather uninformative about H_0 .

Using gravitational waves to measure the Hubble constant with standard sirens or the dark sirens (binary black hole mergers) provides a direct and independent method that complements other cosmological measurements. This approach is not affected by the same systematic uncertainties as some traditional methods (e.g., those based on the cosmic microwave background or type Ia supernova), making it valuable for improving the precision of our understanding of the current expansion rate of the Universe. The comparison of the different methods is given in Figure 5.

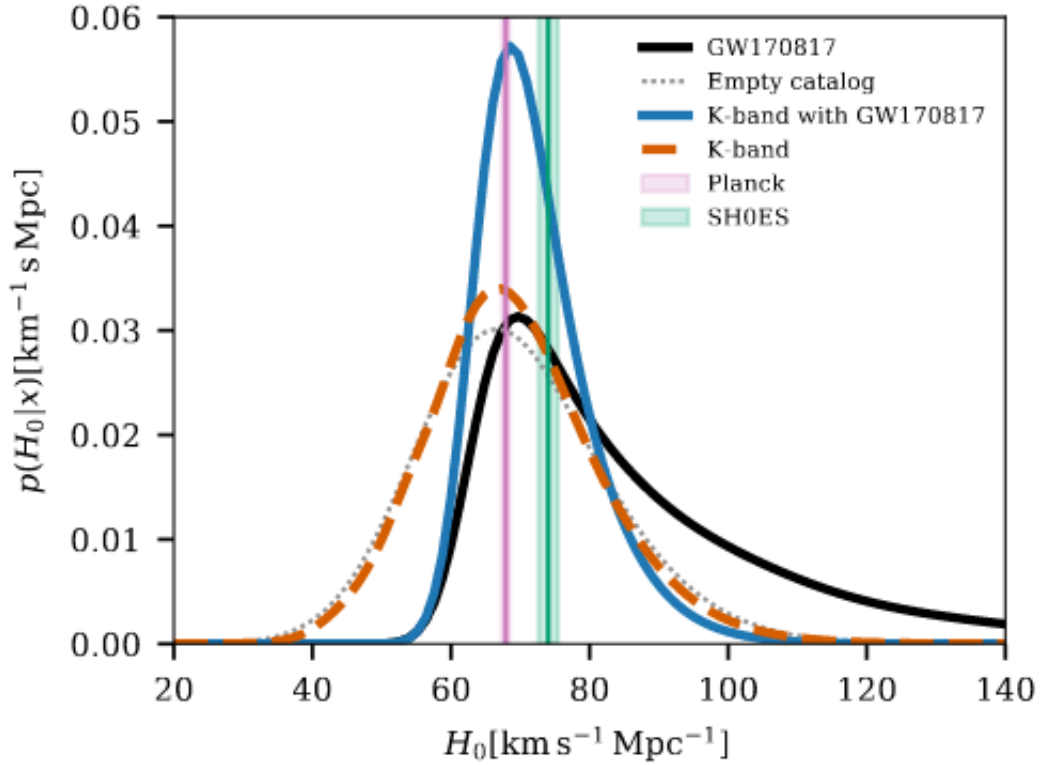


Figure 5: Hubble constant posterior for several cases: posterior obtained using all dark sirens without any galaxy catalog information and fixing the BBH population model (gray dotted line), posterior using all dark sirens with GLADE+ K-band galaxy catalog information and fixed population assumptions (orange dotted line). Posterior using GW170817 (black line). In blue, posterior combining all previous posteriors. The pink and green shaded areas identify the 68% confidence interval constraints on H_0 inferred from the CMB anisotropies and in the local Universe from type Ia supernovae. Figure from Abbott et al., 2023c.

2.3 Testing general relativity

As already mentioned, gravitational-wave observations provide a unique opportunity to test and confirm various aspects of the theory of general relativity under extreme conditions. Some of the main tests of general relativity facilitated by gravitational waves include:

- **Waveform Consistency:** One of the primary tests involves comparing the observed gravitational waveforms with the predictions of general relativity. Any deviations in the waveform could indicate the presence of alternative theories of gravity or additional phenomena not accounted for in general relativity.

- Speed of Gravitational Waves: general relativity predicts that gravitational waves propagate at the speed of light. By precisely measuring the arrival times of gravitational waves at different detectors, scientists can test this prediction and constrain potential deviations from the speed of light.
- Polarization of gravitational waves: gravitational waves can have different polarizations, and the patterns of these polarizations are dictated by general relativity. Observations of gravitational-wave polarization can provide additional confirmation of the theory.
- Mass and spin measurements: gravitational-wave signals from binary black hole or neutron star mergers contain information about the masses and spins of the involved objects. Comparing these measurements with the predictions of general relativity allows to test the theory in strong-field environments.
- No-hair theorem: The no-hair theorem in general relativity suggests that the observable properties of a black hole are determined solely by its mass, its spin and its charge. Gravitational-wave observations help test and confirm this theorem by providing precise measurements of the events' properties.

By subjecting general relativity to tests in environments with strong gravitational fields and dynamics, gravitational-wave astronomy contributes to the understanding of gravity and provides an opportunity to discover potential deviations from Einstein's theory. So far, the observations have been consistent with general relativity (Abbott et al., 2023d).

3. CONCLUSION

Gravitational-wave detections have provided valuable insights into the population of black holes, revealing information about their masses, spins, and the nature of their mergers. Many observations have already changed our description of the content of the Universe. Gravitational-wave observations have helped establish a mass spectrum for black holes. Prior to these detections, the masses of stellar-mass black holes were only indirectly inferred. We now know the mass spectrum is more complex and there might be a continuum between neutron star and the lightest black hole as well as no mass gap between 65 and 130 M_{\odot} . Gravitational-wave signals also carry information about the spins of the merging black holes. The analysis of these spins provides insights into the formation and evolution of binary systems, as well as the dynamics of massive stellar collapse. Gravitational-wave events have provided constraints on the possible formation scenarios for binary black hole systems. For example, they have contributed to our understanding of the role of common envelope evolution, metallicity, the stability of massive binary systems, and the importance of dynamical interactions in dense stellar environments. Gravitational-wave observations have implications for cosmology, as they provide a new tool for measuring distances to merging black hole systems and testing the expansion of the Universe. Finally they are a unique probe to test general relativity in a strong field regime.

So far only compact binary mergers have been detected. Yet, other sources of gravitational waves are possible: core collapse supernovae, pulsars, neutron star binary systems, newly formed black holes, or even early Universe inflation. The observation of these types of events would be extremely significant for contributing to knowledge in astrophysics and cosmology. Gravitational waves from the Big Bang would provide unique information of the Universe at its earliest moments. Observations of core-collapse supernovae will yield a gravitational snapshot of these extreme cataclysmic events. Pulsars are neutron stars that can spin on their axes at frequencies up to hundreds of hertz, and the signals (due to a slight non-spherical shape) from these objects will help to decipher their characteristics and aid in studying ultra-dense nuclear matter.

To continue observing new sources of gravitational waves we need a performant network of detectors. Increasing the sensitivity of ground based detectors turns out to be extremely challenging. It is expected that the LIGO-Virgo-KAGRA network be joined by another detector in India before the end of the decade. In the longer term, the space-mission LISA, whose launch is planned in 2035, will complement ground-based gravitational-wave detectors in the milliHertz regime.

4. REFERENCES

- Aasi, J. et al., 2015, "Advanced LIGO", *Class. and Quant. Gravity* 32(7), 074001, doi:10.1088/0264-9381/32/7/074001
- Abbott, B. et al., 2017a, "GW170817: Observation of Gravitational Waves from a Binary Neutron Star Inspiral", *Phys. Rev. Lett.* 119 (16) 161101, doi.org/10.1103/PhysRevLett.119.161101
- Abbott, B. et al., 2017b, "Multi-messenger Observations of a Binary Neutron Star Merger", *Astrophys. J.* 848 (2) L12, doi.org/10.3847/2041-8213/aa920c
- Abbott, B. et al., 2017c, "A gravitational-wave standard siren measurement of the Hubble constant", *Nature* 551 (7678) 85–88, doi.org/10.3847/2041-8213/aaf96e
- Abbott, B. et al., 2020a, "GW190425: Observation of a Compact Binary Coalescence with Total Mass $\sim 3.4 M_{\odot}$ ", *Astrophys. J. Lett.* 892 (1) L3, doi.org/10.3847/2041-8213/ab75f5
- Abbott, R. et al., 2020b, "GW190814: Gravitational Waves from the Coalescence of a 23 Solar Mass Black Hole with a 2.6 Solar Mass Compact Object", *Astrophys. J. Lett.* 896 (2) L44, doi.org/10.3847/2041-8213/ab960f
- Abbott, R. et al., 2020c, "GW190521: A Binary Black Hole Merger with a Total Mass of $150 M_{\odot}$ ", *Phys. Rev. Lett.* 125 (10) 101102, doi.org/10.1103/PhysRevLett.125.101102
- Abbott, R. et al., 2021, "Observation of Gravitational Waves from Two Neutron Star's Black Hole Coalescences", *Astrophys. J. Lett.* 915 (1) L5, doi.org/10.3847/2041-8213/ac082e
- Abbott, R. et al., 2023a, "GWTC-3: Compact Binary Coalescences Observed by LIGO and Virgo during the Second Part of the Third Observing Run", *Phys. Rev. X* 13 (4) 041039, doi.org/10.1103/PhysRevX.13.041039
- Abbott, R. et al., 2023b, "Population of Merging Compact Binaries Inferred Using Gravitational Waves through GWTC-3", *Phys. Rev. X* 13 (1) 011048, doi.org/10.1103/PhysRevX.13.011048
- Abbott, R. et al., 2023c, "Constraints on the Cosmic Expansion History from GWTC-3", *Astrophys. J.* 949 (2) 76, doi.org/10.3847/1538-4357/ac74bb
- Abbott, R. et al., 2023d, "Tests of General Relativity with GWTC-3", accepted for publication, arXiv:2112.06861
- Acernese, F. et al., 2015, "Advanced Virgo: a second-generation interferometric gravitational wave detector", *Class. and Quant. Gravity* 32(2), 024001, doi.org/10.1088/0264-9381/32/2/024001
- Akutsu, T. et al., 2021, "Overview of KAGRA: Detector design and construction history", *PTEP*, 2021(5), 05A101, doi.org/10.1093/ptep/ptaa125
- Christensen, N., Meyer, R., 2022, "Parameter estimation with gravitational waves", *Rev. Mod. Phys.* 94(2), 025001, doi.org/10.1103/RevModPhys.94.025001
- Cornish, N, Littenberg, T., 2015, "BayesWave: Bayesian Inference for Gravitational Wave Bursts and Instrument Glitches", *Class. and Quant. Gravity* 32(13), 135012, doi.org/10.1088/0264-9381/32/13/135012
- de Sá, L., Bernardo, A., Bachega, R., Horvath, J., Rocha, L., Moraes, P., 2022, "Quantifying the Evidence Against a Mass Gap between Black Holes and Neutron Stars", *Astrophys. J.* 941 (2) 130, doi.org/10.3847/1538-4357/aca076
- The LIGO-Virgo-KAGRA collaboration, 2024, "The International Gravitational-wave Network observing plan", <https://observing.docs.ligo.org/plan/>

RESULTS FROM THE SEARCH FOR THE VERY-LOW FREQUENCY GRAVITATIONAL WAVES WITH THE EPTA DR2 AND THE INPTA DR1

A. CHALUMEAU^{1,2}. On behalf of the European Pulsar Timing Array collaboration.

¹ Dipartimento di Fisica “G. Occhialini”, Università degli Studi di Milano-Bicocca,

Piazza della Scienza 3, I-20126 Milano, Italy - aurelien.chalumeau@unimib.it

² INFN, Sezione di Milano-Bicocca, Piazza della Scienza 3, I-20126 Milano, Italy

ABSTRACT. The European Pulsar Timing Array (EPTA) and Indian Pulsar Timing Array (InPTA) collaborations have measured a very-low frequency (nano-Hertz) common signal with correlation properties compatible with a gravitational wave (GW) signal. This paper presents the results of the gravitational wave background search and the implications of such measurements on different expected GW sources. This extensive effort has been carried out in coordination with other Pulsar Timing Array collaborations, resulting in four independent analysis. The last part of the paper is focusing on a cross-check comparison analysis of the different results applied by the International Pulsar Timing Array (IPTA) collaboration, followed by a brief discussion on the prospects for the GW search and characterization with the forthcoming IPTA Data Release 3.

1. INTRODUCTION

Pulsar Timing Arrays (PTAs) use ultra-precise measurements of pulse arrival times (referred as “times of arrival”, or ToAs) from millisecond pulsars (MSPs) to probe the gravitational waves in the $10^{-9} - 10^{-7}$ Hz band. This signal is expected to be mainly observed as a stochastic background (GWB) appearing as a delay in the ToAs that is coherent among pulsars. The quadrupolar nature of gravitational waves implies a particular signal correlation for each pair of pulsars, described analytically by the Hellings-Downs curve (Hellings & Downs 1983) for an isotropic GWB. These correlations allow us to (1) confirm the gravitational nature of the signal, and (2) precisely separating and characterize it from any other noise in the data.

The European PTA (EPTA) and the Indian PTA (InPTA) collaborations have recently combined their efforts to search for very-low frequency gravitational waves (GWs) with their most precise data sets, leading to the first measurements with evidence for such GWs. A serie of six articles have been published on June 29 2023, presenting the data set, the timing and noise analysis, the GW searches and the interpretation of the measured signal on expected GW sources. In the same day, three other PTA collaboration have published their own results on the search for nano-Hertz GWs with consistent results. This document first describes the results obtained by the EPTA and the InPTA, firstly on the signal measurement and then on the interpretation on the GW sources. The last section briefly presents a consistency check analysis that was performed by the International Pulsar Timing Array (IPTA) collaboration aiming to ensure a proper comparison among the different results.

2. DATA AND RESULTS

This section briefly introduces the EPTA DR2 data sets and describes the timing, noise and GWB analysis that are respectively presented in EPTA Collaboration et al., 2023a, EPTA Collab-

oration et al., 2023b and EPTA Collaboration et al., 2023c.

1.1 The data set

The EPTA uses data from five large European radio telescopes: the Effelsberg 100-m radio telescope in Germany, the 76-m Lovell telescope in the United Kingdom, the large Nançay radio telescope in France, the 64-m Sardinia radio telescope in Italy and the Westerbork Synthesis Radio Telescope in the Netherlands. These instruments regularly observe simultaneously to operate as the Large European Array for Pulsars (LEAP), which offers an equivalent diameter of 194-m. The second data release (DR2) of the EPTA (EPTA Collaboration et al., 2023a) is composed of ~ 25 years of data for 25 of the most stable and precisely timed MSPs. These pulsars have been chosen from a previous analysis (Speri et al., 2022) which provided a pulsar ranking scheme to select a sufficient number of MSPs without losing theoretical sensitivity to GWs. The EPTA DR2 was also combined with low radio frequency pulsar timing data from the InPTA DR1 (Tarafdar et al., 2022) for 10 MSPs that are common to the EPTA DR2. For the analysis, we considered two versions of the data set: the full EPTA DR2 ("DR2full") and a truncated version that only includes the data collected with new generation of pulsar observing systems ("DR2new"). If the DR2full has a larger observing time span (~ 25 years vs. ~ 10 years), allowing to search at lower frequencies which also improves the GW frequency resolution, the DR2new only includes precised pulsar timing data with significantly higher observing cadence (\sim weekly). The DR2new also contains data with mostly large radio frequency observing bandwidths, which is crucial to correct for the dispersion effects of the ionized interstellar medium (IISM) on the radio pulses.

1.2 Timing and noise analysis

The pulsar timing analysis consists of fitting a timing model to the ToAs for each pulsar. The timing model typically includes the pulsar spin frequency and its first derivative, its sky position and proper motions, the measure of IISM dispersion (constant and first time-dependent derivatives), and the keplerian and post-newtonian orbital components if presence of a companion. For each of the 25 pulsars in the EPTA DR2, we evaluated a precise timing model (EPTA Collaboration et al., 2023a), from which we derived astrophysical quantities such as distances, transverse velocities, binary pulsar masses and annual orbital parallaxes. The differences between the observed ToAs and the ones predicted by the timing model are the pulsar timing residuals which might contain the very-low frequency GWs. It is in practice crucial to properly model the remaining noise that is not included in the timing model. The standard analysis includes the stochastic noise often named after its spectral properties. The "white noise" (with a flat spectrum) is modeled to take into account the ToA measurement noise and the pulse shape stochasticity (jitter). The "red noise", with an increasing Power Spectral Density (PSD) amplitude to the low frequencies, corresponds to the long-term effects such as pulsars' internal processes modulating the pulsar's rotational frequency, or the presence of unmodelled massive bodies (exoplanets, asteroids, etc.) in the vicinity of the pulsar. Temporal variations of the dispersion caused by stochastic fluctuations of the electron density in the IISM between the pulsar and the Earth induce a red noise which in turn depends on the radio frequency, where dispersion represents a pulse delay inversely proportional to the square of the observed radio frequency. It is thus important for PTAs to have sufficient radio frequency coverage to correct for the time variations of the IISM dispersion. Before to run the GW searches, we have performed detailed noise analysis for each of the EPTA DR2 pulsars (EPTA Collaboration et al., 2023b), and improved the approach proposed in Chalumeau et al. (2022) to optimize the noise models for each pulsars based on a Bayesian model selection scheme.

1.3 The Gravitational Wave Background search

After obtaining the timing and noise models, we could perform the search for the GWB signal expected to appear as a red noise in the timing residuals with Hellings & Downs spatial correlations

(EPTA Collaboration et al., 2023c). The search has been performed by using two pipelines with independent softwares to model the signals and noise components. Both Bayesian and frequentist analysis have been applied to constrain the spectral properties of the GWB and evaluate the significance of the signal (i.e., model selection for the Bayesian part). The GWB spectrum is modeled as a simple powerlaw defined with a spectral index γ_{GWB} and a PSD amplitude A_{GWB} set at a reference frequency of $f_{\text{yr}} = 1\text{yr}^{-1}$, as

$$S_{\text{GWB}}(f) = \frac{A_{\text{GWB}}^2}{12\pi^2} \left(\frac{f}{1f_{\text{yr}}} \right)^{-\gamma_{\text{GWB}}} \frac{f_{\text{yr}}^{-3}}{T}, \quad (1)$$

where T is the total time span of the analysed data set. With these units, the spectral index of a signal generated by a population of circular and GW-driven supermassive black hole binaries (SMBHBs) would be at $\hat{\gamma}_{\text{GWB}} = -13/3$.

For the Bayesian analysis, the two-dimensional parameter posterior distributions of A_{GWB} ("gw_log10_A") and γ_{GWB} ("gw_gamma") are shown in the right panel of Figure 1. The DR2full data, in orange, yields to an amplitude at $\log_{10} A_{\text{GWB}} = -14.54^{+0.28}_{-0.41}$ (median and 90% credible regions) and a spectral index at $\gamma_{\text{GWB}} = 4.19^{+0.73}_{-0.63}$, thus consistent with the expected value from a population of SMBHBs. However, the DR2new (blue) constrains a shallower spectrum, with a higher amplitude at f_{yr} : $\log_{10} A_{\text{GWB}} = -13.94^{+0.23}_{-0.48}$ and $\gamma_{\text{GWB}} = 2.71^{+1.18}_{-0.73}$. Nevertheless, the two results remain consistent in the sense that the two posterior probabilities overlap and lie on the same $A - \gamma$ degeneracy line that corresponds to fixing the total Hellings-Downs correlated power. Therefore, this correlated power measured in DR2full and DR2new is comparable, although the spectral shape is not well constrained and appears to be different in the two data sets (cf. left panel of Figure 1). For the model selection analysis, the PTA community generally uses a model that contains both the noise and a non-spatially correlated common red noise (CURN) as a null hypothesis, while the GWB signal includes the Hellings-Downs signature for the common red noise.

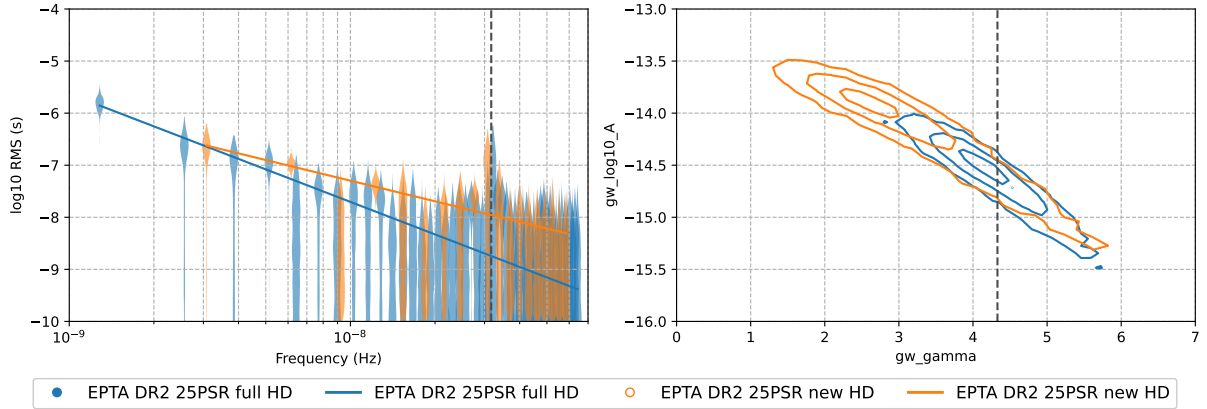


Figure 1: Spectral properties of a GWB measurements with the EPTA DR2full (blue) and the DR2new (orange), either by fitting for the amplitude at each PSD frequency independently (left panel), or by modeling the GWB with a power-law PSD (right panel) with a spectral index "gw_gamma" and an amplitude "gw_log10_A", referenced at the frequency $f_{\text{yr}} = 1\text{yr}^{-1}$. The solid lines in the left panel are the power-law models with best-fit parameters, while the vertical dashed line indicates the position of f_{yr} . The black vertical dashed line in the right panel indicates $\hat{\gamma}_{\text{GWB}}$, the expected spectral index from a SMBHB population. EPTA Collaboration et al. (2023c).

The Bayes factor between these two models leads to significant results for the DR2new with a value of $\mathcal{B}_{\text{CURN}}^{\text{GWB}} = 60$, that is however only 4 for the DR2full. It is still under investigation why the significance of the signal is reduced when including the first half of the data in the analysis.

The diluted significance of the signal might be due to a lack of radio frequency coverage of the older data, where the time-variations of the dispersion could be hardly separated from the subtle GWB signal. If it is the case, combining the data with other collaborations at the IPTA level could potentially resolve the issue.

For the frequency analysis, we fix the spectral index to $\gamma_{\text{GWB}} = 13/3$, and compute the amplitude and signal-to-noise S/N estimates of the GWB following a method developed in Vigeland et al. (2018) and references therein. We obtained measurements at $A_{\text{GWB}}^2 = 2.7^{+3.0}_{-2.5} \times 10^{-30}$ (DR2full) and $A_{\text{GWB}}^2 = 10.0^{+5.1}_{-4.9} \times 10^{-30}$ (DR2new) with S/N estimates respectively at $1.3^{+1.3}_{-1.2}$ and $3.5^{+2.4}_{-1.7}$. Both measurements overlap with the Bayesian credible regions, and consistently the signal appears brighter for the DR2new. To estimate a significance of the hypothesis that a GWB signal is present in the data, a null hypothesis distribution must be constructed. However, since we are observing a persistent signal ("permanent background"), it is unfortunately not possible for PTA experiments to perform other realizations and obtain a correct p-value for the null hypothesis. There are however two approaches allowing to build null realizations of the data: 1) introducing random phase shifts of the signal for every pulsar (Taylor et al., 2017); 2) moving the positions of pulsars in the sky ("sky scrambles"; Cornish & Sampson, 2016). Both methods aim at removing the Hellings & Downs spatial correlations, while keeping the noise properties. From the phase shift approach, we obtained a p-value of 0.07 and < 0.0001 (corresponding to a significance of $> 3.5\sigma$) respectively for DR2full and DR2new. For the latter, the p-value is an upper-limit because the S/N of all the null realizations was below the measured one. The p-values for the sky scramble approach were obtained at 0.08 (DR2full) and 0.004 (DR2new).

2. IMPLICATIONS FOR MASSIVE BLACK HOLES AND THE EARLY UNIVERSE

The following part focuses on the implication of measurements obtained with the DR2new only on chosen GW sources. It describes part of the analysis presented in Antoniadis et al. (2023).

2.1 The supermassive black hole binaries

The primary expected source of the GWB is the nearby population ($z \leq 2$) of SMBHBs with masses greater than $10^7 M_{\odot}$, formed via the multiple interactions of their host galaxies throughout the history of the Universe. The frequency band visible by PTA allows us to observe a phase of quasi-stable orbits with periods of around 0.1 to 10 years, preceding the merger phase that will be visible by the future LISA detector. Characterizing the GWB spectrum at the nano-Hertz would place unique constraints on the properties of SMBHBs and their close environment (stars, accretion disk, ...), which would provide a new observable for models of galaxy formation and evolution (Sesana, 2013).

Many studies have been focused on the investigation of the GWB produced by a population of SMBHBs, leading to predictions on the expected signals by employing different models and techniques. The SMBHB models could be classified into two categories: empirical models based on observed properties of galaxy pairs coupled to SMBH-host galaxy relations (Sesana, 2013; Rosado et al., 2015), and self-consistent theoretical models for SMBH evolution within their galaxies (Sesana et al., 2008; Izquierdo-Villalba et al., 2022), which contains both semianalytical models and large cosmological simulations. The main difference is that self-consistent models are constructed to reproduce a large array of observations related to galaxies and the SMBH they host (redshift-dependent galaxy mass function, quasar luminosity function, ...). Conversely, empirical models are, by construction, consistent with the observations upon which they are based, but are usually not tested against independent constraints. As a consequence, they can generally produce higher GWB amplitudes, but consistency with other observations is not necessarily guaranteed. As for my presentation, this part only focuses on the comparison study between the measured signal with

the DR2new and predictions of empirical models: an extended version of the Rosado et al. (2015) models including binary eccentricity and environmental coupling. In total, about 324k realizations of GWB signals from carefully chosen SMBHB models have been drawn. The distribution of all signals are represented in Figure 2 as green violin histogram spectrum, and compared with the DR2new measurements shown in orange violins. The two set of distributions are in good agreement in the few lowest frequency bins, where measurements are the most constraining. Note that the model prediction distributions are highly non-Gaussian and asymmetric, with long tails extending upwards, due to the fact that low number of very massive and/or nearby SMBHBs can sometimes produce exceptionally loud signals, as illustrated by the 100 individual GWBs realizations plotted as black transparent lines in Figure 2. This property could in fact explain the extra power measured in the 4th lowest frequency bin. Note that the 9th lowest bin corresponds to a frequency near $\sim f_{yr}$, where PTAs have very poor sensitivity caused by the motion of the earth in the solar system. The empirical models can indeed account for the observed signal, shown by the black solid line in Figure 2, which represents an arbitrary GWB realization that is almost perfectly coinciding with the DR2new spectrum.

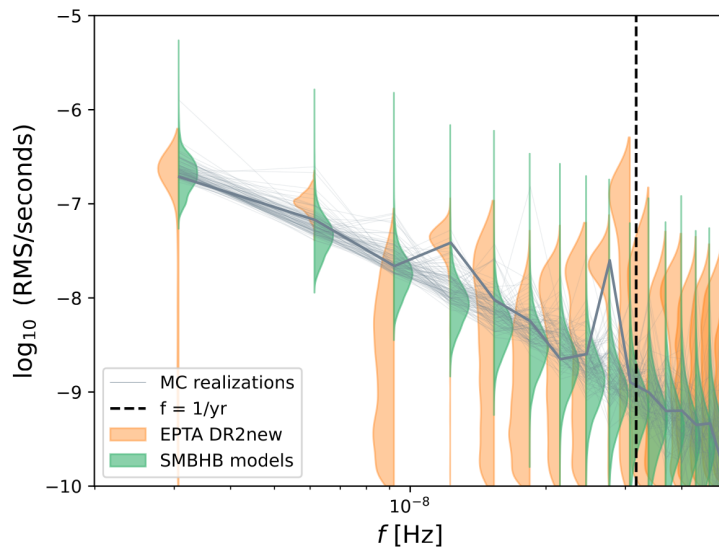


Figure 2: Free spectrum violin plot comparing measured (orange) and expected (green) signals. Overlaid to the violins are the 100 Monte Carlo realizations of one specific model; among those, the thick one represents an example of a SMBHB signal consistent with the excess power measured in the data at all frequencies. Antoniadis et al. (2023).

2.2 GW sources from the early Universe

Other exotic sources could contribute to the GWB in the PTA band such as processes related to the early Universe. As for the SMBHB, their signal will appear as a red noise with Hellings & Downs correlations in the timing residuals. They still might induce different spectral shapes which can help to disentangle different origins of backgrounds. However, due to the low significance of the signal in the EPTA data, each model has been analysed separately and no model selection was performed. Four possible scenarios have been considered: (1) a GWB from a network of cosmic strings, where both "BOS" and "LRS" models were tested; (2) a GWB from vortical (M)HD turbulence at the QCD energy scale; (3) an inflationary GWB from the amplification of quantum fluctuations of the gravitational field; (4) a scalar-induced GWB inflationary scalar perturbations at the 2nd order in perturbation theory. In Figure 3 are shown the spectral properties of stochastic GWB backgrounds from each of the considered sources by fixing their model parameters to values inferred from the DR2new (grey violins).

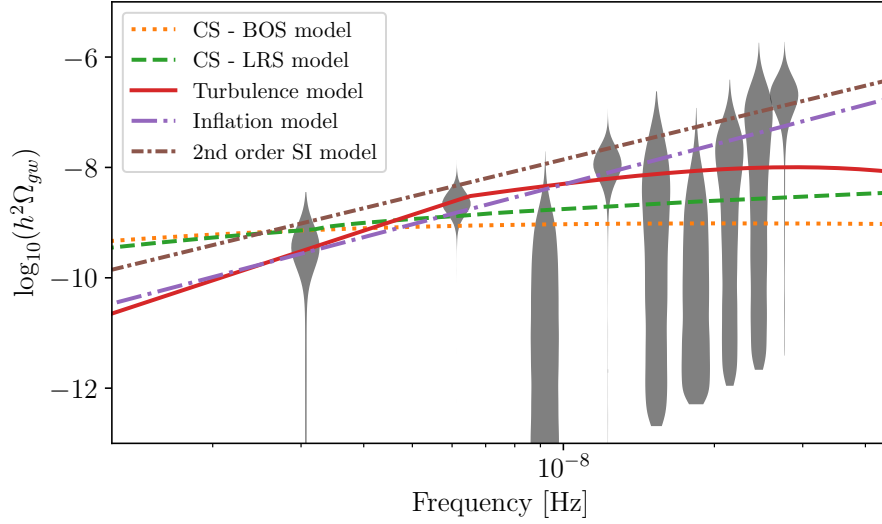


Figure 3: Stochastic GWB spectra (in terms of $\log_{10} h^2 \Omega_{gw}$) inferred by using the EPTA DR2new (grey violin areas) for four different early Universe GWB models: a cosmic string network modeled with two approaches, BOS and LRS; turbulence at the QCD energy scale; amplified quantum fluctuations of the gravitational field from inflation; inflationary scalar perturbations at the 2nd order in perturbation theory. Antoniadis et al. (2023).

- *Cosmic string network*: Cosmic strings are line-like topological defects that may form after a symmetry-breaking phase transition in the early Universe. These one-dimensional objects are characterized by the string tension $G\mu$ (or equivalently their energy per unit length) which is related to the energy scale of the phase transition. As seen in Figure 3, the most favored set of parameters for both BOS and LRS models cannot properly fit the measured with DR2new, mainly because the predicted GWB from cosmic strings is generally steeper.
- *Turbulence at the QCD energy scale*: Turbulence can arise in the early Universe in the aftermath of a first-order phase transition, or can be driven by pre-existing primordial magnetic fields. If the (magneto-)hydrodynamic turbulence were present around the QCD epoch, when the Universe had a temperature of $T_* \sim 100$ MeV, it would generate a GWB in the PTA band. The characteristic scale of the turbulence, determining the characteristic GW frequency, is in fact related to the (comoving) Hubble radius at that epoch. In Figure 3 is shown that (M)HD turbulence at the QCD energy scale can potentially explain the signal measured with DR2new, but it would require either high turbulent energy densities, of the same order of the radiation energy density, or a characteristic turbulent scale close to the horizon at the QCD epoch.
- *Primordial (inflationary) GWs*: In the standard inflationary scenario, tensor quantum vacuum fluctuations of the metric are amplified by the accelerated expansion and generate a GWB as they subsequently re-enter the horizon during the radiation or matter era. The DR2new spectrum is consistent with such GWB (cf. Figure 2), but it would require non-standard inflationary scenarios breaking the slow-roll consistency relation.
- *2nd order perturbation theory*: Scalar curvature perturbations will source propagating tensorial modes (GWs) at the 2nd order in perturbation theory. Such scalar curvature perturbations and associated primordial density fluctuations inevitably exist in the Universe and can be directly constrained by observations of the Cosmic Microwave Background (CMB). The GWB model also fits well with DR2new constraints, but only if an excess of the scalar perturbation

primordial spectrum is present at large wavenumbers compared to the level derived from CMB observations at small wavenumbers.

3. CONTEXT & FUTURE PROSPECTS

Along with the EPTA, other PTA collaborations have simultaneously published their work on the search for the very-low frequency GWs: NANOGrav (Agazie et al., 2023), Parkes Pulsar Timing Array (PPTA; Reardon et al., 2023), and the Chinese PTA (Xu et al., 2023). A follow-up analysis has been performed within the IPTA to ensure the consistency among the published results (The International Pulsar Timing Array Collaboration et al., 2023). In Figure 4 are shown the GWB measurements from the various PTAs and their broad consistency. Some of these differences are likely caused by the very different properties of data sets (radio frequency coverage, cadence, time span, ...). To respond to this issue, the full noise analysis and a GWB analysis have been reproduced by using similar noise models. This detailed study has confirmed the high consistency of the results, and allowed us to target the pulsars where inconsistencies in the data analysis should be further investigated.

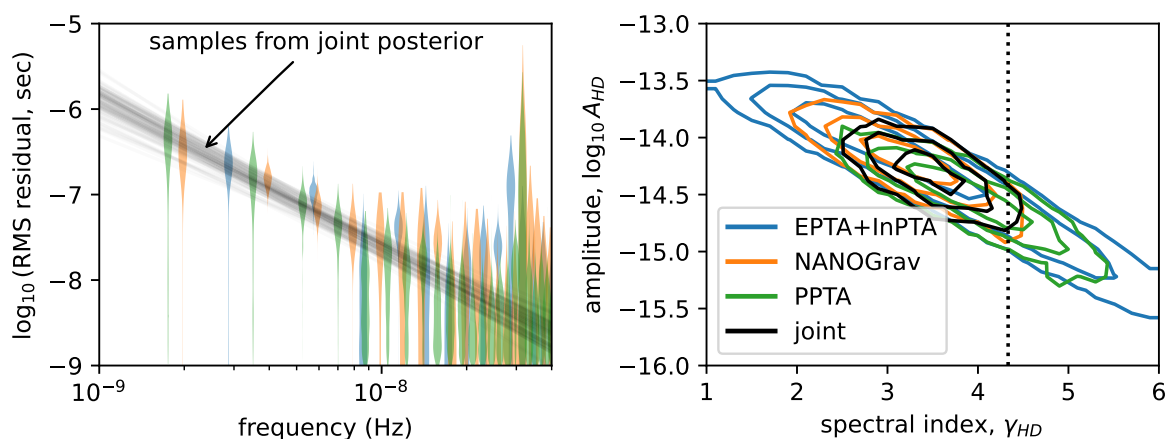


Figure 4: *Left*: Free spectral posteriors for each PTA collaboration showing the measured Hellings-Downs correlated GWB power in several frequency bins under no spectral shape assumption. Each PTA used a different Fourier basis set by their own maximum observing time. The semitransparent gray lines are 100 samples from the joint 2D power law posterior distribution, showing the spread of powerlaw models that are consistent with all of the PTA's data. *Right*: 2D posterior for Hellings-Downs correlated power law GWB parameters. Contours show 68, 95, and 99.7% of the posterior mass. The vertical dotted line is at $\gamma = 13/3$. The International Pulsar Timing Array Collaboration et al. (2023).

The global effort is currently mainly centered on building the third data release of the IPTA collaboration, which will contain most of the world's accessible data in order to obtain the best sensitivity achievable for the next few years. If the gravitational origin of the signal is confirmed, it will be necessary to use such improved data quality to understand its origins (astrophysical ? cosmological ?).

4. REFERENCES

Agazie, G., et al., 2023, "The NANOGrav 15 yr Data Set: Evidence for a Gravitational-wave Background", *ApJL*, 951, L8

- Antoniadis, J., et al., 2023, "The second data release from the European Pulsar Timing Array: V. Implications for massive black holes, dark matter and the early Universe", arXiv e-prints, arXiv:2306.16227 (in press, accepted in A&A)
- Chalumeau, A., et al., 2022, "Noise analysis in the European Pulsar Timing Array data release 2 and its implications on the gravitational-wave background search", MNRAS 509, 5538
- Cornish, N. J., Sampson, L., 2016, "Towards robust gravitational wave detection with pulsar timing arrays", Phys. Rev. D 93, 104047
- EPTA Collaboration et al., 2023a, "The second data release from the European Pulsar Timing Array. I. The dataset and timing analysis", A&A 678, A48
- EPTA Collaboration et al., 2023b, "The second data release from the European Pulsar Timing Array. II. Customised pulsar noise models for spatially correlated gravitational waves", A&A 678, A49
- EPTA Collaboration et al., 2023c, "The second data release from the European Pulsar Timing Array. III. Search for gravitational wave signals", A&A 678, A50
- Hellings, R. W., and Downs, G. S., 1983, "Upper limits on the isotropic gravitational radiation background from pulsar timing analysis.", ApJL 265, L39
- Izquierdo-Villalba, D., et al., 2022, "Massive black hole evolution models confronting the n-Hz amplitude of the stochastic gravitational wave background", MNRAS 509, 3488
- Speri, L., et al., 2022, "Quality over quantity: Optimizing pulsar timing array analysis for stochastic and continuous gravitational wave signals", MNRAS 518, 1802
- Tarafdar, P., et al., 2022, "The Indian Pulsar Timing Array: First data release", PASA 39, e053
- Reardon, D. J., et al., 2023, "Search for an Isotropic Gravitational-wave Background with the Parkes Pulsar Timing Array", ApJL 951, L6
- Rosado, P. A., et al., 2015, "Expected properties of the first gravitational wave signal detected with pulsar timing arrays", MNRAS 451, 2417
- Sesana, A., et al., 2008, "The stochastic gravitational-wave background from massive black hole binary systems: implications for observations with Pulsar Timing Arrays", MNRAS 390, 192
- Sesana, A., 2013, "Systematic investigation of the expected gravitational wave signal from super-massive black hole binaries in the pulsar timing band.", MNRAS 433, L1
- Taylor, S. R., et al., 2017, "All correlations must die: Assessing the significance of a stochastic gravitational-wave background in pulsar timing arrays", Phys. Rev. D 95, 042002
- The International Pulsar Timing Array Collaboration, et al., 2023, "Comparing recent PTA results on the nanohertz stochastic gravitational wave background", arXiv e-prints, arXiv:2309.00693
- Vigeland, S. J., et al., 2018, "Noise-marginalized optimal statistic: A robust hybrid frequentist-Bayesian statistic for the stochastic gravitational-wave background in pulsar timing arrays", Phys. Rev. D 98, 044003
- Xu, H., et al., 2023, "Searching for the Nano-Hertz Stochastic Gravitational Wave Background with the Chinese Pulsar Timing Array Data Release I", RAA 23, 075024

THE MICROSCOPE SPACE MISSION TO TEST THE EQUIVALENCE PRINCIPLE

G. MÉTRIS¹, M. RODRIGUES², J. BERGÉ²

¹ Université Côte d'Azur, Observatoire de la Côte d'Azur, CNRS, Géoazur - France
- gilles.metris@oca.eu

² DPHY, ONERA, Université Paris Saclay - France

ABSTRACT. The MICROSCOPE mission tested the Weak Equivalence Principle (WEP) with an unprecedented precision of order 10^{-15} , two orders of magnitude better than the previous best lab experiments. While the WEP, the cornerstone of General Relativity (GR), does not sway, the decade-long problems faced by fundamental physics stay still: how can we unify GR with the Standard Model, and how can we explain the acceleration of the cosmological expansion? As most beyond-GR models predict a violation of the WEP, albeit at an unknown level, it remains critical to even better test the WEP. In this paper, we review the MICROSCOPE mission and give its final constraint on the WEP.

1. INTRODUCTION

The universality of free-fall (UFF) has been recognised since Galileo rolled objects down inclined planes and found that, locally, they all undergo the same gravitational acceleration: all objects within the same gravitational field fall at the same rate, independently of their mass and composition. With Newton's second law, the UFF can be restated as the proportionality between the gravitational mass m_G and the inertial mass m_I , with the same proportionality constant for all bodies: this is the usual definition of the weak equivalence principle (WEP). The Equivalence Principle, as generalised by Einstein, was the starting point to general relativity (GR).

GR describes gravitation as the simple spacetime's curvature, while recovering Newton's description of gravitation as a classical inverse-square law force in weak gravitational fields and for velocities small compared to the speed of light. As a highly predictive theory, it has so far successfully passed all experimental tests [1, 2]. Standing next to GR, the Standard Model (SM) was built from the realisation that the microscopic world is intrinsically quantum.

Although both GR and SM leave few doubts about their validity in their respective regimes, scientists have been faced with difficulties for decades. Firstly, the question of whether GR and the SM should and could be unified remains open: major theoretical endeavours delivered models such as string theory, but still fail to provide a coherent vision of the world. Secondly, the unexpected dark matter and dark energy make up most of the Universe's mass-energy budget.

The WEP has been tested for four centuries with increased precision [3, 4, 5, 6, 7, 8, 9, 10]. The concept of a test in space emerged in the 1970s [11, 12], motivated by the quiet environment that space can provide and by the benefit of test periods much longer than on-ground experiments. In 1999, ONERA (Office National d'Etudes et de Recherches Aérospatiales) and OCA (Observatoire de la Côte d'Azur) proposed the MICROSCOPE mission (MICRO-Satellite à Compensation de traînée pour l'Observation du Principe d'Equivalence) to CNES.

MICROSCOPE was finally launched in 2016. After successfully dealing with unexpected anomalies [13], the mission provided two and a half years of useful data. In 2017, a first analysis based on only 7% of the eventual science data allowed us to verify the WEP at 2×10^{-14} sensitivity level [14, 15]. In 2022, the full data allowed us to improve that precision by one order of magnitude [16,

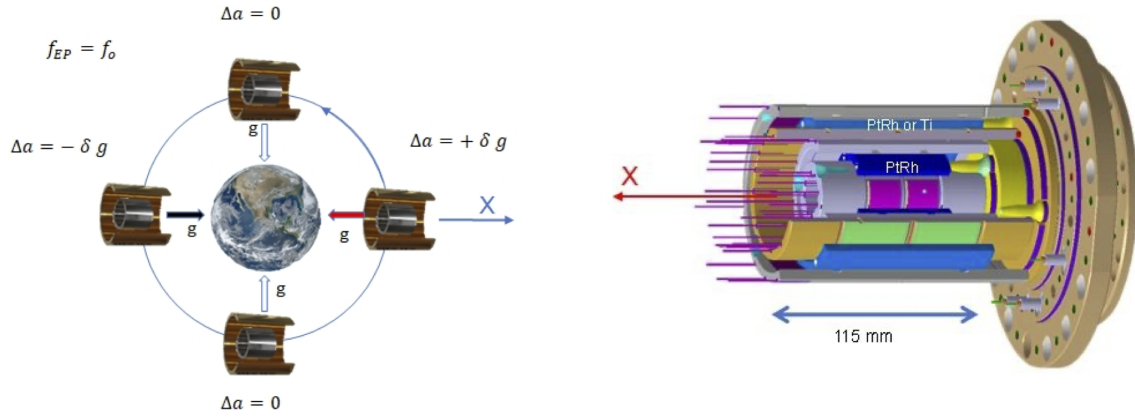


Figure 1: Experimental principle (left) and accelerometer core (right).

17]. In this paper, we first describe MICROSCOPE in Sect. 2. In Sect. 3, we describe the data processing and provide the upper bound provided by MICROSCOPE on the validity of the WEP.

2. MICROSCOPE MISSION OVERVIEW

2.1 WEP test experiment principle

The measurement relies on comparing the accelerations of two concentric bodies – cylinders in the case of MICROSCOPE – in orbit around the Earth. As shown in Fig. 1, the measurement is performed along the cylinders' X-axis, which is aligned with their main axis. In an inertial pointing configuration, it is pointing in the same direction of the Earth's gravity field vector once per orbit. In a perfect case, the difference of acceleration is proportional to the Eötvös parameter defined by the relative ratio of difference of gravitational-to-inertial masses m_{gj}/m_{ij} between two materials j :

$$\delta(2, 1) = 2 \frac{a_2 - a_1}{a_2 + a_1} = 2 \frac{m_{g2}/m_{i2} - m_{g1}/m_{i1}}{m_{g2}/m_{i2} + m_{g1}/m_{i1}}, \quad (1)$$

where a_j are the acceleration undergone by the two bodies.

In MICROSCOPE, the test-masses are part of a double concentric accelerometer. The test-masses are finely controlled by electrostatic forces to be motionless with respect to the surrounding electrodes as illustrated in the right panel of Fig. 1. The forces applied by the set of electrodes are determined by the voltage applied on the test-mass and on each electrode [18]. The combination of these voltages with the geometry of the instrument defines the electrostatic forces and torques applied to each test-mass in order to counteract all the other effects that prevent the test-mass to stay motionless with respect to the satellite.

Thus, if a WEP violation exists, it can be detected as a signal with a well-known frequency (the orbital frequency f_{orb} in the case of Fig. 1) in the differential acceleration measured by the accelerometer (i.e., the difference of electrostatic force per unit mass between the two test masses). The measurement precision can be improved by rotating the satellite about the axis normal to the orbital plane. This increases the modulation frequency of the Earth's gravity vector projected onto the X-axis, to put it closer to the minimum of the instrumental noise. The WEP-violation frequency becomes $f_{EP} = f_{orb} + f_{spin}$, with f_{spin} the rotation frequency of the satellite. Two spin frequencies have been used during the mission, leading to two test measurement data sets at $f_{EP} \approx 0.9 \times 10^{-3}$ Hz and $f_{EP} \approx 3.1 \times 10^{-3}$ Hz.

2.2 Payload

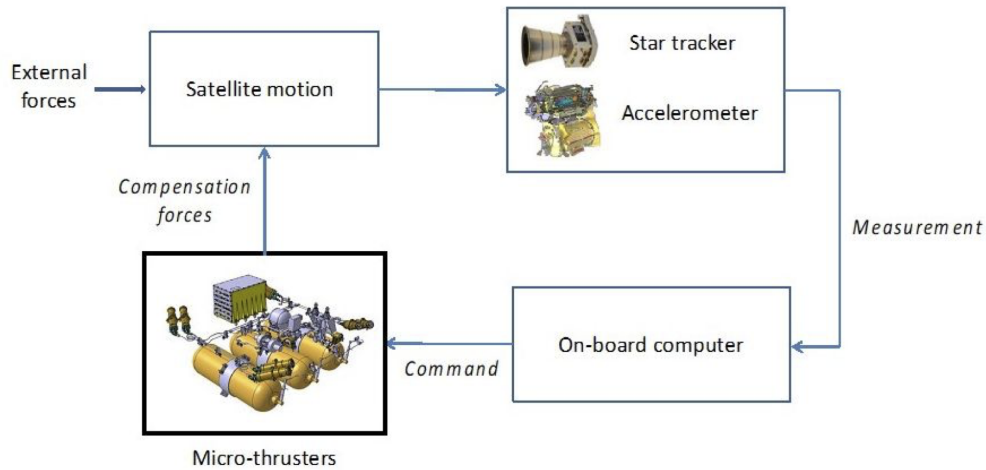


Figure 2: Satellite Drag-Free and Attitude Control System

The payload [18] is composed of two identical differential accelerometers also called sensor units (SUs) except for the test-mass material. Each SU has two concentric hollow cylindrical test-masses surrounded by electrodes engraved on gold-coated silica parts. Each SU is connected to a front-end electronics unit (FEEU) which delivers the voltages to the test-masses and electrodes and transmits the data to the interface control unit (ICU). Each ICU connected to the FEEU contains all the digital electronics and software to operate the test-mass control servo-loops and data conditioning for the satellite and then the ground telemetry. The SU and the FEEU are integrated in a thermal cocoon placed at the core of the satellite which offers a micro-Kelvin stability around the measurement frequencies.

The first SU, called SUREF, comprises two test-masses of the same material: PtRh10 platinum-rhodium alloy containing 90% by mass of Pt ($A = 195.1$, $Z = 78$) and 10% Rh ($A = 102.9$, $Z = 45$). SUREF is dedicated to experiment and accuracy verification (in orbit or on ground within the data processing) as it is supposed to give a null signal at f_{EP} . The second SU, called SUEP, comprises two test-masses of different material: the same PtRh10 alloy for the inner test-mass and an aeronautic titanium alloy (TA6V) for the outer test-mass with the atomic composition 90% of titanium ($A = 47.9$, $Z = 22$), 6% of aluminium ($A = 27.0$, $Z = 13$) and 4% of vanadium ($A = 50.9$, $Z = 23$). SUEP is dedicated to the WEP test.

Each test-mass defines a six-degree-of-freedom accelerometer. In order to operate in the most quiet environment and to get the most accurate orientation of the satellite, the accelerometer outputs are used by the satellite's drag-free and attitude control system (DFACS): it applies the necessary commands to the cold gas thrusters (Fig. 2). Atmospheric drag, Sun and Earth radiation forces, magnetic torques and all other disturbing sources are therefore compensated in order to nullify the common mode of one of the SU (i.e., either the mean acceleration of the two concentric test-masses or one of the acceleration output). The accelerometer's output or its internal servo-loop can be artificially biased at a particular frequency to stimulate the test-mass or the satellite (linear or angular motion) during calibration sessions.

2.3 Drag-free satellite

One of the challenges of the mission objectives is to make the satellite environment as quiet as possible for the payload to prevent any corruption of acceleration measurements.

The MICROSCOPE mission has been developed on the basis of scientific missions exploiting

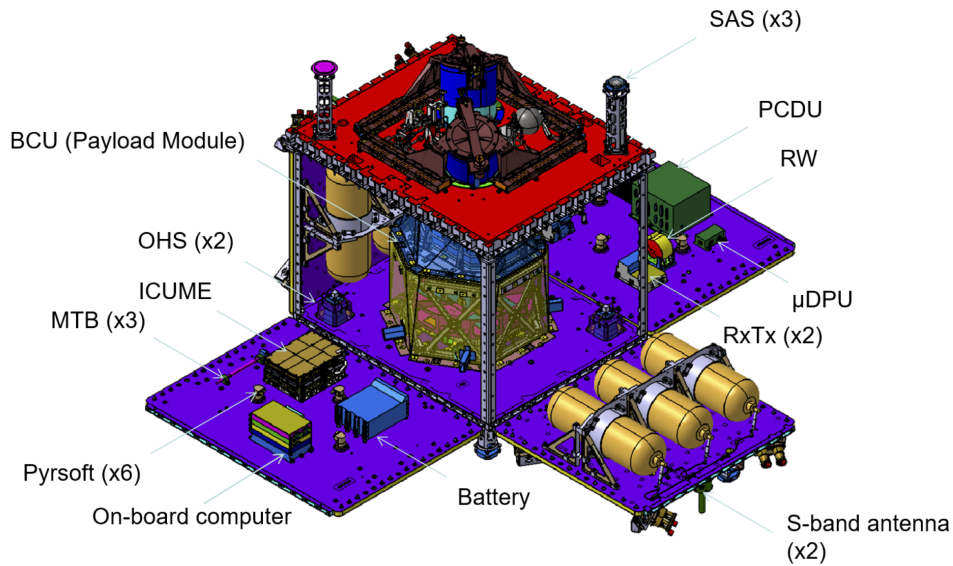


Figure 3: The cube forming the satellite is open in the picture, the instrument T-SAGE is at the center surrounded by the two 2×3 tanks of the cold gas propulsion system. Once closed the satellite cube measures $1.4 \text{ m} \times 1 \text{ m} \times 1.5 \text{ m}$ and weighs about 300 kg.

the CNES MYRIADE microsatellite product line whose architecture comprises a platform with generic functional chains (energy, communication, computer, structure, etc.). Some adaptations and modifications were necessary to cope with the unusual performance requirements. Usually, the payloads of the MYRIADE satellites are located on the decoupled upper part of the platform but MICROSCOPE payload module has been accommodated at the center of the spacecraft where it could take advantage of a more stable thermal environment (Fig. 3).

The satellite thermal design has been optimised to offer the payload a tight temperature stability: the required stability around the WEP test frequency f_{EP} was set to 1 mK at the sensor unit interface and to 10 mK at the associated analog electronics interface. Active heaters did not operate during the science operations in order to avoid any interference with the payload measurements. Consequently, the thermal control on the satellite purely relied on passive methods: the dissipation of the electronic units was ensured by satellite external radiators. The in-orbit estimated thermal performance exceeded requirements and expectations. The payload was also shielded from the Earth and satellite magnetic field. In addition, the mechanical or electronic micro disturbances were minimized by a careful design and analysis to ensure an optimal environment: choice of multi-layer insulation (MLI) to minimize cracking, minimisation of current loops, study of thermoelastic deformations to estimate internal gravitational effects. . .

To counteract non-gravitational forces and torques, an active control of accelerations and attitude of the satellite was implemented through the DFACS (Fig. 2). The DFACS used the scientific instrument itself as main sensor for delivering the linear as well as the angular accelerations hybridized with the star tracker measurements. The control laws for acceleration and attitude estimated the total forces and torques to be applied on the satellite which were transformed into eight micro-thrust commands sent to the cold gas propulsion system placed on two opposite walls of the satellite (Fig. 3). Each of the eight pods of thrusters actually comprises two thrusters: one nominal and one redundant not operating but that could be switched on in case of failure of the nominal. The DFACS in-orbit performances allowed to reduce the disturbances by 90 dB

around f_{EP} leading to a controlled linear acceleration better than $3 \times 10^{-13} \text{ m s}^{-2}$, one order of magnitude better than expectation. The satellite attitude was controlled to better than $1 \mu\text{rad}$ at f_{EP} with an angular velocity stability better than $3 \times 10^{-10} \text{ rad s}^{-1}$ at f_{EP} in rotating mode, one order of magnitude better than expectation as well. The induced angular acceleration was controlled to better than $10^{-11} \text{ rad s}^{-2}$ at f_{EP} , limiting centrifugal effects due to the off-centring of the test-masses.

Besides, the DFACS was able to receive additional external sine signals at particular frequencies in order to calibrate the instrument (differential scale factor, test-mass alignments and off-centerings, coupling between axes, non-linearity). Particular sessions were also dedicated to thermal sensitivities thanks to dedicated heaters.

3. DATA PROCESSING AND RESULTS

3.1 Measurement equation

A single accelerometer (called inertial sensor) measures the difference of acceleration between the test-mass of the accelerometer and the center of mass of the satellite. A differential accelerometer yields the difference $\vec{\Gamma}^{(d)} = \vec{\Gamma}^{(1)} - \vec{\Gamma}^{(2)}$ of two such accelerations for two test-masses. The accelerometers are not perfect, in the sense that we look for very small signals and thus any little defect can make deviate from an ideal response: they have bias, scale factors departing from unity, non-zero coupling between axes [19]. Moreover, their orientation in the satellite, in space and with respect to the Earth's gravity field, is not perfectly known. That is why the measured differential acceleration $\vec{\Gamma}^{(d)}$ is not identical to the real one $\vec{\gamma}^{(d)}$, but is related to it as [19]:

$$\vec{\Gamma}^{(d)} = \vec{b}_0^{(d)} + [\mathbf{A}^{(c)}] \vec{\gamma}^{(d)} + 2 [\mathbf{A}^{(d)}] \vec{\gamma}^{(c)} + \vec{n}^{(d)}, \quad (2)$$

where

- $\vec{b}_0^{(d)}$ is the difference of bias between the two inertial sensors;
- $[\mathbf{A}^{(c)}]$ is the common mode sensitivity matrix, close to the identity matrix, which includes scale factors, coupling between axes and global rotation common to the two sensors;
- $[\mathbf{A}^{(d)}]$ is the differential mode sensitivity matrix, very small, which takes into account the difference of characteristics of the two sensors;
- $\vec{\gamma}^{(c)}$ is the common mode acceleration which is mainly due to non-gravitational accelerations acting on the satellite and not on the enclosed test-masses; these non-gravitational accelerations include drag and radiation pressures and the thrust applied to the satellite which is servo-controlled in order to considerably reduce $\vec{\gamma}^{(c)}$ in the frequency band of interest;
- $\vec{n}^{(d)}$ is the (colored) noise.

In addition, couplings with angular accelerations and nonlinearities can also arise. These terms are not formally included in the above equation but specific measurement sessions have been dedicated to the identification of such effects and demonstrated that they are negligible [20].

The potential WEP-violation signal, $\delta(2, 1) \vec{g}$, is included in $\vec{\gamma}^{(d)}$ which also contains the gravity gradient and the differential angular acceleration due to the small residual off-centring between the two test-masses [19]:

$$\vec{\gamma}^{(d)} = \delta(2, 1) \vec{g}(O_{\text{sat}}) + ([\mathbf{T}] - [\mathbf{In}]) \vec{\Delta} + \vec{b}_1^{(d)}, \quad (3)$$

where

- $\vec{g}(O_{\text{sat}})$ is the gravity acceleration;
- $[T]$ is the gravity gradient tensor;
- $[In]$ is the gradient of inertia matrix;
- $\vec{\Delta}$ is the off-centring vector from the center of test-mass (1) to the center of test-mass (2);
- $\vec{b}_1^{(d)}$ contains the differences between the other small (mainly non gravitational) perturbations acting on the two test-masses.

Only the axis of the cylindrical test-masses, called X , which is much more precise than the other axes is used to estimate the EP signal. Therefore Eq. (2) has to be projected onto the X -axis. This leads to numerous terms [19] but the following considerations lead to simplifications for the reader's convenience:

- the more impacting components of the sensitivity matrix are estimated thanks to dedicated calibrations [21];
- the projection of the common mode is corrected thanks to the calibration of $[\mathbf{A}^{(d)}]$ and the measurement of $\vec{\gamma}^{(c)}$ (which is roughly assimilated to $\vec{\Gamma}^{(c)}$);
- the effect of the angular acceleration (anti-symmetric part of matrix $[In]$) is neglected (in practice we can correct for it but we have verified that this has no impact at the f_{EP} frequency thanks to the very good stability of the attitude control);
- small terms as the effect of the out-of-orbital-plane component of the off-centring are corrected thanks to dedicated calibrations;
- the tiny impact of the bias at the f_{EP} frequency is included in the evaluation of the systematic effects.

The remaining model used to analyse the measurements along the X -axis reads

$$\Gamma_{x,\text{corr}}^{(d)} = \sum_{j=0}^3 \alpha_j (t - t_0)^j + \delta_x g_x + \delta_z g_z + \Delta'_x S_{xx} + \Delta'_z S_{xz} + n_x^{(d)}, \quad (4)$$

where

- $\delta_x \approx A_{(1,1)}^{(c)} \delta(2, 1)$ ($A_{(1,1)}^{(c)}$ being the scale factor along X) is very close to the Eötvös ratio;
- δ_z , a small fraction of $\delta(2, 1)$, is in principle too small to be estimated but is included in the model to check the absence of anomaly;
- S_{xx} and S_{xz} are components of the matrix $[S]$ which is the symmetric part of $[T] - [In]$;
- Δ'_x (close to Δ_x) and Δ'_z (close to Δ_z) are "effective" components of the off-centring taking into account the sensitivity matrix;
- $\sum_{j=0}^3 \alpha_j (t - t_0)^j$ is an empirical polynomial term aiming to absorb the effect of the bias and its slow drift (mainly due to thermal effects).

3.2 Results

The final results of the MICROSCOPE mission are based on eighteen sessions for SUEP and nine sessions for SUREF [17]. A few sessions were discarded because of non-linearities at the

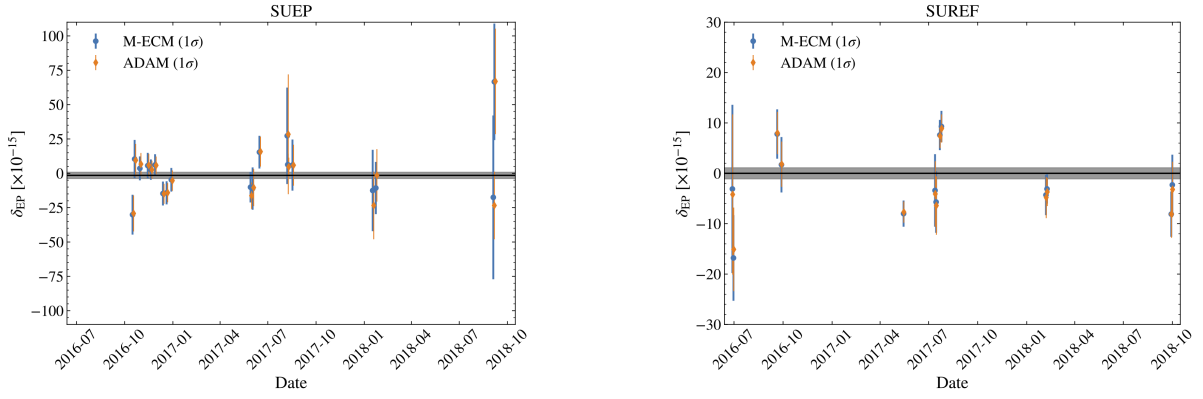


Figure 4: Eötvös parameter estimates for each SUEP (left panel) and SUREF (right panel) session and their 68% confidence error bars. Blue circles show M-ECM's estimates and orange ones Adam's.

beginning of the mission (before the control loop's electronics was upgraded) and a few others were discarded because of rare anomalies.

Beside EP-test sessions, in-flight calibration sessions were designed to estimate parameters so that the (perturbing) signals they source have a favourable signal-to-noise ratio (each session being dedicated to one or two parameters). We use the fact that parameters are almost independent to simplify and better control the estimation process with an iterative method based on the Adam (Accelerometric Data Analysis for MICROSCOPE) code to estimate parameters in the frequency domain [22].

In practice, instrumental defects are parameterized by the $\vec{b}_1^{(d)}$ and $\vec{\Delta}$ vectors, as well as the $[A^{(d)}]$ and $[A^{(c)}]$ matrices in Eq. (4), with only some of their components impacting the projected acceleration [19, 21]. The estimation of Δ'_x and Δ'_z uses their couplings with the Earth gravity gradient, whose strong spectral line at $2f_{EP}$ allows for a direct determination in science data based on an accurate Earth gravity model. Dedicated five-orbit sessions were used to measure Δ'_y , where the satellite was oscillated about the z -axis at a frequency f_{cal} to create a measurable signal driven by Δ'_y . The elements of the first row of the $[A^{(d)}]$ matrix a_{d1i} were measured by shaking the satellite at frequency f_{cal} along each axis (x to measure a_{d11} , y for a_{d12} and z for a_{d13}) in order to drive a measurable signal dependent on those parameters. The a_{d11} sessions also allowed for a measurement of the differential quadratic factor $K_{2d,xx}$ at $2f_{cal}$. Once the above iterative process converges, the Eötvös parameter is estimated on calibrated data following Eq. (4).

Two different methods have been developed for these estimations. The first one relies on a modified expectation-maximization algorithm (M-ECM), an iterative process which estimates the model parameters together with the missing data [23] until a convergence criterion is reached. The second method, Adam (Accelerometric Data Analysis for MICROSCOPE) estimates the parameters by means of a weighted least square regression in the frequency domain [22].

In a first step, the Eötvös parameter was estimated separately on each session. The results are depicted on Fig. 4.

A meticulous analysis of systematic errors, dominated by thermal effects, has been conducted based on numerous specific sessions dedicated to quantifying these effects. This led to a maximum systematic error for each session[21].

In a second step, measurements from all sessions were accumulated for a global estimate of the Eötvös parameter. The final MICROSCOPE's constraint on the validity of the WEP is [22, 9]:

$$\delta(\text{Ti, Pt}) = [-1.5 \pm 2.3 \text{ (stat)} \pm 1.5 \text{ (syst)}] \times 10^{-15}, \quad (5)$$

where the statistical error is given at 1σ .

The reference instrument provided a null result, $\delta(\text{Pt}, \text{Pt}) = [0.0 \pm 1.1 (\text{stat}) \pm 2.3 (\text{syst})] \times 10^{-15}$, showing no sign of unaccounted systematic errors in Eq. (5). As expected from its higher sensitivity, SUREF's result has a smaller statistical error than SUEP's. On the opposite, it has higher systematic errors (dominated by thermal effects), since they were estimated with less optimal sessions than SUEP's ones [6].

4. CONCLUSION

The MICROSCOPE mission has delivered its final measurement on October 2018. Since then, the science team has put a lot of effort into verifying all the data. The estimation of systematic errors have been improved with respect the first results obtained in 2017 to a few 10^{-15} in Eötvös parameter units. This allowed for an unprecedented precision on the test of the WEP.

With the lessons learned from the MICROSCOPE mission, we identified key parts of the instrument, satellite and operations that can be improved to beat MICROSCOPE's precision on the test of the WEP by two orders of magnitude. A space mission, as similar as possible to MICROSCOPE (which we tentatively call MICROSCOPE 2) could be designed with only almost off-the-shelf technology. Indeed, most improvements have already been shown to work in space, while others, more demanding, are not compulsory for the success of such as mission. We could thus expect a follow-up mission to MICROSCOPE to fly in the next few decades, on a low enough budget, but with high science outcomes about GR's validity and about ultra-light dark matter.

MICROSCOPE data are available at <https://cmsm-ds.onera.fr>.

Acknowledgments

The authors express their gratitude to all the different services involved in the mission partners and in particular the French space agency CNES in charge of the satellite. This work is based on observations made with the T-SAGE instrument, installed on the CNES-ESA-ONERA-CNRS-OCA-DLR-ZARM MICROSCOPE mission. ONERA authors' work is financially supported by CNES and ONERA fundings. Authors from Observatoire de la Côte d'Azur (OCA) have been supported by OCA, the French National Center for Scientific Research (CNRS), and CNES. ZARM authors' work is supported by the German Space Agency DLR, with funds of the BMWi (FKZ 50 OY 1305 and FKZ 50 LZ 1802) and by the Deutsche Forschungsgemeinschaft DFG (LA 905/12-1). The authors would like to thank the Physikalisch-Technische Bundesanstalt institute in Braunschweig, Germany, for their contribution to the development of the test-masses with funds from CNES and DLR.

5. REFERENCES

- [1] Will, C. M., 2014, "The Confrontation between General Relativity and Experiment", *Living Reviews in Relativity*, 17, 4.
- [2] Ishak, M., 2019, "Testing general relativity in cosmology", *Living Reviews in Relativity* 22, 1.
- [3] Eötvös, L., Pekár, D., Fekete, E., 1922, "Beiträge zum Gesetz der Proportionalität von Trägheit and Gravität", *Ann. Phys.* 68, p. 11.
- [4] Bessel, F. W., 1832, "Versuche über die Kraft mit welcher die Erde Körper von verschiedene Beschaffendheit anzieht", *Ann. Phys. Chem. (Poggendorf)* 25, 401–417.
- [5] Roll, P. G., Krotkov, R., Dicke, R.H., 1964, "The equivalence of inertial and passive gravitational mass, *Annals Phys.* 26, 442–517.
- [6] Braginskii, V. B., Panov V. I., 1971, "Verification of equivalence of inertial and gravitational masses, *Zh. Eksp. Teor. Fiz.* 61, 873–879.

- [7] Schlamminger, S., Choi, K.-Y., Wagner, T. A., Gundlach, J. H., Adelberger, E. G., 2008, "Test of the Equivalence Principle Using a Rotating Torsion Balance", *Physical Review Letters* 100 (4), 041101.
- [8] Wagner, T. A., Schlamminger, S., Gundlach, J. H., Adelberger, E. G., 2012, "Torsion-balance tests of the weak equivalence principle", *Class. Quant. Grav.* 29, 18, p. 184002.
- [9] Williams, J. G., Turyshev, S. G., Boggs, D. H., 2012, "Lunar laser ranging tests of the equivalence principle", *Classical and Quantum Gravity* 29, 18, p. 184004.
- [10] Viswanathan, V., Fienga, A., Minazzoli, O., Bernus, L., Laskar, J., Gastineau, M., 2018, "The new lunar ephemeris INPOP17a and its application to fundamental physics", *MNRAS* 476, 1877–1888.
- [11] Chapman, P. K. and Hanson, A. J., 1970, "An Eötvös Experiment in Earth Orbit, Davies, R. W. (Ed.)", *Proc. Conf. on Experimental Tests of Gravitation Theories*, JPL TM, 333-499, p. 228.
- [12] Everitt, C. W. F., Damour, T., Nordtvedt, K., Reinhard, R., 2003, "Historical perspective on testing the Equivalence Principle", *Advances in Space Research* 32, 1297–1300.
- [13] Rodrigues, M. et al., 2022, "MICROSCOPE Mission scenario, ground segment and data processing", *Classical and Quantum Gravity* 39, 204004.
- [14] Touboul, P. et al., 2017, "MICROSCOPE Mission: First Results of a Space Test of the Equivalence Principle", *Physical Review Letters* 119, 231101.
- [15] Touboul, P. et al, 2019, "Space test of the equivalence principle: first results of the MICROSCOPE mission", *Classical and Quantum Gravity* 36, 22.
- [16] Touboul, P. et al, 2022, "MICROSCOPE Mission: Final Results of the Test of the Equivalence Principle", *Physical Review Letters* 129, 121102.
- [17] Touboul, P. et al, 2022, "Result of the MICROSCOPE weak equivalence principle test", *Classical and Quantum Gravity* 39, 204009.
- [18] Liorzou, F. et al., 2022, "MICROSCOPE instrument description and validation.", *Classical and Quantum Gravity* 39, 204002.
- [19] Touboul, P. et al, 2022, "MICROSCOPE mission analysis, requirements and expected performance", *Classical and Quantum Gravity* 39, 204001.
- [20] Chhun, R. et al, 2022, "MICROSCOPE instrument in-flight characterization", *Classical and Quantum Gravity* 39, 204005.
- [21] Rodrigues, M. et al, 2022, "MICROSCOPE: systematic errors", *Classical and Quantum Gravity* 39, 204006.
- [22] Bergé, J. et al, 2022, "MICROSCOPE mission: data analysis principle", *Classical and Quantum Gravity* 39, 204007.
- [23] Baghi, A., Métris, G., Bergé, J., Christophe, B., Touboul, P., Rodrigues, M., 2016, "Gaussian regression and power spectral density estimation with missing data: The MICROSCOPE space mission as a case study", *Physical Review D* 93, (12), 122-007.

TESTING GENERAL RELATIVITY AND ALTERNATIVE THEORIES WITH PLANETARY AND LUNAR EPHEMERIDES

A. FIENGA¹, O. MINAZZOLI^{2,3}, V. MARIANI, A. HEES⁴, L. BERNUS⁵, L. BIGOT⁶,
A. DI RUSCIO^{1,7}, D. DURANTE⁷, M. GASTINEAU⁵, J. LASKAR⁵, L. IESS⁷

¹ Géoazur - France - agnes.fienga@oca.eu

² Artemis, Université Côte d'Azur, CNRS, Observatoire Côte d'Azur - France

³ Bureau des Affaires Spatiales, Monaco

⁴ SYRTE, Observatoire de Paris, PSL University - France

⁵ IMCCE, Observatoire de Paris, PSL University - France

⁶ Lagrange, Université Côte d'Azur, CNRS, Observatoire Côte d'Azur - France

⁷ CRAS, La Sapienza - Italy

ABSTRACT. In this paper, we describe how planetary ephemerides are built in the framework of General Relativity and how they can be used to test alternative theories. After a review on the existing planetary and lunar ephemerides and the framework used for their construction, we summarize the results obtained considering full modifications of the ephemeris framework with direct comparisons with and fit to observations. We then discuss other formalisms such as Einstein-dilation theories, the massless graviton. We conclude with some comments and prospects with the BepiColombo mission.

1. INTRODUCTION

The full content of this paper can be found in more details in the review paper published in the Living Review (Fienga and Minazzoli, 2023).

Planetary ephemerides are often used as an appropriate laboratory for testing gravitation laws in the weak field regime. Indeed, with the exploration of the solar system with space probes, the measurements of the planetary distances reach the meter-level accuracy, or below, and allow great progress in the dynamical modelling of the natural object dynamics. However, planetary ephemerides are constructed in a very specific framework defined by the IAU — the one of general relativity (GT) — and it is crucial to keep consistency at the different levels of the dynamical modelling (time scale definition, equation of motion, photon path) when one wants to modify the relativistic environment of the ephemerides. On Table 1, are described two types of tests that can be found in the literature: i) the direct tests where the alternative theory is fully integrated in the ephemerides from the definition of the metric in space and time to the full adjustment of the modelling parameters by comparison to observations ii) the indirect tests which interpret constraints obtained with ephemerides developed in GR framework for alternative theories.

2. PLANETARY EPHEMERIDES FRAMEWORK

The planetary ephemerides are built in the IAU 2000 recommendation framework (Soffel et al., 2003). They are defined using the kinematically fixed BCRS, with TCB and harmonic gauge conditions. The positions and velocities of the solar system barycenter are obtained by integration of the Eqs. (1) up to the c^{-2} order, together with Eqs. (2)

$$\begin{cases} \sum_i \mu_i^* \mathbf{r}_i = 0 \\ \sum_i \mu_i^* \mathbf{v}_i + \dot{\mu}_i^* \mathbf{r}_i = 0 \end{cases} \quad (1)$$

$$\begin{cases} \sum_i \mu_i^* \mathbf{r}_i = 0 \\ \sum_i \mu_i^* \mathbf{v}_i + \dot{\mu}_i^* \mathbf{r}_i = 0 \end{cases} \quad (2)$$

Tests	Pros	Cons
Direct A new ephemeris written in an alternative framework with equation of motion, time scale and light path modified, fit included	Totally consistent results with uncertainties and correlations	Quite heavy to develop
Indirect Interpretation of derived quantities (i.e. advance of perihelia) in terms of constraints	Very fast and relatively easy	Highly inconsistent with underestimated uncertainties, and overoptimistic constraints

Table 1: Tests of alternative theories with planetary ephemerides. Examples of indirect tests can be found in (Fienga and Minazzoli 2023)

where r_i , v_i are planet- i positions and velocities, μ_i its inertial mass. The equations of motion are the one defined as the Einstein-Infeld-Hoffmann-Droste-Lorentz equation where the mass parameter is the gravitational mass. In term of modelling of the photon path, the planetary ephemerides account for the Shapiro delay (with inertial mass) and the frame-dragging effect induced by the rotation of the Sun, the Earth and the Moon. The details of these equations can be found in (Fienga and Minazzoli, 2023).

3. TESTS OF GENERAL RELATIVITY AND ALTERNATIVE THEORIES

We present here the main results obtained by different groups for direct testing of PPN formalism, $\dot{\mu}/\mu$, graviton mass estimations and its interpretation in terms of Yakawa suppression and fifth force as well as massless dilaton and its interpretation as strong equivalence principle violation. These results are direct tests as defined in Table 1.

3.1 Parametrized Post-Newtonian theory (PPN) and $\dot{\mu}/\mu$

The metric theories such as PPN impose by construction no coupling between gravitational field and matter. This implies that the weak equivalence principle is always respected. They often appear as a generalization of the GR metrics for which $\beta = \gamma = 1$. Considering that the total acceleration to account for the equation of motion of a planet- i includes not only the central acceleration and the mutual planetary interactions in PPN but also the effect of the second degree term of the sun gravitational potential (J_2^\odot) and the frame-dragging effect due to the sun rotation (Lense-Thirring), important correlations arise between orbital planetary elements and PPN parameters β and γ (Anderson et al., 1978). It is then important to keep in mind such correlations when one considers the published uncertainties, especially in the case of global adjustments. In combining published intervals for β and γ values since 2008 obtained by different groups using planetary orbit constraints, we obtain no violation of GR with $(\beta - 1) = (-0.45 \pm 1.75) \times 10^{-5}$ and $(\gamma - 1) = (0.55 \pm 1.35) \times 10^{-5}$. We stress that we consider here only the main terms of the PPN formalism (β and γ) as the extended PPN formalism does not meet the harmonic gauge requirements imposed by the IAU 2000 recommendation (see Fienga and Minazzoli section 4.1.4 for discussion).

For $\dot{\mu}/\mu$, correlations are weaker and good constraints can be obtained. However, if one wants to extract a constraint on \dot{G}/G , some hypothesis on the solar mass loss are required. For example, the mass brought by comet fall on the sun has to be assess as well as the quantity of matter ejected by the sun. These quantities are difficult to estimate and introduce important uncertainties in the estimation of \dot{G}/G . At the date of this publication, the best estimation is obtained by (Pitjeva et

al., 2021) with $\dot{\mu}/\mu = -10.2 \pm 1.4$ and $\dot{G}/G = 0.85 \pm 3.75$. It is interesting to note that pulsar timing provides limits which are one order of magnitude higher (Zhu et al., 2018).

3.2 Graviton, Yukawa suppression and fifth force

The massive graviton theories propose a graviton with a non-zero mass, which leads to various predictions. One prediction is the acquisition of a Yukawa suppression in the $1/r$ falloff of the Newtonian potential (de Rham, 2014) which is a modification of the gravitational force at short distances. The strength of the Yukawa suppression depends on the Compton wavelength, λ_g , which measures the scale at which quantum gravity effects become important. The Compton wavelength is related to the mass of the graviton, m_g , the Planck constant, \hbar and the speed of light c by $\lambda_g = \frac{\hbar}{cm_g}$. With (Bernus et al., 2019, 2021), constraints on m_g and λ_g have been obtained in using partial random exploration and a full integration of planetary ephemerides in the massive graviton framework. With (Mariani et al., 2023), new limits have been obtained, still considering full integration and adjustments of planetary orbits in the massive graviton framework but in using MCMC approach leading to $m_g < 0.10 \times 10^{-23}$ eV/c² at C.L. 99.7 %.

3.3 Einstein massless dilaton

With (Minazzoli and Hees, 2016), has been proposed a generic formalism allowing both WEP, GWEP and SEP (respectively: weak, gravitational weak, and strong equivalence principal) violations with the help of non-universal couplings between scalar field and matter (considering two possible interactions: linear or non-linear). Parameters of the new defined metric (such as $\tilde{\alpha}$ and β_0) depend on dilatonic charges (proton, nucleon). In (Bernus et al., 2022), modified equations of motion and photon path have been used for building planetary ephemerides fitted on observations. Only the linear coupling was considered. Random exploration for α_G, α_T and α_0 (respectively: coupling constants for gaseous planets, telluric planets, and universal) starting with flat large priors and cost functions led to constraints on the possible values of the Einstein massless dilaton parameters. In (Mariani et al., 2014), MCMC approach has been used to improve these constraints in the context of the Brans-Dicke theories with $\alpha_G = \alpha_T = 0$ and only α_0 is tested. This result is then interpreted as a new limit of the strong equivalence principle.

3.4 BepiColombo perspectives

With the BepiColombo mission arriving at Mercury in 2026, a new step in the improvement of the dynamical modelling of planetary motion will be reached with a measurement of the Mercury to Earth distances at the centimeter level. With such a measure, new limits in testing GR and alternative theories will be obtained. De Marchi and Cascioli (2021) gives an overview of the expected results in terms of PPN parameter estimations, $\dot{\mu}/\mu$, J_2^\odot and graviton mass. The BepiColombo measurement will also improve the detection of the Sun core rotation as proposed by Fienga et al. (2022).

4. CONCLUSION

Planetary ephemerides are a crucial tool for testing GR and alternative theories in the solar system. It is, however, important to keep in mind that direct tests — realised by the construction of ephemerides with fully consistent metric, equation of motion, time scale, photon path, fitted to observations — are far more preferable than indirect tests that deduced alternative theories constraints based on ephemerides built in the GR framework. This assessment is even more stringent when one uses more and more accurate observations such as the future BepiColombo distance measurements. More details can be found in (Fienga and Minazzoli 2023).

5. REFERENCES

- Anderson J..D., Keesey M..S..W., Lau E.L, Standish J. E. M., Newhall XX, 1978, "Tests of general relativity using astrometric and radio metric observations of the planets" ., *Acta Astronautica*, 5:43–61
- Bernus L, Minazzoli O, Fienga A, Gastineau M, Laskar J, Deram P, 2019, "Constraining the Mass of the Graviton with the Planetary Ephemeris INPOP.", *Phys. Rev. Lett.* 123(16):161103, doi:10.1103/PhysRevLett.123.161103, 1901.04307
- Bernus L., Minazzoli O., Fienga A., Gastineau M., Laskar J., Deram P., Di Ruscio A., 2020, "Constraint on the Yukawa suppression of the Newtonian potential from the planetary ephemeris INPOP19a", *Phys. Rev. D*, 102(2):021501, doi: 10.1103/PhysRevD.102.021501, 2006.12304
- Bernus L., Minazzoli O., Fienga A., Hees A., Gastineau M., Laskar J., Deram P., Di Ruscio A., 2022, "Constraining massless dilaton theory at Solar system scales with the planetary ephemeris INPOP.", *Phys. Rev. D* 105(4):044057, doi: 10.1103/PhysRevD.105.044057
- De Marchi F., Cascioli G., 2020, "Testing general relativity in the solar system: present and future perspectives", *Classical and Quantum Gravity*, 37(9):095007, doi: 10.1088/1361-6382/ab6ae0
- Fienga, A., Minazzoli, O., 2023, "Testing Theories of Gravity with Planetary Ephemerides", *Living Review in Relativity*, Volume 27, article number 1, doi: 10.1007/s41114-023-00047-0
- Fienga, A., Bernus, L., Minazzoli, O., Hees, A., Bigot, L., Herrera, C., Mariani, V., Di Ruscio, A., Mary, D., 2022, "INPOP Planetary ephemerides and applications in the frame of the BepiColombo mission including new constraints on the graviton mass and dilaton parameters.", In: Auge E, Dumarchez J, Tran Thanh Van J (eds) *Proceedings, 56nd Rencontres de Moriond on Gravitation: La Thuile, Italy, January 30- February 6, 2022*, ARISF, URL <http://arxiv.org/abs/2211.04881>
- Mariani, V., Fienga, A., Minazzoli, O., Gastineau, M., Laskar, J., 2023., "Bayesian test of the mass of the graviton with planetary ephemerides.", *Physical Review D*, 108, doi:10.1103/PhysRevD.108.024047
- Mariani, V., Minazzoli, O., Fienga, A., Laskar, J., Gastineau, M., 2024., "Bayesian test of Brans-Dicke theories with planetary ephemerides: Investigating the strong equivalence principle", *Astron. Astrophys.*, in press, . doi: 10.48550/arXiv.2310.00719
- Minazzoli O., Hees A., 2016, "Dilatons with intrinsic decouplings", *Phys Rev D*, 94:064038, doi: 10.1103/PhysRevD.94.064038
- Pitjeva E.V., Pitjev NP, Pavlov DA, Turygin CC, 2021, "Estimates of the change rate of solar mass and gravitational constant based on the dynamics of the Solar System.", *Astron. Astrophys.*, 647:A141, doi:10.1051/0004-6361/202039893,
- de Rham C., 2014, "Massive Gravity", *Living Reviews in Relativity* ,17:7, doi: 10.12942/lrr-2014-7, 1401.4173
- Soffel M., 2003, "The IAU 2000 Resolutions for Astrometry, Celestial Mechanics, and Metrology in the Relativistic Framework: Explanatory Supplement.", *Astronomical Journal*, 126:2686–2706
- Zhu W. W., Desvignes G., et al., 2018, "Tests of gravitational symmetries with pulsar binary J1713+0747.", *Monthly Notices of the Royal Astronomical Society* 482(3):3249–3260, doi: 10.1093/mnras/sty2905

GENERAL RELATIVITY TESTS BY THE DYNAMICS OF THE SOLAR SYSTEM

D. Pavlov¹, I. Dolgakov²

¹St. Petersburg State University, Russia - d.a.pavlov@spbu.ru

²Institute of Applied Astronomy, St. Petersburg, Russia

ABSTRACT. Lunar laser ranging (LLR) data, as well as high-precision ranging observations of Mercury and Mars orbiters, allow to put constraints on deviations of the physical laws in the Solar system from ones predicted by General relativity. We use the latest EPM lunar-planetary ephemeris to study the possibility to confirm the Lense-Thirring effect and to derive bounds of possible violation of strong equivalence principle. We also study the possibility of estimating the possible variation of gravitational constant via lunar ephemeris and LLR.

1. INTRODUCTION

The Solar system, with its vast distances, numerous massive bodies, and long time spans of precise ranging observations, is one of the best “laboratories” for testing General relativity.

Many results have been obtained in this area since the onset of precision astrometry. Some recent results are: estimate of the change rate of gravitational constant (Pitjeva et al., 2021); test of equivalence principle (Williams et al., 2012; Viswanathan et al., 2018); both of those and also bounds for PPN parameters β and γ and geodetic precession (Hofmann & Müller 2018); distance rate (Williams et al., 2014).

In this work, we study the Lense-Thirring effect, making the direction of the Sun’s rotational axis a determined parameter. We also put bounds on the strong equivalence principle, using the same approach as in earlier works. Finally, we study the possibility of estimating the possible variation of gravitational constant via lunar laser ranging observations, and find out that the indeterminate effects of Earth tides pose a difficulty here.

We base our calculations exclusively on lunar-planetary ephemeris EPM2021 (Pitjeva et al., 2022) with only some additions in recent LLR observational data made in Apache Point (Colmenares et al., 2023), Grasse (Courde et al., 2018), and Wettzell (Eckl et al., 2019).

2. LENSE-THIRING EFFECT

The Lense-Thirring (LT) precession (also named gravitomagnetic frame-dragging effect) can be formulated in the form of an additional acceleration that acts on a body in vicinity of a large rotating mass (in this work, the Sun):

$$\ddot{\mathbf{r}}^{\text{LT}} = \frac{2}{c^2} G S_{\odot} \frac{1}{r_S^3} R_z(\alpha_z) R_x(\alpha_x) \left(\dot{\mathbf{r}}_i \times \mathbf{z} + 3 \frac{\mathbf{z} \cdot \mathbf{r}_S}{r_S^2} \mathbf{r}_S \times \dot{\mathbf{r}}_S \right)$$

where \mathbf{r} is the position of the body in the barycentric (inertial) frame, \mathbf{r}_S is the position of the body w.r.t. the Sun, $\mathbf{z} = (0, 0, 1)$, $R_z(\alpha_z) R_x(\alpha_x)$ is the rotation matrix from \mathbf{z} to the Sun’s pole, S_{\odot} is the angular momentum of the Sun, and G is the gravitational constant.

The reference values of α_z and α_x are $16^{\circ}13$ and $26^{\circ}13$, respectively (Archinal et al., 2018). The reference value of S_{\odot} is $190 \cdot 10^{39}$ kg m²/s (Pijpers, 1998).

The LT acceleration is significant in the motion of Mercury, and also visible in the motion of Venus and Earth. The most precise measurements that can allow to verify the LT effect are

MESSENGER radio ranging (Solomon et al., 2001; Park et al., 2017). However, those observations (as well as other ranging observations of the inner planets) are sensitive also to solar oblateness. The solar oblateness factor ($J_{2\odot}$) is not perfectly known and is normally a determined parameter in planetary ephemeris solutions like EPM or DE (Park et al. 2021). Also affected by $J_{2\odot}$ are Venus Express ranges (Morley & Budnik, 2009) and Earth–Mars ranges obtained with multiple spacecraft, most notably Odyssey and Mars Reconnaissance Orbiter (Konopliv et al., 2011). It is difficult to separate the $J_{2\odot}$ effect and the LT effect on Earth–planetary ranges because of high anti-correlation (see Fig. 1).

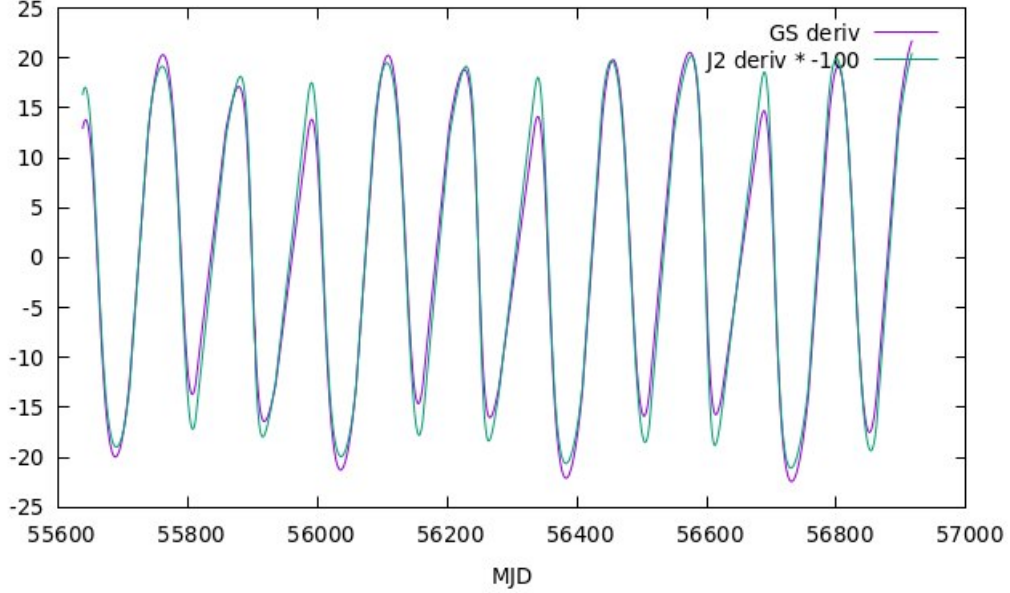


Figure 1: Derivatives of Earth–Mercury ranges w.r.t solar angular momentum times the gravitational constant (GS_{\odot}) and solar oblateness ($J_{2\odot}$). The latter derivative has a factor of -100 to better show anti-correlation.

Despite the impossibility to reliably determine $J_{2\odot}$ and S_{\odot} in the same solution due to the said anti-correlation, we can still examine whether the non-dynamical estimates of $J_{2\odot}$ and S_{\odot} are compatible with each other in the dynamical model.

If we fix S_{\odot} to its reference value (see above), we determine the following bounds for solar oblateness:

$$J_2 = (228 \pm 2) \cdot 10^{-9}$$

(the given error is 3σ). However, in (Pijpers, 1998), not only $S_{\odot} = (190 \pm 2) \cdot 10^{39}$ was determined using helioseismology, but $J_{2\odot}$ as well: $(218 \pm 6) \cdot 10^{-9}$. In later helioseismology work by (Mecheri & Meftah, 2021) the value of $J_{2\odot}$ was revised to be $(221 \pm 1) \cdot 10^{-9}$ (3σ). It can be seen that both helioseismology estimates are not compatible to the dynamical estimate. More research is needed to interpret this result.

If we fix $J_{2\odot}$ to e.g. $219 \cdot 10^{-9}$ and make S_{\odot} a free parameter, its value will be determined at $(96 \pm 30) \cdot 10^{39}$ (3σ), which is not at all compatible with the helioseismology estimation.

It is also important to say that both solar oblateness effect and the LT effect are dependent of the direction of the Sun’s axis of rotation. In this work, the angles α_z and α_x were made determined parameters. The obtained estimates are:

$$\alpha_z = 18.2 \pm 1^{\circ}5$$

$$\alpha_x = 27.6 \pm 0^{\circ}9$$

(the given errors are 3σ). It is easy to see that the values are not quite compatible with the IAU values of 16.13 and 26.16 (the accuracy of the latter is supposed to be at least one tenth of a degree, see Archinal et al., 2018).

3. EQUIVALENCE PRINCIPLE

We question the principle of equivalence of gravitational (g) and inertial (i) masses in the case of the Earth–Moon system in presence of Sun’s gravity:

$$\left(\frac{m^g}{m^i}\right)_M \stackrel{?}{=} \left(\frac{m^g}{m^i}\right)_E$$

The nominal value of m^g/m^i for either body is 1. We denote $\delta_M = (m^g/m^i)_M - 1$, and similarly for δ_E . Let us consider the Newtonian acceleration of the Moon (\mathbf{r}_M) w.r.t. Earth (\mathbf{r}_E) in presence of Sun (\mathbf{r}_S) and keeping inertial and gravitational masses separate. After some transformations, we get

$$\begin{aligned} \mathbf{a}_M - \mathbf{a}_E = & - \frac{G [(1 + \delta_M)m_E^g + (1 + \delta_E)m_M^g]}{r_{EM}^3} \mathbf{r}_{EM} \\ & + Gm_S^g \left[\frac{\mathbf{r}_{SE}}{r_{SE}^3} - \frac{\mathbf{r}_{SM}}{r_{SM}^3} \right] \\ & + Gm_S^g \left[\frac{\mathbf{r}_{SE}}{r_{SE}^3} \delta_E - \frac{\mathbf{r}_{SM}}{r_{SM}^3} \delta_M \right] \end{aligned}$$

where the last two terms are the acceleration of the geocentric Moon due to the Sun. Now, keeping in mind that $1 + \delta \approx 1$ and $\mathbf{r}_{SE} \approx \mathbf{r}_{ME}$, we get

$$\mathbf{a}_M - \mathbf{a}_E \approx - \frac{Gm_E^g + Gm_M^g}{r_{EM}^3} \mathbf{r}_{EM} + Gm_S^g \left[\frac{\mathbf{r}_{SE}}{r_{SE}^3} - \frac{\mathbf{r}_{SM}}{r_{SM}^3} \right] + Gm_S^g \frac{\mathbf{r}_{SE}}{r_{SE}^3} [\delta_E - \delta_M]$$

The last term allows us to solve for the parameter $[\delta_E - \delta_M]$ in the lunar solution. The obtained estimate is

$$\delta_E - \delta_M = (10 \pm 30) \cdot 10^{-15}$$

(the given error is 3σ). So there is no sign of Earth’s and Moon’s accelerations in gravity of the Sun being different above the level of $3 \cdot 10^{-14}$ (dimensionless units). Possible difference in accelerations may be a violation of the strong equivalence principle (SEP) or the weak equivalence principle (WEP). It is probably not possible to separate SEP and WEP using only the dynamics of the Solar system (Viswanathan et al., 2018), though WEP was recently confirmed to accuracy below $1.6 \cdot 10^{-14}$ (3σ , see Touboul et al., 2022), so we can say that probably SEP is not violated above $3.5 \cdot 10^{-14}$.

4. ATTEMPT TO ESTIMATE \dot{G} using LLR

An attempt was made to estimate possible time variation of the gravitational constant G from LLR measurements, using the approach similar to (Pitjeva et al., 2021) and earlier works. The approach is based on the addition of the time derivative of the gravitational parameter GM into the model (in our case, GM of the Earth–Moon system):

$$GM_{EM}(t) = GM_{EM}(t_0) + \dot{GM}_{EM}(t - t_0)$$

and then using the relation

$$\frac{\dot{G}}{G} = \frac{(\dot{GM})_{EM}}{(GM)_{EM}} - \frac{\dot{M}_{EM}}{M_{EM}}$$

However, it was found out that we can not reliably estimate \dot{GM}_{EM} in the lunar solution because its effect is hard to separate from that of Earth's tides. More specifically, \dot{GM}_{EM} correlates with rotational delays of Earth's diurnal and semi-diurnal tides in the DE tidal model (Williams et al., 2014) that is used in the EPM lunar model. The correlation of \dot{GM}_{EM} with τ_{1R} and τ_{2R} is 91.7% and 99.6%, respectively. Alternatively, there is the IERS tidal model (Petit & Luzum 2010) that does not need to be fit to LLR observations, but it does not provide as good fit as the DE tidal model (Pavlov et al., 2016; Pavlov, 2020). More research on the Earth's tides effect is needed before estimating \dot{G} via LLR.

5. CONCLUSION

- While it is not possible to simultaneously estimate solar oblateness factor $J_{2\odot}$ and solar angular momentum S_{\odot} to confirm Lense-Thirring acceleration from MESSENGER and other radio ranging measurements, we found out that the present estimates of those values obtained from a non-dynamic method (helioseismology) are not compatible with each other in the EPM dynamical model. More research is needed to interpret this.
- The direction of the Sun's rotational axis w.r.t. in the inertial frame was estimated in the planetary solution through effect of solar oblateness and, to a lesser extent, Lense-Thirring effect. The found estimates differ from the widely accepted values by more than 0°5 in both latitude and longitude of the Sun's north pole in the equatorial system (with uncertainties taken into account). More research is needed to interpret this.
- The Earth and the Moon are affected by the gravity of the Sun in the same manner to the level of $3 \cdot 10^{-14}$ (3σ). Using a recent result about bounds of possible violation of WEP, we can say that probably SEP is not violated above $3.5 \cdot 10^{-14}$.
- Estimating the possible time variation of the gravitational constant G from LLR measurements can not be done because of correlations with parameters of Earth's tides in the lunar solution. More research on Earth's tides is needed.

6. REFERENCES

- Archinal. B. et al., 2018. "Report of the IAU working group on cartographic coordinates and rotational elements: 2015". *Celest Mech Dyn Astr* 130(22), doi: 10.1007/s10569-017-9805-5.
- Colmenares, N. R., Battat, J. B. R., Gonzales, D. P., Murphy Jr, T. W., Sabhlok, S., 2023. "Fifteen Years of Millimeter Accuracy Lunar Laser Ranging with APOLLO: Data Reduction and Calibration". *PASP* 135, 104503, doi: 10.1088/1538-3873/acf787.
- Courde, C., Torre, J.M., Samain, E., Martinot-Lagarde, G., Aimar, M., Albanese, D., Exertier, P., Fienga, A., Marley, H., Metris, G., Viot, H., Viswanathan, V., 2017. "Lunar laser ranging in infrared at the Grasse laser station". *A&A* 602, A90, doi: 10.1051/0004-6361/201628590
- Eckl, J., Schreiber, U., Schüler, T., 2019. "Lunar laser ranging utilizing a highly efficient solid-state detector in the near-IR". *Quantum Optics and Photon Counting, Proceedings Volume 11027*, doi: 10.1117/12.2521133.

- Hofmann, F., Müller, J., 2018. “Relativistic tests with lunar laser ranging”. *Class. and Quant. Grav.* 35(3), 035015. doi: 10.1088/1361-6382/aa8f7a.
- Mecheri, R., Meftah, M., 2021. “Updated values of solar gravitational moments J_{2n} using HMI helioseismic inference of internal rotation”. *MNRAS* 506(2), pp. 2671–2676, doi: 10.1093/mnras/stab1827.
- Morley, T., Budnik, F., 2009. “Mars Express and Venus Express range residuals for improving planetary ephemerides”. In: 21st International Symposium on Space Flight Dynamic”. URL http://issfd.org/ISSFD_2009/OrbitDeterminationI/Morley.pdf.
- Konopliv, A.S. et al, 2011. “Mars high resolution gravity fields from MRO, Mars seasonal gravity, and other dynamical parameters”. *Icarus* 211(1), 401–428, doi: 10.1016/j.icarus.2010.10.004.
- Petit, G., Luzum, B., 2010. “IERS Conventions” (IERS Technical Note 36) Frankfurt am Main: Verlag des Bundesamts für Kartographie und Geodäsie, ISBN: 3-89888-989-6
- Park R. S., Folkner W. M., Konopliv A. S., Williams J. G., Smith D. E., Zuber M. T., 2017. “Precession of Mercury’s Perihelion from Ranging to the MESSENGER Spacecraft”. *AJ* 153(3), 121, doi: 10.3847/1538-3881/aa5be2.
- Park R. S., Folkner W. M., Williams J. G., Boggs D. H., 2021. “The JPL Planetary and Lunar Ephemerides DE440 and DE441” *AJ* 161, doi: 10.3847/1538-3881/abd414.
- Pavlov, D., 2020, “Role of lunar laser ranging in realization of terrestrial, lunar, and ephemeris reference frames”. *J Geod* 94(5), doi: 10.1007/s00190-019-01333-y.
- Pijpers, F. P., 1998. “Helioseismic determination of the solar gravitational quadrupole moment”. *MNRAS* 297, L76–L80.
- Pitjeva, E., Pitjev, N., Pavlov, D., Turygin, S., 2021. “Estimates of the change rate of solar mass and gravitational constant based on the dynamics of the Solar System”. *A&A* 647, A141, doi:10.1051/0004-6361/202039893.
- Pitjeva, E., Pavlov, D., Aksim, D., Kan, M., 2022. “Planetary and lunar ephemeris EPM2021 and its significance for Solar system research”. *Proc. IAU*, vol. 15 (S364), doi: 10.1017/S1743921321001447.
- Solomon, S. et al. “The MESSENGER mission to Mercury: scientific objectives and implementation”, 2001. *Planetary and Space Science* 49, pp. 1445-1465, doi: 10.1016/S0032-0633(01)00085-X.
- Touboul, P. et al., 2022. “MICROSCOPE Mission: Final Results of the Test of the Equivalence Principle”. *Phys. Rev. Lett.* 129, 121102, doi: 10.1103/PhysRevLett.129.121102
- Viswanathan, V., Fienga, A., Minazzoli, O., Bernus, L., Laskar, J., Gastineau, M., 2018. “The new lunar ephemeris INPOP17a and its application to fundamental physics”. *MNRAS* 476(2), 1877–1888 (2018). doi: 10.1093/mnras/sty096.
- Williams, J.G., Turyshv, S.G., Boggs, D.H., 2012. “Lunar laser ranging tests of the equivalence principle”. *Class. Quant. Grav.* 29(18), 184004. doi: 10.1088/0264-9381/29/18/184004.
- Williams, J.G., Boggs, D.H., Folkner, W. M., 2014. “DE430 Lunar Orbit, Physical Librations, and Surface Coordinates”, JPL IOM 335, URL: https://naif.jpl.nasa.gov/pub/naif/generic_kernels/spk/planets/de430_moon_coord.pdf.
- Williams, J.G., Turyshv, S.G., Boggs, D.H., 2014. “The past and present Earth-Moon system: the speed of light stays steady as tides evolve”. *Planetary Science* 3(1), 2. doi: 10.1186/s13535-014-0002-5.

RELATIVISTIC TESTS WITH LUNAR LASER RANGING AND PLANETARY RADIO TRACKING DATA

W. TIAN¹

¹ Shanghai Astronomical Observatory, Chinese Academy of Science, China - tianwei@shao.ac.cn

ABSTRACT. A new planetary and lunar ephemeris PETREL19 was constructed on a solar system ephemeris platform developed by the authors. However, two Parametrized Post-Newtonian (PPN) parameters β and γ , measuring curvature of space geometry and nonlinearity of gravity, respectively, are fixed to unity in PETREL19. Given that considerable precise lunar laser ranging (LLR) normal points and planetary ranging measurements to Messenger and other planetary orbiters are available, in this work we will implement relativistic tests on two PPN parameters β and γ on basis of our ephemeris platform. In addition, Strong Equivalence Principle (SEP) test and an estimation of solar angular momentum factor on basis of gravito-magnetic effect are addressed as well.

1. INTRODUCTION

Various types of experiments to confirm the general theory of relativity (GRT) were done in fields of weak or strong gravity after the theory was proposed in 1915. For the solar system (the quality $\epsilon \sim GM/Rc^2 < 10^{-5}$), this is a classic regime of weak gravity (Will 2018). The dynamical equations of translational motion and rotational motion of the celestial bodies in the solar system expressed in first post-Newtonian approximation are widely accepted as the fundamentals in the construction of planetary and lunar ephemeris (e.g., Park et al., 2021; Pitjeva and Pitjev, 2014; Fienga et al., 2021). Since 1970s, considerable radio tracking data to planetary probes is available, the acquired high precision range/doppler measurements and VLBI astrometry enable one implement a series of relativistic tests in the regime of weak gravity, such as the test of the parameter γ by measuring light deflection of X&Ka bands carrier waves of the Cassini probe by the Sun (Bertotti et al., 2003), the perihelion shift of the Mercury by measuring range variations between the Earth and the Mercury (e.g., Park et al., 2017; Genova et al., 2018), etc. In addition, relativistic gravitational tests were also done with LLR measurements (e.g., Shapiro et al., 1988; Williams et al., 2004; Hofmann and Mueller, 2018).

Relativistic gravitational tests in the solar system with planetary ephemerides have been overviewed in the work published on Living Reviews in Relativity by Fienga et al (2024), where one can find latest results of relativistic tests with three different ephemeris families (DE, INPOP and EPM). Since a new planetary and lunar ephemeris PETREL19* was published (Tian 2023), the alike relativistic tests have not been implemented on our platform, called PETREL (**Plan**ETary and luna**R** Ephemeris **p**Latform). In this work we will report our preliminary results of several relativistic tests on the platform. After the introduction, the adopted dynamic model of the planetary and lunar ephemeris in this work is discussed in Sect.2. The tests on PPN parameters β and γ , SEP test, and an estimation of solar angular momentum factor on basis of gravito-magnetic effect are presented in Sect.3-5. Conclusions are given shortly at the end.

2. THE ADOPTED DYNAMIC MODEL

The dynamic model used in the initial version of our planetary and lunar ephemeris, PETREL19,

*Ephemeris data is available on Github, <https://github.com/TIAN-we/petrel19>

is described in detail in the work of Tian (2023). In comparison with PETREL19, the dynamical model used in this work is improved in the following aspects:

- 1 Earth tide model consistent with IERS2010 model is adopted.
- 2 Sun inducing tidal variations of lunar gravity of degree 2 is considered.
- 3 Geodetic and Lense-Thirring precession of lunar rotation is taken into account.
- 4 Lense-Thirring effect induced by solar angular momentum on acceleration of other bodies is considered.

2.1 Earth tide model

The tide model given in the IERS 2010 conventions (Petit and Luzum, 2010) consists of two parts: (1) frequency-independent part, and (2) frequency-dependent part which is induced by an-elasticity of mantle and dynamical effects of ocean tides. The complete description of the IERS2010 model and following formulae in the rest of this section can be found in the IERS 2010 conventions (Petit and Luzum, 2010).

Periodic variations in the normalized Stokes' coefficients $\Delta\bar{C}_{2m}$ and $\Delta\bar{S}_{2m}$ generated from dynamical effects of ocean tides read

$$\Delta\bar{C}_{nm} - i\Delta\bar{S}_{nm} = \sum_f (\mathcal{C}_{f,nm}^+ - i\mathcal{S}_{f,nm}^+) e^{i\theta_f} + \sum_f (\mathcal{C}_{f,nm}^- + i\mathcal{S}_{f,nm}^-) e^{-i\theta_f}, \quad (1)$$

where, the coefficients $(\mathcal{C}_{f,nm}^+, \mathcal{S}_{f,nm}^+)$ and $(\mathcal{C}_{f,nm}^-, \mathcal{S}_{f,nm}^-)$ are prograde and retrograde terms of main (tidal) waves of the FES2004 ocean tide model[†] (Lyard et al., 2006) recommended by IERS 2010 conventions, respectively. θ_f is phase expressed as a linear combination of the Greenwich Mean Sidereal Time GMST ($+\pi$) and five Delaunay variables (l, l', F, D, Ω) of the considered wave at frequency f . It is notable that the retrograde terms $(\mathcal{C}_{f,nm}^-, \mathcal{S}_{f,nm}^-)$ and cross terms consisting of

- long period ($m = 0$) ocean tides inducing variations in \bar{C}_{21} , \bar{S}_{21} , \bar{C}_{22} and \bar{S}_{22} .
- diurnal ($m = 1$) ocean tides inducing variations in \bar{C}_{20} , \bar{C}_{22} and \bar{S}_{22} .
- semi-diurnal ($m = 2$) ocean tides inducing variations in \bar{C}_{20} , \bar{C}_{21} and \bar{S}_{21} .

can not be incorporated into tide models of Five-Time-Delay type, which is firstly introduced by Williams et al. (2016) to handle frequency-dependent tidal effects of the Earth on the orbital motion of the Moon. In order to keep the Earth tide model in the development of planetary and lunar ephemeris as consistent as possible with the IERS recommended model, these retrograde terms and cross-over terms of the second degree are taken into account in the dynamic model, separately. For the prograde terms, we adopted a revised Earth tide model of Five-Time-Delay type (Tian, 2022).

2.2 Sun inducing tidal variations of lunar gravity of degree 2

Tidal variations of low degree harmonic induced by the Sun and Earth are considered in the GRAIL solution of lunar gravity model (e.g., Konopliv et al., 2013). In order to utilize the static and tidal components of lunar gravity model consistently, tidal variations of the 2nd degree harmonic induced by the Sun are considered in lunar gravity modelling. The associated terms impact both the orbital and rotational motion of the Moon.

2.3 Geodetic and Lense-Thirring precession of lunar rotation

[†]ftp://tai.bipm.org/iers/conv2010/chapter6/tidemodels/fes2004_Cnm-Snm.dat

In analogy to the relativistic theory of Earth rotation of Klioner et al. (2003), Coriolis torques from relativistic precession can be incorporated into the Euler dynamical equations of the lunar mantle and core written in the lunar mantle frame (e.g. Park et al., 2021),

$$\dot{\boldsymbol{\omega}} = \mathbf{I}_m^{-1} [-\dot{\mathbf{I}}_m \boldsymbol{\omega} - (\boldsymbol{\omega} - \boldsymbol{\Omega}_{iner}) \times (\mathbf{I}_m \boldsymbol{\omega}) + \boldsymbol{\Gamma}] \quad (2)$$

and

$$\dot{\boldsymbol{\omega}}_c = \mathbf{I}_c^{-1} [-(\boldsymbol{\omega} - \boldsymbol{\Omega}_{iner}) \times \mathbf{I}_c \boldsymbol{\omega}_c - \boldsymbol{\Gamma}_{CMB}] , \quad (3)$$

where the moment of inertia of the mantle $\mathbf{I}_m = \mathbf{I}_t - \mathbf{I}_c$ can be computed from the moment of inertia of the whole Moon \mathbf{I}_t and that of the fluid core \mathbf{I}_c . The torque $\boldsymbol{\Gamma}$ exerted on the Moon composes of three terms: (1) torque $\boldsymbol{\Gamma}_{M \leftarrow B}$ exerting on the Moon's figure by a point mass B ; (2) torque $\boldsymbol{\Gamma}_{M \leftarrow J_{2,E}}$ exerting on Moon's figure by the Earth's oblateness, and (3) torque $\boldsymbol{\Gamma}_{CMB}$ caused by the interaction between the mantle and the fluid core of the Moon.

Relativistic precession $\boldsymbol{\Omega}_{iner}$ consists of three components, geodetic precession and Lense-Thirring precession and Thomas precession. For the smallness of Thomas precession with respect to other two terms, it is not considered in this work. The adopted formula of relativistic precession reads

$$\boldsymbol{\Omega}_{iner} = \frac{1}{c^2} \sum_{A=\text{Sun,Earth}} \frac{\mu_A \mathbf{r}_{AM}}{r_{AM}^3} \times \left(\frac{3}{2} \mathbf{v}_M - 2 \mathbf{v}_A \right) \quad (4)$$

where μ_A is mass parameters of body A , \mathbf{r}_{AM} and r_{AM} are relative position vector and distance from body A to Moon. \mathbf{v}_A and \mathbf{v}_M are barycentric coordinate velocity of body A and Moon. c is the speed of light.

Relativistic rotation theory of the Moon implemented in our program is not completed. Post-Newtonian part of torques $\boldsymbol{\Gamma}_{M \leftarrow B}$ and $\boldsymbol{\Gamma}_{M \leftarrow J_{2,E}}$ are not considered. The time scale used in the Euler dynamical equations for the Moon is supposed to be a Selenocentric time scale, however, in this work, the time scale TDB is still used in the dynamical Eqs (2) and (3).

2.4 Lense-Thirring acceleration induced by solar angular momentum

Lense-Thirring (LT) effect first discovered by Lense and Thirring (1918) has impacts on both rotational motion discussed in the above subsection and orbital motion of a celestial body. The LT acceleration excited by angular momentum of a rotating body can be written as (e.g, Soffel and Langhans, 2013, Will, 2014)

$$\mathbf{a}_{LT} = -\frac{2(1+\gamma)}{c^2} \mathbf{v} \times (\nabla \times \mathbf{w}_\odot), \quad (5)$$

where \mathbf{v} is coordinate velocity of the accelerated body, and the solar angular momentum induced gravito-magnetic potential reads

$$\mathbf{w}_\odot = G \left[-\frac{(\mathbf{x} - \mathbf{x}_\odot) \times \mathbf{S}_\odot}{2|\mathbf{x} - \mathbf{x}_\odot|^3} \right], \quad (6)$$

where G is gravitational constant, \mathbf{x} and \mathbf{x}_\odot are positions of accelerated body and Sun. $\mathbf{S}_\odot = S \mathbf{k}$ is the angular momentum of the Sun with $S = 190.0 \times 10^{39} \text{kg} \cdot \text{m}^2 \cdot \text{s}^{-1}$ from helioseismology (Pijpers, 1998), and the unit vector \mathbf{k} depicting the direction of the solar rotation pole is derived from right ascension and declination of the pole recommended by Archinal et al. (2018).

3. RELATIVISTIC EFFECTS IN THE DEVELOPMENT OF PLANETARY AND LUNAR EPHEMERIS

The relativistic effects appearing in planetary and lunar ephemeris consist of two parts. One part impacts on dynamical equations. For point-like masses, the equation of motion in the first post-Newtonian approximation was obtained by Lorentz and Droste (1937) and Einstein et al (1938),

and often named (LD-)EIH equations. Will and Nordtvedt (1972) generalized the EIH equations in the parametrized post-Newtonian formalism with ten parameters. The version with β and γ to measure the amount of non-linearity and curvature of space respectively is widely adopted by planetary and lunar ephemeris groups.

As additional accelerations \mathbf{a}_η from the violation of the SEP and \mathbf{a}_{LT} induced by gravitomagnetic potential of the Sun are taken into account, the gravitational acceleration for a point mass A (exerted by other considered point masses) is written as

$$\begin{aligned}
\mathbf{a}_A^{\text{pm}} &= \sum_{B \neq A} \mu_B \frac{\mathbf{r}_{AB}}{r_{AB}^3} - \frac{1}{c^2} \sum_{B \neq A} \mu_B \frac{\mathbf{r}_{AB}}{r_{AB}^3} \left\{ 2(\gamma + \beta) \sum_{C \neq A} \frac{\mu_C}{r_{AC}} \right. \\
&+ (2\beta - 1) \sum_{C \neq B} \frac{\mu_C}{r_{BC}} + \frac{3(\mathbf{r}_{AB} \cdot \dot{\mathbf{x}}_B)^2}{2r_{AB}^2} - \frac{1}{2} \sum_{C \neq B} \mu_C \frac{\mathbf{r}_{AB} \cdot \mathbf{r}_{BC}}{r_{BC}^3} \\
&\left. - (1 + \gamma) \dot{\mathbf{x}}_B \cdot \dot{\mathbf{x}}_B - \gamma \dot{\mathbf{x}}_A \cdot \dot{\mathbf{x}}_A + 2(1 + \gamma) \dot{\mathbf{x}}_A \cdot \dot{\mathbf{x}}_B \right\} \\
&- \frac{1}{c^2} \sum_{B \neq A} \frac{\mu_B}{r_{AB}^3} \left\{ \mathbf{r}_{AB} \cdot [2(1 + \gamma) \dot{\mathbf{x}}_A - (2\gamma + 1) \dot{\mathbf{x}}_B] \right\} (\dot{\mathbf{x}}_A - \dot{\mathbf{x}}_B) \\
&+ \frac{1}{c^2} \left(2\gamma + \frac{3}{2} \right) \sum_{B \neq A} \frac{\mu_B}{r_{AB}} \sum_{C \neq B} \mu_C \frac{\mathbf{r}_{BC}}{r_{BC}^3} + \mathbf{a}_\eta + \mathbf{a}_{LT}, \tag{7}
\end{aligned}$$

where position \mathbf{x}_A (or \mathbf{x}_B) and velocity $\dot{\mathbf{x}}_A$ (or $\dot{\mathbf{x}}_B$) for body A (or B) are given in the global reference system. The term \mathbf{a}_{LT} is given in Sect. 2.4, while the term \mathbf{a}_η reads (e.g., Klioner, 2016),

$$\mathbf{a}_\eta = \frac{1}{c^2} \eta \frac{\Omega_A}{\mathcal{M}_A} \sum_{B \neq A} \mu_B \frac{\mathbf{r}_{AB}}{r_{AB}^3}, \tag{8}$$

where η a factor measuring violation of the SEP, \mathcal{M}_A and Ω_A are mass and gravitational self-energy of a considered major body A .

Another part of relativistic effect impacts on observation equation of ranging measurements. If a radio signal is emitted from $\vec{\mathbf{x}}_1$ at t_1 and is received at $\vec{\mathbf{x}}_2$ at t_2 , the coordinate time interval of propagation reads (e.g., Moyer 2000)

$$t_2 - t_1 = \frac{|\vec{\mathbf{x}}_2(t_2) - \vec{\mathbf{x}}_1(t_1)|}{c} + \sum_J \frac{(1 + \gamma)\mu_J}{c^3} \ln\left(\frac{r_{J1} + r_{J2} + \rho}{r_{J1} + r_{J2} - \rho}\right), \tag{9}$$

where the sum is carried out over all bodies J at \mathbf{x}_J and where $r_{J1} = |\vec{\mathbf{x}}_1 - \vec{\mathbf{x}}_J|$, $r_{J2} = |\vec{\mathbf{x}}_2 - \vec{\mathbf{x}}_J|$ and $\rho = |\vec{\mathbf{x}}_2 - \vec{\mathbf{x}}_1|$. The coordinate time TDB is often used as time scale for integration of dynamic equations and in the light-time equation (9) in the TDB-compatible global reference system. Therefore, due to relativistic effect existing in time scale transformation between TDB and TT or UTC, which is adopted to record ranging measurements, it will enter implicitly into their observation equation.

4. OBSERVATIONS

The adopted observations[‡] in the relativistic tests are same as PETREL19. In general, precise ranging measurements play dominated roles in the relativistic tests with planetary ephemeris. The

[‡]https://ssd.jpl.nasa.gov/planets/obs_data.html, <http://www.geoazur.fr/astrogeo/?href=observations/base>, and https://ilrs.gsfc.nasa.gov/data_and_products/data/index.html.

planetary ranging measurements consist of Messenger range measurements from 2011 to 2015, Venus Express range measurements from 2006 to 2011, ranging measurements to several Martian orbiters (e.g., Mars Express from 2005 to 2015, MGS from 1999-2006, MRO from 2006 to 2014, ODY from 2002 to 2013) and landers (e.g., Viking -1 and -2 from 1976 to 1982, and Pathfinder in 1997). The lunar laser ranging data up to 2021 is processed instantaneously with other types of planetary measurements.

5. TEST RESULTS WITH PETREL EPHEMERIS

In each test, the list of fitted parameters consists of: (1) PETREL19 parameters, such as initial values for major bodies and for the lunar rotation angles, mass parameters, solar parameters, Lunar and terrestrial parameters, station coordinates, and biases, etc.; (2) the tested parameter(s), for example, β , γ , η and angular momentum factor of the Sun S . It is notable that the solar oblateness J_2 is fixed to 0.223, which is estimated in a non-GRT solution in order to avoid strong correlation between the parameter J_2 and tested parameter(s) in a particular solution.

For tests on PPN parameter β and γ , three solutions with different parameter space are obtained. In solutions 1 and 2, single PPN parameter β and γ are estimated respectively. For both solutions, the estimated β and γ will converge to be value of 1. The estimated results are given in table 1. In solution 3, β and γ are estimated, simultaneously. Nevertheless, due to high correlation between two parameters (~ 0.998), which is much higher than in Fienga et al. (2015, 2022), the estimated values do not converge (see Fig. 1). In addition, the formal errors are about one order of magnitude larger than those of solutions 1 and 2.

	Sol. 1	Sol. 2	Sol. 3
$\beta - 1$	$(0.66 \pm 1.75) \times 10^{-5}$	Fixed to 0	$(42.7 \pm 3.3) \times 10^{-4}$
$\gamma - 1$	Fixed to 0	$(-1.34 \pm 9.06) \times 10^{-6}$	$(21.4 \pm 1.70) \times 10^{-4}$

Table 1: Comparison of estimated PPN parameters β and γ in three solutions (3σ).

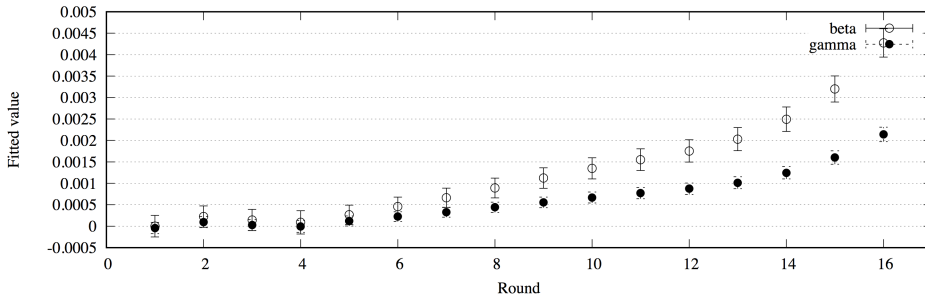


Figure 1: Estimation of β and γ simultaneously from LLR and planetary ranging measurements. Round 1-16 indicates the number of iterations to obtain a solution.

For the factor η depicting violation of the SEP, the estimated value $(11 \pm 5.3) \times 10^{-5}(3\sigma)$ is obtained. In comparison with the estimated value $\eta = (-6.6 \pm 7.2) \times 10^{-5}$ of Genova et al. (2017), where only Messenger tracking data was used, a smaller uncertainty is obtained. Nevertheless, a significant offset about 2 times larger than 3σ exists in our test.

As a confirmation of Lense-thirring effect having detectable impacts on our dynamical model, the solar angular momentum factor S is estimated. The estimated $S = (7.63 \pm 0.91) \times 10^{23} \text{kg} \cdot \text{AU}^2 \cdot \text{Day}^{-1}$ agrees well the value $S_0 = 7.34 \times 10^{23} \text{kg} \cdot \text{AU}^2 \cdot \text{Day}^{-1}$ from helioseismology (Pijpers, 1998). Due

to strong correlation between S and solar oblateness J_2 as mentioned by Iorio (2005), at present, we have not succeeded in decoupling the strong correlation between two parameters and estimated them simultaneously in one solution yet.

6. CONCLUSIONS

In this paper, several relativistic gravitational tests are implemented on the ephemeris platform PETREL for the first time. Preliminary results on two PPN parameters β and γ , parameter of violation of SEP η and solar angular momentum factor S are given. Nevertheless, for the tests in which two PPN relativistic parameters were simultaneously estimated, our result is still significantly affected by correlations between fitted parameters and non-convergence through iterative adjustment. Therefore, decoupling correlations between several pairs of fitted parameters, e.g., PPN parameters (β , γ), solar parameters (S , J_2), and evaluating the actual uncertainty of the fitted parameters will be investigated in the near future.

Acknowledgement. This work is supported by the National Natural Science Foundation of China (NSFC) under grant No. 42241137.

7. REFERENCES

- Archinal, B. A., Acton, C. H., A'Hearn, M. F., et al., 2018, Report of the IAU Working Group on Cartographic Coordinates and Rotational Elements: 2015, *Celest. Mech. Dyn. Astr.*, 130(3):22.
- Bertotti, B., Iorio, L., Tortora, P., 2003, A test of general relativity using radio links with the Cassini spacecraft, *Nature*, 425, 374–376.
- Einstein A., Infeld L., Hoffmann B., 1938, The Gravitational Equations and the Problem of Motion, *Annals of Mathematics*, 39(1):65-100.
- Fienga, A., Deram, P., Di Ruscio, A., et al., 2021, INPOP21a planetary ephemerides, *Notes Scientifiques et Techniques de l'Institut de Mécanique Céleste*, 110.
- Fienga, A., Laskar, J., Exertier, P., et al., 2015, Numerical estimation of the sensitivity of INPOP planetary ephemerides to general relativity parameters, *Celest. Mech. Dyn. Astr.*, 123, 325–349.
- Fienga, A., Minazzoli, O., 2024, Testing theories of gravity with planetary ephemerides, *Living Reviews in Relativity* 27. doi:10.1007/s41114-023-00047-0
- Genova, A., Mazarico, E., Goossens, S., et al., 2018, Solar system expansion and strong equivalence principle as seen by the NASA MESSENGER mission, *Nat. Commun.* 9:289.
- Hofmann, F., Müller, J., 2018, Relativistic tests with lunar laser ranging, *Classic. Quant. Grav.*, 35, 035015.
- Iorio, L., 2005, Is it possible to measure the Lense-Thirring effect on the orbits of the planets in the gravitational field of the Sun? *A&A*, 431, 385–389.
- Klioner, S. A., 2016, Parametrized post-Newtonian equations of motion of N mass monopoles with the SEP violation. arXiv e-prints. arXiv:1607.00183.
- Klioner, S. A., Soffel, M., Xu, C., et al., 2003, Earth's rotation in the framework of general relativity: rigid multipole moments, in *Journées 2001 - systèmes de référence spatio-temporels. Influence of geophysics, time and space reference frames on Earth rotation studies*, 13, 232-238.
- Konopliv, A. S., Park, R. S., Yuan, D.-N., et al. 2013, The JPL lunar gravity field to spherical harmonic degree 660 from the GRAIL primary mission, *J. Geophys. Res. (Planets)*, 118, 1415.
- Lense, J., Thirring, H., 1918, Über den Einfluß der Eigenrotation der Zentralkörper auf die Bewegung der Planeten und Monde nach der Einsteinschen Gravitationstheorie, *Physikalische Zeitschrift*, 19, 156

- Lorentz, H. A., Droste, J., 1937, The motion of a system of bodies under the influence of their mutual attraction, according to einstein's theory. In: Lorentz HA (ed) *Collected Papers*. Springer, Dordrecht.
- Lyard, F., Lefevre, F., Letellier, T., et al., 2006, Modelling the global ocean tides: modern insights from FES2004, *Ocean Dyn.*, 56, 394.
- Moyer, T. D., 2000, Formulation for Observed and Computed Values of Deep Space Network Data Types for Navigation, Monography of deep space communications and navigation series, 2.
- Park, R. S., Folkner, W. M., Konopliv, A. S., et al., 2017, Precession of Mercury's Perihelion from Ranging to the MESSENGER Spacecraft, *AJ* , 153.
- Park, R. S., Folkner, W. M., Williams, J. G., et al., 2021, The JPL Planetary and Lunar Ephemerides DE440 and DE441, *AJ* , 161:105.
- Petit, G., Luzum, B., 2010, IERS Conventions (2010), IERS Technical Note, 36, 1.
- Pijpers, F. P., 1998, Helioseismic determination of the solar gravitational quadrupole moment, *MNRAS* , 297, L76.
- Pitjeva, E. V., Pitjev, N. P., 2014, Development of planetary ephemerides EPM and their applications, *Celest. Mech. Dyn. Astr.* , 119, 237-256.
- Shapiro, I. I., Reasenberg, R. D., Chandler, J. F., et al., 1988, Measurement of the de Sitter precession of the Moon: A relativistic three-body effect, *Phys. Rev. Lett.* 61, 2643–2646.
- Soffel, M, Langhans, R., 2013, *Space-Time Reference Systems*, Berlin:Springer Berlin Heidelberg.
- Tian, W., 2022, Revisiting Earth tide parameters used in the development of planetary and lunar ephemeris, *Celest. Mech. Dyn. Astr.* , 134, 56.
- Tian, W., 2023, PETREL19: a new numerical solution of planetary and lunar ephemeris, *Celest. Mech. Dyn. Astr.* , 135:38.
- Will, C. M., Nordtvedt, J. K., 1972, Conservation Laws and Preferred Frames in Relativistic Gravity. I. Preferred-Frame Theories and an Extended PPN Formalism, *AJ* , 177:757.
- Will, C. M., 2014, The Confrontation between General Relativity and Experiment, *Living Reviews in Relativity* 17. doi:10.12942/lrr-2014-4
- Will, C. M., 2018, *Theory and Experiment in Gravitational Physics*, Cambridge: Cambridge University Press.
- Williams, J. G., Boggs, D. H., 2016, Secular tidal changes in lunar orbit and Earth rotation, *Celest. Mech. Dyn. Astr.* , 126, 89.
- Williams, J. G., Turyshev, S. G., Boggs, D. H., 2004, Progress in Lunar Laser Ranging Tests of Relativistic Gravity, *Phys. Rev. Lett.* 93, 261101.

BAYESIAN APPROACHES FOR ORBITOGRAPHY: APPLICATION TO FUNDAMENTAL PHYSICS

V. MARIANI¹, A. FIENGA^{1,2}, O. MINAZZOLI^{3,4}, J.LASKAR², M. GASTINEAU²

¹ Géoazur, Université Côte d'Azur, Observatoire de la Côte d'Azur, CNRS, 250 av. A. Einstein, 06250 Valbonne, France - vincenzo.mariani@geoazur.unice.fr

² IMCCE, Observatoire de Paris, PSL University, CNRS, 77 av. Denfert-Rochereau, 75014 Paris, France

³ Université Côte d'Azur, Observatoire de la Côte d'Azur, CNRS, Artemis, bd. de l'Observatoire, 06304, Nice, France

⁴ Bureau des Affaires Spatiales, 2 rue du Gabian, 98000 Monaco

ABSTRACT. Bayesian approaches and machine learning techniques are opening up new perspectives in inverse problems in all areas of physics. In the field of orbit determination, least-squares methods are widely used, but encounter difficulties when the uncertainties of the observations are poorly known, or when the dynamic model has too many parameters to solve for. We show some results obtained in the domain of fundamental physics tests within the solar system, tackling the problem with a bayesian approach. Combining Gaussian Processes and Markov Chain Monte Carlo methods, we show how it is possible to get the posterior distribution of the mass of the graviton, taking into account the full dynamics of the solar system. Similarly, we test the Brans-Dicke class of scalar tensor theories: we find marginal evidence suggesting that the effect of violation of the Strong Equivalence Principle can no longer be assumed as negligible in planetary ephemerides with the current data.

1. INTRODUCTION

Bayesian approaches and machine learning techniques are opening up new perspectives in inverse problems in all areas of physics. In the field of orbit determination, least-squares methods are widely used, but encounter difficulties when the uncertainties of the observations are poorly known, or when the dynamic model has too many parameters to solve for. The motion of the celestial bodies in the solar system can be solved directly by integrating numerically their equations of motion. The improved accuracy in measurements of observables from space missions (e.g. Cassini-Huygens, Mars Express, BepiColombo, Juice, etc.) makes the solar system a suitable environment for testing general relativity theory (GRT) as well as alternative theories of gravity by means of solar system orbitography. For a detailed review regarding the use of planetary ephemerides for testing GRT, we refer to Fienga & Minazzoli 2024. In the present work we use INPOP21a planetary ephemerides (Fienga et al., 2021), which benefit from the latest Juno and Mars orbiter tracking data up to 2020, and from radio-science observations from space missions such as Cassini-Huygens, Mars Express and Venus Express. Moreover, a fit of the Moon-Earth system to Lunar Laser Ranging (LLR) observations up to 2020 is included. The dynamical modelling used in INPOP21a takes into account the eight planets of the Solar System, as well as Pluto, the Moon, the asteroids, the Kuiper belt, the Sun oblateness, and the Lense-Thirring effect. We refer to Fienga et al. (2021) for a detailed review of this version of INPOP. We are going to present the results of the Bayesian methodology proposed in Mariani et al. (2023) applied to two different cases: first, we show the results concerning the posterior distribution of the mass of the graviton (see Mariani et al., 2023); second, we show a test on the potential violation of the Strong Equivalence Principle (SEP) in the

solar system, within the context of the Brans-Dicke theory. For the full description of the results on the potential SEP violation see Mariani et al. (2024).

2. METHODOLOGY

In this section we are going to describe briefly the methodology applied to obtain the results. The description is done in the case of the mass of the graviton, however it is totally similar for the test of the Brans-Dicke theory.

The main tool to assess the goodness of the INPOP fit with respect to modifications in the equations of motion or in the global framework of the ephemeris is the χ^2 . In particular the computation of the INPOP χ^2 plays an essential role to determine which data or model would significantly improve the ephemeris computation. In our work, the computation of $\chi^2(m_g)$ is the output, for a given value of m_g , of the INPOP iterative fit, after adjustment of all its astronomical parameters. The $\chi^2(m_g)$ is computed as follows:

$$\chi^2(m_g, \mathbf{k}) \equiv \frac{1}{N_{\text{obs}}} \sum_{i=1}^{N_{\text{obs}}} \left(\frac{g^i(m_g, \mathbf{k}) - d_{\text{obs}}^i}{\sigma_i} \right)^2 \quad (1)$$

where m_g is a fixed value, \mathbf{k} are the astronomical parameters fitted with INPOP, N_{obs} is the number of observations, the function g^i represents the computation of observables, the vector $\mathbf{d}_{\text{obs}} = (d_{\text{obs}}^i)_i$ is the vector of observations and σ_i are the observational uncertainties. In order to produce the posterior distribution for m_g we start computing $\chi^2(m_g)$ for some m_g spread over the domain of our interest. Whereupon a Gaussian Process Regression (GPR) is computed, obtaining the interpolation $m_g \mapsto \tilde{\chi}^2(m_g)$ with the corresponding uncertainty. Such an approximation is useful to quickly compute the likelihood and to apply the Metropolis-Hastings (MH) algorithm as part of Markov Chain Monte Carlo (MCMC) methods. The outcome is the posterior for the mass of the graviton m_g . In Figure 1 is shown the sketch of the used processing pipeline.

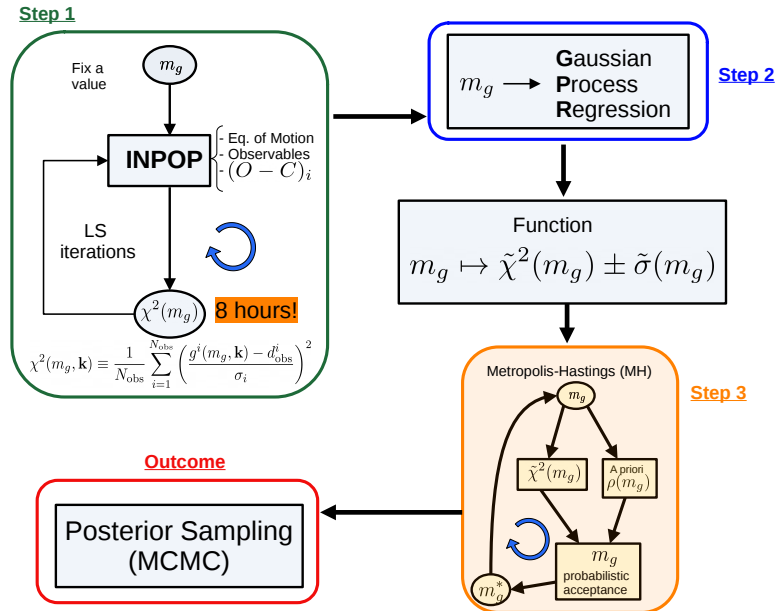


Figure 1: Block diagram representing the general pipeline used to obtain the posterior of m_g .

3 RESULTS

In the following subsections we are going to describe the results obtained in the two considered cases: in Sec. 3.1, we briefly describe the results on the posterior for the mass of the graviton; in Sec. 3.2, we describe the results obtained for the test on the strong equivalence principle in the case of the Brans-Dicke theories.

3.1 Results: the mass of the graviton

In terms of prior for the mass of the graviton, we firstly chose an uniform distribution with large intervals of values encompassing the latest results from Bernus et al. (2020) but without giving preference to any possible values. Following the Steps 2 and 3 of Figure 1, for each value of the graviton mass proposed by the MH algorithm, the value $\tilde{\chi}^2(m_g)$ is computed (using the GPR) instead of $\chi^2(m_g)$.

MH algorithm and Gaussian Process Regression (GPR) In Figure 2 is plotted the posterior density of probability obtained with MH algorithm associated with GPR, supposing an uniform prior. Contrarily to a detection curve (see i.e. Mariani et al., 2023) from Figure 2, we do not have a single figure that we could choose as value for the mass of the graviton. Indeed the shape is not a *bell*, nor does it show an individual peak. The quantile at 97% is $0.0985 \times 10^{-23} \text{ eV}c^{-2}$. The posterior plotted on Figure 2 also tends to concentrate close to $m_g = 0$ with decreasing steps for larger m_g up to $m_g < 0.15 \times 10^{-23} \text{ eV}c^{-2}$. The conclusion drawn is that, within the GPR approximation of χ^2 , we do not have any detection for $m_g \neq 0$. Thus we can't provide an estimated value for the mass of the graviton, but we can give a 99.7% upper limit as quantile of the deduced mass posterior, that is $m_g \leq 0.98 \times 10^{-24} \text{ eV}c^{-2}$.

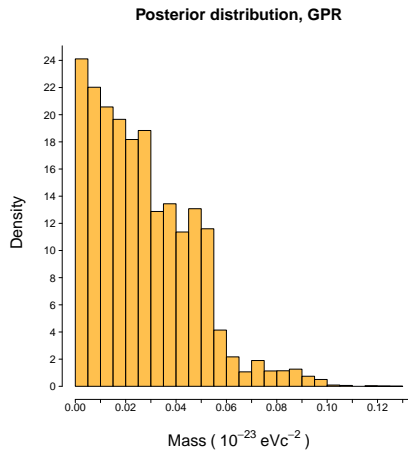


Figure 2: Density for the posterior probability distribution used as target probability. The prior was a uniform prior between 0 and $3.62 \times 10^{-23} \text{ eV}c^{-2}$.

Uncertainty Assessment In order to explore the uncertainties induced by the GPR interpolation on $\tilde{\chi}^2(m_g)$ values, we ran 300 MCMC using MH algorithm. Each MH is performed on a different Gaussian Process Uncertainty Estimation (GPUE). One GPUE is a perturbation of the GPR within the uncertainty provided by the GPR itself. Running the MCMC on the GPUE is a way to propagate the uncertainty induced by the GPR in the posterior sampling. We, therefore, built a posterior distribution presented in blue in Figure 3 accounting for the GPR uncertainty, and we call such a posterior Gaussian Process Uncertainty Realization (GPUR). We are able, then, to provide limits

for the mass m_g . The upper bound for GPUR we would provide at 99.7% C.L. is $m_g \leq 1.01 \times 10^{-24} \text{ eV}c^{-2}$. This represents an improvement of about 1 order of magnitude from the previous estimations in terms of upper limit provided for m_g at 99.7% C.L. . Such a limit is taken from the GPUR posterior (see Figure 3) since it takes into consideration also the GPR uncertainty.

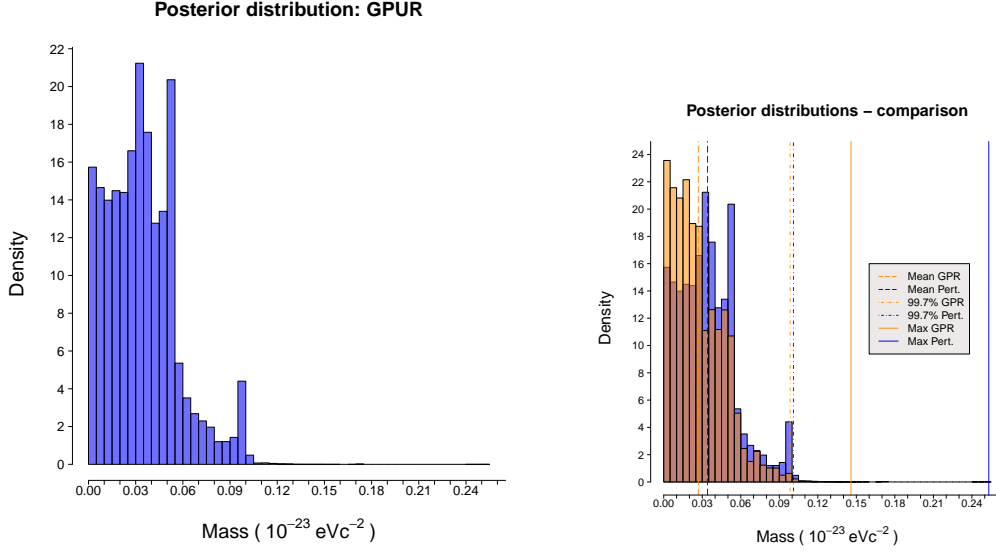


Figure 3: On the left, the posterior probability distribution obtained including GPR error assessment called GPUR. On the right two densities overlapped: the posterior probability distributions obtained from GPR (in orange) and the posterior with GPR error assessment (in blue). The dashed lines on the left represent the averages of the posterior with GPR and GPUR (respectively orange and blue). The dot-and-dashed lines represent the 99.7% quantiles of the two densities. The solid lines are instead in place of the maximum m_g for each one of the two densities. The brown area of the histogram represents the overlaid zone among the two posteriors presented.

Results with the half-Laplace prior distribution The absence of positive detection can be interpreted in two ways: either because the data employed are not sensitive enough, or because GRT is sufficient to explain the data. The lack of detection could also depend on the hypothesis made on our a priori knowledge of the mass of the graviton. In order to discriminate between the former and the latter and to test the sensitivity of our results to the prior, we made an additional experiment, changing the prior density for m_g in the MH algorithm from an uniform prior to a half-Laplace distribution. We run the MH algorithm again, with the same GPR, in using a half-Laplace prior (red line in Figure 4). The underlying idea of half-Laplace prior is to give preference to the mass value $m_g = 0$, being in our case representative of GRT. As one can see in Figure 4, the MH algorithm does not provide the same outcome with the two different priors, and in particular the new posterior (green in Figure 4) turns out to be piled up around $m_g = 0$. We may see, then, whether the new posterior (green in Figure 4) resembles the old one (orange in Figure 4) or not: we found that it is not the case. We can thus conclude that the information contained in the data set (and by using this methodology) is not strong enough to move the narrow half-Laplace prior density towards a more uniform density since the MH algorithm is choosing to remain stuck on GRT, and slightly even more peak toward $m_g = 0$. This can be understood as GRT is slightly preferred to explain completely the observational data within this interval.

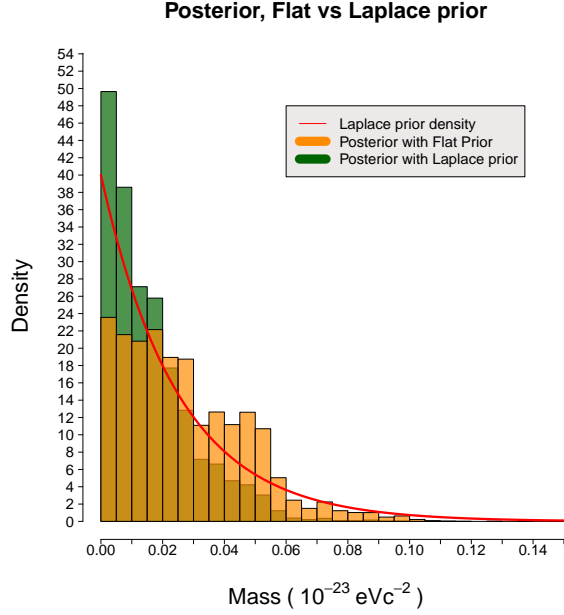


Figure 4: Densities for the posterior probability distributions obtained from GPR with an uniform (flat) prior (in orange) and with a half-Laplace prior (dark green). In red, the shape of the half-Laplace prior used. The brown area is the overlaid zone of the two posteriors

3.2 Results: the strong equivalence principle

In order to evaluate the impact of the method proposed within a well-known context, we first estimated the possible violation of general relativity by considering $1 - \gamma \neq 1$ without considering possible SEP violation (i.e. $\eta = 0$). With this configuration, our results are comparable to classical conjunction tests like the one obtained during the Cassini interplanetary phase when the radio-science signal of the Cassini s/c grazed the Sun before reception on earth. During this conjunction, the Shapiro delay is at its maximum and Bertotti et al. (2003) deduced the best constraint on γ so far with a global fit of s/c orbit parameters and γ . As this part of the mission (interplanetary phase) is supposed to be the least affected by complex gravitational interactions or maneuvers, the determination is in principle the most accurate and the least affected by biases or noise. Because of the estimation method (least square), the Bertotti et al. (2003) constraint, $1 - \gamma = (-2.1 \pm 2.3) \times 10^{-5}$, is given at 1σ , assuming a Gaussian distribution of the noise. Two main differences between our approach and the results obtained by Bertotti et al. (2003) have to be stressed. First, by construction of our model, only values of γ where $1 - \gamma > 0$ are tested. Once we compare our results with Bertotti et al. (2003), we have to compare with the absolute value of their interval as it is represented in Figure 5. Second, we use a Bayesian approach using a uniform prior with a maximum value for $1 - \gamma$ of 15×10^{-5} and providing a posterior distribution of acceptable $1 - \gamma$ values. In this context, for comparisons of results, it is important to consider the confidence level (C.L.) deduced from the posteriors. In Figure 5, we see the limit of about 4.4×10^{-5} at 66.7% C.L. (1σ) of the $\|1 - \gamma\|$ interval deduced from Bertotti et al. (2003) shown as black dashed line (Figure 5), and in yellow, the posterior distribution of $\|1 - \gamma\|$ obtained with this work. At 99.7% C.L., we obtain a limit of 2.5×10^{-5} (red dot-dashed line in Figure 5) and of about 1.73×10^{-5} at 66.7% C.L. (blue dotted line in Figure 5). It is interesting to note, at this stage, that the limits we obtain are of the same order of magnitude as those obtained by Bertotti

Posterior, without SEP violation

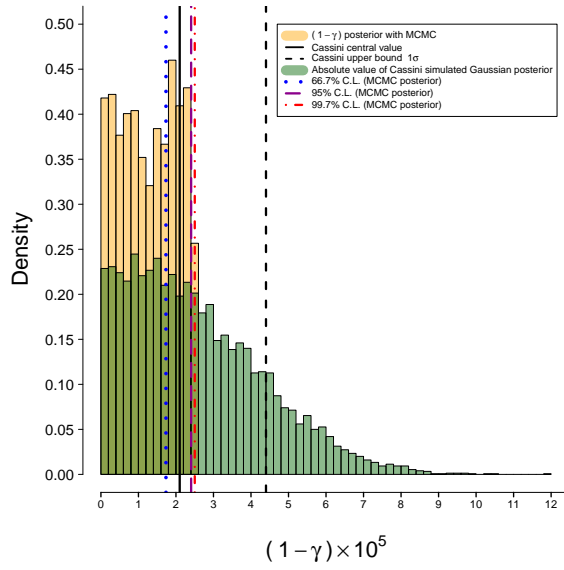


Figure 5: Posterior distributions without SEP violation. Yellow: Posterior distribution for $1 - \gamma$ without the implementation of the SEP violation. Green: Absolute value of the simulated posterior for the determination of $1 - \gamma$ with Cassini. Red line (dot-dashed): 99.7 % C.L. ($(1 - \gamma) = 2.50 \times 10^{-5}$). Blue line (dotted): 66.7 % C.L. ($(1 - \gamma) = 1.73 \times 10^{-5}$). Purple line (dashed): 95 % C.L. ($(1 - \gamma) = 2.40 \times 10^{-5}$). The prior for $(1 - \gamma)$ is a uniform prior between 0 and 15×10^{-5} . Solid black line: Absolute value of Cassini central value estimation ($(1 - \gamma) = -2.1 \times 10^{-5}$). Dashed black line: Upper bound estimation from Cassini at 1σ C.L.

et al. (2003). However, we stress that these results were obtained while exploring only γ values smaller than 1.

Limit on γ and α_0 with SEP violation After considering the results of an exploration of the $1 - \gamma$ without SEP violation, we now switch to the full Brans-Dicke formalism with SEP violation. We used the method described in Sect. 2 for the determination of acceptable values for the parameter α_0 . Figure 6 shows the posterior of $1 - \gamma$ and the deduced α_0 . At 99.7 % C.L., we obtain a limit on $\|1 - \gamma\|$ of about 2.83×10^{-5} , leading to a constraint on α_0 of about 3.76×10^{-3} . From the constraint on α_0 and on γ , one can deduce limits for the Nordtvedt parameter $\eta = \gamma - 1$. In particular at 99.7 % C.L., $\eta > -2.83 \times 10^{-5}$, at 95 % C.L., $\eta > -2.70 \times 10^{-5}$, and at 66.7 % C.L., $\eta > -1.92 \times 10^{-5}$ (see Mariani et al., 2024 for further details).

It is interesting to note that the limit obtained for $1 - \gamma$ in the BD framework with the SEP violation is larger than that obtained without the SEP violation (see Figure 5). We interpret this as marginal evidence that, at the level of accuracy of current planetary ephemerides, the effect of the SEP violation is no longer negligible. Indeed, adding the effect increases the correlations between γ and planetary parameters, which in this context derives from the additional correlations that exist between δ_T and planetary parameters (masses, initial conditions, etc.). This leads to the usual reduction in the accuracy of the estimation of the constraint on the theoretical parameter being tested. Indeed, with a greater number of correlations, more freedom is provided to better fit the data, however this leads to weaker constraints. Also, because we observed that including the SEP violation leads to slightly more stable solutions for the planetary orbits, we believe that including the SEP violation in alternative theories—that is, $\eta \neq 0$ —is more consistent at the dynamical level

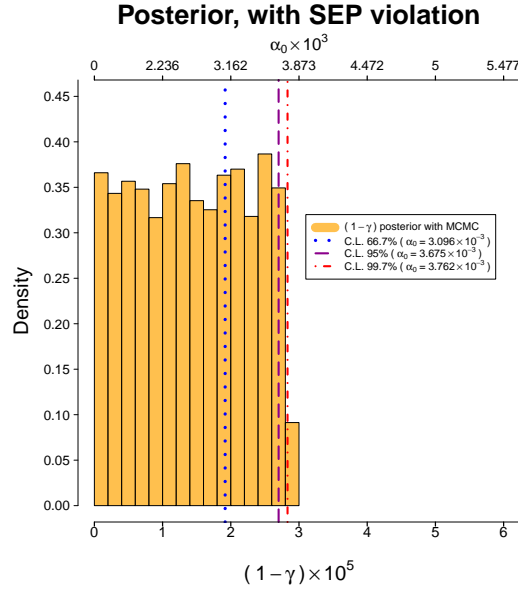


Figure 6: Posterior distribution for $1 - \gamma$ and the corresponding values of α_0 in the Brans-Dicke framework with the implementation of the SEP violation. Red line (dot-dashed): 99.7 % C.L. ($(1 - \gamma) = 2.83 \times 10^{-5}$ and $\alpha_0 = 3.762 \times 10^{-3}$). Blue line (dotted): 66.7% C.L. ($(1 - \gamma) = 1.92 \times 10^{-5}$ and $\alpha_0 = 3.096 \times 10^{-3}$). Purple line (dashed): 95 % C.L. ($(1 - \gamma) = 2.70 \times 10^{-5}$ and $\alpha_0 = 3.675 \times 10^{-3}$). The prior for $(1 - \gamma)$ is a uniform prior between 0 and 15×10^{-5} .

than not including it.

4. CONCLUSIONS

In the present work we described the results obtained in two different contexts but with the same methodology. We presented our work on the use of MCMC algorithm in order to get an improvement of the detection limit of the mass of the graviton m_g using the solar system dynamics as arena. From the posterior obtained, we can provide an upper bound of $m_g \leq 1.01 \times 10^{-24} eV c^{-2}$ at 99.7% C.L. . Next to this, we showed with a change of the prior (from uniform to half-Laplacian) that no significant information is detectable with planetary ephemerides for masses smaller than this limit. Moreover, we used the same Bayesian methodology in order to obtain the latest constraints from planetary ephemerides on the Brans-Dicke theory of gravity. In this context, we find that $\|1 - \gamma\| < 1.92 \times 10^{-5}$ at the 66.7% C.L., while the previous best Solar System constraints from ranging data of the Cassini spacecraft Bertotti et al. (2003) on γ led to $\|1 - \gamma\| < 4.4 \times 10^{-5}$ at 66.7% C.L. At the 99.7% C.L., the new planetary ephemerides constraint reads $\|1 - \gamma\| < 2.83 \times 10^{-5}$.

5. REFERENCES

- Fienga, A., Minazzoli, O. "Testing theories of gravity with planetary ephemerides". Living Rev Relativ 27, 1 (2024). <https://doi.org/10.1007/s41114-023-00047-0>
- Fienga, A., Deram, P., Di Ruscio, A., Viswanathan, V., Camargo, J. I. B., Bernus, L., Gastineau, M., Laskar, J. "INPOP21a planetary ephemerides", Notes Scientifiques et Techniques de l'Institut de Mécanique Céleste, S110. 2021, 19 pp.
- Mariani V., Fienga, A., Minazzoli, O., Gastineau, M., Laskar, J. "Bayesian test of the mass of the graviton with planetary ephemerides" Phys. Rev. D 108, 024047, July 2023.
- Mariani V., Minazzoli, O., Fienga, A., Laskar, J. and Gastineau, M. "Bayesian test of Brans–Dicke theories with planetary ephemerides: Investigating the strong equivalence principle" A&A, 682,

- A175 (2024).
- Bernus, L., Minazzoli, O., Fienga, A., Gastineau, M., Laskar, J., Deram, P., and Di Ruscio, A. "Constraint on the Yukawa suppression of the Newtonian potential from the planetary ephemeris INPOP19a", *Phys. Rev. D* 102, 021501 (2020).
- Bernus, L., Minazzoli, O., Fienga, A., Gastineau, M., Laskar, J., and Deram, P. "Constraining the Mass of the Graviton with the Planetary Ephemeris INPOP", *Phys. Rev. Lett.* 123, 161103 (2019).
- Bertotti, B., Iess, L., Tortora, P. "A test of general relativity using radio links with the Cassini spacecraft" *Nature* volume 425, 374- 376 (2003).

SOLAR SYSTEM PHENOMENOLOGY OF ENTANGLED RELATIVITY

O. MINAZZOLI^{1,2}

¹Université Côte d'Azur, Observatoire de la Côte d'Azur, CNRS, Artemis, bd. de l'Observatoire, 06304, Nice, France.

²Bureau des Affaires Spatiales, 2 rue du Gabian, 98000 Monaco.
- olivier.minazzoli@oca.eu

ABSTRACT. Entangled Relativity is a non-linear reformulation of Einstein's general theory of relativity (General Relativity) that is more parsimonious in its formulation. It accurately recovers the results of General Relativity in many astrophysical situations, particularly in the Solar System, where the theory currently cannot be distinguished from General Relativity. This paper will explore how this might change in the near future.

1. INTRODUCTION

Entangled Relativity is essentially a non-linear reformulation of General Relativity. Its name does not refer to *quantum entanglement*, but rather to the fact that matter and curvature (gravity) are intertwined at the foundational level of the theory's formulation. In this framework, one cannot define matter and curvature separately; both must be present simultaneously to even define the theory. This differs from General Relativity, where one can envisage a world with only gravity: an entire universe in a vacuum. This notably leads to an infinite set of non-trivial solutions to the vacuum field equations, ranging from black hole solutions to universes entirely filled with black holes—a kind of potential absolutely dark universe.

However, there is a compelling reason to be dissatisfied with a relativistic theory that permits vacuum solutions, even if they are not exactly realized in nature due to the presence of matter fields in our universe. This reason is rooted in the violation of one of the three founding principles that Einstein used to construct his general theory of relativity: the *principle of relativity of inertia*, also known as *Mach's principle*. In particular, General Relativity violates this principle, as Einstein eventually acknowledged several years after de Sitter found a vacuum solution to Einstein's equation with a cosmological constant. To better understand this issue, I recommend reading [Hoeffler, 1995] and [Pais, 1982].

While this might seem anecdotal in comparison to the other merits of the theory, Entangled Relativity, by forbidding the definition of the theory without matter fields, naturally satisfies this principle. Therefore, Entangled Relativity is not only more parsimonious than General Relativity but also more closely aligns with Einstein's vision of a satisfactory relativistic theory. In his own words: "In a consistent theory of relativity there cannot be inertia relatively to "space" but only an inertia of masses relatively to one another" [Einstein, 1917]. This metaphysical demand explains the introduction of the principle of relativity of inertia, which states that "[the metric]-field is completely determined by the masses of the bodies", such that, indeed, "[with this principle], according to the field equations of gravitation, there can be no [metric]-field without matter. Obviously, [this principle] is closely connected to the spacetime structure of the world as a whole, because all masses in the universe will partake in the generation of the [metric]-field". [Einstein, 1918]

1.1 Mathematical formulation

The definition of Entangled Relativity is based on its path integral:

$$Z_{ER} = \int [Dg] \prod_i [Df_i] \exp \left(-\frac{i}{2\epsilon^2} \int d_g^4 x \frac{\mathcal{L}_m^2(f, g)}{R(g)} \right), \quad (1)$$

where $\int [D]$ relates to the sum over all possible (non-redundant) field configurations, R is the usual Ricci scalar that is constructed upon the metric tensor g , $d_g^4 x := \sqrt{-|g|} d^4 x$ is the spacetime volume element, with $|g|$ the metric g determinant, and \mathcal{L}_m is the Lagrangian density of matter fields f —which could be the current *standard model of particle physics* Lagrangian density, but most likely a completion of it. It also depends on the metric tensor, a priori through to the usual *comma-goes-to-semicolon rule* [Misner, Thorne and Wheeler, 1973]. The only parameter of the theory is the quantum of energy squarred ϵ^2 . In order to recover standard quantum field theory in a limit that corresponds to our observable universe, ϵ has to be the (reduced) Planck energy [Minazzoli, 2023].

1.2 Comparison with standard physics

Eq. (1) should be compared with the path integral of the Core theory*, which is expressed as

$$Z_C = \int [Dg] \prod_i [Df_i] \exp \left[\frac{i}{\hbar c} \int d_g^4 x \left(\frac{R(g)}{2\kappa_{GR}} + \mathcal{L}_m^{SM}(f, g) \right) \right], \quad (2)$$

where f_i are the matter fields of the standard model (SM) of particle physics—such as fermions and gauge bosons, and the Higgs. There are three universal constants in this formulation: the quantum constant \hbar (Planck's), the causal structure constant c and the constant of gravity $G = c^4 \kappa_{GR} / (8\pi)$ (Newton's). From these constants, one can construct an energy scale, a mass scale, a time scale and a length scale, known as the Planck energy (E_P), mass (m_P), time (t_P) and length (l_P) respectively:

$$E_P = \sqrt{\frac{\hbar c^5}{G}}, m_P = \frac{E_P}{c^2}, t_P = \sqrt{\frac{\hbar G}{c^5}}, l_P = ct_P. \quad (3)$$

The difference between the two theories lies in how curvature (gravity) and matter are coupled within the quantum phase Θ of the path integral, where $Z = \int [Dg] \prod_i [Df_i] \exp(i\Theta)$. Classical physics corresponds to the variational paths for which the quantum phase is stationary $\delta\Theta = 0$. The reason being that for classical, or “*macroscopic*”, phenomena, destructive interferences cancel any contribution from other paths to the path integral, whereas constructive interferences are maximal for paths that lead to a stationary phase. Usually, one talks about the *Principle of Least Action*, because if \hbar is a fundamental constant, then $\Theta = S/\hbar$ and $\delta\Theta = 0 \Leftrightarrow \delta S = 0$, where S has the dimension of an action. In other words, classical physics is quantum physics in some limit, and the *Principle of Least Action* of classical physics simply is a consequence of quantum physics.

1.3 The Parsimonious Nature of Entangled Relativity

In the formulation of Entangled Relativity, as expressed in Eq. (1), there are only two universal fundamental constants: the squared energy constant ϵ^2 and the causal structure constant c . This represents one less constant than is required in standard physics. Specifically, the coupling constant κ_{GR} between matter and curvature in General Relativity disappears due to the non-linear coupling of the two in Entangled Relativity. Consequently, the formulation of Entangled Relativity is more parsimonious in terms of constants than that of standard physics (General Relativity with matter fields).

*That is, the current standard model of physics, as named by [Wilczek 2016].

However, this leads to two significant implications. Firstly, there is no quantum of action in the formulation of Entangled Relativity, meaning that \hbar cannot be a fundamental constant in this framework. Instead, it must emerge as a limit of the theory—see Sec. 2.3 for details. More crucially, the absence of a quantum of action means one cannot construct a notion of elementary length or time scales using only these two dimensionful constants. This is particularly relevant as many of the challenging issues in quantum general relativity are linked to the concept that a smooth and continuous spacetime may cease to exist at the Planck length and time scale (l_P and t_P in Eq. (3)). This dilemma led to various hypothesis, such as the concept of *spacetime foam* or the existence of a fundamental discrete structure composed of elementary *spacetime atoms* [Loll, Fabiano, Frattulillo, Wagner, 2022].

1.4 Field equations

Classical physics corresponds to the paths in the path integral that lead to a stationary quantum phase $\delta\Theta = 0$. Therefore, extremizing the quantum phase with respect to the various fields lead to the classical field equations that follow [Ludwig, Minazzoli and Capozziello, 2015]:

$$G_{\mu\nu} = \kappa T_{\mu\nu} + f_R^{-1} [\nabla_\mu \nabla_\nu - g_{\mu\nu} \square] f_R, \quad (4)$$

where

$$T_{\mu\nu} := -\frac{2}{\sqrt{-g}} \frac{\delta(\sqrt{-g}\mathcal{L}_m)}{\delta g^{\mu\nu}}. \quad (5)$$

and $G_{\mu\nu} := R_{\mu\nu} - 1/2 R g_{\mu\nu}$ is the usual Einstein tensor, with

$$\kappa = -\frac{R}{\mathcal{L}_m}, \quad \left(f := -\frac{1}{2\epsilon^2} \frac{\mathcal{L}_m^2}{R}, \quad f_R := \frac{\partial f}{\partial R} = \frac{1}{2\epsilon^2} \frac{\mathcal{L}_m^2}{R^2} = \frac{1}{2\epsilon^2 \kappa^2} \right). \quad (6)$$

Let us note that $\kappa_{GR} = -R/T$ in General Relativity instead. The stress-energy tensor is not conserved in general, as one has

$$\nabla_\sigma \left(\frac{\mathcal{L}_m}{R} T^{\alpha\sigma} \right) = \mathcal{L}_m \nabla^\alpha \left(\frac{\mathcal{L}_m}{R} \right). \quad (7)$$

The matter field equation, for any tensorial matter field χ , gets modified due to the non-linear coupling between matter and curvature as follows

$$\frac{\partial \mathcal{L}_m}{\partial \chi} - \frac{1}{\sqrt{-|g|}} \partial_\sigma \left(\frac{\partial \sqrt{-|g|} \mathcal{L}_m}{\partial (\partial_\sigma \chi)} \right) = \frac{\partial \mathcal{L}_m}{\partial (\partial_\sigma \chi)} \frac{R}{\mathcal{L}_m} \partial_\sigma \left(\frac{\mathcal{L}_m}{R} \right). \quad (8)$$

It has been shown already that these equations lead to a classical phenomenology that is very close (or even indistinguishable) to the one of general relativity in many cases, while it also (surprisingly) has standard quantum field theory as a limit. It all boils down to the *intrinsic decoupling* that was originally found for scalar-tensor theories in [Minazzoli and Hees, 2013]. Indeed, as usual in $f(R)$ theories, the trace of the metric field equation produces the differential equation for the extra scalar degree-of-freedom κ , which is

$$3\kappa^2 \square \kappa^{-2} = \kappa (T - \mathcal{L}_m). \quad (9)$$

Therefore, whenever $\mathcal{L}_m = T$ on-shell, the extra degree-of-freedom is not sourced and become constant in many occurrences, and one recovers general relativity minimally coupled to matter, and without a cosmological constant, to a very good accuracy. Let us recall that $\mathcal{L}_m = T$ for a universe that would entirely be made of dust and electromagnetic radiation for instance, which turns out to be a very good approximation of the current content of our universe. As a side note, whenever $\mathcal{L}_m = T$, one recovers the relation $\kappa = -R/T$ of General Relativity.

1.5 Equivalent classical formulation

The whole set of equations can be recovered by the following phase instead

$$\Theta \propto \int d_g^4 x \frac{1}{\kappa} \left(\frac{R}{2\kappa} + \mathcal{L}_m \right), \quad (10)$$

where κ is a dimensionful scalar-field. Equivalently, if one wants to deal with a dimensionless scalar-field that looks more usual instead, the phase can be written as follows

$$\Theta \propto \int d_g^4 x \left(\frac{\varphi^2 R}{2\bar{\kappa}} + \varphi \mathcal{L}_m \right), \quad (11)$$

where $\bar{\kappa}$ is a dimensionful normalization constant. Or, alternatively again,[†] in order to look more like an usual Brans-Dicke theory, or like the more general theory explored in [Minazzoli and Hees, 2013], from the following phase:

$$\Theta \propto \int d_g^4 x \left(\frac{\Phi R}{2\bar{\kappa}} + \sqrt{\Phi} \mathcal{L}_m \right). \quad (12)$$

In particular, one has $\Phi \propto f_R$, and the scalar field differential equation reads

$$3\Phi^{-1}\square\Phi = \frac{\bar{\kappa}}{\sqrt{\Phi}} (T - \mathcal{L}_m), \quad (13)$$

where $\bar{\kappa}$ is a dimensionful normalization constant, and with

$$\sqrt{\Phi} = -\bar{\kappa} \frac{\mathcal{L}_m}{R}. \quad (14)$$

This alternative formulation of the theory looks much more familiar, and therefore allows one to get a better intuition about how it may work. But ultimately, there are no difference between the two formulations— $f(R, \mathcal{L}_m)$ -like or Einstein-dilaton-like.

2. SOLAR SYSTEM PHENOMENOLOGY

2.1 Post-Newtonian metric

Modeling Solar System bodies by perfect fluids with conserved rest-mass energy densities $\nabla_\sigma(\rho_0 U^\sigma) = 0$, where U^α is the proper four-velocity of the fluid, the on-shell value for the matter Lagrangian is $\mathcal{L}_m = -\rho$, where ρ is the total energy density defined by [Minazzoli and Harko, 2013]

$$\rho = \rho_0 \left(1 + \int \frac{P(\rho_0)}{c^2 \rho_0^2} d\rho_0 \right). \quad (15)$$

From there, one can see that the source term of the scalar-field equation (13) only is pressure, which is a $\mathcal{O}(c^{-2})$ term with respect to ρ_0 in post-Newtonian regimes. Therefore, at the post-Newtonian level, the scalar-field is weakly sourced by matter. In particular, one has

$$\Phi^{-1}\square\Phi = \frac{\bar{\kappa}}{\sqrt{\Phi}} P. \quad (16)$$

Then, from Eq. (4), one can check that one has

$$g \left(R^{ij} - \frac{1}{2} g^{ij} R \right) = \mathcal{O}(c^{-4}), \quad (17)$$

[†]Provided that $\varphi > 0$ everywhere, which should be the case in the entire observable universe because it has been shown that φ does not vary more than a few percent in the densest objects in the universe that are not hidden behind an event horizon [Arruga, Rousselle and Minazzoli, 2021].

where g is the metric's determinant. Therefore, as in General Relativity, there exist a system of coordinates that satisfies the Strong Spatial Isotropy Condition (SSIC) [Damour, Soffel and Xu, 1991]—that is $-g_{00}g_{ij} = \delta_{ij} + \mathcal{O}(c^{-4})$. This notably means that the post-Newtonian parameters γ and β are both equal to one, such that the post-Newtonian metric can be written as follows

$$g_{00} = -1 + 2\frac{w}{c^2} - 2\frac{w^2}{c^4} + \mathcal{O}(1/c^6) \quad (18a)$$

$$g_{0i} = -4\frac{w^i}{c^3} + \mathcal{O}(1/c^5) \quad (18b)$$

$$g_{ij} = \delta_{ij} \left(1 + 2\frac{w}{c^2}\right) + \mathcal{O}(1/c^4), \quad (18c)$$

Injecting this metric in the metric field equation gives the equation on the potential w and w^i that follow

$$\begin{aligned} w &= w_{GR} - \frac{1}{c^2} G \int \frac{P(\mathbf{x}') d^3x'}{|\mathbf{x} - \mathbf{x}'|} + \mathcal{O}(1/c^4), \\ &:= w_{GR} + \frac{1}{c^2} \delta w + \mathcal{O}(1/c^4), \end{aligned} \quad (19a)$$

$$w^i = w_{GR}^i + \mathcal{O}(1/c^2) \quad (19b)$$

where w_{GR} and w_{GR}^i are the expressions of the potentials predicted by general relativity, and $8\pi G := c^4 \bar{\kappa}$. The scalar-field equation on the other-hand is

$$\frac{\phi}{\Phi_0} = 2\delta w + \mathcal{O}\left(\frac{1}{c^2}\right), \quad (20)$$

where $\phi \equiv c^4(\Phi - \Phi_0)$ and Φ_0 the background ‘‘astrophysical’’ value of Φ . Let us note that the derivation follows the one in [Minazzoli and Hees, 2013], since Eq. (12) turns out to be a special case of the class of scalar-tensor theories considered in [Minazzoli and Hees, 2013].

2.2 Trajectories and Shapiro delay

The non-conservation of the stress-energy tensor in Eq. (7) implies an additional gravitational force acting on free-fall particles. However, this additional force turns out to exactly cancel out the modification of the metric with respect to the metric of General Relativity. The result is that the equation of motion for free-fall objects is the same as in General Relativity at the post-Newtonian level, despite the metric being different at the post-Newtonian level—because of the δw term. Indeed, using the conservation of the rest-mass energy density $\nabla_\sigma(\rho_0 U^\sigma) = 0$, the non-conservation equation reduces to

$$U^\sigma \nabla_\sigma U^\mu = -\frac{1}{2} (g^{\mu\sigma} + U^\mu U^\sigma) \frac{\partial_\sigma \Phi}{\Phi}, \quad (21)$$

where $U^\alpha = dx^\alpha/d\tau$ is the proper four-velocity of the particles, which leads to

$$\frac{d^2 x^i}{dt^2} = a_{GR}^i + c^{-2} \left[\partial_i \delta w - \frac{1}{2} \frac{\partial_i \phi}{\Phi_0} \right] + \mathcal{O}(1/c^4) \quad (22)$$

$$= a_{GR}^i + \mathcal{O}(1/c^4), \quad (23)$$

where a_{GR}^i is the standard acceleration in General Relativity.

The unsourced electromagnetic field equation on the other hand reads

$$\nabla_\sigma \left(\sqrt{\Phi} F^{\mu\sigma} \right) = 0, \quad (24)$$

where $F^{\mu\nu}$ is the standard Faraday tensor. One can show that in the geometric optic limit, it implies that photons still follow null-geodesics of spacetime [Minazzoli and Hees, 2013]. But since the metric only differs from the one of General Relativity at the $\mathcal{O}(c^{-4})$ level, it means that the trajectory of light is the same as in General Relativity at the $\mathcal{O}(c^{-2})$ level, which is the only level that can be probed with the current accuracy of Solar System tests. In particular, the Shapiro delay is the same as in General Relativity at the current level of accuracy of radioscience experiments.

It follows that Entangled Relativity is currently indistinguishable from General Relativity from radioscience and ephemerides in the Solar System. This is a rather remarkable result, given the non-linear formulation that one started with in Eq. (1), and given the fact that it did not require adjusting any sort of free parameter. Indeed, the only parameter of the theory is the quantum of energy squared ϵ^2 , whose value affects only the paths that are not stationary in the path integral—that is, ϵ^2 affects purely quantum phenomena only.

2.3 The variation of \hbar

Planck's quantum of action \hbar does not appear in the formulation of Entangled Relativity. It necessarily implies that \hbar is not a constant in this theory. We have just seen that the variation Φ in the solar system is even smaller than the variation of gravitational potentials w and w^i . In terms of the original formulation of the theory, it means that the ratio between R and \mathcal{L}_m varies less than the gravitational potentials. This is not surprising, if one keeps in mind that $\kappa_{GR} = -R/T$ is a constant in General Relativity, while one has $\mathcal{L}_m \approx T$ at leading order for perfect fluid with conserved rest-mass energy densities, such that $\kappa \approx -R/T$ in that situation in Entangled Relativity. This means that when one neglects gravity, the variation of the ratio between R and \mathcal{L}_m can also be neglected. In that situation, Eq. (1) would reduce to [Minazzoli, 2023]

$$Z_{ER-QFT} = \int \prod_i [Df_i] \exp\left(\frac{i}{\kappa\epsilon^2} \int d^4x \mathcal{L}_m(f)\right). \quad (25)$$

Because one wants to recover standard quantum field theory when gravity is neglected, it means that

$$\kappa\epsilon^2 = c\hbar. \quad (26)$$

It implies that \hbar actually varies proportionally to κ in general. In other words, it means that \hbar varies akin to a new gravitational field. But, more importantly, one now has determined the value of the quantum of energy ϵ : it is the reduced Planck energy. Let us note that this is similar to how one determines the value of κ_{GR} in General Relativity: by demanding that General Relativity recovers the theory of Newton at leading order—which imposes that $\kappa_{GR} = 8\pi G/c^4$. Here, it is the requirement to recover standard quantum field theory in the limit where gravity can be neglected that dictates the value of ϵ .

Let's evaluate the variation of \hbar in the Solar System, from Eq. (26) and Eqs. (10-12), one has

$$\frac{\delta\hbar}{\hbar} = \frac{\delta\kappa}{\kappa} = -\frac{1}{2} \frac{\delta\Phi}{\Phi}. \quad (27)$$

Then, from Eq. (20) and (19a), one deduces that for a spherical body A one has

$$\frac{\delta\hbar}{\hbar} = \delta\left(\frac{GM_A^P}{c^2 r}\right), \text{ with } M_A^P := 4\pi \int_A \frac{r^2 P(r)}{c^2} dr, \quad (28)$$

which is a mass term defined from pressure rather than from the density. One can evaluate M_P for the Sun and the Earth, they are respectively $M_{SUN}^P = 2.3 \times 10^{24}$ kg and $M_{EARTH}^P = 8.0 \times 10^{14}$ kg—to be compared with their masses that are $M_{SUN} = 2.0 \times 10^{30}$ kg and $M_{EARTH} = 6.3 \times 10^{24}$

kg. The maximal fractional observable variation of \hbar in the solar system is between the surface of the Sun and a remote observer, and is therefore given by

$$\frac{\delta\hbar}{\hbar} \approx \frac{GM_{\text{SUN}}^P}{c^2 R_{\text{SUN}}} \approx 2.5 \times 10^{-12}, \quad (29)$$

where R_{SUN} is the radius of the Sun. Whether such a small fractional variation can be probed experimentally remains to be investigated. (The details of the derivations will be checked and then communicated in a peer-reviewed journal).

2.4 The c^{-4} Shapiro delay

Preliminary calculations—which, if confirmed, will be communicated in a peer-reviewed journal—indicate that the whole c^{-4} metric of Entangled Relativity surprisingly simply reads as follows

$$g_{\alpha\beta} = g_{\alpha\beta}^{GR} + \delta_{\alpha\beta}^{00} \frac{2\delta w}{c^4} + \mathcal{O}(c^{-5}), \quad (30)$$

where $g_{\alpha\beta}^{GR}$ is the solution of general relativity, δw is defined in Eq. (19a), and $\delta_{\alpha\beta}^{00}$ is a Kronecker symbol. As a consequence, the coordinate propagation time between an emission (e) and a reception (r) in Entangled Relativity would read as follows

$$\begin{aligned} c(t_r - t_e)_{ER} = & R + \sum_A (1 + \gamma_A) \frac{GM_A}{c^2} \ln \left(\frac{\vec{n} \cdot \vec{r}_{rA} + r_{rA}}{\vec{n} \cdot \vec{r}_{eA} + r_{eA}} \right) \\ & + c(t_r - t_e)_{GR}^{(4)} + \mathcal{O}(c^{-5}), \end{aligned} \quad (31)$$

where $c(t_r - t_e)_{GR}^{(4)}$ are the remaining c^{-4} terms that are the same as in General Relativity. Hence, surprisingly, the c^{-4} correction to the Shapiro delay due to Entangled Relativity looks like an usual post-Newtonian correction. However, it is important to emphasize a few key aspects. First, unlike in usual alternative theories, its value is body-dependent. Moreover, it can be fully calculated for each body A without any free parameter at the theoretical level. Finally, the value of γ_A is expected to be very small, again without any free parameter at the theoretical level. Indeed, while the exact derivation and numerical estimations will be published in a peer-reviewed journal, it is roughly estimated that $1 - \gamma_A \propto M_A^P/M_A$, while M_A^P/M_A is at best of the order of 10^{-6} in the Solar System (for the Sun).

While testing the Shapiro delay at the 10^{-6} level in the Solar System is currently beyond the reach of experimental accuracy, the MORE experiment on BepiColombo is approaching this level of precision [Cappuccio et al., 2020]. Therefore, it is not too much of a stretch to consider that it may be possible to verify this prediction in the not-too-distant future.

3. CONCLUSION

Entangled Relativity is a novel general theory of relativity that is more economical than General Relativity in its formulation. Nevertheless, it predicts very small deviations from General Relativity in weak field situations, such as those in the Solar System. Additionally, it implies several significant conceptual shifts at the theoretical level. One notable example is the proposition that the quantum of action, \hbar , would not be a constant, but rather vary as a new gravitational field. In this communication, I explained that the deviations from General Relativity, which do not depend on any free theoretical parameters, are quite small in the Solar System, yet they might still be detectable in future experiments.

4. REFERENCES

- Denis Arruga, Olivier Rousselle, and Olivier Minazzoli. Compact objects in entangled relativity. *Phys. Rev. D*, 103(2):024034, January 2021. doi: 10.1103/PhysRevD.103.024034.
- Paolo Cappuccio, Ivan di Stefano, Gael Cascioli, Luciano Iess, Comparison of light-time formulations in the post-Newtonian framework for the BepiColombo MORE experiment. *Class Quantum Grav* 38 (22):227001 (2021). doi: 10.1088/1361-6382/ac2b0a.
- Thibault Damour, Michael Soffel, and Chongming Xu, General-relativistic celestial mechanics. I. Method and definition of reference systems, *Phys. Rev. D* 43, 3273–3307 (1991). doi: 10.1103/PhysRevD.43.3273.
- Albert Einstein, Kosmologische Betrachtungen zur allgemeinen Relativitätstheorie, *Sitzungsberichte der Königlich Preußischen Akademie der Wissenschaften* (1917).
Translation available at <https://einsteinpapers.press.princeton.edu/vol6-trans/433>.
- Albert Einstein, Prinzipielles zur allgemeinen Relativitätstheorie, *Annalen der Physik* (1918).
Translation available at <https://einsteinpapers.press.princeton.edu/vol7-trans/49>.
- Carl Hoefer. Einstein’s Formulations of Mach’s Principle. In Julian B. Barbour and Herbert Pfister, editors, *Mach’s Principle: From Newton’s Bucket to Quantum Gravity*, page 67, Boston University, January 1995. Birkhäuser.
- Abraham Pais. *Subtle is the Lord. The science and the life of Albert Einstein*. Oxford University Press, Oxford, 1982.
- Renate Loll, Fabiano G., Frattulillo D., Wagner F., Quantum Gravity in 30 Questions, Lectures given by R. Loll at the School on Quantum Gravity Phenomenology in the Multi-Messenger Approach, Corfu, Greece, Sep 2021, eprint arXiv:2206.06762.
- Hendrik Ludwig, Olivier Minazzoli, and Salvatore Capozziello. Merging matter and geometry in the same Lagrangian. *Physics Letters B*, 751:576–578, December 2015.
doi: 10.1016/j.physletb.2015.11.023.
- Olivier Minazzoli, Standard quantum field theory from entangled relativity, Proceedings of the 2023 Gravitation session of the 57th Rencontres de Moriond.
- Olivier Minazzoli and Tiberiu Harko, New derivation of the Lagrangian of a perfect fluid with a barotropic equation of state, *Phys. Rev. D* 86, 087502 (2012), doi: 10.1103/PhysRevD.86.087502.
- Olivier Minazzoli and Aurélien Hees, Intrinsic Solar System decoupling of a scalar-tensor theory with a universal coupling between the scalar field and the matter Lagrangian. *Phys. Rev. D*, 88:041504, September 2013. doi: 10.1103/PhysRevD.88.041504.
- Charles W. Misner, Kip S. Thorne, and John Archibald Wheeler. *Gravitation*. 1973.
- Franck Wilczek. *A Beautiful Question*. Penguin Random House, UK, 2016.

TOTAL LIGHT DEFLECTION IN THE GRAVITATIONAL FIELD OF SOLAR SYSTEM BODIES

S. ZSCHOCKE

TU Dresden, Institute of Planetary Geodesy - Germany - sven.zschocke@tu-dresden.de

ABSTRACT. The total light deflection represents a concept, which allows one to decide which multipoles need to be implemented in the light trajectory for a given astrometric accuracy. The fundamental quantity of total light deflection is the tangent vector of the light trajectory at future infinity. It has been found that this tangent vector is naturally given by Chebyshev polynomials. It is just this remarkable fact, which allows one to determine strict upper limits of total light deflection for each individual multipole of solar system bodies. Special care is taken about the gauge terms. It is found that these gauge terms vanish at spatial infinity. The results are applied to the case of light deflection in the gravitational fields of Jupiter and Saturn.

1. INTRODUCTION

Angular measurements of stellar objects have made impressive advancements during recent decades. In particular, the astrometry missions *Hipparcos* and *Gaia* of European Space Agency (ESA) have reached the milli-arcsecond (mas) and the micro-arcsecond (μas) level of accuracy, respectively. The next goal in astrometric science is to arrive at the sub-micro-arcsecond (sub- μas) or even the nano-arcsecond (nas) scale of accuracy. The objectives of such highly precise measurements are overwhelming, e.g.: detection of earth-like planets, stringent tests of relativity, mapping of dark matter from areas beyond the Milky Way, and direct distance measurements of stellar standard candles up to the closest galaxy clusters; see also (Johnston, 2000).

In fact, several missions have been proposed to ESA, aiming at such levels in astrometric precision, like *Theia* and *Gaia-NIR*, which are primarily designed to study local dark matter properties, to detect Earth-like exoplanets, and to study the physics of highly compact objects (white dwarfs, neutron stars, black holes). A further promising candidate is *NEAT* (Near Infrared Astrometric Telescope), originally designed for an precision of about 50 nas.

The fundamental assignment in relativistic astrometry is the precise interpretation of observational data, which requires an accurate modeling of trajectories of light signals through the curved space-time of the solar system. In view of recent achievements in astrometric angular observations as well as in view of missions proposed to ESA, a corresponding development in the theory of light propagation is indispensable. The investigation of the total light deflection is a further step towards these directions.

2. THE METRIC TENSOR

The curved space-time is described by the pair $(\mathcal{M}, g_{\alpha\beta})$ where \mathcal{M} is a four-dimensional differentiable manifold, while $g_{\alpha\beta}$ is the metric tensor of the manifold, and each point $\mathcal{P} \in \mathcal{M}$ represents a space-time event. The metric tensor is governed by the field equations of gravity (Einstein, 1915), which relate the metric tensor $g_{\alpha\beta}$ of the physical manifold \mathcal{M} to the stress-energy tensor of matter $T_{\alpha\beta}$. These exact field equations can only be solved in closed form for highly symmetric bodies, like spherically symmetric bodies or bodies of ellipsoidal shape, but not for realistic bodies of the solar system. Therefore, approximative approaches of general relativity are essential for further progress in the theory of gravity and in the theory of light propagation. In the solar system the

gravitational fields are weak and, therefore, one may apply the theory of linearized gravity. In that approximation, the covariant components of the metric tensor are decomposed into the flat Minkowski metric $\eta_{\alpha\beta} = (-1, +1, +1, +1)$ plus a metric perturbation $h_{\alpha\beta}$,

$$g_{\alpha\beta} = \eta_{\alpha\beta} + h_{\alpha\beta} \quad \Longrightarrow \quad \bar{g}^{\alpha\beta} = \eta^{\alpha\beta} - \bar{h}^{\alpha\beta}, \quad (1)$$

where $\bar{g}^{\alpha\beta} = \sqrt{-g} g^{\alpha\beta}$ are the contravariant components of the metric density, with $g = \det(g_{\mu\nu})$ being the determinant of the metric. The decomposition (1) implies that the metric perturbations $h_{\alpha\beta}$ can be thought of as symmetric tensorial fields which propagate in the flat background manifold \mathcal{M}_0 . The metric of the flat background manifold is given by $\eta_{\alpha\beta}$. Thus, the flat background space-time is described by the pair $(\mathcal{M}_0, \eta_{\alpha\beta})$, and the diffeomorphism between the physical manifold \mathcal{M} and the flat background manifold \mathcal{M}_0 implies a one-to-one correspondence of the points $\mathcal{Q} \in \mathcal{M}_0$ to the points $\mathcal{P} \in \mathcal{M}$.

The metric perturbation $h_{\alpha\beta}$ and the metric density perturbation $\bar{h}_{\alpha\beta}$ are uniquely related to each other: $h_{\alpha\beta} = \bar{h}_{\alpha\beta} - \frac{1}{2} \bar{h} \eta_{\alpha\beta}$ with $\bar{h} = \bar{h}^{\mu\nu} \eta_{\mu\nu}$. The weak-field condition $|h_{\alpha\beta}| \ll 1$ inherits $|\bar{h}^{\alpha\beta}| \ll 1$. In linearized gravity, the tensor indices are lowered and raised by the flat Minkowskian metric, e.g. $h^{\alpha\beta} = h_{\mu\nu} \eta^{\mu\alpha} \eta^{\nu\beta}$.

Inserting (1) into the field equations of gravity and keeping terms linear in the metric perturbation, yields the field equations of linearized gravity (cf. Eq. (18.5) in (Misner, Thorne, Wheeler, 1973)). They are considerably simplified by the harmonic gauge, which implies that the coordinates $\{x\}$, which cover the flat background manifold \mathcal{M}_0 , satisfy the equation $\square x^\mu = 0$, where $\square = \eta^{\mu\nu} \partial_\mu \partial_\nu$ is the flat d'Alembertian. Then, the linearized field equations of gravity read

$$\square \bar{h}_{\alpha\beta} = -\frac{16\pi G}{c^4} T_{\alpha\beta}. \quad (2)$$

Imposing Fock-Sommerfeld boundary conditions ensures a unique solution of (2) in the coordinates $\{x\}$. Though, the harmonic gauge, $\square x^\mu = 0$, does not uniquely determine these coordinates, but allows for small deformations (Box 18.2 in (Misner, Thorne, Wheeler, 1973) or Eq. (3.521) in (Kopeikin, Efroimsky & Kaplan, 2012))

$$x_{\text{can}}^\alpha = x^\alpha + \xi^\alpha(x^\beta), \quad (3)$$

if the vector fields ξ^α satisfy $\square \xi^\alpha = 0$. The label of these new coordinates $\{x_{\text{can}}\}$ abbreviates the term "canonical". The transformation (3) implies a transformation of the metric tensor,

$$g_{\alpha\beta}(t, \mathbf{x}) = \frac{\partial x_{\text{can}}^\mu}{\partial x^\alpha} \frac{\partial x_{\text{can}}^\nu}{\partial x^\beta} g_{\mu\nu}^{\text{can}}(t_{\text{can}}, \mathbf{x}_{\text{can}}). \quad (4)$$

By inserting (3) into (4) and performing a series expansion of the metric tensor on the r.h.s. around the old coordinates $\{x\}$, one obtains (with notation $\partial_\alpha f \equiv \partial f / \partial x^\alpha$):

$$g_{\alpha\beta}(t, \mathbf{x}) = g_{\alpha\beta}^{\text{can}}(t, \mathbf{x}) + \partial_\alpha \xi_\beta(t, \mathbf{x}) + \partial_\beta \xi_\alpha(t, \mathbf{x}), \quad (5)$$

up to terms of higher order, i.e. up to non-linear terms. As stated above, by imposing the Fock-Sommerfeld boundary condition, the solution for the metric tensor $g_{\alpha\beta}$ in (5) is unique. This unique solution can be expressed in terms of six Cartesian symmetric and tracefree (STF) multipoles $\{\hat{M}_L, \hat{S}_L, \hat{W}_L, \hat{X}_L, \hat{Y}_L, \hat{Z}_L\}$ (Thorne, 1980); the *hat* over the multipoles indicates STF. The canonical piece $g_{\alpha\beta}^{\text{can}}$ in (5) depends on two multipoles only: mass-multipoles and spin-multipoles $\{\hat{M}_L, \hat{S}_L\}$. Accordingly, the gauge transformation of the metric tensor, as given by Eq. (5), results in the following form for the metric perturbations ((Thorne, 1980) and (Blanchet & Damour, 1986) and (Damour & Iyer, 1991)):

$$h_{\alpha\beta}(t, \mathbf{x}) = h_{\alpha\beta}^{\text{can}}[\hat{M}_L, \hat{S}_L] + \partial_\alpha \xi_\beta[\hat{W}_L, \hat{X}_L, \hat{Y}_L, \hat{Z}_L] + \partial_\beta \xi_\alpha[\hat{W}_L, \hat{X}_L, \hat{Y}_L, \hat{Z}_L]. \quad (6)$$

The metric of the curved space-time in the exterior of the massive body is assumed to be time-independent. Then, the canonical metric perturbations in (6) are separated into two pieces, $h_{\alpha\beta}^{\text{can}} = h_{\alpha\beta}^{(2)\text{can}} + h_{\alpha\beta}^{(3)\text{can}}$, which are given by

$$h_{00}^{(2)\text{can}} = \frac{2G}{c^2} \sum_{l=0}^{\infty} \frac{(-1)^l}{l!} \hat{M}_L \hat{\partial}_L \frac{1}{r} \quad \text{and} \quad h_{0i}^{(3)\text{can}} = \frac{4G}{c^3} \sum_{l=1}^{\infty} \frac{(-1)^l l}{(l+1)!} \epsilon_{iab} \hat{S}_{bL-1} \hat{\partial}_{aL-1} \frac{1}{r}, \quad (7)$$

while $h_{ij}^{(2)\text{can}} = h_{00}^{(2)\text{can}} \delta_{ij}$ and the multipoles \hat{M}_L and \hat{S}_L are given by Eqs. (5.33) and (5.35) in (Damour & Iyer, 1991). The gauge functions in (6) have been determined by (Thorne, 1980) and (Blanchet & Damour, 1986) and (Damour & Iyer, 1991) and read:

$$\xi^0 = + \frac{4G}{c^3} \sum_{l=0}^{\infty} \frac{(-1)^l}{l!} \hat{\partial}_L \frac{\hat{W}_L}{r} \quad (8)$$

$$\xi^i = - \frac{4G}{c^2} \sum_{l=0}^{\infty} \frac{(-1)^l}{l!} \hat{\partial}_{iL} \frac{\hat{X}_L}{r} - \frac{4G}{c^2} \sum_{l=1}^{\infty} \frac{(-1)^l}{l!} \hat{\partial}_{L-1} \frac{\hat{Y}_{iL-1}}{r} - \frac{4G}{c^2} \sum_{l=1}^{\infty} \frac{(-1)^l}{l!} \frac{l}{l+1} \epsilon_{iab} \partial_{aL-1} \frac{\hat{Z}_{bL-1}}{r}. \quad (9)$$

Here, $r = |\mathbf{x}|$, and

$$\hat{\partial}_L = \text{STF}_{i_1 \dots i_l} \frac{\partial}{\partial x^{i_1}} \cdots \frac{\partial}{\partial x^{i_l}}, \quad (10)$$

where the *hat* in $\hat{\partial}_L$ indicates STF operation with respect to the indices $L = i_1 \dots i_l$. The multipoles $\hat{W}_L, \hat{X}_L, \hat{Y}_L, \hat{Z}_L$ of the gauge functions in (8) and (9) are given in (Damour & Iyer, 1991), but their explicit form is not relevant here, because we will show that the gauge terms in (6) have no impact on the unit tangent vector at future infinity and, therefore, no impact on the total light deflection. This result is an example of the general fact that $g_{\alpha\beta}$ and $g_{\alpha\beta}^{\text{can}}$ in (5) are physically equivalent, because they lead to same observables.

3. THE GEODESIC EQUATION

The light signal is assumed to propagate in the flat background manifold \mathcal{M}_0 which is covered by harmonic coordinates, $x^\mu = (x^0, x^1, x^2, x^3)$, where the origin of the spatial axes is located at the center of mass of the body. The exact light trajectory can be written in the following form,

$$\mathbf{x}(t) = \mathbf{x}_0 + c(t - t_0) \boldsymbol{\sigma} + \Delta \mathbf{x}(t), \quad (11)$$

where $\Delta \mathbf{x}$ denotes the corrections to the unperturbed light trajectory, $\mathbf{x}_N(t) = \mathbf{x}_0 + c(t - t_0) \boldsymbol{\sigma}$, and N stands for Newtonian (e.g. Kopeikin, Efroimsky & Kaplan, 2012). Furthermore, we introduce the unit tangent vectors along the light trajectory at past and future infinity,

$$\boldsymbol{\sigma} = \left. \frac{\dot{\mathbf{x}}(t)}{c} \right|_{t \rightarrow -\infty} \quad \text{and} \quad \boldsymbol{\nu} = \left. \frac{\dot{\mathbf{x}}(t)}{c} \right|_{t \rightarrow +\infty}, \quad (12)$$

where a dot means total derivative with respect to coordinate time, and from (12) follows $\boldsymbol{\sigma} \cdot \boldsymbol{\sigma} = 1$ and $\boldsymbol{\nu} \cdot \boldsymbol{\nu} = 1$. The total light deflection is the angle between these unit vectors,

$$\delta(\boldsymbol{\sigma}, \boldsymbol{\nu}) = \arcsin |\boldsymbol{\sigma} \times \boldsymbol{\nu}|. \quad (13)$$

The evaluation of this quantity is essential, in order to decide which multipoles need to be implemented in the relativistic model of light propagation for a given astrometric accuracy.

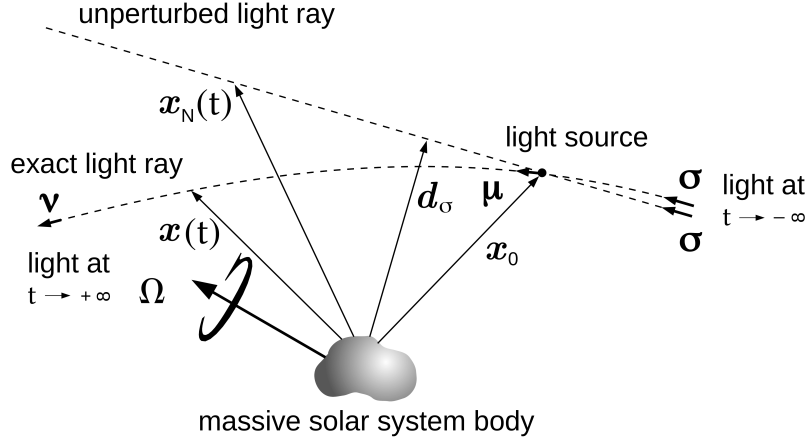


Figure 1: The light signal is emitted by the celestial light source at \mathbf{x}_0 in the direction of unit-vector $\boldsymbol{\mu}$ and propagates along the exact trajectory $\mathbf{x}(t)$. The origin of the spatial coordinates is located at the center of mass of the body, and the spatial coordinate axes are aligned with the principal axes of the body. The body is in rotational motion around some axis with angular velocity Ω . The unit tangent vectors $\boldsymbol{\sigma}$ and $\boldsymbol{\nu}$ of the light trajectory at past infinity and future infinity are defined by Eqs. (12), while $\mathbf{d}_\sigma = \boldsymbol{\sigma} \times (\mathbf{x}_0 \times \boldsymbol{\sigma})$ is the impact vector of the unperturbed light ray.

The geodesic equation for light rays in the post-Newtonian (PN) scheme in 1.5PN approximation reads (Kopeikin, Efroimsky & Kaplan, 2012) (with notation $f_{,i} \equiv \partial f / \partial x^i$):

$$\frac{\ddot{x}^i(t)}{c^2} = \frac{1}{2} h_{00,i} - h_{00,j} \sigma^i \sigma^j - h_{ij,k} \sigma^j \sigma^k + \frac{1}{2} h_{jk,i} \sigma^j \sigma^k - h_{0i,j} \sigma^j + h_{0j,i} \sigma^j - h_{0j,k} \sigma^i \sigma^j \sigma^k, \quad (14)$$

where the double-dot means twice the total derivative with respect to the coordinate time. Eq. (14) is valid up to terms of the post-post-Newtonian order $\mathcal{O}(c^{-4})$, and all those terms have been omitted which contain a derivative of the metric perturbations with respect to time, because we consider the stationary case, that is the case of time-independent metric. Note, that in stationary case the geodesic equation in 1.5PN approximation in (14) and the geodesic equation in 1PM approximation of the post-Minkowskian (PM) scheme agree with each other; cf. Eqs. (A.4) and (A.6) in (Klioner & Peip, 2003). If one inserts the metric perturbation (6) into the geodesic equation (14), one may separate the geodesic equations into a canonical term, $\ddot{\mathbf{x}}_{\text{can}}$, plus a gauge term, $\ddot{\mathbf{x}}_{\text{gauge}}$, as follows:

$$\frac{\ddot{\mathbf{x}}(t)}{c^2} = \frac{\ddot{\mathbf{x}}_{\text{can}}(t)}{c^2} + \frac{\ddot{\mathbf{x}}_{\text{gauge}}(t)}{c^2}, \quad (15)$$

where the spatial components of these terms are

$$\frac{\ddot{x}_{\text{can}}^i(t)}{c^2} = h_{00,i}^{(2)\text{can}} - 2 h_{00,j}^{(2)\text{can}} \sigma^i \sigma^j - h_{0i,j}^{(3)\text{can}} \sigma^j + h_{0j,i}^{(3)\text{can}} \sigma^j - h_{0j,k}^{(3)\text{can}} \sigma^i \sigma^j \sigma^k, \quad (16)$$

$$\frac{\ddot{x}_{\text{gauge}}^i(t)}{c^2} = \partial_j \xi_{,k}^0 \sigma^i \sigma^j \sigma^k - \partial_j \xi_{,k}^i \sigma^j \sigma^k. \quad (17)$$

The metric perturbations in (16) are given by (7), while the gauge functions in (17) are given by (8) and (9); notice $\mathbf{x} = \mathbf{x}_N + \mathcal{O}(c^{-2})$ and $r = |\mathbf{x}_N| + \mathcal{O}(c^{-2})$ according to Eq. (11). The first integration of (15) yields the coordinate velocity of the light signal,

$$\frac{\dot{\mathbf{x}}(t)}{c} = \boldsymbol{\sigma} + \frac{\dot{\mathbf{x}}_{\text{can}}(t)}{c} + \frac{\dot{\mathbf{x}}_{\text{gauge}}(t)}{c}, \quad (18)$$

and the unit tangent vectors (12) are obtained from (18) by taking the limit at plus and minus infinity. In the Appendix it is shown that the gauge terms (17) do not contribute to these unit tangent vectors at infinity, because their first time derivative vanishes at plus and minus infinity,

$$\lim_{t \rightarrow \pm\infty} \frac{\dot{x}_{\text{gauge}}(t)}{c} = 0. \quad (19)$$

Accordingly, only the canonical terms in (16) contribute to the unit tangent vector and, therefore, contribute to the total light deflection.

4. TOTAL LIGHT DEFLECTION IN FIELD OF ARBITRARY BODY

As stated above, the gauge terms in (17) do not contribute to the unit tangent vectors at plus and minus infinity (see Appendix), and there is no need to account for these terms. The first integration of the canonical terms (16) in the geodesic equation has been performed in (Kopeikin, 1997). Taking the limit at plus infinity one arrives at the following expression for the unit tangent vector in (12),

$$\nu = \sigma + \sum_{l=0}^{\infty} \nu_{1\text{PN}}^{M_L} + \sum_{l=1}^{\infty} \nu_{1.5\text{PN}}^{S_L} + \mathcal{O}(c^{-4}). \quad (20)$$

The individual terms in (20) are given by (limits of Eqs. (34) and (37) in (Kopeikin, 1997)),

$$\nu_{1\text{PN}}^{M_L} = -\frac{4G}{c^2} \frac{(-1)^l}{l!} \hat{M}_L P^{ij} \frac{\partial}{\partial \xi^j} \hat{\partial}_L \ln |\xi|, \quad (21)$$

$$\nu_{1.5\text{PN}}^{S_L} = -\frac{8G}{c^3} \frac{(-1)^l}{l!} \frac{l}{l+1} \sigma^c \epsilon_{ijbc} \hat{S}_{bL-1} P^{ij} \frac{\partial}{\partial \xi^j} \hat{\partial}_L \ln |\xi|, \quad (22)$$

where $P^{ij} = \delta^{ij} - \sigma^i \sigma^j$, and $\xi^i = P_j^i x_N^j$ which will later be identified with the impact vector \mathbf{d}_σ (cf. text below Eq. (32)). The differential operator in (21) and (22) is given by (cf. Eq. (24) in (Kopeikin, 1997) or Eq. (30) in (Zschocke, 2022))

$$\hat{\partial}_L = \text{STF}_{i_1 \dots i_l} \sum_{p=0}^l \frac{l!}{(l-p)! p!} \sigma_{i_1} \dots \sigma_{i_p} P_{i_{p+1}}^{j_{p+1}} \dots P_{i_l}^{j_l} \frac{\partial}{\partial \xi^{j_{p+1}}} \dots \frac{\partial}{\partial \xi^{j_l}} \left(\frac{\partial}{\partial c\tau} \right)^p. \quad (23)$$

The operator (10) is w.r.t. spatial coordinates x^a , while the operator (23) is w.r.t. new variables $c\tau$ and ξ^a , and the notation *hat* in (10) and *wide hat* in (23) refers to this fact.

Because $\ln |\xi|$ in (21) and (22) is independent of variable $c\tau$, only the term $p = 0$ in (23) is relevant, which considerably simplifies the differential operator in (23). A longer algebraic calculation leads finally to the following remarkable result (Zschocke, 2023):

$$\hat{\partial}_L \ln |\xi| = \frac{(-1)^{l+1}}{|\xi|^l} \text{STF}_{i_1 \dots i_l} \sum_{n=0}^{[l/2]} G_n^l P_{i_1 i_2} \dots P_{i_{2n-1} i_{2n}} \frac{\xi_{i_{2n+1}} \dots \xi_{i_l}}{|\xi|^{l-2n}}, \quad (24)$$

which is valid for any natural number $l \geq 1$. The scalar coefficients in (24) are given by

$$G_n^l = (-1)^n 2^{l-2n-1} \frac{l!}{n!} \frac{(l-n-1)!}{(l-2n)!}. \quad (25)$$

Remarkably, these coefficients coincide with the coefficients of the power series representation of Chebyshev polynomials of first kind T_l in (28) up to a constant factor $(l-1)!$. In other words, the

expression in (24) is the generating function of the coefficients of Chebyshev polynomials of first kind.

5. TOTAL LIGHT DEFLECTION IN FIELD OF AXISYMMETRIC BODY

In order to determine the mass-multipoles \hat{M}_L and spin-multipoles \hat{S}_L in (21) and (22), the solar system bodies are described by a rigid axisymmetric structure and with arbitrary radial-dependent mass-density. Furthermore, the body is assumed to be in uniform rotational motion around its symmetry axis \mathbf{e}_3 . For such an axisymmetric body the mass-multipoles and spin-multipoles have been calculated in (Zschocke, 2022) and depend on four physical parameters of the body: mass M , equatorial radius P , zonal harmonic coefficients J_l , angular velocity Ω . Then, it has been shown in (Zschocke, 2023) that for such an axisymmetric body the mass-multipole in (21) and spin-multipole terms in (22) are given by Chebyshev polynomials of first kind and second kind,

$$\nu_{1\text{PN}}^{jM_L} = -\frac{4GM}{c^2} \frac{J_l}{l} \left[1 - (\boldsymbol{\sigma} \cdot \mathbf{e}_3)^2\right]^{[l/2]} P^{ij} \frac{\partial}{\partial \xi^j} \left(\frac{P}{|\boldsymbol{\xi}|}\right)^l T_l(x), \quad (26)$$

$$\nu_{1\text{PN}}^{jS_L} = -\frac{8GM}{c^3} \Omega P \frac{J_{l-1}}{l+4} \left[1 - (\boldsymbol{\sigma} \cdot \mathbf{e}_3)^2\right]^{[l/2]} P^{ij} \frac{\partial}{\partial \xi^j} \frac{(\boldsymbol{\sigma} \times \mathbf{d}_\sigma) \cdot \mathbf{e}_3}{d_\sigma} \left(\frac{P}{|\boldsymbol{\xi}|}\right)^l U_{l-1}(x), \quad (27)$$

where the power representations of the Chebyshev polynomials read (Arfken & Weber, 1995),

$$T_l(x) = \frac{l}{2} \sum_{n=0}^{[l/2]} \frac{(-1)^n}{n!} \frac{(l-n-1)!}{(l-2n)!} (2x)^{l-2n} \quad \text{and} \quad U_l(x) = \sum_{n=0}^{[l/2]} \frac{(-1)^n}{n!} \frac{(l-n)!}{(l-2n)!} (2x)^{l-2n}, \quad (28)$$

with $T_0 = 1$. The real variable x in (26) and (27) is defined by

$$x = \left(1 - (\boldsymbol{\sigma} \cdot \mathbf{e}_3)^2\right)^{-1/2} \left(\frac{\mathbf{d}_\sigma \cdot \mathbf{e}_3}{d_\sigma}\right) \quad \text{where} \quad -1 \leq x \leq +1. \quad (29)$$

It is just this highly remarkable fact, that the tangent vector $\boldsymbol{\nu}$ is given by Chebyshev polynomials, which allows for a strict determination of the upper limits of the angle of total light deflection in (13). This is because the upper limits of Chebyshev polynomials are given by

$$|T_l| \leq 1 \quad \text{and} \quad |U_{l-1}| \leq l. \quad (30)$$

Accordingly, in the 1.5PN approximation the total light deflection (13) is given by

$$\delta(\boldsymbol{\sigma}, \boldsymbol{\nu}) = \sum_{l=0}^{\infty} \delta(\boldsymbol{\sigma}, \boldsymbol{\nu}_{1\text{PN}}^{M_L}) + \sum_{l=1}^{\infty} \delta(\boldsymbol{\sigma}, \boldsymbol{\nu}_{1.5\text{PN}}^{S_L}). \quad (31)$$

The individual terms are given by ((Kopeikin, 1997), (Klioner, 1991), (Zschocke, 2023))

$$\delta(\boldsymbol{\sigma}, \boldsymbol{\nu}_{1\text{PN}}^{M_L}) = -\boldsymbol{\nu}_{1\text{PN}}^{M_L} \cdot \frac{\mathbf{d}_\sigma}{d_\sigma} \quad \text{and} \quad \delta(\boldsymbol{\sigma}, \boldsymbol{\nu}_{1.5\text{PN}}^{S_L}) = -\boldsymbol{\nu}_{1.5\text{PN}}^{S_L} \cdot \frac{\mathbf{d}_\sigma}{d_\sigma}, \quad (32)$$

where $\mathbf{d}_\sigma = \boldsymbol{\sigma} \times (\mathbf{x}_0 \times \boldsymbol{\sigma})$ is the impact vector, pointing from the body towards the unperturbed light ray at their closest distance. The absolute value, $d_\sigma = |\mathbf{d}_\sigma|$, is the impact parameter. By inserting (26) and (27) into (32) one obtains the following expressions for the individual mass-multipole and spin-multipole terms in the angle of total light deflection (31) (Zschocke, 2023):

$$\delta(\boldsymbol{\sigma}, \boldsymbol{\nu}_{1\text{PN}}^{M_L}) = -\frac{4GM}{c^2 d_\sigma} J_l \left(\frac{P}{d_\sigma}\right)^l \left[1 - (\boldsymbol{\sigma} \cdot \mathbf{e}_3)^2\right]^{[l/2]} T_l(x), \quad (33)$$

$$\delta(\boldsymbol{\sigma}, \boldsymbol{\nu}_{1.5\text{PN}}^{S_L}) = -\frac{8GM}{c^3} J_{l-1} \frac{\Omega l}{l+4} \left(\frac{P}{d_\sigma}\right)^{l+1} \frac{(\boldsymbol{\sigma} \times \mathbf{d}_\sigma) \cdot \mathbf{e}_3}{d_\sigma} \left[1 - (\boldsymbol{\sigma} \cdot \mathbf{e}_3)^2\right]^{[l/2]} U_{l-1}(x), \quad (34)$$

where (33) is valid for $l \geq 0$, while (34) is valid for $l \geq 3$. Thus far, it has not been possible to determine the upper limits of the total light deflection terms in (33) and (34), because these scalar functions are pretty much involved. In order to determine their upper limits, one actually would have to calculate their first derivatives with respect to variable x , and then to solve the corresponding algebraic equation of some order n , which is increasing with increasing multipole order l . However, according to the group theory of (Galois, 1846) there exist, in the general case, no radicals for solving such equations for orders $n > 4$. Therefore, it is essential to recognize that the angle of total light deflection is just given in terms of Chebyshev polynomials of first and second kind. Only because of this important fact it is possible to determine the upper limits of (33) and (34) by means of relations (30). Because the impact parameter is larger or equal to the equatorial radius of the body, $d_\sigma \geq P$, one obtains from (33) and (34),

$$\left| \delta \left(\boldsymbol{\sigma}, \boldsymbol{\nu}_{1\text{PN}}^{M_l} \right) \right| \leq \frac{4GM}{c^2} \frac{|J_l|}{P} \quad \text{and} \quad \left| \delta \left(\boldsymbol{\sigma}, \boldsymbol{\nu}_{1.5\text{PN}}^{S_l} \right) \right| \leq \frac{8GM}{c^3} \Omega \frac{l^2}{l+4} |J_{l-1}|, \quad (35)$$

where the inequality on the l.h.s. and r.h.s. are valid for $l \geq 0$ and $l \geq 3$, respectively; for the case of spin-dipole ($l = 1$) one finds $\left| \delta \left(\boldsymbol{\sigma}, \boldsymbol{\nu}_{1.5\text{PN}}^{S_1} \right) \right| \leq \frac{4GM}{c^3} \Omega \kappa^2$ (Klioner, 1991), where κ^2 is the dimensionless moment of inertia. These inequalities (35) for the total light deflection are strictly valid in the 1PN and 1.5PN, and can be used to decide, whether a specific multipole term needs to be taken into account in the light propagation model for a given goal accuracy of future astrometry missions aiming at the sub-micro-arcsecond and nano-arcsecond level. Some numerical values are presented in Table 1 for the case of light deflection of the giant planets Jupiter and Saturn.

Table 1: The upper limits of total light deflection at giant planets Jupiter and Saturn caused by their mass-multipoles and spin-multipoles according to Eqs. (35). All values are given in micro-arcsecond (μas). A blank entry indicates the light deflection is smaller than a nano-arcsecond (nas). For the physical parameters M, P, J_l, Ω standard values are used (Zschocke, 2023).

Light deflection	Jupiter	Saturn	Light deflection	Jupiter	Saturn
$ \delta(\boldsymbol{\sigma}, \boldsymbol{\nu}_{1\text{PN}}^{M_0}) $	16.3×10^3	5.8×10^3	$ \delta(\boldsymbol{\sigma}, \boldsymbol{\nu}_{1.5\text{PN}}^{S_1}) $	0.17	0.04
$ \delta(\boldsymbol{\sigma}, \boldsymbol{\nu}_{1\text{PN}}^{M_2}) $	239	94	$ \delta(\boldsymbol{\sigma}, \boldsymbol{\nu}_{1.5\text{PN}}^{S_3}) $	0.026	0.008
$ \delta(\boldsymbol{\sigma}, \boldsymbol{\nu}_{1\text{PN}}^{M_4}) $	9.6	5.41	$ \delta(\boldsymbol{\sigma}, \boldsymbol{\nu}_{1.5\text{PN}}^{S_5}) $	0.001	—
$ \delta(\boldsymbol{\sigma}, \boldsymbol{\nu}_{1\text{PN}}^{M_6}) $	0.55	0.50	$ \delta(\boldsymbol{\sigma}, \boldsymbol{\nu}_{1.5\text{PN}}^{S_7}) $	—	—
$ \delta(\boldsymbol{\sigma}, \boldsymbol{\nu}_{1\text{PN}}^{M_8}) $	0.04	0.06	$ \delta(\boldsymbol{\sigma}, \boldsymbol{\nu}_{1.5\text{PN}}^{S_9}) $	—	—
$ \delta(\boldsymbol{\sigma}, \boldsymbol{\nu}_{1\text{PN}}^{M_{10}}) $	0.003	0.01	$ \delta(\boldsymbol{\sigma}, \boldsymbol{\nu}_{1.5\text{PN}}^{S_{11}}) $	—	—

6. CONCLUSION

The determination of the upper limits of the angle of total light deflection provides a criterion, up to which order in l the mass-multipoles \hat{M}_L and the spin-multipoles \hat{S}_L need to be taken into account. Such a criterion simplifies considerably the relativistic modeling of light trajectories for future ultra-high precision astrometry missions on the sub- μas level of accuracy. In our investigation we have determined the unit tangent vector of the light ray at future infinity of the light trajectory by Eqs. (26) and (27) as well as strict upper limits for the total light deflection angle by Eqs. (35) for higher mass-multipoles and spin-multipoles. The remarkable fact, that the unit tangent vector of the light ray at future infinity is naturally given by Chebyshev polynomials, allows for a strict

mathematical statement about the upper limits of the total light deflection.

Acknowledgment

This work was funded by Deutsche Forschungsgemeinschaft (DFG): grant number 447922800.

APPENDIX

In this appendix we will demonstrate the limit (19). We shall use $\mathbf{x} = \mathbf{x}_N + \mathcal{O}(c^{-2})$ and hence $r = |\mathbf{x}_N| + \mathcal{O}(c^{-2})$. The gauge terms in the geodesic equation (17) consist of two pieces, $\ddot{\mathbf{x}}_{\text{gauge}} = \ddot{\mathbf{x}}_{\text{g1}} + \ddot{\mathbf{x}}_{\text{g2}}$. Their spatial components are given by

$$\frac{\ddot{x}_{\text{g1}}^j(t)}{c^2} = +\partial_j \xi^0_{,k} \sigma^i \sigma^j \sigma^k \quad \text{and} \quad \frac{\ddot{x}_{\text{g2}}^j(t)}{c^2} = -\partial_j \xi^i_{,k} \sigma^j \sigma^k, \quad (36)$$

where the gauge vectors are given by Eqs. (8) and (9). Let us consider the first term in (36). Using $(r^{-1})_{,jk} = 3x_j x_k / r^5 - \delta_{jk} / r^3$, one obtains

$$\frac{\ddot{\mathbf{x}}_{\text{g1}}(t)}{c^2} = +\frac{8G}{c^3} \sum_{l=0}^{\infty} \frac{(-1)^l}{l!} \hat{\partial}_L \frac{\hat{W}_L}{r^3} \boldsymbol{\sigma} - \frac{12G}{c^3} \sum_{l=0}^{\infty} \frac{(-1)^l}{l!} \hat{\partial}_L \frac{\hat{W}_L}{r^5} (d_\sigma)^2 \boldsymbol{\sigma}, \quad (37)$$

where $(\boldsymbol{\sigma} \cdot \mathbf{x})^2 = r^2 - (d_\sigma)^2 + \mathcal{O}(c^{-2})$ has been used. This expression has to be integrated over the time variable. To apply the advanced integration methods developed by (Kopeikin, 1997), we have to transform (37) from (ct, \mathbf{x}) into terms of two new variables, $c\tau = \boldsymbol{\sigma} \cdot \mathbf{x}_N$ and $\xi^i = P^{ij} x_N^j$, which are independent of each other, and obtain (note that $\boldsymbol{\xi} = d_\sigma$ hence $(d_\sigma)^2 = \boldsymbol{\xi} \cdot \boldsymbol{\xi} = \xi^2$)

$$\frac{\ddot{\mathbf{x}}_{\text{g1}}(\tau)}{c^2} = +\frac{4G}{c^3} \sum_{l=0}^{\infty} \frac{(-1)^l}{l!} \hat{W}_L \hat{\partial}_L \left(\frac{2}{(r_N)^3} - \frac{3(\xi)^2}{(r_N)^5} \right) \boldsymbol{\sigma}, \quad (38)$$

where the double-dot in (38) means twice the total derivative with respect to variable τ . The differential operator (38) has been given by Eq. (23). To get the coordinate velocity of the light signal, one has to integrate (38) over variable $c\tau$ (note that $dc\tau = dct$) and obtains for the spatial components

$$\frac{\dot{x}_{\text{g1}}^i}{c} = +\frac{4G}{c^3} \frac{\partial}{\partial c\tau} \sum_{l=0}^{\infty} \frac{(-1)^l}{l!} \hat{\partial}_L \frac{\hat{W}_L}{r} \sigma^i. \quad (39)$$

A similar calculation can be performed for the second gauge term in (36), which yields

$$\frac{\dot{x}_{\text{g2}}^j}{c} = -\frac{4G}{c^2} \frac{\partial}{\partial c\tau} \left(\sum_{l=0}^{\infty} \frac{(-1)^l}{l!} \hat{\partial}_{lL} \frac{\hat{X}_L}{r} + \sum_{l=1}^{\infty} \frac{(-1)^l}{l!} \hat{\partial}_{l-1L} \frac{\hat{Y}_{lL}}{r} + \sum_{l=1}^{\infty} \frac{(-1)^l}{l!} \frac{l}{l+1} \epsilon_{iab} \hat{\partial}_{aL-1} \frac{\hat{Z}_{bL-1}}{r} \right). \quad (40)$$

By inserting (23) into (39) and (40) one finds that these terms vanish at infinity, and we get

$$\lim_{\tau=\pm\infty} \frac{\dot{\mathbf{x}}_{\text{gauge}}(\tau)}{c} = \lim_{\tau=\pm\infty} \frac{\dot{\mathbf{x}}_{\text{g1}}(\tau)}{c} + \lim_{\tau=\pm\infty} \frac{\dot{\mathbf{x}}_{\text{g2}}(\tau)}{c} = 0. \quad (41)$$

Thus, by transforming (41) back from $(c\tau, \boldsymbol{\xi})$ into (ct, \mathbf{x}) , we have shown the validity of (19).

7. REFERENCES

Arfken, G.B., Weber, H.J., 1995, "Mathematical methods for physicists", London, Academic Press, 4th Edition, 1995.

- Blanchet, L., Damour, T., 1986, "Radiative gravitational fields in general relativity: I. General structure of the field outside the source", *Phil. Trans. R. Soc. London A*, 320, pp. 379 - 430.
- Damour, T., Iyer, B.R., 1991, "Multipole analysis for electromagnetism and linearized gravity with irreducible Cartesian tensors", *Phys. Rev. D*, 43, pp. 3259 - 3272.
- Einstein, A., 1915, "Die Feldgleichungen der Gravitation", *Sitz.ber. Akad. Wiss. Berlin*, 2, pp. 844 - 847.
- Galois, E., 1846, "Mémoire sur les conditions de résolubilité des équations par radicaux", *Journal de Mathématiques Pures et Appliquées*, 11, pp. 381 - 444.
- Johnston, K.J., McCarthy, D.D., Luzum, B.J., Kaplan, G.H., 2000, "Towards Models and Constants for Sub-Microarcsecond Astrometry", *Proceedings of IAU Colloquium 180*, U.S. Naval Observatory, Washington D.C., March 26 - April 2, 2000.
- Klioner, S.A., 1991, "Influence of the quadrupole field and rotation of objects on light propagation", *Sov. Astron.*, 35, pp. 523 - 530.
- Klioner, S.A., Peip, M., 2003, "Numerical simulations of the light propagation in the gravitational field of moving bodies", *A & A*, 410, pp. 1063 - 1074.
- Kopeikin, S.M., 1997, "Propagation of light in the stationary field of multipole gravitational lens", *J. Math. Phys.*, 38, pp. 2587 - 2601.
- Kopeikin, S., Efroimsky, M., Kaplan, G., 2012, "Relativistic Celestial Mechanics of the Solar System", Wiley-VCH, Signapore.
- Misner, C.W., Thorne, K.S., Wheeler, J.A., 1973, "Gravitation", New York: W.H. Freeman.
- Thorne, K.S., 1980, "Multipole expansions of gravitational radiation", *Rev. Mod. Phys.*, 52, pp. 299 - 339.
- Zschocke, S., 2022, "Time delay in the quadrupole field of a body at rest in 2PN approximation", *Phys. Rev. D*, 106, 104052, pp. 1 - 35.
- Zschocke, S., 2023, "Total light deflection in the gravitational field of an axisymmetric body at rest with full mass and spin multipole structure", *Phys. Rev. D*, 107, 124055, pp. 1 - 25.

POSTFACE

Journées “Systèmes de Référence Spatio-temporels”

Previous editions

- October 7-9 2019, Observatoire de Paris & Université Pierre et Marie Curie, Paris : "Astrometry, Earth Rotation, and Reference Systems in the GAIA era". <https://syrte.obspm.fr/astro/journees2019/LATEX/JOURNEES2019.pdf>
- September 25-27 2017, Universidad de Alicante : "Journées des Systèmes de Référence et de la Rotation Terrestre: Furthering our knowledge of Earth Rotation". <https://web.ua.es/journees2017/>
- September 22-24 2014, Pulkovskaya Observatoriya, St. Petersburg : "Furthering our knowledge of Earth Rotation". <https://syrte.obspm.fr/jsr/journees2014/pdf/>
- September 16-18 2013, Observatoire de Paris-Meudon, France : "Scientific developments from highly accurate space-time reference systems". <https://syrte.obspm.fr/jsr/journees2013/pdf>
- September 19-21 2011, TU Wien, Vienna: "Earth rotation, reference systems and celestial mechanics: synergies of geodesy and astronomy". <https://syrte.obspm.fr/jsr/journees2011/pdf/>
- September 20-22 2010, Observatoire de Paris & Ecole Normale Supérieure, Paris: "New challenges for Reference Systems and Numerical Standards in Astronomy". <https://syrte.obspm.fr/jsr/journees2010/pdf/>
- September 22-24 2008, Lohrmann Observatorium, TU Dresden: "Astrometry Geodynamics and Astronomical Reference Systems". <https://syrte.obspm.fr/jsr/journees2008/pdf/>
- September 17-19 2007, Observatoire de Paris : "The Celestial Reference Frame for the Future". <https://syrte.obspm.fr/jsr/journees2007/pdf/>
- September 19-21 2005, Centrum Badań Kosmicznych, Warsaw: "Earth dynamics and reference systems five years after adoption of the IAU 2000 resolutions". <https://syrte.obspm.fr/jsr/journees2005/pdf/>
- September 20-22 2004, Observatoire de Paris: "Fundamental astronomy : New concepts and models for high accuracy observation". <https://syrte.obspm.fr/jsr/journees2004/pdf/>
- September 22-25 2003, Institut Pribladnoy Astronomii, St. Petersburg: "Astrometry, Geodynamics and Solar System Dynamics : from milliarcsseconds to microarcseconds". <https://syrte.obspm.fr/jsr/journees2003/pdf/>

- September 25-28 2002, Institutul Astronomic al Academiei Române, Bucharest: Astronomy from ground and from space. <https://syrtte.obspm.fr/jsr/journees2002/pdf/>
- September 24-26 2001, Observatoire Royal de Belgique, Brussels: Influence of geophysics, time and space reference frames on Earth rotation studies. <https://syrtte.obspm.fr/jsr/journees2001/pdf/>
- September 18-20 2000, Observatoire de Paris: "J2000, a fundamental epoch for origins of reference systems and astronomical models". Proceedings ed. by N. Capitaine.
- September 13-15 1999, Lohrmann Observatorium, TU Dresden: "Journées 1999 & IX. Lohrmann-Kolloquium: Motion of Celestial Bodies, Astrometry and Astronomical Reference Frames". Proceedings ed. by M. Soffel & N. Capitaine.
- September 21-23 1998, Observatoire de Paris: "Conceptual, conventional and practical studies related to Earth rotation". Proceedings ed. by N. Capitaine.
- September 22-24 1997, Astronomický ústav, Prague Planetarium: "Reference systems and frames in the space era: present and future astrometric programmes". Proceedings ed. by J. Vondrák & N. Capitaine.
- September 23-25 1996, Observatoire de Paris: "Deux siècles d'évolution du Système du Monde. Hommage à Laplace". Proceedings ed. by N. Capitaine.
- September 18-20 1995, Centrum Badań Kosmicznych, Warsaw: "Earth Rotation, Reference Systems in Geodynamics and Solar System". Proceedings ed. by N. Capitaine, B. Kolaczek, S. Débarbat.
- June 13-14 1994, Observatoire de Paris: "Les systèmes de référence et les constantes astronomiques fondamentales". Proceedings ed. by N. Capitaine.
- June 1-2 1992, Observatoire de Paris: "Géodynamique Globale et Systèmes de Référence"
- June 3-4 1991, Observatoire de Paris: "Métrologie et Astrométrie". Proceedings ed. by N. Capitaine.
- May 28-30 1990, Observatoire de Paris: "Colloque André Danjon". Proceedings ed. by N. Capitaine & S. Débarbat.
- April 24-25 1989, Observatoire de Paris: "Astrométrie et relativité". Proceedings ed. by N. Capitaine.
- June 20-21 1988, Observatoire de Paris: "Journées Systèmes de référence spatio-temporels". Proceedings ed. by N. Capitaine.